Structural assessment of the historical wrought iron tie rods used in the Duomo di Milano

Master Thesis

Simone van der Meer

TU Delft

POLITECNICO MILANO 1863

Structural assessment of the historical wrought iron tie rods used in the Duomo di Milano

By

S.L. van der Meer

in partial fulfilment of the requirements for the degree of

Master of Science

in Materials Science and Engineering

Faculty of Mechanical, Maritime and Materials Engineering,

at the Delft University of Technology,

to be defended publicly on Thursday July 13, 2017 at 14:00 AM.

Student number:	4418042	
Supervisor:	Dr. Ir. M. Janssen,	TU Delft
Thesis committee:	Prof. R. Felicetti,	Politecnico di Milano
	Prof. Dr. Ir. J. Sietsma,	TU Delft
	Dr. V. Popovich,	TU Delft

TU Delft

POLITECNICO MILANO 1863

Acknowledgements

I would like to express my sincere gratitude to Prof. Roberto Felicetti, from the Department of Civil and Environmental Engineering at Politecnico di Milano, for giving me the opportunity to work on this project and his guidance during the thesis. I would further like to thank Mariagrazia Bellanova for her continuous support throughout the thesis.

Furhermore, I would like to express my gratitude to Dr. Ir. Janssen for his supervision and support during the thesis and in particular for the technical feedback on the fracture mechanical aspects.

I would like to acknowledge the tests made by the Material and Testing Laboratory (LPM) and the Laboratory of the Mechanical Engineering Department at Politecnico di Milano.

I want to thank my friends from Milan for making my experience abroad unforgettable. I also want to thank the rest of my friends and family for their encouragements and laughter, while being in Milan and after returning to the Netherlands.

Special thanks go out to my parents for always being there for me, wherever I am.

Abstract

The tie rods in the Duomo are structural elements, subject to monotonic loading and cyclic loading. Non-destructive testing is used to find cracks and determine their geometry. Lamb waves are applied initially to determine whether there are cracks present in the tie rod and to estimate their positions. The cracks are subsequently located using eddy current testing. Finally the geometries of the cracks are determined using active infrared (IR) thermography. Experimental testing in the field of fracture mechanics is done to determine the fracture toughness of the wrought iron of which the tie rods are made. Combining the geometry of the crack with the fracture toughness of the material, leads to an estimation of the critical crack size.

The tie rods are made of wrought iron. The material properties are very heterogeneous, in terms of microstructure and inclusions. A tie rod is made out of multiple wrought iron bars of 1-1.5 meters. These bars are welded together under an angle of 27°. Cracks of two damaged tie rods are found to be under such an angle. The search for cracks will thus be concentrated on inclined cracks with a repetition of 1-1.5 meters.

Lamb waves is the first technique applied. An ultrasonic tomograph A1040 MIRA is used for testing. This device has in total 48 transducers, that can be used both as transmitter and as receiver. The modelling of Lamb waves travelling in tie rods and the signal processing are based on the possibilities of the MIRA. The dispersion behaviour of Lamb waves is modelled to understand the wave propagation in tie rods and the influence it has on the testing done with the MIRA. Using this knowledge, proper testing settings are found. Subsequently, signal processing is considered. The main objective of this part is to increase the signal-to-noise ratio, to be able to identify cracks present in the tie rods. Multiple techniques are of interest, like the dispersion compensation technique.

The position of the cracks in the tie rod is determined using eddy current testing. Commercial eddy current probes are too sensitive to the surface and to small discontinuities to be applied to tie rods. Therefore, new probes are developed to overcome these drawbacks. The inclination of the crack is taken into account in the design of these probes. Two probes are designed, both for the horizontal face and for the vertical face of the tie rod. The vertical face of the tie rods, in function in the Duomo, are best accessible. Therefore, on-site testing is done with the probe specially designed for that face.

Active infrared thermography is implemented to establish the size and the geometry of the crack. A finite element analysis has been performed to model the propagation of heat through a tie rod with a crack. This is followed by experimental testing in the laboratory carried out on a broken tie rod. Finally, the results of the modelling and of the experimental testing are compared.

The last part has a fracture mechanical nature. The fracture toughness of the material is determined assuming both linear-elastic and elastic-plastic material behaviour. Also the fatigue behaviour is evaluated. The values obtained from experimental testing have been applied to a simplified model of the crack geometry to determine the critical crack size of the tie rod, for monotonic loading, and the threshold crack size, for cyclic loading. Fatigue life is predicted taking the threshold crack size as the initial crack size and the critical crack size as the final crack size.

Table of Contents

CHAPTER 1: INTRODUCTION

1.1 ENGINEERING IN BUILT HERITAGE

The preservation and maintenance of cultural heritage is one of the present-day challenges. From a structural point of view, it means ensuring a high enough bearing capacity to support the loads of everyday use, but also in case of natural disasters. This must be done without changing its heritage value, so that future generations are able to enjoy the cultural heritage as the current generation does. The long lifetime of historical buildings makes the durability of these structure one of the key issues. The compatibility and the durability of the intervention needs to be ensured. An adequate intervention should therefore be based on the cause of the problem and not on the consequence.

In vaulted constructions, including masonry cathedrals, metallic ties were often used during the construction stage as a structural element [1]. These tie rods are handmade elements and can be older than 600 years. They are usually made of wrought iron. The basic material properties of wrought iron, like tensile strength and fracture toughness, are unknown and difficult to determine. In the case of cultural heritage, it is preferable to determine these values with non-destructive methods. In this way the heritage value of the structure does not get compromised. The disadvantage is that the results of non-destructive testing are often difficult to interpret.

Ancient builders used the trial and error approach to the construction of heritage structures. Decisions were made based on previous negative or positive experiences, while nowadays these decisions are based on modern structural theory. The knowledge on historical structures and the materials used was partially lost in the last two centuries, due to the focus of the scientific community on the use of modern materials.

Currently, it is recognized that in case of cultural heritage a multidisciplinary approach should be used for solving the problems. This can be accomplished by combining several fields of expertise, like history of art, architecture, civil, mechanical and materials engineering. The final diagnosis and safety evaluation should be made by exploiting the combination of investigation techniques of the different fields of expertise.

1.2 THE CATHEDRAL OF MILAN ("DUOMO DI MILANO")

1.2.1 Structural History

The construction of the Duomo di Milano started in the 14th century. The different building stages of the Duomo are shown in Figure 1.1. This map is based on a historical investigation. It is partly designed in a Gothic style and it has the highest main nave compared to other cathedral from the same period. Part of the Duomo is built on the remains of a previous church, the Santa Maria Maggiore. This church was demolished for the construction of the current Duomo. The remains of this church are still present underneath the Duomo. The current Duomo does not have a bell tower, but historical drawings show evidence that a provisional bell tower existed. It was situated above the main nave vault in the 6th bay. There is evidence that the bell tower was demolished in 1866, due to severe damage. The cause of the damage is unknown. The Duomo is one of the few cathedrals that have permanent metallic tie rods as part of its construction. In other cathedrals, these ties might have been used during the construction and removed afterwards.

1.2.2 Important Events

Events during the structural life of the Duomo have to be taken into account, because they potentially influence the initiation and propagation of damage [3], [4]. Damage in a certain zone can also influence damage in another zone. This is due to load redistribution that occurs when a certain structural element fails.

In the 15th century the four piers under the *tiburio* were damaged. Hidden arches were constructed to support the structure above. They were built with an offset of 90 cm relative to the axis of the piers. This caused the failure of the ties connecting these four piers. These ties remained broken for 500 years until the restoration in 1980-1984 [5], [6]. The ties were replaced with ties made of

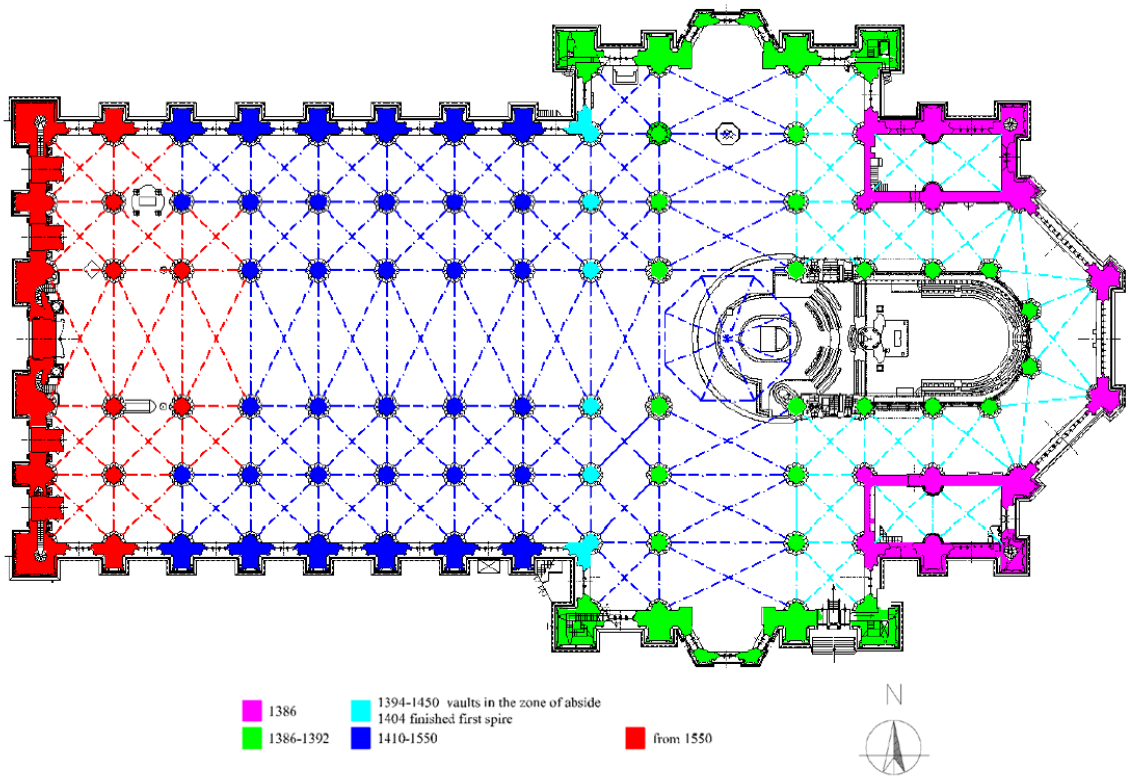

Figure 1.1: Building stages of the Duomo [2].

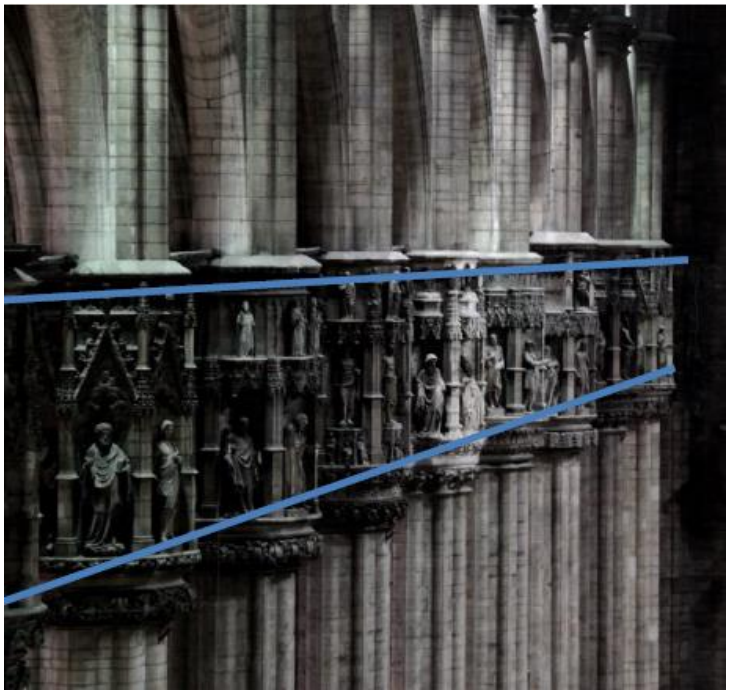

Figure 1.2: Differences in the levelling of piers in the Duomo [8].

modern steel. This event caused significant deformation of the columns in that zone. It also might have caused redistribution of the load to other zones of the Duomo.

In the 19th and 20th century industrial companies caused severe water drainage from the soil under the Duomo. This resulted in a lowering of the ground water level of 20 meters in the last 200 years [7]. This caused a differential settlement under the piers. The possible consequence of the differential settlement is the differences in the levelling of the piers, shown in Figure 1.2. This might have resulted in the high stress present in the transversal arches *voussoirs*, which were replaced in the past and are still visible as new stones [5], [6]. The damage that occurred under the *tiburio* accelerated due to this settlement.

Seismic loading should always be taken into account in built heritage. The zone of Milan is a low-seismicity zone and no significant seismic events have been recorded in the past. The metro, present under the Duomo since 1964, does cause vibrations. The influence of these vibrations on the structural behaviour is still unknown.

1.2.3 Tie Rods Used in the Duomo

The French architect Mignot expressed his concern at the beginning of the construction about the slenderness of the elements used [9]. After hearing this critique, the ancient builders of the Duomo decided to connect the piers with iron tie rods. The tie rods, piers and buttresses work in a combined action [4]. This ensures the structural stability throughout the Cathedral.

The tie rods in the Duomo are covered with dirt, dust and an oxidised reddish layer. They are clamped in the masonry through a fork connection. This clamping system enables the transfer of the axial force to the masonry structure. The ties were handmade in a time span of 200 years and contain many impurities, voids and other defects on the inside and on the outside of the material. Also due to the long time span in which they were made, they can differ in chemical composition and in material characteristics. Damage of these rods can be caused by combinations of different factors: inherent problems in the material, overstressing, environmental effects, use of the building, events

and poor maintenance. Another source of damage can be daily and yearly thermal cycles experienced by the tie rods. The daily thermal cycles are due to the presence of illumination lamps and can cause a concentration of stresses in the zones around the lamps. This problem has been reduced in severity, by using LED lamps for the lighting of the cathedral. The yearly thermal cycle is caused by the difference in temperature due to the seasons.

Most of the tie rods present in the Duomo could be the original, because there is no evidence of their failure or replacement. Figure 1.3 shows the position of the tie rods in the Duomo on which information is available. Historical evidences dating back to the 70's are present in the archives of the Veneranda del Fabbrica del Duomo, the historic organisation responsible for the preservation and the restoration of the Duomo. They concern nine tie rods, which were damage at the anchorage. The four tie rods under the *tiburio* [4] failed in 1470. Two other tie rods failed more recently and were replaced. The failure of tie rod 58-88 was discovered in May 2009 during periodic measurements [10]. The annual variation of the verticality of pier 88 did not correspond to the trend of the previous years. This tie was replaced with a new steel tie rod. During a visual inspection a few years later, it was discovered that tie rod 61-91 had a heavy thorough crack. This rod was replaced in 2013.

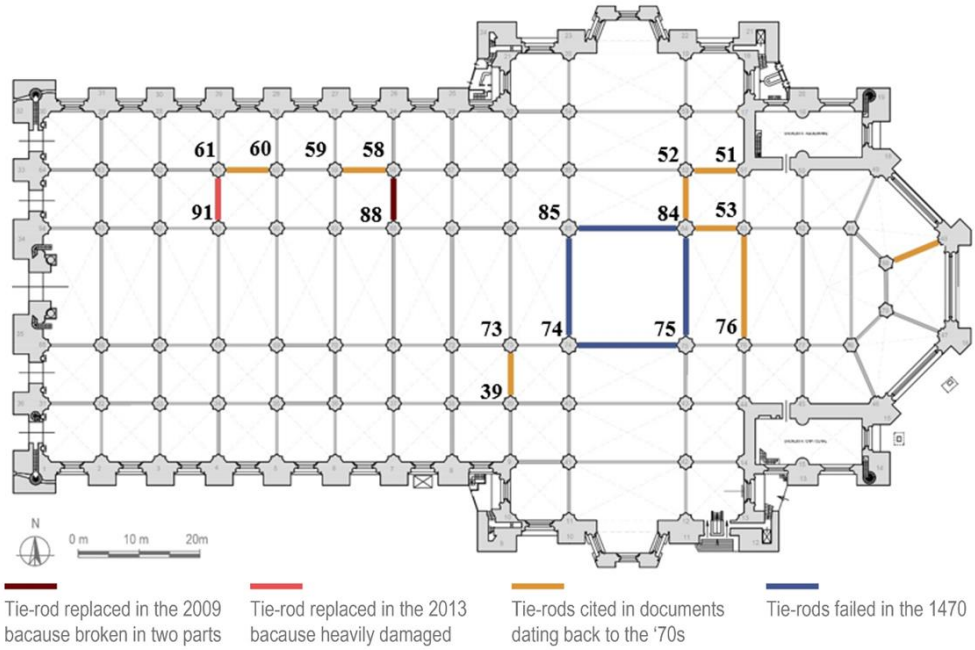

Figure 1.3: Position of tie rods on which information is available.

1.3 Focus of the Thesis

The structural safety of wrought iron tie rods in the Duomo di Milano will be examined in the following thesis. This is done by linking two aspects. The first aspect is the identification and characterization of defects using non-destructive testing (NDT). The second aspect is the fracture mechanical properties of the material.

First the general theory, needed for the remainder of the thesis, is introduced. Starting with the theory on wrought iron as a material, in Chapter 2. In this chapter the manufacturing techniques and the material properties of wrought iron are examined, followed by a description of the known properties of the wrought iron used in the tie rods in the Duomo. Chapter 3 gives general information about non-destructive testing (NDT), including the application of NDT on the tie rods in the Duomo. There are three main levels involved in the identification of cracks and for each scale a NDT technique is chosen.

NDT starts at the global level, at which the presence of flaws in a tie rod is established, studied in Chapter 4. The method used is guided ultrasonic waves, called Lamb waves. The behaviour of Lamb waves in tie rods is modelled and the obtained information is used to be able to determine the optimum settings for experimental settings. Lastly, the signal processing is investigated to increase the readability of the measurements.

The next level is the intermediate level, discussed in Chapter 5. At this level, the location of the crack along the tie rod is found. The method applied is eddy current testing. First a commercial low frequency eddy current probe is considered. Subsequently, two probes are designed for the purpose of scanning the tie rods of the Duomo. Lastly, the commercial probe and one of the two customized probes are used in on-site.

The local level is the last level, considered in Chapter 6. At this scale the geometry of the defects, found at the other two levels, is determined. The method employed at this level is active infrared thermography. First the Finite Element Method is employed to model the heat wave propagation in a tie rod with a crack. Afterwards, the experimental testing is done. The experimental results can be compared with the model to better interpret the results.

The second part of this thesis considers the fracture mechanics of wrought iron, in Chapter 7. The fracture toughness of the material is determined, using the linear elastic fracture mechanics (LEFM) approach and the elastic-plastic fracture mechanics (EPFM) approach. The obtained fracture toughness is used to obtain the critical crack size for cracks in a tie rod. The geometry of this crack may be very complex and therefore a simplified model is assumed. Next to the monotonic loading, also fatigue due to seasonal temperature changes is considered. The crack length, at which crack propagation occurs due to fatigue, and the critical crack length, due to monotonic loading, are of interest for determining the fatigue life prediction.

1.4 REFERENCES

[1] M. L'Hèritier, P. Dillmann, A. Timbert, and P. Bernardi, "The role of iron armatures in gothic constructions: reinforcement, consolidation or commissioner's choice," in *Proceedings of the 4th International Congress of Construction History*, 2012, pp. 557–564.

[2] G. Majo, A., & Vigini, "Il Duomo di Milano : dizionario storico artistico e religioso," vol. Milano: NE, 1986.

[3] P. Roca, "Considerations on the significance of history for the structural analysis of ancient constructions," *Struct. Anal. Hist. Constr. IV*, pp. 63–73, 2004.

[4] D. Coronelli, B. Caggioni, and F. Zanella, "Cathedral of Milan: Structural History of the Load-Bearing System," *Int. J. Archit. Herit.*, vol. 9, no. 4, pp. 510–528, 2015.

[5] C. Ferrari da Passano, *Il Duomo rinato*. Vigevano: Diakronia, 1988.

[6] C. Ferrari da Passano, *Il Nuovo per Salvare l'antico: Il Restauro Statico Conservativo dei Monumenti Vincolati*. Milano: Veneranda Fabbrica del Duomo, 2005.

[7] C. Niccolai, "Il sottosuolo del territorio di Milano (The underground of Milan's Territory)," *Riv. Ital. di Geotec. (Italian Geotech. Journal)*, vol. 1, pp. 7–33, 1967.

[8] M. Vasic, "A Multidisciplinary Approach for the Structural Assessment of Historical Constructions with Tie-rods," Politecnico di Milano, 2015.

[9] F. del D. di Milano, "Annali della Fabbrica del Duomo di Milano dall'origine fino al presente (The annals of Fabbrica del Duomo from the origins till the present) Vol. I." p. 203, 1877.

[10] A. Giussani, "Relazione sulle misure eseguite per il controllo delle deformazioni del Duomo di Milano nei giorni 21, 23 e 28 Novembre 2011 (Report on deformation monitoring in the Cathedral of Milan on dates 21, 23 and 28 November 2011," Lecco: Politecnico di Milano, 2011.

CHAPTER 2: WROUGHT IRON

Archaeological iron can be subdivided into two categories; wrought iron and cast iron. Wrought iron is used for the tie rods in the Duomo. This category of iron contains less than 0.15 wt% carbon. The material consists out of two main components: high purity iron and slag. This slag is a glasslike substance that is mechanically interlocked with the iron. The addition of slag occurs during the manufacturing process and causes a fibrous structure. Much research has been done on historical wrought iron structures from the 18th century and later [1]–[4]. However, not much research can be found on wrought iron from the 14th to the 17th century [5], [6], in which the Duomo was constructed.

In this chapter, first the manufacturing techniques of wrought iron, employed in the time span the tie rods were made, are discussed. In Section 2.2, the structure of wrought iron is elaborated on. The mechanical properties are reviewed in Section 2.3. Lastly, the known material properties for the wrought iron of the tie rods in the Duomo are examined in Section 2.4.

2.1 MANUFACTURING

The manufacturing process of wrought iron differs from other manufacturing processes of iron, because the iron is not molten. The iron exists in a red hot pasty condition and the impurities are beaten or rolled out. This manufacturing process results in the typical characteristics of wrought iron.

2.1.1 The Bloomery Method

Wrought iron is made with the bloomery method. The iron ore is processed in a furnace in a carbon rich environment with a temperature of around 1200 ˚C. The iron does not melt in these conditions, but the iron oxides are reduced and they become a solid mass of metal called “bloom”. The bloom can be further processed in the desired shape by hot working. The main by-product of this process is an iron oxide-rich slag, formed by the reaction between iron oxide and silica. Other impurities present in the iron ore are often integrated in the slag. The type of impurities and thus the morphology of the slag depends on the raw materials, furnace design and operating parameters.

The stages of the production from bloom to product are shown in Figure 2.1. During the bloomery smelting particles of slag and charcoal become incorporated in the bloom. Then primary smithing is carried out by hammering the hot bloom. This is done to remove the slag on the surface and to expel the slag and charcoal present inside the bloom. In the meantime the bloom becomes a more manageable bar. This is followed by secondary smithing, where the metal bar is made into its final product. The bar is repeatedly heated and hammered in the required shape. Welding is done with a forge-welding process. The process needs to be carried out below the melting temperature (1538 ˚C) and above half of this temperature [7]. In this temperature range the iron is made of an austenitic ductile phase, in which the movement of dislocations is fast. The metal should be soft and the surface of the metal should be clean to obtain diffusion bonding. During this process a lot of metal is lost due to oxidisation of the iron. The oxidised crust needs to be removed before welding by hammering or the addition of flux. If the welding of wrought iron is not properly done, a plane of weakness can be the result. The slag is never fully removed during primary and secondary smithing. Hence primary slag inclusions are left in the wrought iron. Secondary slag inclusions can also be introduced during later stages of the production.

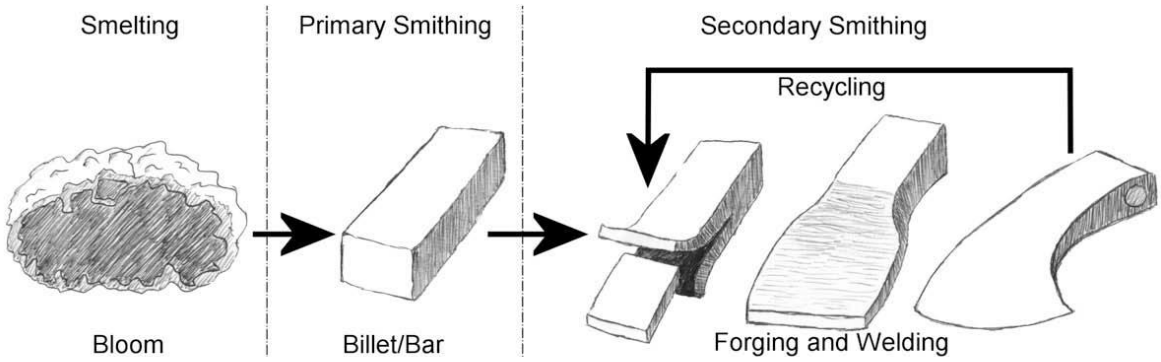

Figure 2.1: Production stages from bloom to a product made of wrought iron [7].

2.1.2 Direct and Indirect Method

For the production of wrought iron two methods exist: direct and indirect. The direct method was followed by the more complex indirect method. The transition period between the two methods is from the 14th to the 16th century [5]. In the direct method the iron ore is reduced in one step. The granulated ore reacts with fuel and becomes a porous iron bloom. The iron is never in a liquid state, but the SiO_2-rich slag is present in a liquid state. In this way the slag can be separated from the iron. The indirect method contains two steps, executed in two different furnaces. Granulated iron ore and fuel reacts in the blast furnace. This produces molten pig iron containing 4% carbon and some other elements like silicon, manganese and phosphorus. This pig iron is further refined in a separate fining hearth. In this step the iron is slowly remelted and solidified into a bloom. To remove excessive slag, the bloom is manipulated and hammered.

The direct method reduces iron and phosphorus oxides for the biggest part. The exact composition of the slag depends on the reduction efficiency. The first part of the indirect process, completely reduces iron and phosphorus oxides. The refining step defines the composition of the slag. Some compounds are not completely reduced or are reoxidised at the end of the process. The presence and amount of these non-reduced compounds depend on the ores and furnaces used. The identification of non-reduced compounds can therefore be used as a signature for the used system.

2.2 STRUCTURE

The structure of wrought iron depends strongly on its manufacturing process. This can be observed from a microscopic to a macroscopic scale. In this section first the microstructure will be discussed. Subsequently, zooming out from the microstructure, the material heterogeneity due to the slag inclusions will be considered.

2.2.1 Microstructure

The final microstructure of iron depends mainly on its chemical composition and the employed cooling rate. At room temperature the stable phase of pure iron is ferrite (α-phase), which has a body-centered cubic (BCC) crystal structure. Ferrite transforms to austenite (γ-phase) at 912˚C. Austenite has a face-centered cubic (FCC) crystal structure. Wrought iron has an average carbon content of 0.1 wt%. The Fe-C phase diagram is given in Figure 2.2, with wrought iron given as the red line. During the manufacturing process the iron ore is heated to 1200 ˚C and it is transformed to austenitic iron. When the iron is cooled down to around 900 ˚C, part of the austenite starts transforming into ferrite. Below the eutectoid temperature of 723 ˚C, the remaining austenite becomes pearlite. The pearlite phase is an alternating layered microstructure containing two phases, ferrite and cementite (Fe_3C). The thickness of the alternating layers becomes smaller if the cooling rate is increased. If the material is quenched from 1200 ˚C to room temperature, a metastable phase is formed called martensite. Martensite has a body-centred tetragonal (BCT) crystal structure. The morphology depends on its chemical composition. The structure is made up of needles, if the carbon content is below 0.6 wt%.

Another typical microstructure of wrought iron is the Widmanstätten structure [8], represented in Figure 2.3. This microstructure mainly occurs in low C steels (<0.3 wt%C), if the conditions are optimal. These conditions are coarse austenitic grains and a fast cooling from this phase. The Widmanstätten structure is made of needle-like proeutectoid ferrite, grown from the grain boundaries into the austenitic phase. Upon further cooling the austenitic phase is transformed into pearlite. In the final structure the Widmanstätten structure of proeutectoid ferrite is present in a pearlite matrix.

The typical microstructure of wrought iron is shown in Figure 2.4. In the figure on the left slag inclusions are observed. These slag inclusions are recognisable as the black element encircled. It can be seen in the figure on the right that wrought iron has a microstructure containing ferrite, pearlite and Widmanstätten ferrite-pearlite. The proeutectoid ferrite can be distinguished as the light part at the grain boundaries, while the pearlite is located within the grains.

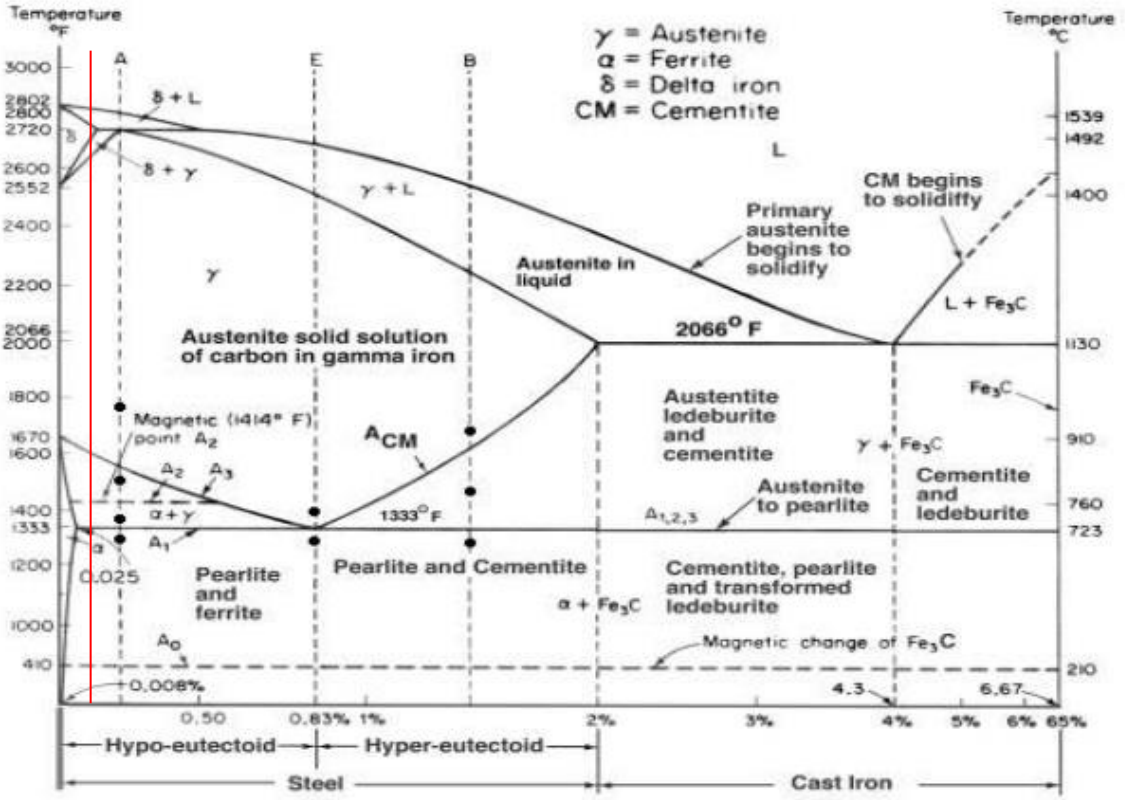

Figure 2.2: Phase diagram of Fe-C, wrought iron (red line).

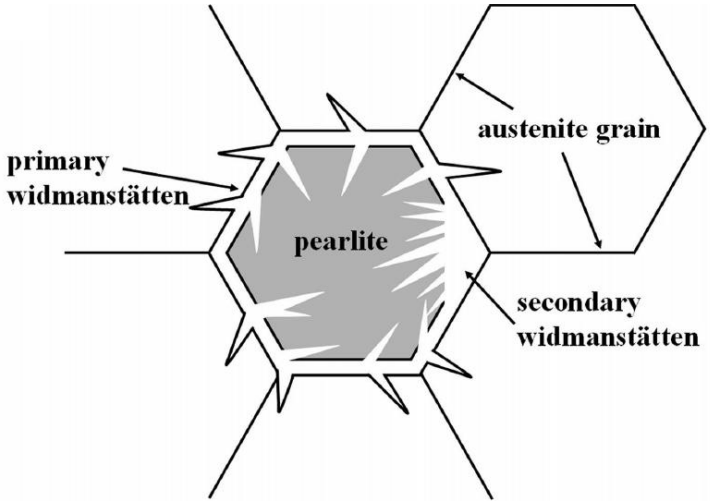

Figure 2.3: Schematic representation of Widmanstätten structure [8].

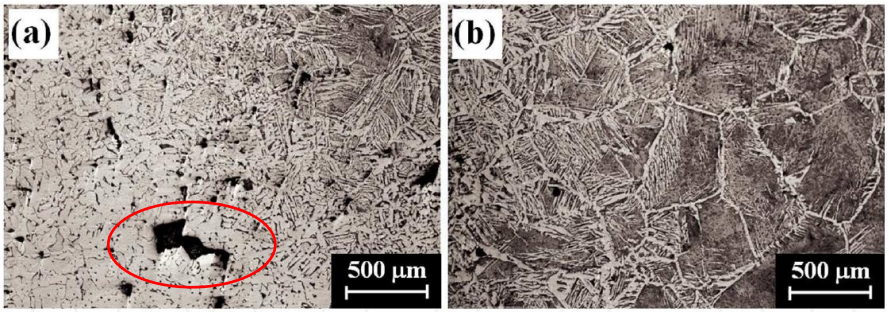

Figure 2.4: Optical microscopy images of the microstructure of wrought iron [8].

2.2.2 Heterogeneity

Wrought iron is a fibrous material due to its manufacturing process and the slag present in the material [9]. This fibrous structure can be clearly observed if the material fails, as shown in Figure 2.5. Small slag inclusions can be seen in Figure 2.4. These fibres are however due to bigger pockets of slag existing throughout the material, when the iron is in the red hot pasty condition. When the bloom is rolled to squeeze the slag out, these pockets of slag become elongated in one direction. In this way the fibres of slag become dispersed through the whole material. This makes wrought iron an anisotropic material.

The material properties of wrought iron depend on the iron ore used and the manufacturer. This combined with the heterogeneous microstructure creates an inconsistency of the material properties. The heterogeneous nature of wrought iron causes the performance of the material to vary significantly in time and location [5]. This can also be observed in the Duomo, where the tie rods have been made over a period of 200 years.

Figure 2.5: Fibrous nature of wrought iron [9].

2.3 Mechanical Properties

In the 19th century the steel production increased, phasing out wrought iron as a structural material. As a consequence, the knowledge about the mechanical properties of wrought iron has not been as well documented as for steel.

2.3.1 Strength

Wrought iron has a stress-strain curve of a typical ductile metal. Figure 2.6 shows the stress-strain plots for different specimen of wrought iron. These curves show the typical ductile behaviour, but also show the diversity in yield and ultimate tensile strengths. The strength of wrought iron and the ductility depends on multiple factors. One of these factors is the carbon and phosphorus content. Increasing the amount of these two elements in wrought iron, increases the strength and reduces the ductility. Another major factor is the amount and the distribution of the slag fibres, due to the brittle behaviour of the slag at service temperatures.

The distribution and orientation of the slag fibres causes an anisotropic behaviour of wrought iron. Along the extrusion direction, the material is stronger. In this direction for the research done by Hooper *et al*. [4], the yield strength is on average 214 MPa and the ultimate tensile strength is on average 306 MPa. While in the transversal direction, the average yield strength is 186 MPa and the average ultimate tensile strength is 217 MPa. This indicates that wrought iron behaves like a fibre-reinforced composite.

2.3.2 Failure

The suitability of wrought iron as a structural material depends on the balance between strength and toughness. If the toughness is too low, the material will exhibit a brittle behaviour. Good toughness and high strength is the best combination. High toughness allows the redistribution of stresses, when a load is applied. This makes the material capable of bearing high loads before fracturing. Figure 2.7 shows fracture surfaces of wrought iron. These SEM images confirm the fracture mechanism of microvoid coalescence. This failure is caused by the generation of microvoids, which coalesce in the material. This is clearly visible in Figure 2.7a. Stress concentrations cause particle fracture or interfacial debonding and results in failure. Figure 2.7b illustrates elliptical microvoids along the length of the slag fibre. This can be seen when the material is loaded transversely. The failure happens due to the interfacial separation between the iron and the slag. Figure 2.7c shows the fracture surface of a slag fibre. The appearance of this fracture surface is that of a brittle material. This emphasizes that wrought iron consists of brittle slag fibres in a matrix of ductile iron.

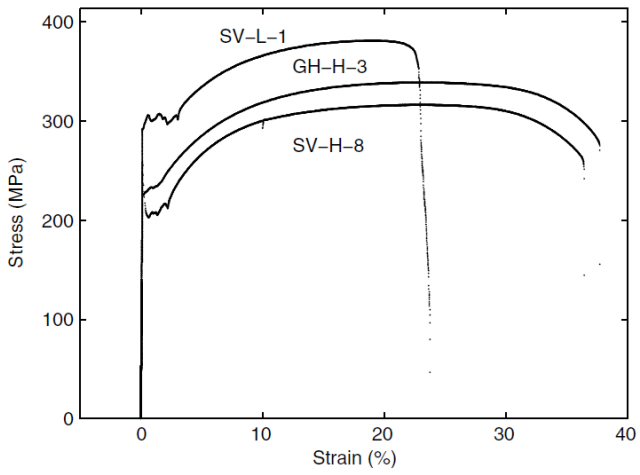

Figure 2.6: Stress-strain diagrams of different wrought iron specimen [2].

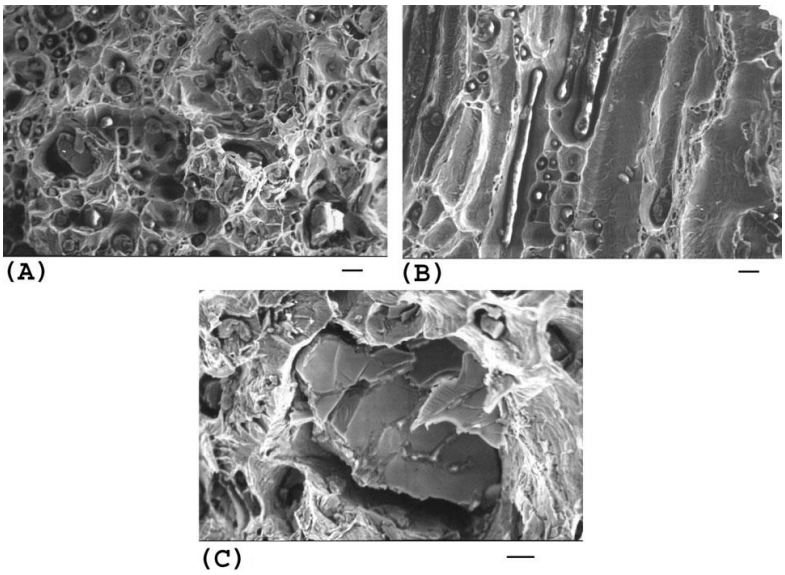

Figure 2.7: Fracture surfaces of wrought iron; bars represent 10 µm [4].

A research done on the wrought iron used in the Titanic [4] concluded that the slag particles fracture around the same time as the onset of yielding in the iron matrix. When the iron starts to yield, the slag particles split into smaller segments. This indicates that the strength of the interface between the slag and the iron matrix is higher than the fracture strength of slag, allowing a continued transfer of stress from iron to slag. The propagation of the crack is featured with blunting around the crack tips as found by Hooper *et al*.

2.3.3 Size Effect

A size effect is observed in wrought iron. The strength increases with decreasing thickness of the wrought iron specimen. A possible explanation is that more work was needed to fabricate specimen of smaller thickness. This extra work resulted in less impurities and a better distribution of the impurities present in the material. Therefore having an overall better quality.

Figure 2.8 illustrates the size effect in wrought iron. The trend line is steeper for the yield strength, indicating that the yield strength is more influenced by the size effect than the ultimate tensile strength.

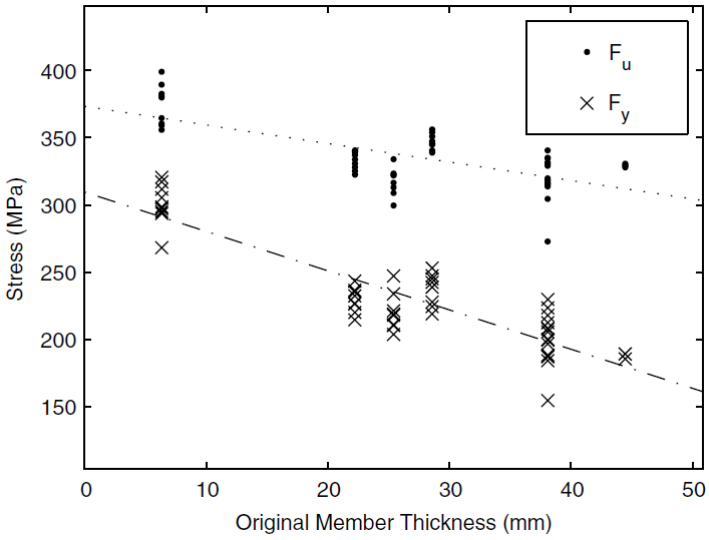

Figure 2.8: Graph stress vs. thickness, where F_y is the yield strength and F_u is the ultimate tensile strength [2].

2.4 Wrought Iron of the Tie Rods

The material properties of wrought iron differ a lot depending on production time and location, as discussed in Section 2.2.2. This means that the material properties measured in the references may differ a lot from the actual material properties of the wrought iron used in the Duomo. Also among the different tie rods material properties may change, because the tie rods were made in a time span of over 200 years. In this section the characteristics of the wrought iron used in the Duomo is discussed. Testing is done on tie rod 58-88, which was found broken in the Duomo. The values of the material properties, given in this section, are used in the rest of the thesis.

2.4.1 Bulk and Surface Properties

As stated before, wrought iron is a heterogeneous material. This heterogeneity is confirmed in the material characterization done, both in terms of defects and microstructure. There are two main microstructural phases: ferrite and pearlite. The distribution of pearlite is shown in Figure 2.9, the grid points are spaced by 10 mm [10]. Ferrite is the main phase in the areas where the amount of pearlite is low, but also small amounts of cementite are detected. In regions with a mainly pearlitic structure many discontinuities were identified, while they were mostly absent in areas with a high percentage of ferrite. The three main inclusions are: iron oxide, spheroidal graphite and silicate core surrounded by oxides. In the ferritic areas also dendritic inclusions are observed, mainly consisting of silicon dioxide, see Figure 2.10. The inclusions containing large amounts of silicon originate from the manufacturing process are referred to as slag inclusions.

Only little is known about the surface properties of these tie rods. The surface layer has a thickness of 0.2-0.3 mm. It could be calamine, an oxide produced during hot working, coupled with a coherent dust layer which sedimented in time. Such a surface layer is often called patina.

2.4.2 Fracture Surface

The fracture surface of the tie rod is characterized by a fibrous appearance. The crack leading to fracture was more opened in the inner part of the tie rod, while the tips were pointing outwards. This crack morphology demonstrates that the crack nucleates in the bulk material at a weaker point, such as a void or an inclusion. These weaker points leads to local stress concentration and subsequently to

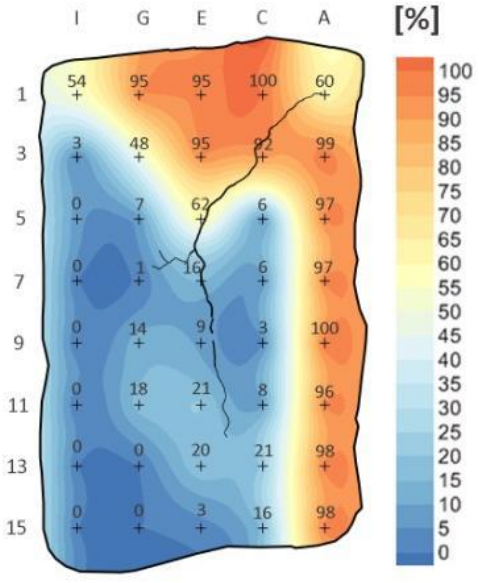

Figure 2.9: Distribution of pearlite in the bulk material, grid points are seperated by 10 mm [10].

Figure 2.10: slag inclusion under an optical microscope [10].

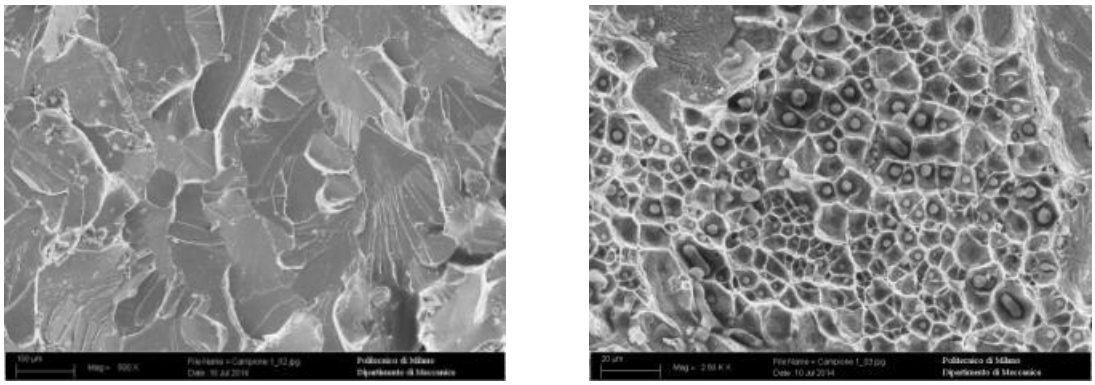

(a) (b)

Figure 2.11: Failure modes observed with SEM on the fracture surface [10].

the initiation of a crack. Necking has been observed along the longitudinal axis of the tie rod, implying that the material exhibited rather ductile behaviour. On the cracked surface black and red oxides can be observed. The dark oxides are produced at forging temperatures and were thus present before the failure of the tie rod. On the other hand, the red oxides are produced at room temperature and are developed after cracking, due to atmospheric conditions.

Two different failure modes can be observed in the material: transgranular brittle failure and microvoid coalescence. Figure 2.11 shows SEM images for both failure modes. Figure 2.11a displays typical transgranular brittle failure, including cleavage planes and river patterns. The dimples in Figure 2.11b clearly indicate microvoid coalescence, a form of ductile failure. Most dimples are found around inclusions.

2.4.3 Mechanical Properties

Tensile testing is done on samples from tie rod 58-88 to obtain values for the Young's modulus, yield strength and tensile strength and the resulting average values are given in Table 2.1 [11]. There is a high dispersion among the values of the parameters due to the heterogeneity of the material. This needs to be taken in account for the rest of the case study.

Table 2.1: Mean values of mechanical properties of the wrought iron used in the Duomo.

	Mean value	**Standard deviation**
Young's modulus (GPa)	200	40
Yield strength (MPa)	180	20
Tensile strength (MPa)	280	50

2.5 REFERENCES

[1] R. Gordon and R. Knopf, "Evaluation of Wrought Iron for Continued Service in Historic Bridges," *J. Mater. Civ. Eng.*, vol. 17, no. 4, pp. 393–399, 2005.

[2] S. L. Kelton, S. R. Arwade, and A. J. Lutenegger, "Variability of the Mechanical Properties of Wrought Iron from Historic American Truss Bridges," *J. Mater. Civ. Eng.*, vol. 21, no. 5, pp. 638–647, 2011.

[3] M. Bowman and A. Piskorowski, "Evaluation and Repair of Wrought Iron and Steel Structures in Indiana," 2004.

[4] J. J. Hooper, T. Foecke, L. Graham, and T. P. Weihs, "Metallurgical Analysis of Wrought Iron From the RMS Titanic," *Meas. Sci. Technol.*, vol. 14, pp. 1556–1563, 2003.

[5] P. Dillmann and M. L'Héritier, "Slag inclusion analyses for studying ferrous alloys employed in French medieval buildings: supply of materials and diffusion of smelting processes," *J. Archaeol. Sci.*, vol. 34, pp. 1810–1823, 2007.

[6] J. Monnier, D. Neff, S. Reguer, P. Dillmann, L. Bellot-Gurlet, E. Leroy, E. Foy, L. Legrand, and I. Guillot, "A corrosion study of the ferrous medieval reinforcement of the Amiens cathedral. Phase characterisation and localisation by various microprobes techniques," *Corros. Sci.*, vol. 52, pp. 695–710, 2010.

[7] E. Blakelock, M. Martinon-Torres, H. A. Veldhuijzen, and T. Young, "Slag inclusions in iron objects and the quest for provenance: an experiment and a case study," *J. Archaeol. Sci.*, vol. 36, pp. 1745–1757, 2009.

[8] D. Ashkenazi, E. Mentovich, D. Cvikel, O. Barkai, A. Aronson, and Y. Kahanov, "Archaeometallurgical Investigation of Iron Artifacts from Shipwrecks – A Review," *Archaeol. New Approaches Theory Tech.*, pp. 169–186, 2012.

[9] E. B. Aston, James and Story, *Wrought iron, its manufacture, characteristics and applications*. A.M. Byers Company, 1939.

[10] M. Bellanova, A. Baggioli, B. Rivolta, R. Felicetti, and A. Cornaggia, "Metallurgical and mechanical characterization of the historical tie-rod of Duomo di Milano," in *XXXI° International Conference of Cultural heritage*, 2015.

[11] M. Vasic, "A Multidisciplinary Approach for the Structural Assessment of Historical Constructions with Tie-rods," Politecnico di Milano, 2015.

CHAPTER 3: NON-DESTRUCTIVE TESTING

Non-destructive testing (NDT) is the use of physical or mechanical methods to test materials without affecting the properties of the material. These methods give mechanical, electrical, magnetic or thermal stimuli to the material. Sensing the response of the material gives indications about the presence of flaws. Mainly differences from the average value of the signal gives information about present abnormalities.

3.1 NDT AND ITS APPLICATION TO THE TIE RODS OF THE DUOMO

The use of NDT in the Duomo is a cost-effective way to maintain the structural safety. Replacing the tie rods reduces the heritage value of the Duomo and is very expensive. Using NDT the cracks present can be found without reducing the heritage value. In the meantime, the structural safety can be guaranteed.

Using NDT becomes easier, when the presence of weak points in the rod are predetermined. The rods are made out of several wrought iron bars, welded together. The material around the welds seems less strong in comparison with the rest of the rod, being more susceptible to the initiation of cracks. This entails that in a periodic way along the rod, there will be a higher chance of finding cracks. This concept is shown in Figure 3.1. The tie rods have been made out of wrought iron bars with a length of 1.0-1.5 meter. The red lines are the welding lines. They were found while looking for cracks, by using eddy current testing. It can be seen that these welding lines have an inclined nature. The average inclination has been found to be 27°. This inclination needs to be taken into account, while looking for cracks with NDT.

There are multiple factors that need to be taken into account for the use of NDT on the tie rods. The overall material properties are of importance. Iron is a ferromagnetic material with a high electrical conductivity, magnetic permeability and heat conductivity. The wrought iron used in the rods is a heterogeneous material, with a very rough surface due to the patina present. The patina works as a non-conductive layer on the iron and has a low electrical and heat conductivity.

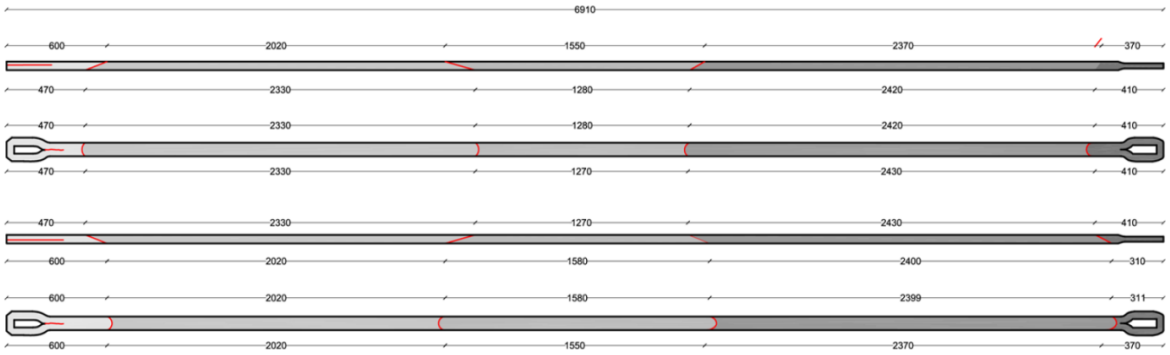

Figure 3.1: Welding lines present in the tie rod 61-91, of the four different faces.

3.2 NDT TECHNIQUES

There are many different NDT techniques on the market, but the compatibility to a certain application differs much. The compatibility depends on the material properties of the inspected element, on the structural geometry and on many other aspects. In this section diverse NDT techniques will be discussed. Their advantages and disadvantages, which are relevant to the case of the iron tie rods, will be elaborated on.

3.2.1 Magnetic Particle Testing

Magnetic particle testing uses one or more magnetic fields to locate surface and near-surface cracks in ferromagnetic materials. A magnetic field is pumped through the material. At cracks in the material there will be leakage of magnetic flux. This leakage attracts the magnetic particles, which are present on the surface of the material. The accumulation of these particles reveals the presence of a crack.

The main advantage of this technique is that it is simple and fast. It is also highly portable, which makes it compatible for fieldwork. There are two main disadvantages of this technique for the application to the iron rods. It only detects surface and near-surface defects. Also the rough surface makes it difficult for the particles to move towards the leakage of the flux.

3.2.2 Radiographic Testing

Radiographic testing is done by exposing a test object to penetrating radiation. The radiation passes through the object and at the opposite side of the object the radiation is caught on an X-ray film. The darkness of the film, in comparison with the overall darkness, indicates the presence of discontinuities.

This technique has the advantage that it can inspect large surface areas, while checking the internal structure. A major disadvantage is the safety, due to the hazardous nature of the radiation. Next to this disadvantage, it is also a very expensive technique.

3.2.3 Ultrasonic Testing

Ultra-high frequency sound is used for ultrasonic testing. The ultrasonic waves are introduced in the test object. If these waves encounter a material with a different acoustic impedance, some of the sound will be reflected back to the emitter. A defect has a different acoustic impedance than the bulk material and will thus reflect the ultrasonic waves.

The main advantage of ultrasonic testing is that the geometry and the position of the flaw can be obtained with high accuracy. Another advantage is its high penetrating power. On the other hand, it requires the use of a couplant and thus requires a clean and smooth surface.

3.2.4 Eddy Current Testing

Eddy current testing (ECT) is based on electromagnetic principles. It uses electromagnetic inductance to identify flaws in conducting materials. An ECT probe is brought in the proximity of the surface of the specimen in which flaws are to be detected. The magnetic field produced by the probe induces eddy currents in the material. Disturbances in the eddy currents are picked up by the same or a second coil and indicate the presence of flaws in the material.

Eddy current testing have several advantages. No couplant is required, while the eddy current probes can be modified for different applications. The technique has a high portability and gives an instantaneous response. Disadvantages are its sensitivity to surface variations and its limited depth of penetration.

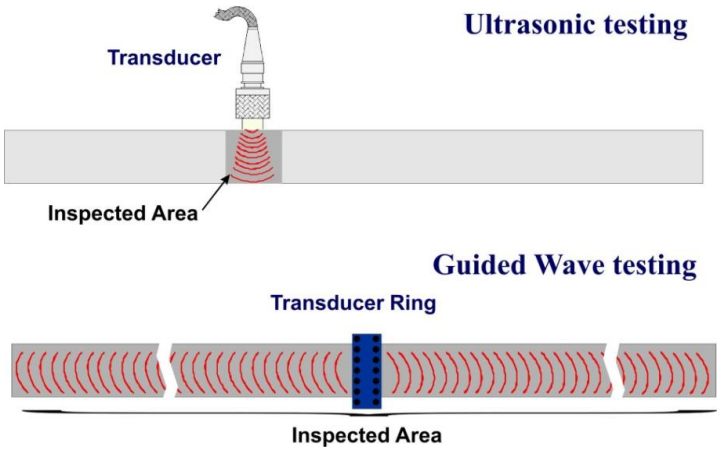

Figure 3.2: Difference between ultrasonic testing and guided wave testing.

3.2.5 Guided Wave Testing

Guided wave testing uses controlled excitation of one or more ultrasonic waveforms. These waveforms are guided by the surfaces of an elongated structure and are reflected by damages. The main difference between ultrasonic testing and guided wave testing is shown in Figure 3.2.

Advantages of guided wave testing are that it is a rapid and long range inspection technique, which can detect both internal and surface cracks. The data is fully recorded and can later be evaluated by signal processing techniques. Disadvantages are the difficulty level of the interpretation of the data and it is problematic for this technique to detect small cracks. Another disadvantage is the need to use a coupling agent. Especially for rough surfaces, this is problematic.

3.2.6 Magnetic Flux Leakage

Magnetic flux leakage is a magnetic method. A strong magnet puts a strong magnetic field through a material. The anomalies of the normal flux patterns, caused by defects, are recorded by a magnetic detector. This is similar to the magnetic particle testing, where the leakage of the flux is shown with the magnetic particles.

This is a simple and cheap technique, which can detect surface and subsurface cracks. The disadvantage is the detection of deep flaws. This technique depends on how far the magnetic field reaches into the material, making it more sensitive to surface defects than defects in the bulk. Also the need to work with very strong magnets is a disadvantage for using this method.

3.2.7 Infrared Thermography

Infrared thermography is a technique to detect cracks by recording changes in temperature. Active thermography needs to be used, because the temperature of the testing material is in equilibrium with the environment. One side of the tested material is heated by an external source and on the other side the thermal response is captured by infrared cameras. The difference in thermal conductivity, due to the presence of a crack in the material, causes a certain temperature profile.

The main advantages of IR thermography is that it can be used on every material and visual pictures can be made of large areas. The shape of the internal cracks can be made visible. The disadvantage is the price of the high quality IR cameras, that are needed for good results. Also the uniform heating of the surface of the tie rod can cause problems, due to the diffusion of heat along the tie rod.

3.3 The Compatible Techniques

The NDT techniques are chosen by their compatibility to the application discussed in Section 3.1. Not only the advantages of a technique are important, but also the possibility to adapt the technique to overcome disadvantages is a major incentive for choosing a certain technique. Radiographic testing is not compatible, due to its hazardous radiation. Magnetic particles testing and magnetic flux leakage are less compatible, because they are focused on surface and subsurface cracks. Also the need for strong magnets is impractical on site. Ultrasonic testing has major advantages of having the capability to detect the geometry and position of the cracks precisely. The need for a couplant on a clean and smooth surface, makes it very difficult to implement this technique to the iron tie rods. The test cannot be done without removing the patina present and this changes the appearance of the tie rods significantly.

Guided waves testing is a compatible technique for doing some primary inspection. The goal would be to scan long stretches of the tie rod, to see whether there are cracks present. Also an estimation of the location of the cracks can be done. Couplants with a spring mechanism build in are able to overcome the problems caused by the need to use couplants on a rough surface. This method is used to be sure that all the couplants are connected to the surface, even if this surface is very rough.

More information about the precise position and an estimate of the crack size can be obtained, using eddy current testing. The drawbacks of the limited depth of penetration and its sensitivity to surface variations, can be overcome by using adjusted probes and low frequencies. These probes can be developed by taking into account the geometry of the iron rods and the characteristics of the surface. As discussed in Section 3.1, the cracks are possibly inclined due to the welding process. The angle of this inclination can be obtained by scanning the area around the crack.

The size and the geometry of the crack can be determined by active IR thermography. The visual picture contains much information about size and shape of the crack. The difference of the visual pictures in time, gives an indication about the depth of the crack. The disadvantage of inhomogeneous heating can be partly overcome by using insulation on the surfaces that are not used for the IR thermography. The heat flow along the rod can be compensated by using post processing techniques.

The three compatible techniques all have their own function and can be subdivided into three scales: global, intermediate and local. Lamb waves is applied on a global scale, to verify the presence of cracks in a tie rod. At the intermediate scale, eddy current testing is employed to find the exact position of the crack. Lastly, active IR thermography is used to determine the geometry of the crack.

CHAPTER 4: LAMB WAVES

The study into Lamb waves started in 1885 by Lord Rayleigh [1]. He was the first to explain wave propagation along a surface. After the work of Lord Rayleigh, Horace Lamb reported waves discovered in plates in 1917 [2]. These waves were named as Lamb waves. In this time not much attention was given to this phenomenon due to its mathematical complexity. The topic was revisited in 1945 by Osborne and Hart, who unveiled the great potential of Lamb waves [3]. Around 1950 a comprehensive solution was found by Mindlin [4]. This solution was followed in more detail by Gazis in 1958 [5] and Viktorov in 1967 [6]. Viktorov was the first who evaluated the dispersive behaviour of Lamb waves. The introduction of Lamb-wave-based damage detection was done between 1940 and 1950 by Firestone and Ling [7], [8]. This immediately created a niche in seismology and non-destructive evaluation. Parallel to the theoretical work, also experimental research was done to understand the fundamentals of Lamb waves. This experimental work was done by Worlton in 1961 [9] and Frederick and Worlton in 1962 [10]. From 1980 to present a lot of success has been booked in the field of Lamb waves, mainly owed to the advances of the computing devices [11]–[16]. This prosperity is mostly in the field of damage identification techniques.

Damage identification by Lamb waves involves several features. The technique is able to inspect large structures, while the coating or insulation can be retained. It is also able to inspect the entire cross sectional area of the structure and it has a low energy consumption. This makes this technique to be very cost-effective. The damage identification has a hierarchy, concerning difficultness. The first step is the qualitative indication of the occurrence of damage. The following step is the quantification of the position of the damage. The last step is the estimation of the severity of the damage. This chapter concerns with the qualitative indication of the occurrence of damage and the estimation of the position of the damage.

This chapter consists out of three parts. The first part is the discussion of the theory involved. Section 4.2 is concerned with the modelling of the behaviour of Lamb waves. The model will take into consideration the geometry of the tie rods. Also the variation from the average geometry and its influence on the behaviour of the Lamb waves will be examined. In this way, a fast approach can be developed for the determination of the characteristics of the Lamb waves under certain boundary conditions. The final part is signal processing in Section 4.3, which takes into account the findings of the modelling section. The optimal settings for taking the measurements will be analysed and a post-processing technique that removes the effect of dispersion will be examined.

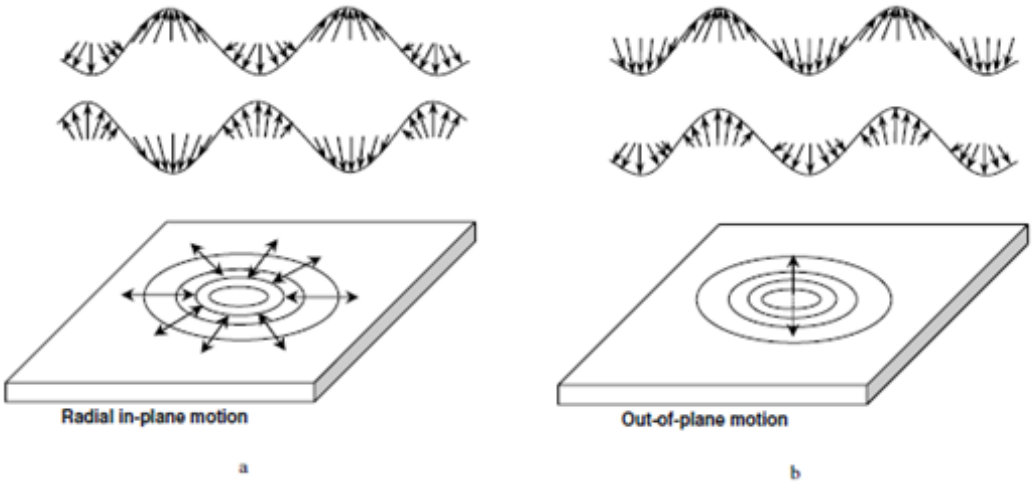

Figure 4.1: a) Symmetric and b) anti-symmetric Lamb wave mode [17].

4.1 THEORY

Lamb waves are elastic waves guided by the free surfaces of the structural element. They are the superposition of longitudinal and transverse modes. This superposition leads to the continuous propagation of waves by the boundaries of the structural element. Their propagation characteristics vary with entry angle, frequency and structural geometry. Lamb waves consist of symmetric and anti-symmetric modes. Figure 4.1 shows the two types of wave modes, orientating from a point source and propagating radially. The two waves displayed for each mode represent the waves on the upper and lower boundary of the plate. Symmetric (S_i) modes have radial in-plane motion, as shown in Figure 4.1a [17]. Figure 4.1b demonstrates that the anti-symmetric (A_i) modes mainly have out-of-plane motion. The magnitude of S_i modes, under the same excitation condition, is normally smaller than the magnitude of the A_i modes. The displacement of these modes are in the same plane as the direction of the wave propagation. There is also another possible motion for the particles, called the shear horizontal waves. These waves also have two type of modes, the symmetric and the anti-symmetric.

The propagation of Lamb waves can be divided in phase (v_p) and group (v_g) velocities. The phase velocity is the propagation velocity at which the phase, at one particular frequency, travels. The group velocity is the velocity measured in experiments. It is the velocity at which the overall shape of the wave propagates, also called the envelope of the wave.

4.1.1 Dispersion Curves

The velocities of the Lamb waves depend on the wave frequency and structural geometry. This phenomenon is called dispersion. A shift in the central frequency is the main consequence of wave dispersion. Dispersion curves are the graphic representations of this phenomenon. They relate frequency, phase/group velocity and thickness to each other.

Figure 4.2 displays the dispersion curves of the symmetric (S) and anti-symmetric (A) modes for a 2 mm thick aluminium plate. A low-dispersion region is visible for the S_0 and A_0 modes at low frequencies. In this range the S_0 and A_o modes travel at almost constant velocities independent on their frequencies. Next to these zero-order modes, there are the higher-order modes. The higher-order modes are introduced above a certain frequency, called the cut-off frequency. In Figure 4.2 the cut-off frequency is just below 1000 kHz, since at this frequency the first higher-order mode (A_1) is introduced in the dispersion curve.

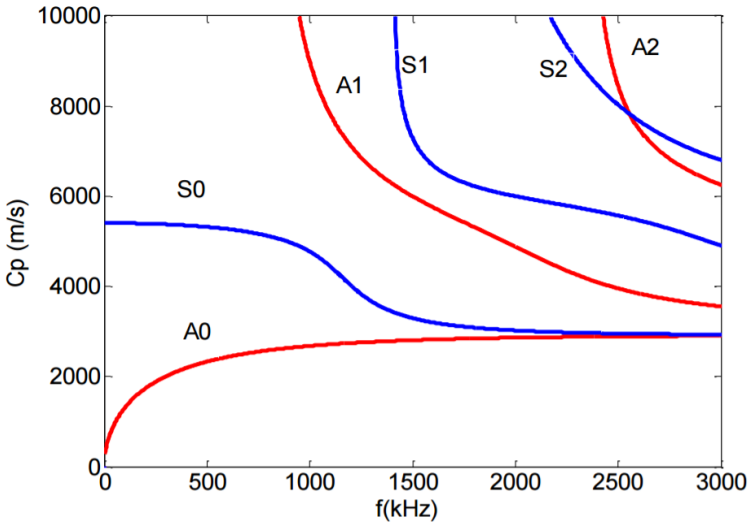

Figure 4.2: Phase velocity dispersion curves for a 2 mm thick aluminium plate [38]*, phase velocity versus frequency.*

4.1.2 Attenuation

Attenuation is the phenomenon of the dissipation of energy with distance or time. The attenuation increases if damage or heterogeneity is present in the material, because these components will absorb some energy from the wave. The anti-symmetric modes have a higher attenuation due to the dominant out-of-plane movement, perpendicular to the surface, which leaks energy to the surroundings. While the symmetric modes mainly have in-plane displacement, parallel to the surface, keeping the energy confined in the material. The magnitude of the wave signals decreases gradually, as shown in Figure 4.3. The decay of the magnitude of the Lamb waves in plates with the travelled distance can be described with the following equation:

$$\frac{A(d_1)}{A(d_2)} = \frac{\sqrt{d_2}}{\sqrt{d_1}} \,. \tag{4.1}$$

The magnitudes, at distances d_1 and d_2 from the actuator, are given by $A(d_1)$ and $A(d_2)$.

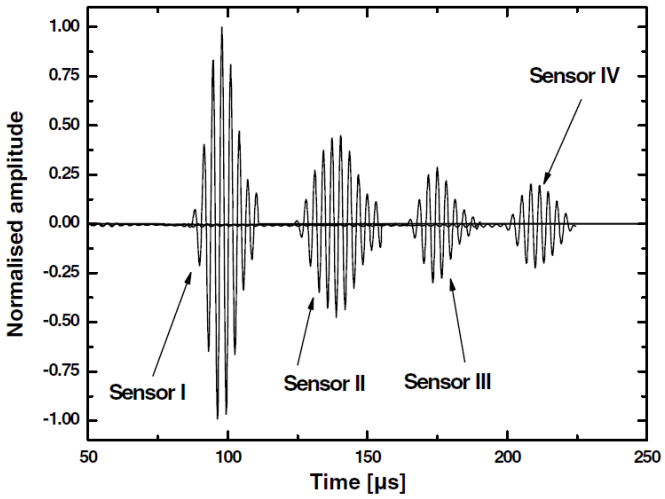

Figure 4.3: Attenuation of Lamb waves with propagation distance.

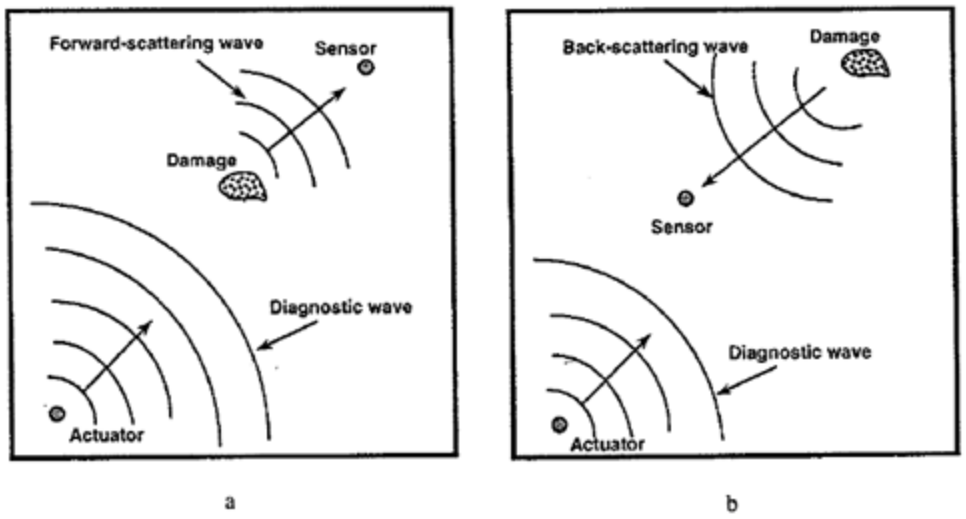

Figure 4.4: a. Pitch-catch and b. pulse-echo configuration.

4.1.3 Influence of Damage

Structural damage can influence the propagation of Lamb waves by wave scattering effects. These effects can be reflection, transmission and mode conversion of the wave. They depend on the orientation, size and relative position of the damage. These factors can be used to develop damage identification approaches.

There are two main configurations for damage identification; pitch-catch and pulse-echo. These configurations are sketched in Figure 4.4. In a pitch-catch configuration, the Lamb wave is emitted from an actuator, travels across the damage and is received on the other side by a sensor. The major disadvantage of this configuration is that the location of the damage cannot be located. In a pulse-echo configuration, the actuator and the sensor are on the same side of the damage. The received signal is the reflected wave from the damage, also called the reflector. This configuration can locate the damage. The disadvantage is that the wave has to travel longer distances and thus more attenuation takes place. Also there can be a blind zone area. This is due to the interference of the outgoing waves and the echoed waves, which can occur in the area between the damage and the sensor. This can be avoided by using diagnostic waves with a short time span. The pulse-echo configuration will be used in the experiments, because this will enable to calculation of the position of the crack.

The crack size influences the strength of the received signal, due to a change in the scattering of the wave. A bigger crack size causes an increase in the reflection coefficient, which is defined as the ratio of the wave energy that is reflected. This increase is caused by the increased surface area. Thus a higher signal is received as the crack size increases. The orientation of the crack has two effects. The first effect is on the reflection coefficient, which decreases due to a relative smaller surface that the waves encounter. The second effect is possible mode conversion. The wave encounters the crack under a different angle, which could lead to mode conversion. The relative position of the damage influences the quality of the signal due to the attenuation of the wave. If the crack is further removed from the sensor, the wave needs to travel a longer distance. This increases the amount of attenuation and thus reduces the amplitude of the received signal.

4.1.4 Damage Identification for Rods

The most straightforward way for damage identification is the difference in time-of-flights (ToFs). The difference in ToFs is defined as the time between the incident wave captured by the sensor and

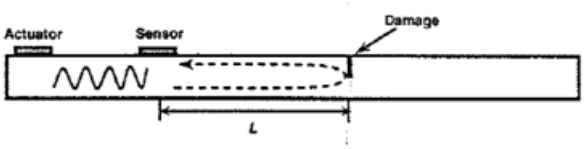

Figure 4.5: Time-of-Flight based damage identification for the pulse-echo configuration.

the scattered wave. This ToF-based damage identification is illustrated in Figure 4.5 for the pulse-echo configuration. The position of the damage can be triangulated from this configuration. For the rod, a one-dimensional scenario can be described. The following equation describes the triangulation:

$$L = \frac{v_g \cdot \Delta t}{2} \ . \tag{4.2}$$

The length between the sensor and the damage is L and Δt is the difference in arrival time between the incident wave and the wave echoed back from the damage. This is a simple calculation, based on the assumption that the group velocity (v_g) remains the same for the outgoing and scattered wave.

4.1.5 Array Transducers

An array transducer consists out of linear arrays of equally spaced transducers. These transducers are both used as transmitters and receivers. They are activated individually as a transmitter with a certain time delay. The transducers are utilized as receivers, when they are not applied as a transmitter. A schematic representation of an array transducer is given in Figure 4.6 [18], for the pulse-echo configuration. The transducer array consists out of N elements separated by a distance d. The generation of the synthetic wave is a process starting with emitting a wave from one of the transducers. The wave will travel in the desired direction and is reflected from discontinuities. The wave will then travel in the opposite direction and be received by another transducer. After all measurements are done, there will be N(N-1) waveforms to process.

An array transducer emits and receives waves with different distances to the defect, depending on the number of the activated transmitter and reducer. This signifies that all individual waves have different original time scales, called the local time scale. The signal processing thus starts with shifting all the waves, so that they originate from the same reference point and have the same global time scale. This process is illustrated in Figure 4.7. The reference point is the first transducer. All the waves are shifted, depending on the number of their transmitter and receiver, so that it seems that they are emitted and received by transducer 1. As an example, the diagnostic wave is emitted by

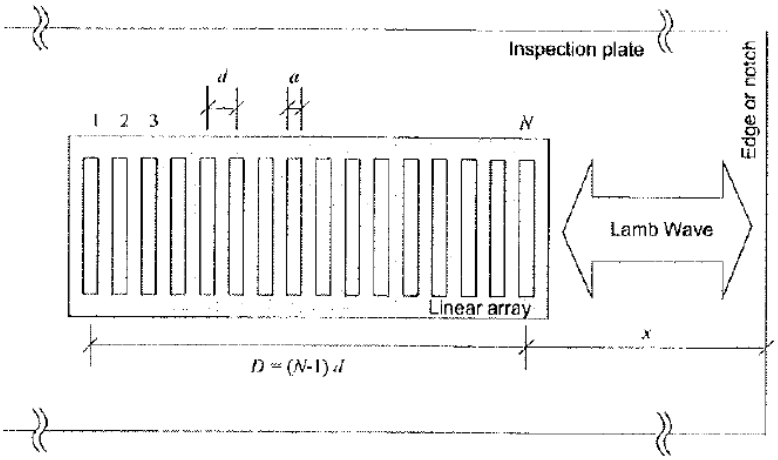

Figure 4.6: Schematic representation of array transducer [18].

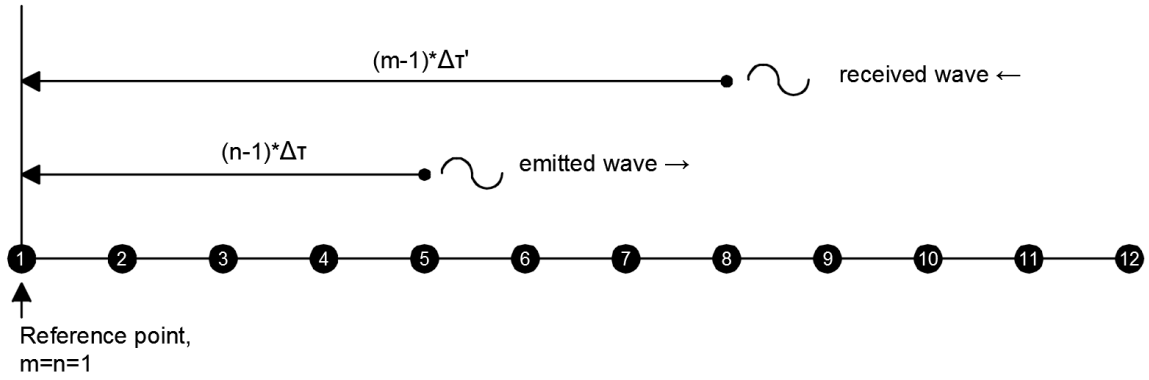

Figure 4.7: Explanation of shifting the diagnostic waves using the concept of time delay for an array transducer consisting out of 12 transducers.

transducer 5 and received by transducer 8. The time it takes for the wave to travel between two neighbouring transducers is given as Δτ and is called the time delay. The total time delay between the reference point and the activated transducer is thus (n-1)* Δτ for the transmitter and (m-1)* Δτ' for the receiver. If all the individual waves are shifted in time, they can be added to obtain the total wave measured by the array transducer at a global time scale, with as reference the first transducer. This signal processing tool is divided in two parts. First all emitted waves are shifted to the reference point and then all received wave are being shifted. This is done in the following sections.

4.1.5.1 The Emitted Wave

All diagnostic waves should be overlapped to get a readable signal. These diagnostic waves can be processed using the concept of time delay, illustrated in Figure 4.7. First the emitted waves will be shifted to a single point in time. The emitted waves from the individual transducers are processed using time delay to shift all the waves to one position in time. This will model one single output signal. The time delay between the different elements is described by the following equation:

$$t_{n+1} = t_n + \Delta\tau, \;\; n = 1,2,3,\dots,N-1 \;\; . \tag{4.3}$$

The reference of the global time scale (t_1=0) is taken as the excitation time for the first element. The time delay is given by

$$\Delta\tau = \frac{d}{v_p} \; . \tag{4.4}$$

The output signal, s_{output}, can be constructed by summing the time-shifted waveforms for all transducers, $s_{individual}$, by the equation:

$$s_{output}(t) = \sum_{n=1}^{N} s_{individual}(t-(n-1)\Delta\tau) \, , \;\; n = 1,2,3,\dots,N, \tag{4.5}$$

where the individual signals are shifted as a function of their respective local time scales, which leads to the expression of the signal in terms of the global one.

Combining Equations (4.4) and (4.5), gives the final equation for the output signal:

$$s_{output}(t) = \sum_{n=1}^{N} s_{individual}\left(t - \frac{(n-1)d}{v_p}\right) \, , \tag{4.6}$$

where $\frac{(n-1)d}{v_p}$ is the shift in time for the emitted wave to the reference point, illustrated in Figure 4.7. Using above equation, all the emitted waves are shifted to originate from only the first transducer.

4.1.5.2 The Received Wave

The emitted wave is reversed in direction by a reflector, which becomes the wave received by the transducers. To reconstruct the received wave a reversed time delay sequence is used, given by the equation:

$$t_{m-1} = t_m + \Delta\tau' \ , \tag{4.7}$$

where Δτ' is the time delay between successive transducers of the wave travelling backwards. A fully constructed synthetic wave can be composed by using the following equation:

$$s_{global}(t) = \sum_{m=1}^{N} s_{output}(t - (m-1)\Delta\tau') \ , \tag{4.8}$$

where s_{global} is expressed in terms of global time scale t and is shifted from the local time scale as depicted in Figure 4.7. The phase velocity for the emitted and received wave is considered to be equal. This means that due to the dependence of wave velocity on wave mode and frequency, as explained in Section 4.1.1, only one singular wave mode at a chosen central frequency can be taken into account. Also the spacing between the transducers remains equal. This implies that the time delay for the emitting and receiving wave is equal and thus gives the following equation:

$$\Delta\tau' = \Delta\tau = \frac{d}{v_p} \ . \tag{4.9}$$

A more efficient way to process the data is to combine Equations (4.5), (4.8) and (4.9), as follows:

$$s_{global}(t) = \sum_{n=1}^{N}\sum_{m=1}^{N} s_{individual}\left(t - \frac{(m+n-2)d}{v_p}\right) . \tag{4.10}$$

Each waveform is summed in Equation (4.10) taking the position of the first transducer as reference for both emitter and receiver, where $\frac{(m+n-2)d}{v_p}$ is the total shift in time applied for every individual wave. After the processing of the signals using this equation, the data is ready for analysis.

4.1.5.3 Directionality of Emitted Waves

The emitted waves generated by the array transducer will travel in the positive and the negative direction of the rod. Thus signals are obtained from both directions. This means that the constructed wave can be calculated for both directions. There are two ways to allow the propagation in the opposite direction, by using negative time delays or by reversing the element index. In both cases the wave propagation sequence is reversed, by choosing transducer N as the first element.

4.1.5.4 MIRA

The ultrasonic tomograph A1040 MIRA generates shear waves in a pulse-echo configuration. It is originally used for concrete and other heterogeneous materials. There is no need for surface preparation, when using this apparatus. The transducer tips are made of wear-resistant ceramic and can be used as dry acoustic contacts. An independent spring suspension is used for every transducer, so that the transducer tip is able to adapt to the roughness of the surface. The measuring block consists of 12 blocks separated by 30 mm. Every block contains 4 elements, giving a total of 48 transducers. These transducers generate shear waves. The nominal frequency of the MIRA is 50 kHz

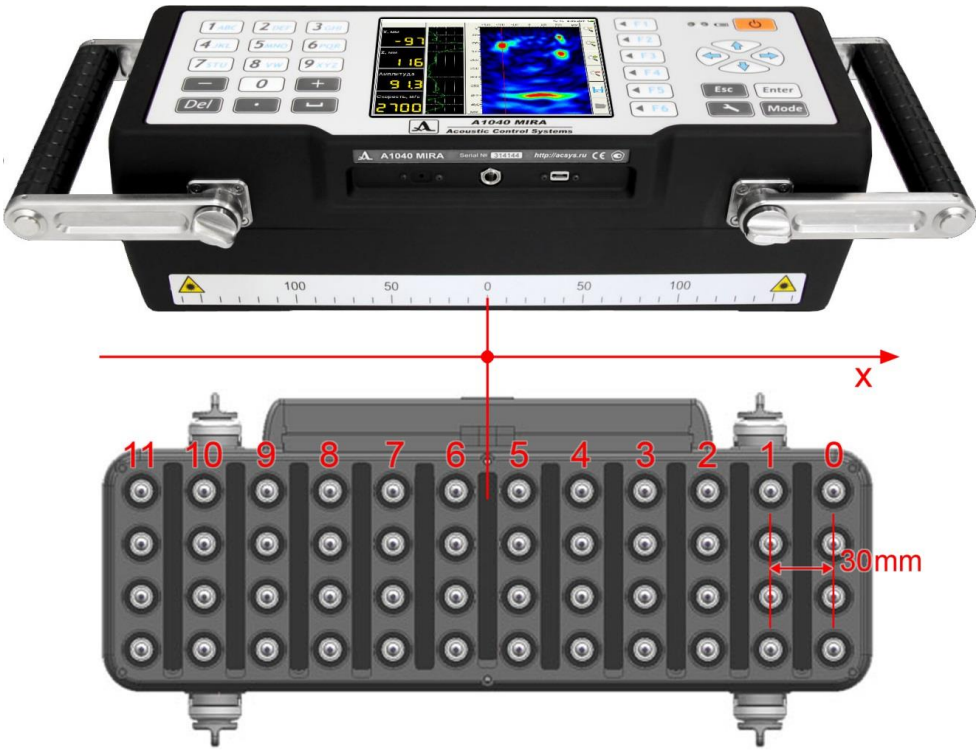

Figure 4.8: Lay-out of the ultrasonic tomograph A1040 MIRA, general view and bottom view.

and the original bandwidth is from 25 to 85 kHz. This bandwidth is adapted to 15 to 85 kHz for this project.

The data acquisition is done in a compact way by MIRA. The lay-out of the MIRA is given in Figure 4.8. There are 48 transducers subdivided in 12 rows. These rows are numbered from 0 to 11 for the rest of the chapter for convenient use during signal processing. The numbering goes from right to left, because the first activated receiver is transducer 0. The data acquisition scheme is devised assuming symmetry, if the transmitter and receiver are interchanged. This assumption on symmetry can be made, if the diagnostic wave send out by transmitter x and measured by receiver y is equal to the diagnostic wave send out by transmitter y and measured by receiver x. The data acquisition is therefore only done for half of the total amount of possible waves. This means that in practice for any possible receiver, only the transmitters with lower numbering are considered. A transducer is not able to act as transmitter and receiver at the same time. This means that there are a total of 66 waves to be processed, as is explained in the following. The sequence of the operations starts with receiver 0 receiving signals from respectively transmitters 1 to 11. Then the following receiver 1 is activated, which receives the signals from transmitters 2 to 11. This goes on until the last waveform measured by receiver 10 and emitted by transmitter 11. This means that the first transducer never acts as a transmitter and that the last one is never used as a receiver. This numbering can be used to calculate the global wave in the leftward propagation. The numbering of the sensors needs to be mirrored in case of rightward propagation as explained in Section 4.1.5.3.

The analysis of the data can be done according to Equation (4.10). It needs to be noticed that there are less waveforms present than the total summation suggests in this equation. Previously the reference point was the first transducer. However, the detection of cracks needs to be done in both the leftward and rightward direction. For this reason the reference point will be moved to the centre of the sensor array, with a shift of 165 mm.

4.1.5.5 "Dead zone"

Another aspect that needs to be taken into account is the so-called "dead zone". The dead zone is a zone, in the time or space domain, at the beginning of the measured signal, which is not reliable due to a distortion of the signal. It consists of two parts. The first is the direct cross talk between transmitter and receiver. The second part is due to the length of the emitted wave leaving the receiver during this direct cross talk. The total dead zone is the summation of these two effects.

The direct cross talk is an effect resulting from the direct measurement of the signal emitted, without it being reflected from a defect. This happens at the beginning of the signal, when the signal from the transmitter first passes the receiver before propagating further in the tie rod to find a defect. The length of the zone influenced by this effect can be calculated by keeping in mind the principles of the array transducer. The first step is to calculate the time that it takes to receive the direct wave from the transmitter (t_{direct}) in seconds, for each receiver/transmitter pair:

$$t_{direct} = \frac{|n-m| \cdot d}{v_p} \ , \tag{4.11}$$

where d is the distance between the transducers in millimetres and the phase velocity is in mm/s. This time needs to be converted to the global time scale of cross talk ($t_{global.cross}$) in seconds, explained at the beginning of Section 4.1.5. In this case all signals originate from the centre of the MIRA. This is done in the following equation:

$$t_{global,cross} = t_{direct} + \frac{(n+m) \cdot d}{v_p} - \frac{2 \cdot 165}{v_p} \ . \tag{4.12}$$

The second term on the right-hand side of this equation is comparable with Equation (4.10), but the -2 is cancelled due to the start of the transducers' numbering from zero. The last term of the equation is the shift to the centre of the MIRA, applied twice to include that this distance needs to be travelled twice. The above equation can be condensed into:

$$t_{global,cross} = \frac{2 \cdot n \cdot d}{v_p} - \frac{2 \cdot 165}{v_p} \ . \tag{4.13}$$

This equation shows that the crosstalk is not dependent on the number of the receiver. The time involved in the crosstalk is determined by the maximum number of transmitter (n_{max}). Equation (4.13) needs to be multiplied by the phase velocity to determine the distance affected by the crosstalk ($x_{crosstalk}$) in mm. This results in the following equation:

$$x_{crosstalk} = \frac{1}{2}(2 \cdot n_{max} \cdot d - 2 \cdot 165) \ . \tag{4.14}$$

A factor of a 0.5 needs to be implemented to take into account the forward and backward propagation of the wave. Inserting the values for n_{max} and d of the MIRA in the equation above, gives a value of 165 mm. This is the exactly the distance from the centre of the MIRA to its end. This means that no reliable information about possible cracks is obtained from the area under the MIRA.

The second effect that contributes to the dead zone is the length of the emitted pulse. The crosstalk is visible in the results until the signal completely leaves the receiver. The length of the emitted pulse is dependent on the frequency and the number of cycles and this second effect depends thus on these factors. The wavelength is described by the following equation:

$$t_{pulse} = \frac{C}{f} \,, \tag{4.15}$$

where C is the number of cycles in the pulse. In the length domain, the equation is as follows:

$$x_{pulse} = \frac{v_p \cdot C}{f} \,. \tag{4.16}$$

The total length of the dead zone follows from Equations (4.14) and (4.16) and is as follows:

$$x_{deadzone} = 165 + \frac{v_p \cdot C}{f} \,, \tag{4.17}$$

where $x_{deadzone}$ is the length of the dead zone in mm. This length of the dead zone thus depends on the phase velocity, the frequency and the number of cycles of the emitted pulse. A lower frequency and a higher number of cycles increases this length and is thus a drawback for using these settings.

4.2 Modelling of Lamb Waves

The interpretation of damage detection results can be simplified by understanding the physical principles of the Lamb wave propagation. Therefore a relationship between wave properties, material properties and geometry of the structure should be established. Even though some guided wave problems can be solved analytically[1], [2], this can only be done for simple geometries. An analytical approach becomes less feasible, when the complexity of the problem is increased. Numerical methods are thus developed to solve these complex problems. Numerical analyses uses numerical approximations to solve mathematical problems.

The finite element method (FEM) has been used for decades to compute wave propagation properties [19]–[21]. FEM is applicable to problems of high complexity and is based on the concept of piecewise polynomial interpolation. This method subdivides a large problem into smaller, simpler parts called finite elements. By connecting the elements, the field quantity becomes interpolated over the whole structure. The assemblage of the finite elements models the entire problem and it approximates a solution by minimizing an associated error function. The main disadvantage is the large computation time.

A method closely related to FEM is the semi-analytical finite element (SAFE) method. In this method, the wave motions in the propagation direction are theoretically approached and the cross section is described using finite elements interpolation functions [22]–[25].The wave propagation is described by exponential functions in the complex domain and the mathematical problem of mode identification is reduced to an eigenvalue problem. A 2D mesh is used for the finite element calculations in the cross section. This reduces the computation time in comparison with the standard FEM.

The orthogonal polynomial approach is another method to model the wave characteristics across the cross section of the investigated structural element [26]–[29]. The idea behind the polynomial method is to approximate wave equations with certain polynomial series. The main advantage of this method is that the boundary conditions are incorporated into the equations of motion. This makes it possible to implement the geometry of the structure in the calculation directly. In the application illustrated in the following, Legendre polynomials are used. Their orthogonality allows neglecting all terms in the equilibrium equations involving their cross products integrals.

The wave propagation is described again by complex exponential functions and the detection of vibration modes is reduced to an eigenvalue problem. In the next section this method is used to model the Lamb waves.

4.2.1 Numerical Analysis Waves in Rod

The modelling procedure starts with defining the coordinate system, shown in Figure 4.9. The tie rod present in the Duomo can be described as a long prism with constant rectangular cross section. The origin is placed at the centroid of the cross section and the x coordinate is perpendicular to both the y- and z coordinate. The wave propagation is in the x direction and the body forces are assumed to be zero. The dynamic equation for a infinitesimally small volume of material in the rod are given by:

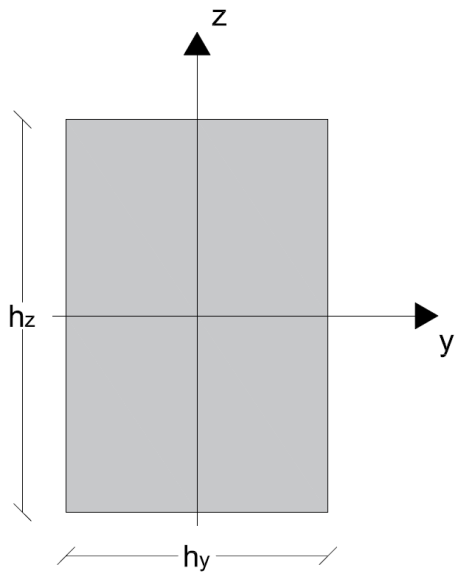

Figure 4.9: Schematic representation of the coordinate system, describing a rectangle as cross section.

$$\begin{aligned}\frac{\partial T_{xx}}{\partial x}+\frac{\partial T_{xy}}{\partial y}+\frac{\partial T_{xz}}{\partial z}&=\rho\frac{\partial^2 u_x}{\partial t^2}\\ \frac{\partial T_{xy}}{\partial x}+\frac{\partial T_{yy}}{\partial y}+\frac{\partial T_{yz}}{\partial z}&=\rho\frac{\partial^2 u_y}{\partial t^2}\\ \frac{\partial T_{xz}}{\partial x}+\frac{\partial T_{yz}}{\partial y}+\frac{\partial T_{zz}}{\partial z}&=\rho\frac{\partial^2 u_z}{\partial t^2}\ ,\end{aligned} \tag{4.18}$$

where T_{ij} and u_i are the stress and displacement components and ρ is the mass density.

The strain (ε_{ij}) and the displacements components can be linked with the following equations:

$$\begin{aligned}&\varepsilon_{xx}=\frac{\partial u_x}{\partial x},\varepsilon_{yy}=\frac{\partial u_y}{\partial y},\varepsilon_{zz}=\frac{\partial u_z}{\partial z}\ ,\\ &\varepsilon_{xz}=\frac{1}{2}\left(\frac{\partial u_x}{\partial z}+\frac{\partial u_z}{\partial x}\right),\varepsilon_{yz}=\frac{1}{2}\left(\frac{\partial u_y}{\partial z}+\frac{\partial u_z}{\partial y}\right),\\ &\varepsilon_{xy}=\frac{1}{2}\left(\frac{\partial u_x}{\partial y}+\frac{\partial u_y}{\partial x}\right)\end{aligned} \tag{4.19}$$

To describe the geometry, the function I(y,z) is introduced. For a rectangular cross section this function is described in the equation below.

$$I(y,z)=\begin{cases}1, & -\frac{1}{2}h_y\leq y\leq\frac{1}{2}h_y \text{ and } -\frac{1}{2}h_z\leq z\leq\frac{1}{2}h_z\\ 0, & \text{elsewhere}\end{cases}. \tag{4.20}$$

This way the stress-free boundary conditions can be automatically implemented. This is done by the following equations of the stress components, assuming that the material exhibit elastic behaviour:

$$\begin{aligned} T_{xx} &= \left(C_{11}\varepsilon_{xx} + C_{12}\varepsilon_{yy} + C_{13}\varepsilon_{zz}\right)I(y,z) \\ T_{yy} &= \left(C_{12}\varepsilon_{xx} + C_{22}\varepsilon_{yy} + C_{23}\varepsilon_{zz}\right)I(y,z) \\ T_{zz} &= \left(C_{13}\varepsilon_{xx} + C_{23}\varepsilon_{yy} + C_{33}\varepsilon_{zz}\right)I(y,z) \\ T_{yz} &= 2C_{44}\varepsilon_{yz}I(y,z) \\ T_{xz} &= 2C_{55}\varepsilon_{xz}I(y,z) \\ T_{xy} &= 2C_{66}\varepsilon_{xy}I(y,z)\ , \end{aligned} \tag{4.21}$$

where C_{ij} are the elastic constants, written in the Voigt notation.

The last relevant set of equations describes the plane wave propagation in the x direction. These equations are as follows, where U(y,z), V(y,z) and W(y,z) represent the amplitudes of the wave in the x-, y- and z direction respectively:

$$\begin{aligned} u_x(x,y,z,t) &= exp(ikx - i\omega t)U(y,z) \\ u_y(x,y,z,t) &= exp(ikx - i\omega t)V(y,z) \\ u_z(x,y,z,t) &= exp(ikx - i\omega t)W(y,z)\ , \end{aligned} \tag{4.22}$$

where k is the wavenumber and ω is the frequency.

By substituting Equations (4.19)-(4.22) into Equation (4.18), the differential equations for the displacement components can be obtained, written in the following equations:

$$\begin{aligned} &\left[C_{55}\frac{\partial^2 U}{\partial z^2} - k^2 C_{11}U + ik(C_{12}+C_{66})\frac{\partial V}{\partial y} + ik(C_{13}+C_{55})\frac{\partial W}{\partial z}\right]I(y,z) \\ &\qquad + C_{55}\left(\frac{\partial U}{\partial z} + ikW\right)\frac{\partial I(y,z)}{\partial z} + C_{66}\left(\frac{\partial U}{\partial y} + ikV\right)\frac{\partial I(y,z)}{\partial y} \\ &\qquad = -\rho\omega^2 U I(y,z) \\ &\left[C_{44}\frac{\partial^2 V}{\partial z^2} - k^2 C_{66}V + C_{22}\frac{\partial^2 V}{\partial y^2} + ik(C_{12}+C_{66})\frac{\partial U}{\partial y} + (C_{23}+C_{44})\frac{\partial^2 W}{\partial y \partial z}\right]I(y,z) \\ &\qquad + C_{44}\left(\frac{\partial V}{\partial z} + \frac{\partial W}{\partial y}\right)\frac{\partial I(y,z)}{\partial z} \\ &\qquad + \left(ikC_{12}U + C_{22}\frac{\partial V}{\partial y} + C_{23}\frac{\partial W}{\partial z}\right)\frac{\partial I(y,z)}{\partial y} = -\rho\omega^2 V I(y,z) \\ &\left[C_{33}\frac{\partial^2 W}{\partial z^2} - k^2 C_{55}W + C_{44}\frac{\partial^2 W}{\partial y^2} + ik(C_{13}+C_{55})\frac{\partial U}{\partial z}\right. \\ &\qquad \left. + (C_{23}+C_{44})\frac{\partial^2 V}{\partial y \partial z}\right]I(y,z) + C_{44}\left(\frac{\partial V}{\partial z} + \frac{\partial W}{\partial y}\right)\frac{\partial I(y,z)}{\partial y} \\ &\qquad + \left(ikC_{13}U + C_{23}\frac{\partial V}{\partial y} + C_{33}\frac{\partial W}{\partial z}\right)\frac{\partial I(y,z)}{\partial z} = -\rho\omega^2 W I(y,z) \end{aligned} \tag{4.23}$$

The waves represented by Equation (4.23) can be found by using a double series of Legendre orthogonal polynomials to express U(y,z), V(y,z) and W(y,z).

$$U(y,z) = \sum_{m,n=0}^{\infty} p_{m,n}^{\alpha} Q_m(z) Q_n(y)$$
$$V(y,z) = \sum_{m,n=0}^{\infty} p_{m,n}^{\beta} Q_m(z) Q_n(y) \qquad (4.24)$$
$$W(y,z) = \sum_{m,n=0}^{\infty} p_{m,n}^{\gamma} Q_m(z) Q_n(y)\,,$$

where $p^{i}_{m,n}$ (i=α,β,γ) are the displacement coefficients. Q_m and Q_n represent the expected waveforms in the rod in the y- an z direction and are expressed by the following equations;

$$Q_m(z) = \sqrt{2m+1}\, h_z P_m$$
$$Q_n(y) = \sqrt{2n+1}\, h_y P_n\,, \qquad (4.25)$$

where P_m and P_n is the m^{th} or n^{th} order Legendre polynomials respectively. The orders m and n theoretically run from 0 to ∞, but in practice it is sufficient to go from 0 to finite values M and N respectively. Thus Equation (4.23) is multiplied by $Q_j(z)$ with j running from 0 to M, and by $Q_p(y)$ with p ranging from 0 to N. Subsequently the equations are integrated over z from - $h_z/2$ to +$h_z/2$ and over y from - $h_y/2$ to +$h_y/2$. The resulting equation can be compactly written as;

$$\begin{bmatrix} A_{11}^{j,p,m,n} & A_{12}^{j,p,m,n} & A_{13}^{j,p,m,n} \\ A_{21}^{j,p,m,n} & A_{22}^{j,p,m,n} & A_{23}^{j,p,m,n} \\ A_{31}^{j,p,m,n} & A_{32}^{j,p,m,n} & A_{33}^{j,p,m,n} \end{bmatrix} \begin{Bmatrix} p_{m,n}^{\alpha} \\ p_{m,n}^{\beta} \\ p_{m,n}^{\gamma} \end{Bmatrix} = -\omega^2 M_{j,p,m,n} \begin{bmatrix} 1 & 0 & 0 \\ 0 & 1 & 0 \\ 0 & 0 & 1 \end{bmatrix} \begin{Bmatrix} p_{m,n}^{\alpha} \\ p_{m,n}^{\beta} \\ p_{m,n}^{\gamma} \end{Bmatrix}, \qquad (4.26)$$

where $A_{a,b}^{j,p,m,n}$ (a,b=1,2,3) and $M_{j,p,m,n}$ are the elements of the non-symmetric matrices, deduced from Equation (4.23) and they are given in Appendix A. The elements $A_{a,b}^{j,p,m,n}$ are functions of wavenumber k, which causes the dependence of the eigenvalues on k. This results in the dispersion of the waves.

Equation (4.26) represents an eigenvalue problem. The eigenvalue ω^2 gives the frequency of the guided wave. The eigenvectors $p^{i}_{m,n}$ are used for the calculation of the particle displacement. The phase velocity can be calculated using the equation, $v_p=\omega/k$, and the group velocity with the equation, $v_g=d\omega/dk$. Standard computer programs can be used to numerically solve Equation (4.26). Matlab R2016a is used to obtain the solutions. These solutions are obtained by using M=N=7. At these values for M and N, the eigenvalues are expected to be converged solutions and they do not change significantly due to a further increase in the matrix dimensions.

4.2.2 Numerical Results Phase Velocity

The dispersion curves for the phase velocity are obtained by using the numerical method described above. The MATLAB code employed to model the dispersion curves is given in Appendix B. For the validation of the method, the dispersion curve is calculated for a rectangle steel rod. A comparison is made between the results of the double polynomial approach by Yu *et al.* [29] to determine how well they agree. The geometry is given by h_y/h_z=2, the width h_y=5.08 cm and the tranversal velocity (v_T) is taken as 3.23 km/s, which represents the material properties Young's modulus, density and Poisson's ratio. Figure 4.10 compares the dispersion curve of Yu et al. [29] and the obtained dispersion curves to check the accuracy of implemented numerical model. There is a shift in frequency for higher modes. At lower frequencies the overlap is very good. The mismatch at higher frequencies is possibly due to the limited number of turns adopted in the polynomial decomposition. The chosen order of Legendre polynomials may not be high enough to get completely converged solutions. The working range will be in the region of the lower frequencies. Thus the offset at higher frequencies might not be of importance. In the further discussion, only the first seven modes will be taken into account.

The shape of the dispersion curves depends on the geometry of the structure and the material properties. First the influence of the geometry will be discussed. The geometry of the cross section is given in Figure 4.9. The two parameters are the height (h_z) and the width (h_y). These two parameters are rewritten to obtain a new parameter, the ratio between the width and the height ($r = h_y/h_z$). The two geometry parameters influencing the dispersion curves are from now on the ratio (r) and the width (h_y). Figure 4.11 displays the influence of this ratio on the dispersion curves. The material properties are the Young's modulus of 200 GPa, a density of 7850 g/m^3 and a Poisson's ratio of 0.3. The width is taken as 0.1 meter. The main difference between a square rod (r=1) and a rectangular rod(r≠1) is that for the square configuration twice two modes overlap and that these modes are not distinguishable in the graph. This is caused by the geometrical symmetry of the square, which makes it possible for the two modes to overlap. These two modes start to differ as the ratio start to deviate from 1. Another consequence is a change in the cut-off frequency. The cut-off frequency is lowered due to the increased ratio between the height and the width. Figure 4.12 demonstrates the influence of the width (h_y) of the rod, keeping the ratio (r) constant. The graph is elongated along the

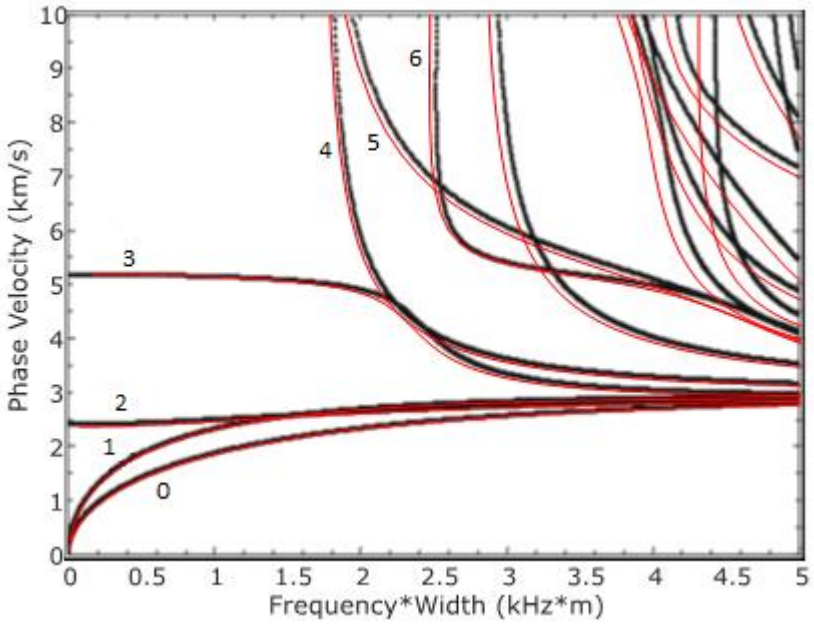

Figure 4.10: Dispersion curve Yu et al. (black lines) and authors' results (red lines), including the numbering for the first seven modes.

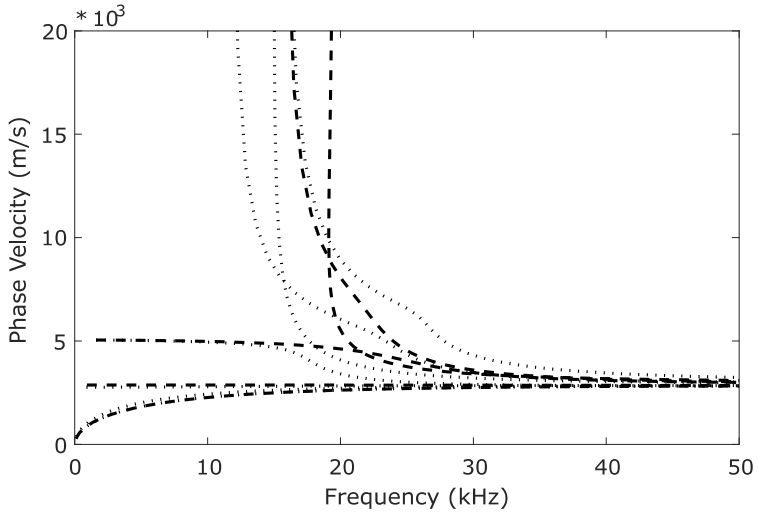

Figure 4.11: Influence of the ratio, r=1 (dashed) and r=0.75 (dotted).

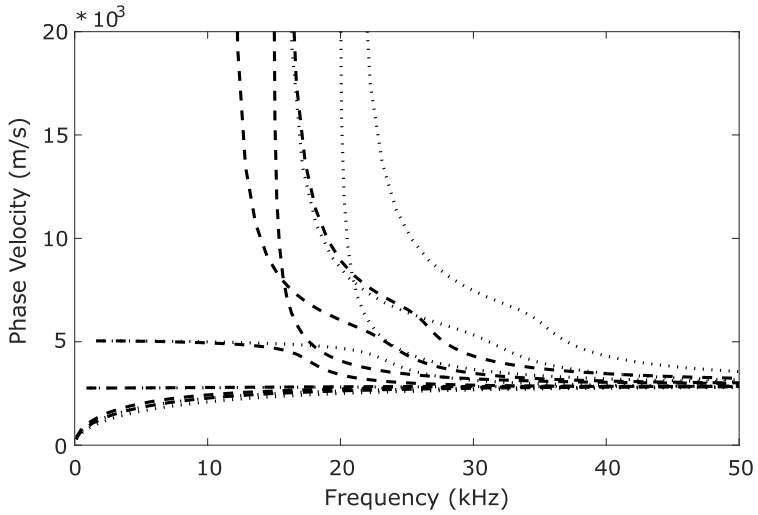

Figure 4.12: Influency of the width, h_y=0.1 m (dashed) and h_y=0.075 m (dotted).

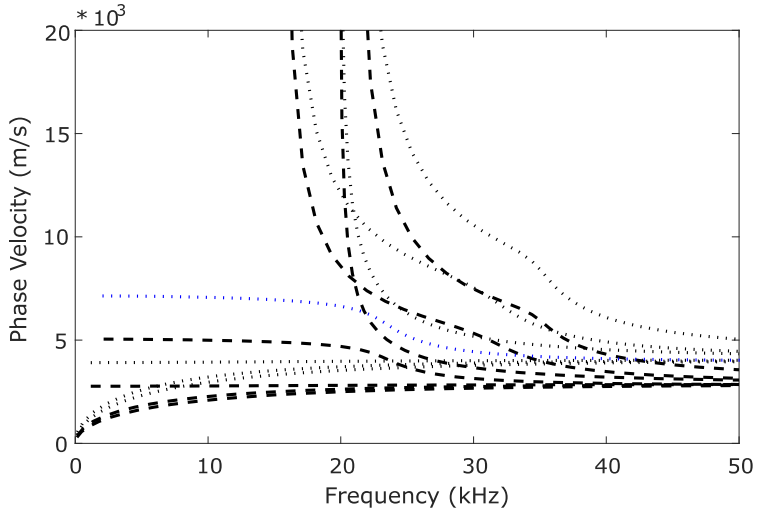

*Figure 4.13: Influence of the material properties, standard (dashed), 2*E or 0.5*ρ (dotted).*

frequency axis, for a shorter width. This means that for a shorter width, the cut-off frequency is increased. The phase velocity axis is unaltered due to this change in width.

The material properties are the other factor that affects the dispersion curves. Figure 4.13 shows the influences due to a change in Young's modulus (E) and density (ρ). As can be seen from the figures, only the phase velocity is affected by a change in these material properties. This entails that the cut-off frequency does not change with a change in material properties. The Poisson's ratio is kept out of consideration, because it does not influence the behaviour of the dispersion curves much. The increase in Young's modulus makes a material stiffer. The extra stiffness causes an increase of the velocity in a material. Furthermore, the velocity increases with a decrease in density.

A normalization of the dispersion curves can be done, that takes into account the influence of the different factors discussed above. The frequency axis is influenced by the width of the beam. By multiplying the frequency with the width, the dispersion curves become independent of the width. The unit of the axis becomes kHz*m. A similar approach can be applied to the phase velocity axis. The material properties are often condensed into the transversal velocity. The transversal velocity depends on the Poisson's ratio, the Young's modulus and the density of the material. It is expressed by the following equation:

$$v_T = \sqrt{\frac{E}{2(1+\nu)\rho}} \, . \tag{4.27}$$

If the phase velocity is divided by the transversal velocity, the axis becomes dimensionless and independent of the material properties. Normalized dispersion curves are used to increase the computational efficiency. To apply these normalized dispersion curves in practice, the frequency axis needs to be divided by the width and the phase velocity axis needs to be multiplied by the transversal velocity. The need to compute new dispersion curves for every geometry and different material properties has been diminished.

Normalized dispersion curves will be used for the case of the tie rods of the Duomo. Three dispersion curves will be computed, for three different ratios of height and width. The minimum, average and maximum ratio of the cross section are respectively 0.49, 0.67 and 0.79. The dispersion curves are shown in Figure 4.14. This shows the possible variation of the dispersion curves, due to a change in ratio. The normalized cut-off frequencies ($f_{cut,norm}$) are different for various size ratios. The minimum, average and maximum normalized cut-off frequency are calculated corresponding to the size ratios of the tie rods and are given in Table 4.1. The minimum, average and maximum width of the tie rods are 43.8 mm, 55.0 mm and 66.1 mm respectively. Using these, the cut-off frequency for every cross section of a tie rod can be computed by multiplying the normalized cut-off frequency of the corresponding size ratio with the width of the tie rod. The cut-off frequencies for the minimum, average and maximum width are also given in Table 4.1 for each size ratio. There is a maximum difference between cut-off frequencies of almost 20kHz. Fortunately, the extreme cases are rare. The general trend, for tie rods present in the Duomo, is that thicker rods tend to be more rectangular, while the thinner rods have a lower value for the ratio between width and length. If this trend is correlated to the values of Table 4.1, this leads to a favourable situation, where there is less variation among cut-off frequencies for the different cross sections of the tie rods. The average cut-off frequency of all tie rods is around 20 kHz.

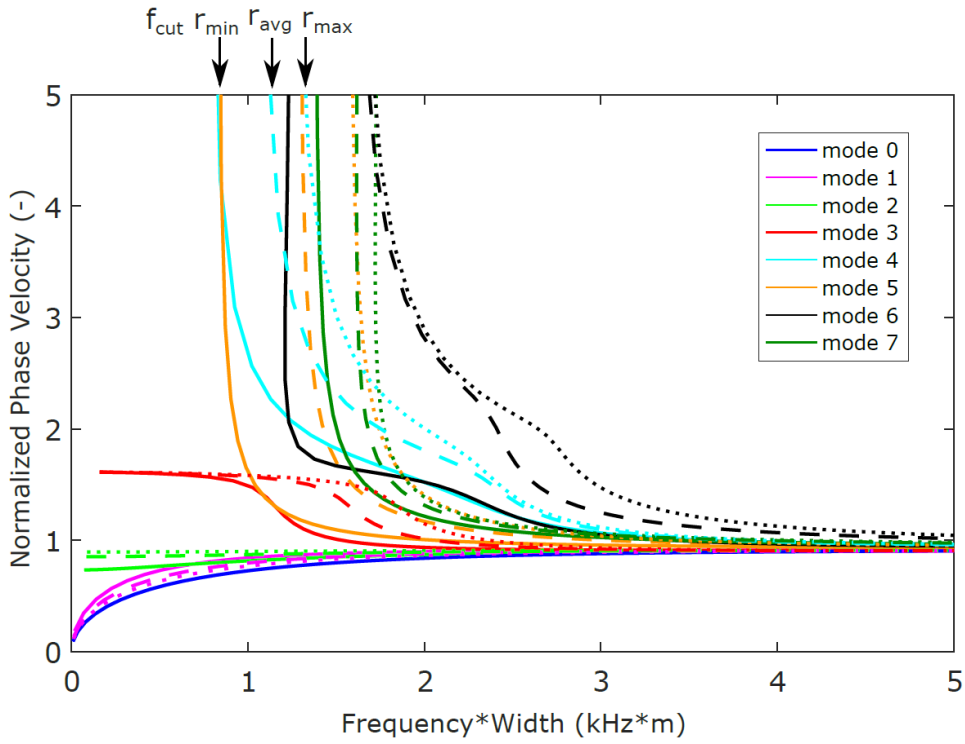

Figure 4.14: Dispersion curve for the case of the Duomo, r_{min}=0.49 (solid), r_{avg}=0.67 (dashed) and r_{max}=0.79 (dotted).

Table 4.1: Cut-off frequencies for minimum, average and maximum ratios and widths of the tie rods in the Duomo.

Ratio (-)	**$f_{cut,norm}$ (kHz*m)**	**$f_{cut,min}$ (kHz)**	**$f_{cut,avg}$ (kHz)**	**$f_{cut,max}$ (kHz)**
0.49	0.7874	18.0	14.3	11.9
0.67	1.107	25.3	20.1	16.7
0.79	1.286	29.4	23.4	19.5

4.2.3 Numerical Results Group Velocity

The group velocity is the velocity with which the envelope of a wave propagates through the medium. It is described in the following equation:

$$v_g = \frac{d\omega}{dk} \ . \tag{4.28}$$

The dispersion curves for the group velocity can be normalized with the same approach as used for the phase velocity dispersion curves. The computation of these curves is more delicate than for the phase velocity, due to the differentiation involved. This differentiation causes the computation to be more sensitive to small variations in the values of the frequency and wavenumber. The convergence of the method, explained in Section 4.2.1, influences the accuracy of the results more significantly. The obtained dispersion curved, shown in Figure 4.15, is compared with the dispersion curve obtained by using the SAFE method [23]. The dots of different grey scale represent different mesh sizes for the SAFE calculations. The overlap between the curves is adequate in region of low frequencies. The group velocity seem to be a bit lower than for the SAFE method. The values begin to deviate from 1.8 kHz*m.

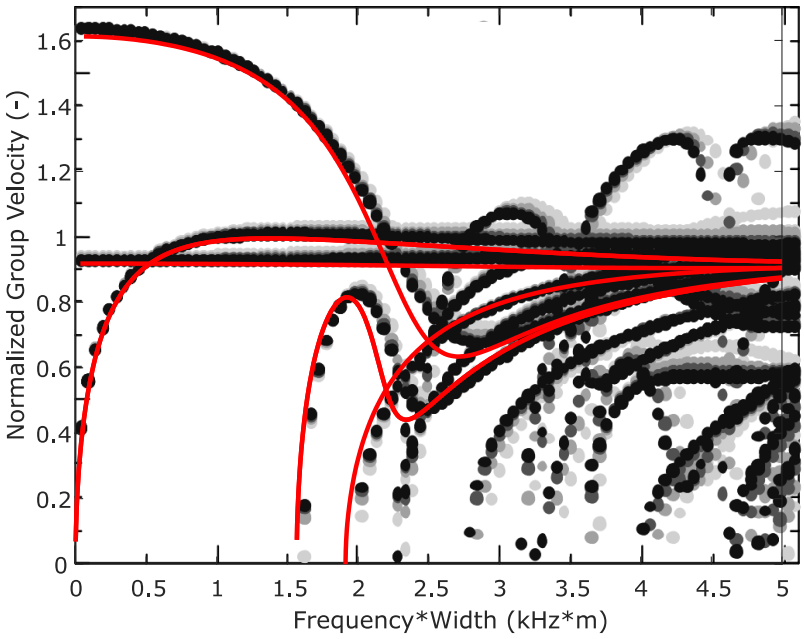

Figure 4.15: Group velocity dispersion curves, SAFE method (black dots) and polynomial approach (red lines).

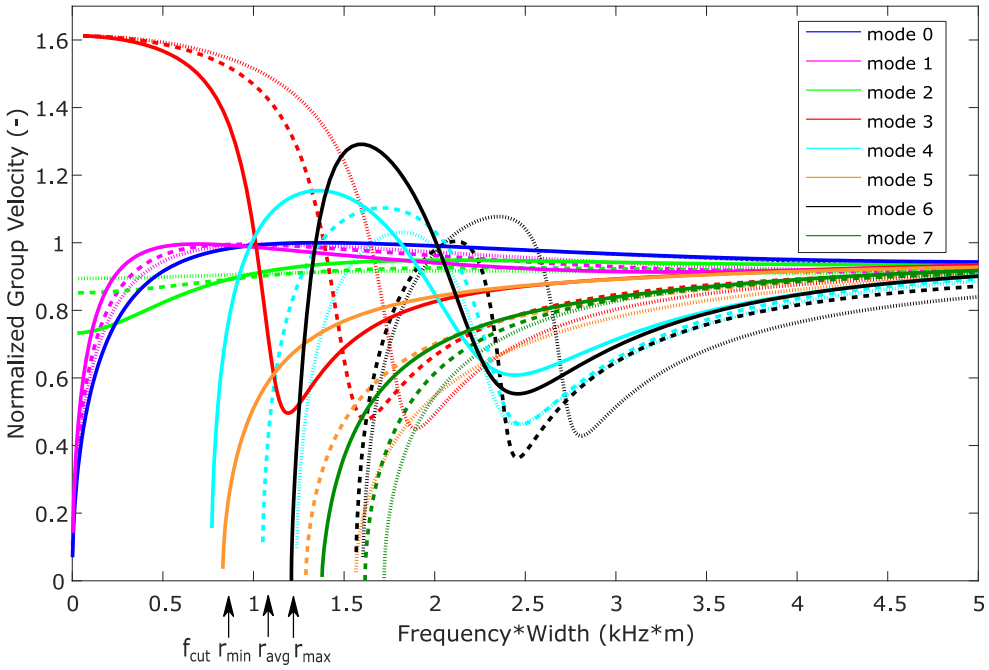

Figure 4.16: Dispersion curve for the group velocity, r_{min}=0.49 (solid), r_{avg}=0.67 (dashed) and r_{max}=0.79 (dotted).

Figure 4.16 displays the normalized dispersion curves of the group velocity applicable for the case of the tie rods. The same ratios between height and width of the cross section are used as for the phase velocity. It can also be seen that the cut-off frequencies are again at the same values as for the phase velocity calculation.

4.2.4 Shape of Vibration Modes

The simulation of the displacement of the Lamb waves is of importance to give a better understanding about the behaviour of the different modes. This information can be used for better signal processing. The detection of the Lamb waves is done by the MIRA, described in Section 4.1.5.4.

There are three or four sensors on the side of the tie-rod, depending on the height. The configuration is given in Figure 4.17. The waves are measured in the z-direction.

The displacement can be computed using Equation (4.22). This equation uses the eigenvectors obtained to calculate the displacement of the wave. Only the wave with the displacement in the z direction is of importance, because in this direction the MIRA transmits and measures the displacement. The movement of the wave in the x direction for one period of wavelength is computed with the following equation:

$$u_z(x, y, z) = exp(i2\pi x)W(y, z) \ . \tag{4.29}$$

Figure 4.18 demonstrates the displacement on the side of the rod in the z direction. The vector field is given of the displacement of the wave for one wavelength in the x direction. Figure 4.19 shows the waves measured by the sensors at the different positions on the tie rod, as displayed in Figure 4.17. The first two modes are used as an example and their displacement is normalized to mode 1. Mode 0 shows that the upper and lower position of the sensors will sense waves of opposite signs. This will result in a value of zero for the average displacement of the combined waves. Hence, no displacement will be sensed by the apparatus. However, for mode 1 the waves are in phase. Thus there is no destructive interference and the displacement will be measured. This mode is thus of interest for the signal processing part of Lamb waves.

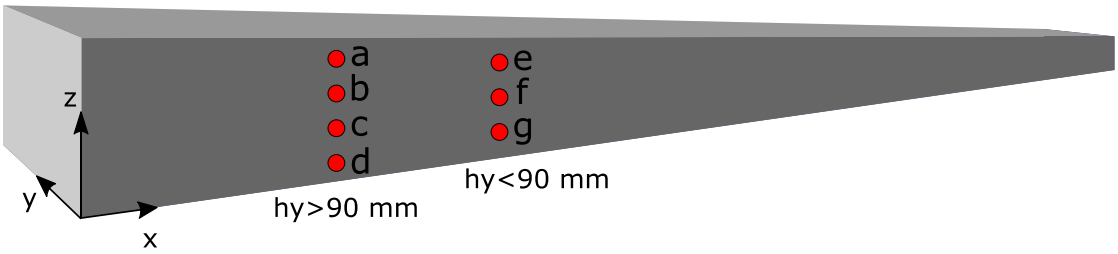

Figure 4.17: Position of the sensors (red dots) of the MIRA on a tie rod.

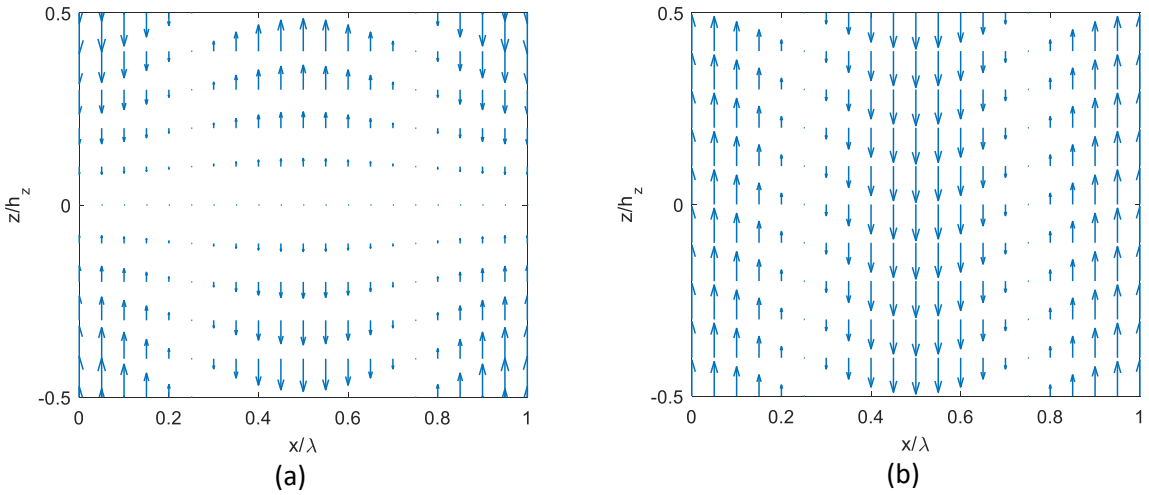

Figure 4.18: Amplitude of the wave in the z-direction for a) mode 0 and b) mode 1.

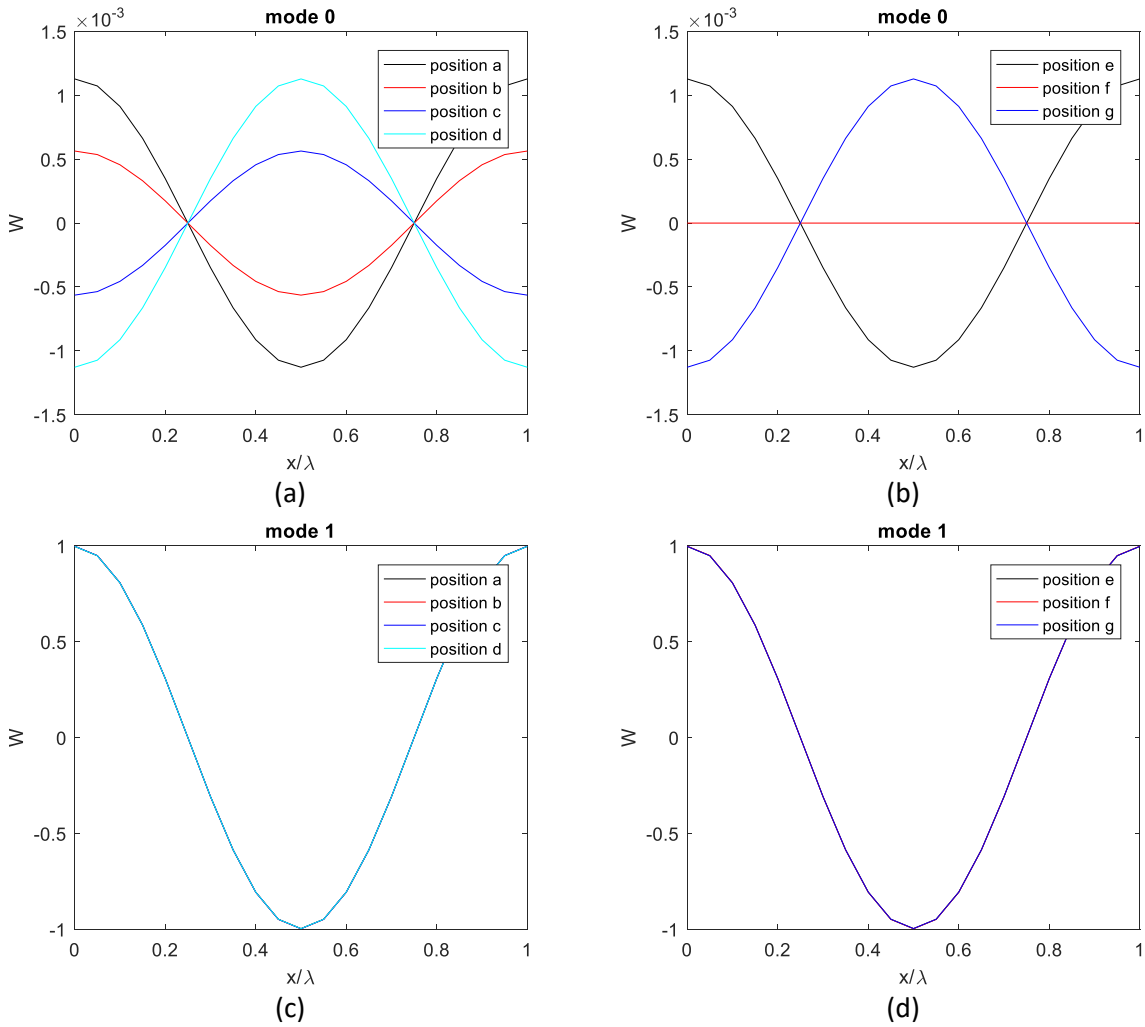

Figure 4.19: Displacement sensed by the MIRA for the positions indicated in Figure 4.17.

The different modes can be classified in 4 different categories; extensional modes, torsional modes, flexural y modes and flexural z modes. The classification depends on the symmetry of the displacements around the y- and z axis. The extensional modes are symmetric over both the y- and z axis, while the torsional modes are both antisymmetric. The flexural modes are symmetric around one axis, but anti-symmetric around the other axis. For example, the flexural z modes have symmetry over the z axis. This means that the amplitudes along the z direction are in phase, as shown in Figure 4.18b.

With this approach more information can be obtained about the different modes and their suitability for signal processing. Figure 4.20 shows the dispersion curve for r=0.75 and the various types of modes are distinguished. The first four modes are all from a different type, but higher modes do not exhibit a clear pattern. Table 4.2 presents the amplitudes of the different modes. These amplitudes are normalized to the amplitude of mode 1. This table shows that mode 1 and 2 are of highest interest, due to their high values for the amplitude. These modes are present under the cut-off frequency and thus are relatively easy to apply. Modes 7 and 10 also have high amplitudes, but are in the frequency range where many modes co-exist. This makes them more complicated to use in signal processing.

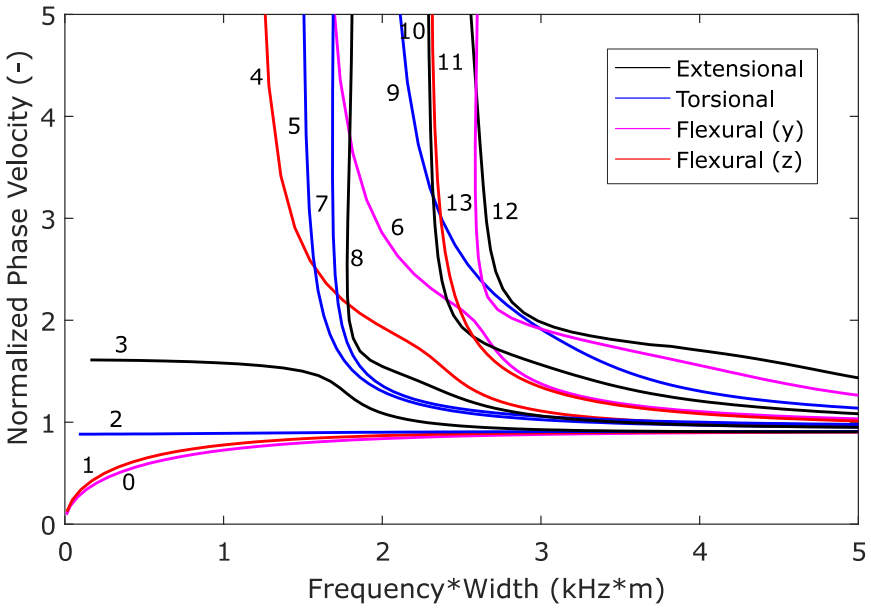

Figure 4.20: Dispersion curve with different types of modes indicated.

Table 4.2: Information about the modes, including amplitudes normalized to mode 1.

Mode	**Type of mode**	**Average amplitude (normalized to mode 1)**
0	Flexural (y)	0.00
1	Flexural (z)	1.00
2	Torsional	0.60
3	Extensional	0.00
4	Flexural (z)	0.07
5	Torsional	0.00
6	Flexural (y)	0.00
7	Torsional	0.67
8	Extensional	0.00
9	Torsional	0.10
10	Extensional	0.60
11	Flexural (z)	0.00
12	Extensional	0.00
13	Flexural (y)	0.00

4.3 Signal Processing

The goal of signal processing is to obtain useful information from the measured signals. This is done to correctly extract information needed for the damage identification. Obtaining this information is intricate due to the presence of multiple wave modes, dispersion and superposition of scattered waves. The measured signal contains the signal and additional noise. The objective is to increase the signal-to-noise ratio to determine the presence of dominant cracks and their estimated position.

The most straightforward method to determine the position of cracks is by using the difference in time-of-flights, as discussed in Section 4.1.4. Often no strong indication of the crack is present in the signal, thus signal processing needs to be applied. The easiest way to achieve a stronger signal is to overlap the received signal, as described for an array transducer in Section 4.1.5. If this is not sufficient, more tools are available to increase the signal-to-noise ratio. One of these common tools is the Hilbert transform [30]. This approach recovers the envelope of the energy distribution of the signal. The wavelet transform is another tool often used for the signal processing of Lamb waves [31]–[33]. The wavelet is a waveform with an average amplitude of zero and a limited duration. The orthogonal wavelet function is the main factor that affects the accuracy and the efficiency of the transform. The proper selection of this function is therefore of primary concern. This will lead to an improved recognisability of the signal, while the signal's energy is conserved.

The information on the behaviour of the Lamb waves in the tie rods is used to obtain improved signals. The first option is to look at the cut-off frequencies for the different geometries of the cross sections. This gives an indication of the operating frequency used for the measurements. The second option discussed is using dispersion compensation to increase the signal-to-noise ratio.

4.3.1 General Processing Tools

The most important settings of the MIRA are the central frequency and the number of cycles in the generated pulses. These parameters have a great influence on the quality of the measurements. As discussed in Section 4.2, the dispersion curve gives much information about the influence of the frequency on the wave propagation. These curves need to be taken into account, while determining the optimum settings for the measurements. The goal is to have a high signal-to-noise ratio (SNR), while having a small signal length. The small signal length is important to reduce the probability of overlapping signals coming from different reflectors. Also the correct position needs to be assigned to the crack, for this multiple techniques in combination with general calibration can be used.

4.3.1.1 Signal Processing

The signal processing is done by overlapping all 66 waves measured by MIRA, as discussed in Section 4.1.5.4. The overlap of the waves can be done using the equations in Section 4.1.5. The number of transducers is implemented in Equation (4.10) and becomes as follows:

$$s(t) = \sum_{n=1}^{12} \sum_{m=1}^{12} s_{individual}\left(t - \frac{(m+n-2)d}{v_p}\right). \tag{4.30}$$

The summation is done with a small alteration. The summation of the equation above is executed over 144 waves, but only 66 are being measured. However, this summation can be done assuming a 12x12 matrix. The elements, that do not contain a measured signal, are filled in with a synthetic signal of zeros. In this way, the full summation of all the waves in the matrix can be done, while the signal containing only zeros will not contribute to the final output. The phase velocity can be extracted from the obtained signal. The best estimate for the phase velocity is the value which leads to the highest combination of direct cross-talk signals, using the following equation:

$$s_{output}(t) = \sum_{n=1}^{12} s_{individual}\left(t + \frac{(m-n)d}{v_p}\right) \quad \text{for t} \leq \text{pulse duration} \tag{4.31}$$

After overlapping the waves, cross correlation can be used to improve the signal to noise ratio. The cross correlation is done by choosing a proper wavelet function. The wavelet is the wave emitted by the transducer and thus depends on the settings of the MIRA. The frequency and the number of cycles need to be taken into account. The wavelet is displaced over the whole signal and the similarity of the two waves is determined. It will give a high value for the correlation, if the wavelet corresponds with that part of the signal. The method amplifies the parts of the signal with a similar shape and similar frequency, while it gives a low value for varying shapes and frequencies.

The results are easier to interpret by applying the envelope of the signal. Another reason for finding the envelope function is that the maximum of the signal might be between two peaks of the oscillating signal, which can be retrieved using the envelope. The upper envelope of the signal can be created by using the Hilbert transform, as shown in the following equation:

$$envelope = \sqrt{f(t)^2 + H\big(f(t)\big)^2}\ , \tag{4.32}$$

where f(t) is the measured signal and H(f(t)) is the Hilbert transform of this measured signal. This envelope portrays the energy distribution of the signal.

The above mentioned processing tools are employed in the rest of this section to improve the obtained signals.

4.3.1.2 Results/Settings MIRA

The goal of this section is to reach a higher signal-to-noise ratio, to reduce the length of the signal and to determine the length of the dead zone, explained in Section 4.1.5.5. These three parameters determine the quality of the measured signals. The settings of the MIRA should be optimized to reach a higher quality. The settings that can be adjusted are the central frequency and the number of cycles. The original settings of the MIRA was limited to a minimum frequency of 25 kHz and a maximum number of cycles of 2. These values have been extended to 15 kHz and 5 cycles. The downside is that this will stretch the sensors and the electronics to their physical limits. Towards these limits, certain unwanted features may occur. The sensors have a high damping coefficient, allowing them to be driven at frequencies beside their natural frequency. Beyond their lower limit, the natural frequency tends to overlap the central frequency, causing the activation of multiple sets of frequencies. For longer pulses, the issue is the amount of power needed for the repeated movement of the transmitters. This is enough to drive 5 cycles. The influence of these settings on the signal processing is examined in this section. Measurements done on the visible crack of tie-rod 61-91 present in the laboratory will be used as a reference for the decision making process for establishing the settings in the MIRA. The distance to the crack is around 1400 mm. However, the crack is inclined, therefore the distance to the crack is over a range of 200 mm.

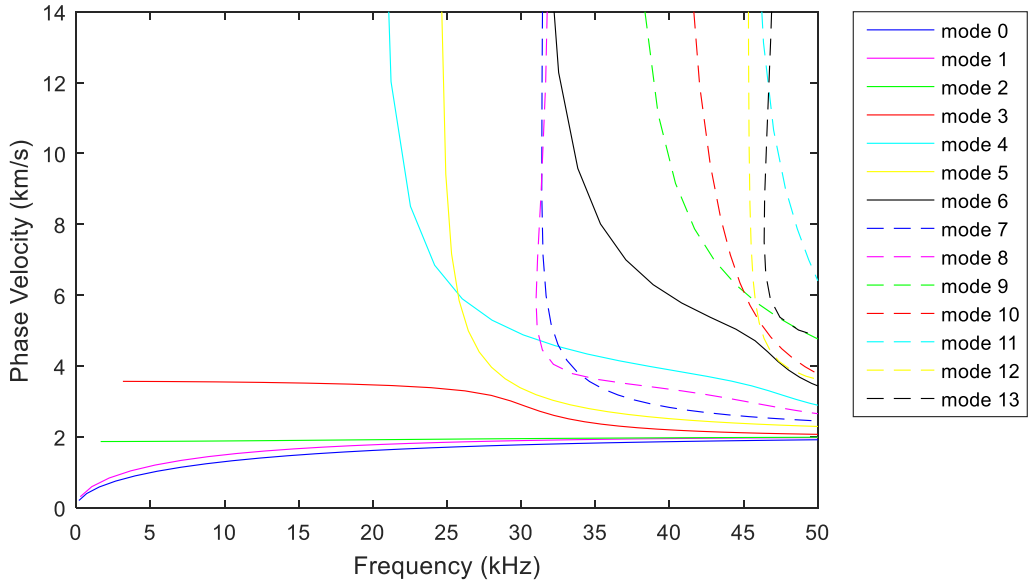

Figure 4.21: Dispersion Curve of Tie Rod 61-91.

The central frequency is chosen taking into account the dispersion curve of the specific tie rod. Figure 4.21 shows the dispersion curve for tie rod 61-91, having a cross section of 78x51 mm. The cut-off frequency is 21.2 kHz for the dimensions of this tie rod. The central frequencies used during the measurements are 15 kHz, 20 kHz and 25 kHz. Another aspect to take into consideration are the results on the relative amplitude of the mode, described in Section 4.2.4. Table 4.2 gives the relative amplitudes of 14 modes. Mode 1 and 2 are the first modes with a significant amplitude. These modes will be activated by all the chosen central frequencies. An interesting feature of these modes is the difference between their phase velocities. This difference increases when the frequency is lowered. This could be observed in the measurements as two single peaks for the same defect. It is thus favourable to have a small difference between these velocities to ensure that a defect only reflects one pulse. This means that a trade-off needs to be made between a small difference of phase velocities and not activating other modes. After modes 1 and 2 the following mode with a high amplitude is mode 7. This leads to the assumption that the true cut-off frequency is the minimum frequency at which mode 7 is present. This frequency has a value of 31.5 kHz. A central frequency must thus be chosen below this value, to avoid influences from other wave modes.

The number of cycles influences the distribution of frequencies around the central one in the pulse spectrum. From this perspective, a higher number of cycles is preferred to reach a low spread from the central frequency. Using a signal with a low deviation will be influenced less by dispersion. The downside of having a high number of cycles is that the time span of the signal increases, reducing the sharpness of any echo and increasing the dead zone of the sensor array. An optimum needs to be chosen between these two effects.

Table 4.3: Values for SNR, signal length and dead zone for different settings of the MIRA.

Frequency (kHz)	**Number of Cycles**	**SNR**	**Signal length (mm)**	**Dead zone (mm)**
15	1	8,02	310	225
	2	9,51	213	315
	3	14,9	301	405
	4	6,67	761	495
	5	10,4	706	585
20	1	14,9	428	203
	2	16,6	438	270
	3	39,6	478	338
	4	77,1	493	405
	5	32,4	546	473
25	1	8,75	407	189
	2	21,3	294	243
	3	22,9	297	297
	4	25,8	298	351
	5	34,3	345	405

Lamb wave measurements are done on the visible crack of tie rod 61-91, using different values for the central frequency and the number of cycles. From the results obtained, the SNR, signal length and dead zone size are calculated. The results are given in Table 4.3. Increasing the number of cycles results in a higher SNR. The signal length is more dependent on the frequency employed. Higher frequencies have reduced signal length. The dead zone size depends on both settings. The size of the dead zone is reduced by increasing the frequency and by decreasing the number of cycles.

The first interesting case is for measurements done with a central frequency of 15 kHz and 3 cycles, shown in Figure 4.22. In these measurements three effects can be observed. In the first part of the signal there is a large peak. This peak comes from the crosstalk between sensors, called the "dead zone". Looking at Table 4.3, the calculated length of the dead zone is 405 mm. This part of the signal should be discarded. The second effect is a second set of frequencies that is present in the signal, besides the chosen central frequency. This effect can be observed in Figure 4.22a by looking at the high frequency component of the signal and is confirmed in Figure 4.22b. The frequency spectrum is deduced from the original signal obtained, before applying cross correlation and the Hilbert envelope. The second set of frequencies has a mean value of 46 kHz. This might result from the resonance frequency of the transducer. This effect causes a lot of extra noise in the system. The last effect is the presence of two peaks around 1400 mm and 1800 mm. This is probably due to the difference in wave velocity between modes 1 and 2, as explained before. The phase velocity of mode 2 is 14% higher than the phase velocity of mode 1, which at longer distances can create two separate peaks for the same reflector. The double peak increases the complexity of the interpretation of signals, which may lead to wrong conclusions. Taking into account the above effects, using a central frequency of 15 kHz can be deemed unsuccessful.

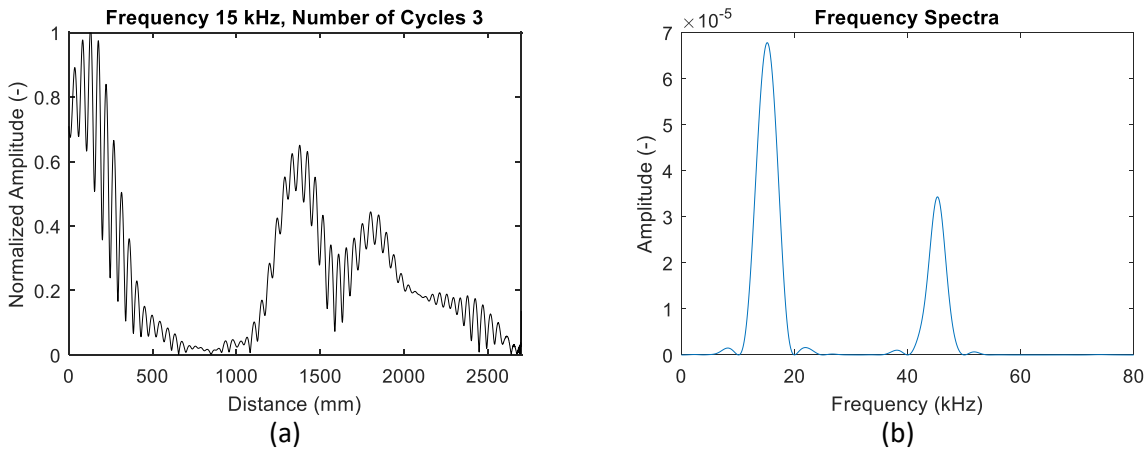

Figure 4.22: Result for settings 15 kHz and 3 cycles, a) the signal after signal processing and b) frequency spectrum of the original signal obtained.

The influences of the three effects described before are also evaluated for 20 kHz and 25 kHz. The dead zone is present for all frequencies, but it decreases with increasing frequency, due to the reduced pulse duration. Thus the influence of this effect becomes smaller. The second effect is the resonance frequency of the transducer, which excites a second set of frequencies. This effect is still present for measurements done with 20 kHz at a frequency of 60 kHz, but it is decreased significantly. While for measurements at 25 kHz, this effect is diminished. Thus the effect of a second set of frequencies has only limited impact on measurements done at higher frequencies. The last effect considered is the presence of multiple peaks for the signal from the same defect. Also this effect does not influence the measured signal at higher frequencies. It can be concluded from this, that both 20 kHz and 25 kHz are usable parameters.

Returning to Table 4.3, the best parameters should be chosen to use for the measurements. A decrease in number of cycles generally lowers the SNR. On the other hand, it also decreases the length of the dead zone, which is favourable to be able to cover a longer length during one single measurement. The signal length is more dependent on the central frequency than the number of cycles. The combination of 25 kHz and 4 cycles gives overall the best results. It gives a high SNR and has one of the smallest signal lengths, while the dead zone is still reasonable. The combination of 20 kHz and 4 cycles gives the best SNR, but has a broader signal width than the previous combination. This broader signal might cause an overlap if two different cracks are closely spaced. If necessary both combinations can be used and the results can be compared. This will enable to form the perfect mix of finding signals with a high SNR, while being able to check whether or not there is overlap.

4.3.1.3 Determination of Defect Position

An approximation of the position of the defect is an important result that needs to be obtained. This can be done using different techniques. One of these techniques needs to be chosen so that a calibration can be done. The simplest way to establish the position of a defect from the measured signal is the determination of the position of the peak. However, there are other ways to determine this position. One of the options is to find the onset time. The onset time is usually picked as the point where the difference from the noise occurs first. This concept is useful, because an inclined crack reflects the signal over a distance range. This can be done using the Akaike Information Criterion (AIC). This is an algorithm that can automatically pick the onset time. This procedure has two strategies. The first one is the global strategy, which scans the whole signal. The other strategy is the iterative strategy, which scans only a certain preselected region of the signal. The AIC needs to be adapted to be suitable for the application of ultrasound signals [34], to take into account that the

signal and noise are often in the same frequency range. A signal is represented by a certain amount of samples and all these samples or a range of samples may be used for the AIC. The following equation is employed for both the iterative and the global strategy:

$$AIC(x_w) = x_w \cdot \log\Big(var\big(R_w(1, x_w)\big)\Big) + (X_w - x_w - 1) \cdot \log\Big(var\big(R_w(1 + x_w, X_w)\big)\Big) \quad (4.33)$$

where R_w is the window selected from the signal and w is the index. In case of the global strategy, R_w contains the entire signal. X_w is the last sample of the chosen window, x_w ranges through all samples of the range and var denotes the variance function. The term R_w (1,x_w) signifies that the variance function is calculated from the first sample until sample x_w and the term $R_w(1+x_w,X_w)$ is the range from sample x_w+1 until the last sample. The point, at which AIC(x_w) is minimum, is the separation point between the noise and the signal and is thus the onset point.

In this section three cases will be considered. The first case is the determination of the position of the defect, by determining the position of the peak. The other two cases are based on the calculation of the AIC using Equation (4.33). The AIC is determined before applying cross correlation (CC) and after applying cross correlation. Figure 4.23 displays the graphs for the frequency of 25 kHz and 4 cycles as an example, because this is the most interesting case as determined in the previous section. Figure 4.23a shows the obtained signal, with the corresponding positions determined by the three different cases. Figure 4.23b gives the values for the AIC applied before the cross correlation for the whole signal. Therefore, R_w of Equation (4.33) is defined as the whole signal, as must be used for the global strategy. The determination of the position is done only for the central frequencies of 20 kHz and 25 kHz, because in the previous section 15 kHz deemed to be unfit. The results are given in Table 4.4.

The general trend in the results is that there is a shift in position between the three cases. The mean values of the defect position for each case are 1210 mm, 1360 mm and 1500 mm, for respectively the AIC after CC, the AIC before CC and the maximum value of the signal. The AIC calculation results in a lower position, because it measures the onset of the signal and not the position of the peak. There is also a shift between the two AIC cases. After applying the cross correlation, the transition

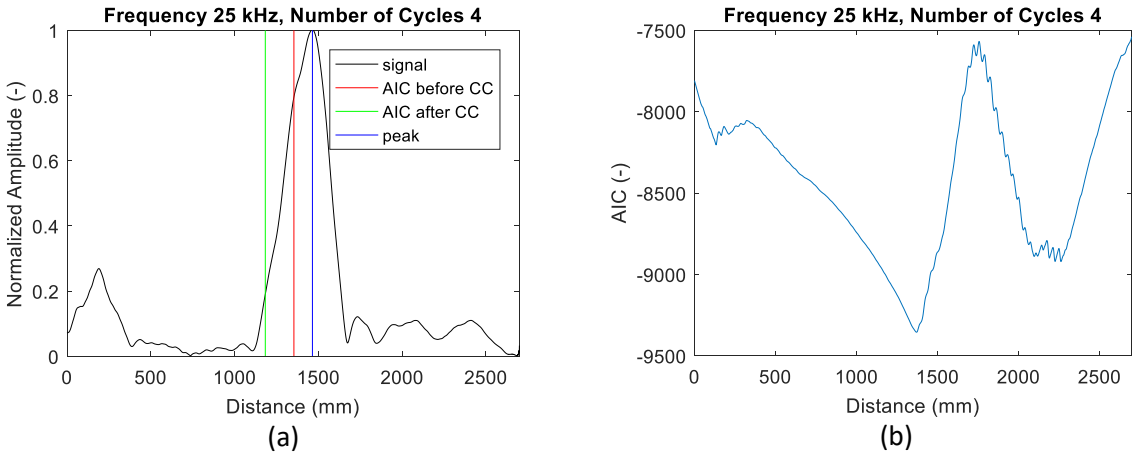

Figure 4.23: Graphs giving a) the determination of position for different techniques used and b) the AIC before the cross correlation.

Table 4.4: Results of determination of defect position, for three cases.

Frequency (kHz)	**Number of Cycles**	**AIC before CC (mm)**	**AIC after CC (mm)**	**Peak (mm)**
20	1	1360	1270	1470
	2	1350	1230	1500
	3	1350	1200	1560
	4	1370	1180	1530
	5	1370	1140	1560
25	1	1340	1270	1510
	2	1360	1260	1510
	3	1340	1230	1480
	4	1350	1180	1470
	5	1350	1120	1460

from noise to signal is sharper. This leads to an earlier onset measured by the AIC after applying the cross correlation. This trend is visible for all measurements.

Another aspect that needs to be taken into account is the standard deviation. If the deviation is small between different settings, the different measurements can be done without having to do an extra calibration. The standard deviation is 10 mm, 50 mm and 40 mm, for respectively the AIC before CC, the AIC after CC and the maximum value of the signal. The deviation is highest for using the AIC after cross correlation, due to the wavelet function involved. This wavelet varies with different settings and thus the onset point is measured with a higher deviation. The lowest deviation is for the AIC before cross correlation. This technique is thus favourable to use, because the result varies the least among the different settings. This also means that the calibration only needs to be done once, without compromising the reliability of the results.

4.3.2 Dispersion Compensation

Dispersion is the phenomenon that causes the energy of the signal to spread out in time and space as it propagates. This results in an increase of the signal duration in comparison with the input signal. It worsens the resolution of the signal and due to possible signal overlap it becomes more difficult to interpret the results. A limited bandwidth in the frequency domain can reduce the effect of dispersion, because the variation in wave velocity reduces with a smaller bandwidth. Nevertheless, dispersion cannot be avoided completely. Signal processing can compensate for the effect of dispersion [35]. This will be done in the following section. First the theory behind dispersion compensation will be described. Next the modelling of this approach will be discussed, to finish with the applicability of the dispersion compensation technique.

4.3.2.1 Theory

Dispersion can be described using mathematical tools. When the transducer emits an output signal, f(t), the Lamb wave will be distorted in time and space. This is denoted as u(x,t), where t represents time and x is the propagation distance measured from the transducer. This can be described by an equation for one mode of interest:

$$u(x,t) = \frac{1}{2\pi} \int_{-\infty}^{\infty} F(\omega) * e^{-i(k(\omega)x - \omega t)} d\omega \ , \tag{4.34}$$

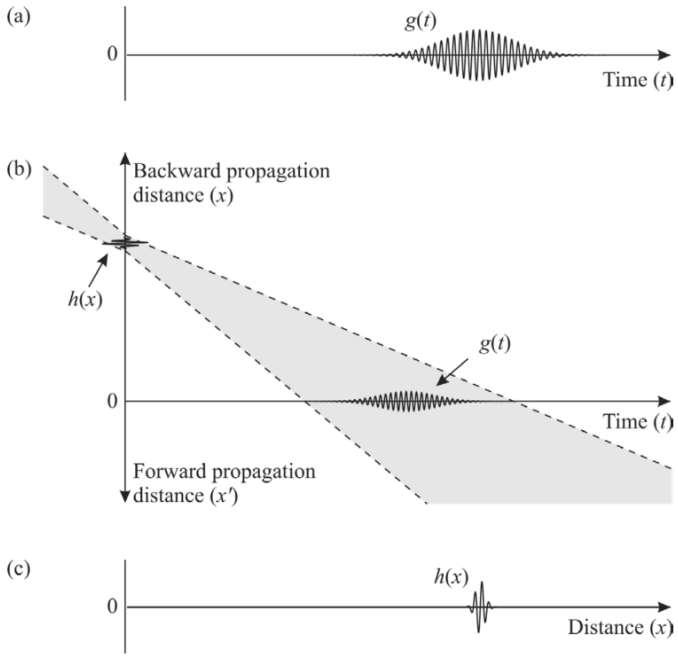

Figure 4.24: The application of the dispersion compensation algorithm: a) received signal g(t), b) the simulation of the backward propagation of g(t)using a distance-time diagram and c) the dispersion compensated signal h(x) [35].

where k(ω) is the wavenumber of the guided wave mode as a function of the angular frequency, ω, and F(ω) is the Fourier transform of f(t), the output signal. This equation represents the waveform after it travelled over a distance x and if k(ω) is not proportional to ω, it results in a dispersed wave.

The transducer works in a pulse-echo configuration. The reflections of the guided waves, called g(t), are measured by the transducers and can be calculated from Equation (4.34). This signal normally exists of multiple overlapped signals and noise. Without dispersion compensation, g(t) can be mapped using the method as described in the previous section. This means that only one value for the group velocity is used. Dispersion compensation replaces the simple term of group velocity by a frequency-dependent velocity. This dependency is described by the dispersion curves, modelled in Section 4.2.2. The relation between the velocity and the frequency of the guided wave mode of interest is applied in this dispersion compensation technique. The technique is outlined in Figure 4.24. Figure 4.24a represents the measured signal g(t) at a certain time by the transducer. The goal is to convert this dispersed signal to a function of propagation distance and to diminish the effect of dispersion. To compensate for the dispersion, a backwards propagation is modelled. Figure 4.24b simulates the convergence in space and time of the backward propagating signal, where there is a switch from the time to the space domain. The backward propagation reaches a minimum at t=0, because after this value the extra distance covered by the signal will increase the effect of dispersion. The backward propagation is taken as the positive direction x. The forward propagation of the signal in the space domain is in the negative direction of x and is called x', where x=-x'. The minimum dispersion of the backward propagation at t=0 can be described by the following equation:

$$h(x) = u(-x', 0) = \frac{1}{2\pi} \int_{-\infty}^{\infty} v_g(\omega) G(\omega) * e^{+ik(\omega)x} d\omega \ , \tag{4.35}$$

where G(ω) is the Fourier transform of g(t) and h(x) is the dispersion compensated distance-trace. This equation uses (inverse) Fourier transforms and the group velocity to go from the time to the space domain. The concept of this equation is extensively explained in the next section. Using this equation the desired mapping from time to propagation distance can be reached, which

compensates for the dispersion of the received signals. Figure 4.24c schematically shows the dispersion compensated signal h(x).

4.3.2.2 Numerical Implementation

The measured signal g(t) is the starting point for the numerical implementation of the dispersion compensation. The general set-up starts by going to the frequency domain using a Fast Fourier Transform, FFT. The frequency-dependent group velocity of the wave is then used to obtain the signal in the wavenumber domain, where the dispersion is taken into account. The last step is to transform this to the space domain using the Inverse Fast Fourier Transform, IFFT.

First an FFT is applied to the measured signal g(t), to obtain G(ω). Attention should be given to the difference between the continuous and discrete form of the FFT. The continuous form is used in the mathematical description, but cannot be used in the numerical implementation. Thus the discrete form is used for the numerical modelling. The exact equation used for the discrete FFT depends on which program is used. The equations in the following part of this section are based on the discrete FFT used in Matlab. Before applying the FFT, the signal is padded with zeros, yielding a time domain signal containing a number of points that is an integral power of two. This will improve the resolution of the Fourier transform and will decrease the computation time. Then the FFT can be found using the following equation:

$$G(\omega) = FFT\big(g(t)\big) \cdot \Delta t \ , \tag{4.36}$$

where Δt is the sampling period of the measured signal and FFT(g(t)) means that the discrete FFT of g(t) will be taken.

The next step is to determine the number of points in the wavenumber domain (n), the size of the wavenumber step (Δk) and the size of the distance step (Δx). This is determined using the Nyquist frequency. The Nyquist frequency (f_{Nyq}) is half the sampling frequency (f_s), calculated using

$$f_{Nyq} = \frac{1}{2\Delta t} \ . \tag{4.37}$$

The angular frequency needs to be used in the dispersion compensation, thus the following equation will be applied:

$$\omega_{Nyq} = 2\pi f_{Nyq} = \frac{\pi}{\Delta t} . \tag{4.38}$$

The relationship between the frequency and the wavenumber is used to calculate the phase and group velocity in Section 4.2. Now this relationship is used to determine the Nyquist wavenumber (k_{Nyq}):

$$k_{Nyq} = k\big(\omega_{Nyq}\big) . \tag{4.39}$$

Now the size of the distance step, Δx, can be calculated using the Nyquist wavenumber,

$$\Delta x = \frac{\pi}{k_{Nyq}} \ . \tag{4.40}$$

The total measured signal should be able to fit on the entire scale, otherwise signal wrapping occurs. To prevent signal wrapping in the distance domain, the following equation must be obeyed:

$$n\Delta x = m v_{max} \Delta t \ , \tag{4.41}$$

where n is the number of points in the wavenumber domain, m is the number of points in the frequency domain and v_{max} is the maximum group velocity in the used frequency domain,

determined by the dispersion curve for the considered mode. Now step size of the wavenumber, Δk, can be determined as follows

$$\Delta k = \frac{2\pi}{n\Delta x} = \frac{2\pi}{m v_{max} \Delta t} \ . \tag{4.42}$$

Combining Equations (4.40) and (4.42), the number of points in the wavenumber domain can be chosen using the following equation:

$$n = \frac{2k_{Nyq}}{\Delta k} \ . \tag{4.43}$$

The following step is to apply the dispersion compensation using the group velocity, given as

$$\Delta\omega = v_g(\omega)\Delta k \ . \tag{4.44}$$

First interpolation needs to be done to transform G(ω) into G(k) for the equally spaced k values. This is done using the relationship between ω and v_g found in Section 4.2.3, which relate to the wavenumber, k. Then also the interpolation of the values of the group velocity for every wavenumber, v_g(k), is done. Multiplying this term by G(k) will give the dispersion compensated H(k). An IFFT must be applied on H(k) to find the desired signal h(x). This is done as follows:

$$h(x) = \frac{IFFT\big(H(k)\big)}{\Delta t} = \frac{IFFT\left(G(k) * v_g(k)\right)}{\Delta t} \ . \tag{4.45}$$

The signal h(x) is now compensated for dispersion of the desired mode. The distance-axis is defined by n steps of Δx, given in Equation (4.40).

4.3.2.3 Validation Dispersion Compensation

The first step of validating the numerical implementation of the dispersion compensation is to describe the dispersion of a synthetic signal. This is done for a signal of 25 kHz travelling in wave mode 1 assuming a cross section of 60x90 mm^2 and results are shown in Figure 4.25. The black signal is the synthetic output signal, f(t). The other curves are the dispersed signal, which travelled a distance of 1,2 and 3 meters respectively. The envelope of the signals clearly show that dispersion causes a decrease in amplitude and a signal with a longer duration.

The next step is to apply dispersion compensation to these signals, as described in the previous section. The result is shown in Figure 4.26. The black curve in Figure 4.26 is the output signal. This signal can also be seen as an emitted wave that travelled a distance of 0 meters and should thus be unaltered. For the travelled signals, the amplitude should return to the original amplitude of the signal after dispersion compensation. However, all signals have a lower amplitude after applying the dispersion compensation.. Even though, the width of the signals cannot be compared due to the different scales applied, it can be seen that there are more oscillations present within the signal. It looks like the dispersion is applied for a second time and not at all compensated for, because more oscillations are present in the signals and their amplitudes are reduced. The onset of the signal is at the proper distance. This suggests that the determination of the position needs to be done using the AIC, as described in Section 4.3.1.3.

A possible reason why it does not work is a shift in the dispersion curve, because the group velocity, wavenumber and frequency are being applied simultaneously. These parameters are being used to switch between the time and space domain. Some alterations in the dispersion curves and the linear interpolation used in the numerical implementation may cause larger deviations in the FFT of h(x). This effect can be reduced by choosing a smaller interval in which the dispersion curves are

calculated. This smaller interval is particularly important around the central frequency used. In this area improvements can be made.

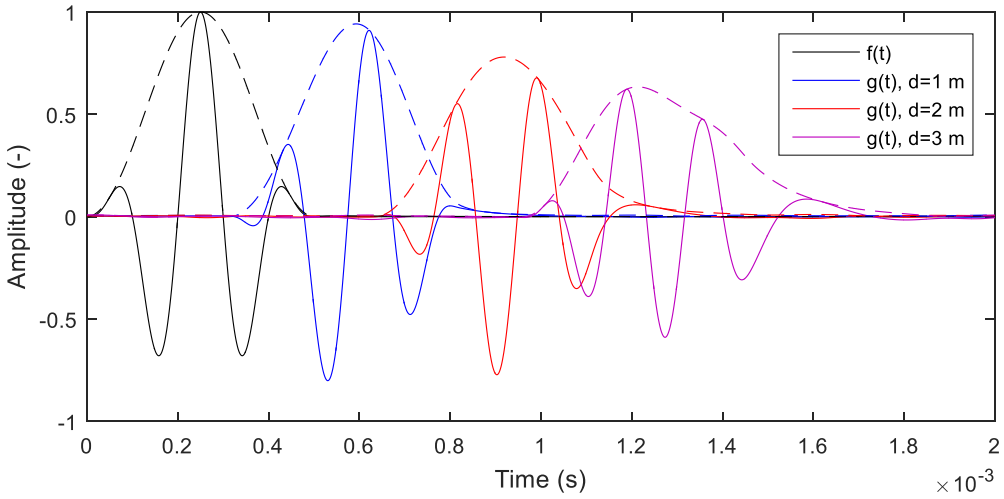

Figure 4.25: The output signal and its dispersed signals, after travelling a distance of 1,2 and 3 meters, where the dashed line is the envelope of each signal.

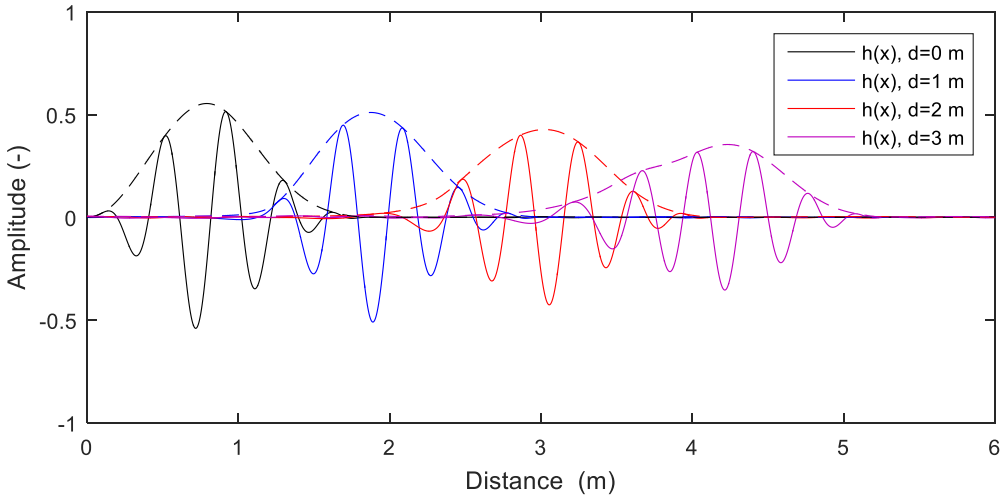

Figure 4.26: The signals after switching to the space domain using dispersion compensation.

4.4 DISCUSSION

In Section 4.2, the dispersion curves for the tie rods have been modelled successfully. The main wave modes of interest are modes 1 and 2, because these modes measured, when using the MIRA, have the highest amplitude. The next step is to model the interaction of the Lamb waves with the defect [36]. The main concern is the inclination of the crack, which causes mode conversion. Mode conversion is dependent on frequency and is strongest using a central frequency below 30 kHz [22], the frequency range used for testing the tie rods. The quality of the processed signals will increase if mode conversion is taken into account. The dispersion compensation can be applied in the mode conversion [35]. In this case, the transmitted and received wave will be compensated for different wave modes.

Section 4.3 describes the signal processing involved. General processing tools described in 4.3.1 are being applied and give reasonable SNR for the big and visible crack present in tie rod 61-91. However, the signal processing tools needs to be improved to find smaller cracks present in the tie rods. That is the reason to investigate other signal processing techniques, as the dispersion compensation. This is a promising technique to reach high values for the SNR, but difficult to implement to function properly. The flaws in the numerical implementation needs to be found before the applicability of this processing technique can be determined.

Another promising signal processing technique is the single mode extraction [37]. This method is aimed on the extraction of one single mode from a signal containing multiple modes. The technique is based on a 2-dimensional FFT (2D-FFT) in the time and space domain and a filtering technique, which takes into account the theoretical dispersion curves. The concept of this method starts with recording the Lamb waves in the time domain at many discrete positions. Then the 2D-FFT is applied to the data, recorded both in time and space directions. A 2D-FFT image is obtained with respect to wavenumber and frequency. A filter function is applied to this image that is determined by theoretical dispersion curves. This filter function retains a mode of interest and eliminates the unwanted modes. After the filtering, a 2-dimensional inverse FFT is applied to the filtered map to give the extracted wave for a single Lamb mode. In this way, one specific mode can be extracted from the other modes and can thus be studied separately. Dispersion compensation, discussed in Section 4.3.2, may be applied after the mode extraction of that specific wave mode.

For this method a significant amount of observation points is needed to get good results. This is the main obstacle of using the MIRA, which only has 12 observation points. This is not sufficient to get a good resolution in the space direction, resulting in low amplitudes of the extracted signal. This means that a device with more observation points needs to be used to be able to apply this method. Another drawback is the dispersion curves of the tie rods. The two main modes of interest, 1 and 2, have similar curves in the dispersion curves. This makes the filtering of one of these modes tricky.

4.5 REFERENCES

[1] Lord Rayleigh, "On Waves Propagated along the Plane Surface of an Elastic Solid," *Proc. London Math. Soc.* , vol. s1-17, no. 1, pp. 4–11, Nov. 1885.

[2] H. Lamb, "On Waves in an Elastic Plate," *Proc. R. Soc. London. Ser. A*, vol. 93, no. 648, p. 114 LP-128, Mar. 1917.

[3] M. F. M. Osborne and S. D. Hart, "Transmission, Reflection, and Guiding of an Exponential Pulse by a Steel Plate in Water. I. Theory," *J. Acoust. Soc. Am.*, vol. 17, no. 1, pp. 1–18, 1945.

[4] R. D. Mindlin, *An introduction to the mathematical theory of vibrations of elastic plates*. US Army Signal Corps Engineering Laboratories Fort Monmouth, NJ, 1955.

[5] D. C. Gazis, "Exact Analysis of the Plane-Strain Vibrations of Thick-Walled Hollow Cylinders," *J. Acoust. Soc. Am.*, vol. 30, no. 8, pp. 786–794, 1958.

[6] V. Igor'A, *Rayleigh and Lamb waves: physical theory and applications*. Plenum press, 1967.

[7] D. Firestone, FA and Ling, "Propagation of waves in plates," Technical report, Sperry products, Danbury, CT, USA, 1945.

[8] D. Firestone, FA and Ling, "Method and means for generating and utilizing vibrational waves in plates." Google Patents, 1951.

[9] D. C. Worlton, "Experimental Confirmation of Lamb Waves at Megacycle Frequencies," *J. Appl. Phys.*, vol. 32, no. 6, pp. 967–971, 1961.

[10] D. Frederick, CL and Worlton, "Ultrasonic thickness measurements with Lamb waves," *J. Nondestruct. Test*, vol. 20, pp. 51–55, 1962.

[11] P. D. Wilcox, G. Konstantinidis, A. J. Croxford, and B. W. Drinkwater, "Strategies for Guided Wave Structural Health Monitoring," *AIP Conf. Proc.*, vol. 894, no. 1, pp. 1469–1476, 2007.

[12] D. Chirnenti, "Guided waves in plates and their use in materials characterization," *Appl. Mech. Rev.*, vol. 50, no. 5, p. 247, 1997.

[13] C. E. Raghavan, Ajay and Cesnik, "Review of guided-wave structural health monitoring," *Shock Vib. Dig.*, vol. 39, no. 2, pp. 91–116, 2007.

[14] J. L. Rose, "A Baseline and Vision of Ultrasonic Guided Wave Inspection Potential," *J. Press. Vessel Technol.*, vol. 124, no. 3, pp. 273–282, Jul. 2002.

[15] A. Giurgiutiu, Victor and Cuc, "Embedded non-destructive evaluation for structural health monitoring, damage detection, and failure prevention," *Shock Vib. Dig.*, vol. 37, no. 2, pp. 83–105, 2005.

[16] D. L. Balageas, "Structural health monitoring R&D at the 'European Research Establishments in Aeronautics' (EREA)," *Aerosp. Sci. Technol.*, vol. 6, no. 3, pp. 159–170, 2002.

[17] Z. Su and L. Ye, *Identification of Damage Using Lamb Waves*, Vol.48. Springer Science & Business Media, 2009.

[18] S. Wooh and Y. Shi, "Synthetic Phase Tuning of Guided Waves," *IEEE Trans. Ultrason. Ferroelectr. Freq. Control*, vol. 48, no. 1, pp. 209–223, 2001.

[19] R. J. Talbot and J. S. Przemieniecki, "Finite element analysis of frequency spectra for elastic waveguides," *Int. J. Solids Struct.*, vol. 11, no. 1, pp. 115–138, 1975.

[20] M. Koshiba, S. Karakida, and M. Suzuki, "Finite-Element Analysis of Lamb Wave Scattering in

an Elastic Plate Waveguide," *IEEE Transactions on Sonics and Ultrasonics*, vol. 31, no. 1. pp. 18–24, 1984.

[21] H. YAMAWAKI and T. SAITO, "NUMERICAL CALCULATION OF SURFACE WAVES USING NEW NODAL EQUATIONS," *Nondestruct. Test. Eval.*, vol. 8–9, no. 1–6, pp. 379–389, Jun. 1992.

[22] I. Bartoli, A. Marzani, F. Lanza di Scalea, and E. Viola, "Modeling wave propagation in damped waveguides of arbitrary cross-section," *J. Sound Vib.*, vol. 295, no. 3–5, pp. 685–707, Aug. 2006.

[23] T. Hayashi, W.-J. Song, and J. L. Rose, "Guided wave dispersion curves for a bar with an arbitrary cross-section, a rod and rail example," *Ultrasonics*, vol. 41, no. 3, pp. 175–183, May 2003.

[24] O. M. Mukdadi, Y. M. Desai, S. K. Datta, A. H. Shah, and A. J. Niklasson, "Elastic guided waves in a layered plate with rectangular cross section," *J. Acoust. Soc. Am.*, vol. 112, no. 5, 2002.

[25] H. Taweel, S. B. Dong, and M. Kazic, "Wave reflection from the free end of a cylinder with an arbitrary cross-section," *Int. J. Solids Struct.*, vol. 37, no. 12, pp. 1701–1726, Mar. 2000.

[26] S. Datta and B. J. Hunsinger, "Analysis of surface waves using orthogonal functions," *J. Appl. Phys.*, vol. 49, no. 2, 1978.

[27] J. E. Lefebvre, V. Zhang, J. Gazalet, and T. Gryba, "Legendre polynomial approach for modeling free-ultrasonic waves in multilayered plates," *J. Appl. Phys.*, vol. 85, no. 7, 1999.

[28] A. A. Maradudin, R. F. Wallis, D. L. Mills, and R. L. Ballard, "Vibrational Edge Modes in Finite Crystals," *Phys. Rev. B*, vol. 6, no. 4, pp. 1106–1111, Aug. 1972.

[29] J. G. Yu, J. E. Lefebvre, C. Zhang, and F. E. Ratolojanahary, "Dispersion curves of 2D rods with complex cross-sections: double orthogonal polynomial approach," *Meccanica*, vol. 50, no. 1, pp. 109–117, 2015.

[30] D. Hilbert, "Grundzüge einer allgemeinen Theorie der linearen Integralgleichungen. Vierte Mitteilung," *Nachrichten von der Gesellschaft der Wissenschaften zu Göttingen, Math. Klasse*, vol. 1906, pp. 157–228, 1906.

[31] I. Daubechies, "The wavelet transform, time-frequency localization and signal analysis," *IEEE Trans. Inf. theory*, vol. 36, no. 5, pp. 961–1005, 1990.

[32] D. and others Newland, "Wavelet analysis of vibration, Part 1: Theory," *Trans. ASME-L-Journal Vib. Acoust.*, vol. 116, no. 4, pp. 409–416, 1994.

[33] D. and others Newland, "Wavelet analysis of vibration, Part 2: Wavelet maps," *Trans. ASME-L-Journal Vib. Acoust.*, vol. 116, no. 4, pp. 417–425, 1994.

[34] J. H. Kurz, C. U. Grosse, and H.-W. Reinhardt, "Strategies for reliable automatic onset time picking of acoustic emissions and of ultrasound signals in concrete," *Ultrasonics*, vol. 43, no. 7, pp. 538–546, 2005.

[35] P. D. Wilcox, "A rapid signal processing technique to remove the effect of dispersion from guided wave signals," *IEEE Transactions on Ultrasonics, Ferroelectrics, and Frequency Control*, vol. 50, no. 4. pp. 419–427, 2003.

[36] T.-O. Kim, G.-S. Lee, H.-Y. Kim, and J.-H. Ahn, "Modeling of eddy current sensor using geometric and electromagnetic data," *J. Mech. Sci. Technol.*, vol. 21, no. 3, pp. 465–475, 2007.

[37] T. HAYASHI and K. KAWASHIMA, “Single Mode Extraction from Multiple Modes of Lamb Wave and Its Application to Defect Detection,” *JSME Int. J. Ser. A Solid Mech. Mater. Eng.*, vol. 46, no. 4, pp. 620–626, 2003.

[38] X. Wan, Q. Zhang, G. Xu, and W. P. Tse, “Numerical Simulation of Nonlinear Lamb Waves Used in a Thin Plate for Detecting Buried Micro-Cracks,” *Sensors*, vol. 14, no. 5. pp. 8528–8546, 2014.

CHAPTER 5: EDDY CURRENT TESTING

Eddy current testing (ECT) is based on the introduction of eddy currents in the test material, induced by a magnetic field originating from a source. This technique has the possibility to identify cracks in conductive materials, both ferromagnetic and non-ferromagnetic. A big advantage is that the method can be applied without any direct physical contact between the sensor and the test material, making it a suitable technique in the field of cultural heritage. However, no former works are available on historical metal components, such as ancient metal tie rods. The present eddy current techniques thus need to be adapted to fit this application of this application.

According to this purpose, eddy current testing is primarily employed to find the exact location of the cracks detected using Lamb waves. The main obstacle is the roughness of the surface. Eddy current testing has a high sensitivity to the materials' surface and this might lead to false indications. Another obstacle is the heterogeneity of the material. The response of the eddy currents depends on material properties and can already differ in one single tie rod. This makes, among others, the calibration of the technique intricate.

The theory of eddy current testing is explained in Section 5.1. Then the requirements of the case study for this technique are established in Section 5.2. After this, the use of the low frequency probe is discussed in Section 5.3. Section 5.4 addresses on the design of new probes, the pancake probe and the U-probe. Lastly, the in-field application of eddy current testing is examined in Section 5.5.

5.1 THEORY

5.1.1 Basic Principles

Eddy current testing is based on the concept of electromagnetism. An electromagnetic coil is excited with an alternating current (AC), which produces an alternating magnetic field. This primary magnetic field generates electric current in the conductive test material, the so-called eddy currents. The eddy currents produce a secondary magnetic field. This field opposes the primary magnetic field. The typical arrangement of currents and magnetic fields is shown in Figure 5.1. If the material is non-ferromagnetic, the opposing magnetic field is the only field that contributes to the overall magnetic field and thus the overall magnetic field is weakened. For ferromagnetic materials this opposing field becomes negligible, due to the high magnetic permeability of the material. This high magnetic permeability causes a concentration of the primary field, which increases the overall magnetic field. The changes occurring in the primary field cause a change in the impedance of the coil (Z).

5.1.2 Electrical Principles

A voltage (V) applied to a circuit with only resistive elements (R) generates a current flow (I), according to Ohm's law given in Equation (5.1). If AC is applied to the circuit the current follows the voltage in phase.

$$V = IR \tag{5.1}$$

This behaviour changes when the circuit only contains an inductor, a coil. The property of this coil is called inductance (L). Inductance is an electrical phenomenon, causing a potential drop between the poles of the element by changing the current. It is defined in Equation (5.2).

$$V = L\frac{dI}{dt} \tag{5.2}$$

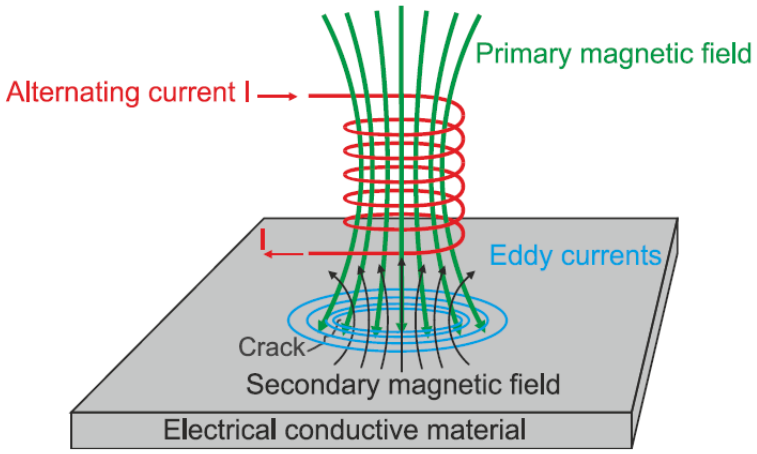

Figure 5.1: Primary and secondary magnetic field for a non-ferromagnetic test material [1].

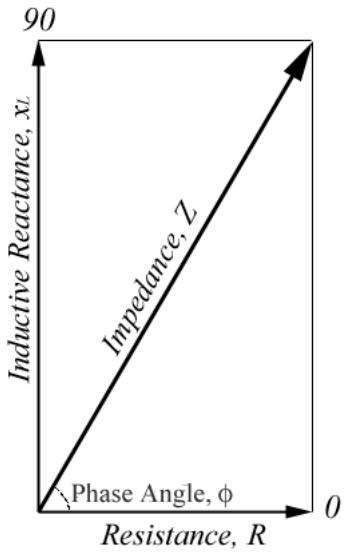

Figure 5.2: Impedance plane.

If a sinus shaped AC flows through this element, the maximum voltage is reached when the current goes through zero. The maximum voltage is thus present, when the rate of change of the current is maximum. This causes a phase shift of 90˚ between the current and voltage. The value of the voltage and current can be calculated with Equation (5.3). The inductive reactance (X_L) is given by Equation (5.4), where f is the frequency.

$$V = IX_L \tag{5.3}$$

$$X_L = 2\pi fL \tag{5.4}$$

Ohm's law changes slightly for the circuit, when a resistance and a coil are connected in series. Equation (5.1) can be rewritten as follows:

$$V = IZ \tag{5.5}$$

The impedance (Z) contains a real part, the total resistance, and an imaginary part, the inductive reactance of the coil. The impedance can be represented in an impedance plane, shown in Figure 5.2. The modulus of the impedance and the phase angle between the resistance and the inductive reactance of the circuit are respectively given in equation (5.6) and equation (5.7).

$$Z = \sqrt{X_L^2 + R^2} \tag{5.6}$$

$$\phi = \tan^{-1}\left({}^{X_L}/_{R}\right) \tag{5.7}$$

These equations are the basis of the impedance planes, used in the diagnostics of eddy current testing. They are explained in Section 5.1.5.

5.1.3 Factors Affecting the Response

There are various factors influencing the eddy current response, of which cracks and other discontinuities will be discussed in the next section. The factors discussed in this section should be held constant or should be eliminated.

The first factor is the electrical conductivity of the material. An increase in conductivity causes greater flow of eddy currents. The conductivity of a base metal can be changed by altering its

composition. This can be done by adding chemical elements and/or other metals. The production process of the material may also alter the conductivity of the material. Residual stresses in the material can cause an unpredictable change in conductivity. This means that eddy current testing is able to identify, for example, an improper heat treatment. Also the ambient temperature has an effect on the conductivity. An increase in temperature normally leads to a decrease in conductivity.

The second factor is the magnetic permeability of the material. The relative permeability of non-ferrous metals is close to one. This is not the case for ferrous metals, of which the relative permeability can go up to a couple of hundreds. This does have a significant influence on the response. The permeability in these metals can locally be altered by localized stresses and heating effects.

Frequency is one of the few factors that can be controlled. Frequency can be used to alter the density and the phase of the induced eddy currents. It can also control the depth of penetration of the primary magnetic field. In general, high frequencies are used to detect surface cracks and low frequencies to detect sub surface cracks.

Concerning the sample geometry, both thickness of the specimen and the edges affect the eddy currents response. If the material thickness is less than the effective depth of penetration, the signal will be influenced by changes in thickness. Eddy currents are also distorted, when the probe reaches an edge of the specimen. If the probe is too close to an edge, the eddy currents have no place to flow. This is called the edge effect. This effect can also be seen at the interface of different materials. It can be weakened by using shielded probes, which confine the magnetic field to the area of the probe.

Another important factor is the lift-off. The strength of the secondary magnetic field depends on the amount of flux of the primary magnetic field interacting with the conductor. As the distance between the coil and the surface increases, the flux of the primary magnetic field that reaches the test surface becomes smaller. This changes the impedance of the coil, due to the decrease of the secondary magnetic field.

The last factor is the probe handling. The response signal is influenced by a difference in probe angle, contact pressure with the surface and the way a probe is held. This is especially important, if the probe is hand held. The effect can be reduced by using probes with special spring loading.

5.1.4 Influence of Cracks

The presence of cracks in the material will cause a distortion of the eddy current field. This is due to the fact that the eddy currents have to flow around them. This phenomenon is shown in Figure 5.3. This results in an increased resistance and a reduction of the strength of the eddy currents. Figure 5.3 also shows that the detection of the cracks depends on their direction. A crack parallel to the eddy currents cannot be detected, because the flow of the current is not disrupted. The maximum detectability is when the crack is perpendicular to the direction of the eddy currents. The maximum change in current flow happens for this direction and hence the largest change in impedance of the coil.

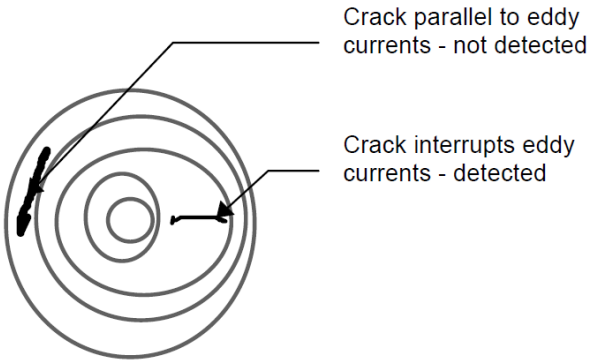

Figure 5.3: Influence of the direction of the cracks on the distortion of the eddy currents.

The size of the eddy current field influences the resistance encountered by the electrons. A small eddy current field increases the resistance and thus increases the sensitivity to cracks. A larger eddy current field decreases the overall resistance of the signal received, because only part of the field is disrupted by the crack.

5.1.5 Impedance Plane

The basic concept of the impedance plane is explained in Figure 5.2. For interpreting the measurements in an easier way, the normalized impedance plane is used. If there is no sample close to the coil sensor, the impedance Z_0 is given in Equation (5.8).

$$Z_0 = R_0 + jX_0 \tag{5.8}$$

When the coil approaches a conductive sample, eddy currents are introduced on the test piece. These eddy currents cause a secondary field. This field interacts with the primary field and the new impedance of the coil Z_c is measured. This impedance is as follows:

$$Z_c = R_c + jX_c \ . \tag{5.9}$$

The real and imaginary (R_c and X_c) can be redefined as R_{cn} and X_{cn} to obtain the normalized impedance plane, shown in Figure 5.4. The transformation can be performed by employing the equations:

$$R_{cn} = \frac{R_c - R_0}{X_0};\ X_{cn} = \frac{X_c}{X_0} \tag{5.10}$$

This transformation has a point, called air point P_0. At this point there is no test piece near the coil. This point is always at R_{cn}=0 and X_{cn}=1.

5.1.5.1 Non-Ferromagnetic Materials

If the coil probe approaches the surface of a conductive, non-ferromagnetic material, the normalized impedance plane is displaced from P_0 to P_1. This point is given in Figure 5.4. The line connecting P_0 and P_1 is the lift-off line for a material with a conductivity σ_1. The value of X_{cn1} is below 1, which shows that $X_c < X_0$. This is the result of the weakening effect of the overall magnetic field measured by the sensor. This is due to the opposite direction of the secondary magnetic field, as explained in Section 5.1.1. The eddy currents cause extra power dissipation on the test piece and hence R_{cn1} reaches values above zero.

The lift-off line depends on the conductivity of the material. The lift-off line changes if the material is less conductive (σ_2), going from P_0 to P_2. The secondary magnetic field of P_2 is not as strong as for P_1. This means that the value for X_{cn2} is in between X_{cn1} and 1. The change of resistivity in the coil is

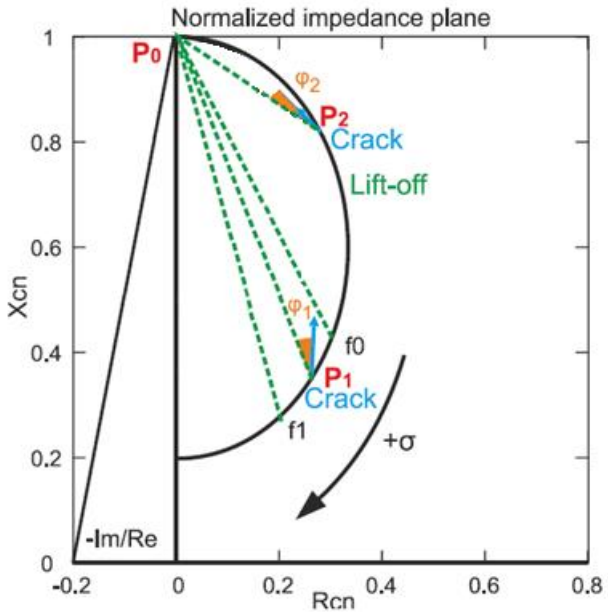

Figure 5.4: Normalized impedance plane [1].

smaller as well, because the eddy current flow is decreased. Thus the value of R_{cn2} is in between 0 and R_{cn1}.

When a crack is present in the material, there will be a displacement from point P_1 or P_2, depending on the material. This crack hinders the flow of the eddy current and thus causes a longer pathway for the eddy currents. The size of the secondary magnetic field is reduced and thus the value of $X_{cn+crack}$ comes closer to 1. The trajectory of this displacement is shown with the blue arrow in Figure 5.4. For materials with a lower conductivity, the difference between the lift-off direction and the defect direction is smaller. The trajectory from point P_2 is less pronounced than from point P_1. That makes the detectability of cracks for materials with a lower conductivity more complicated.

5.1.5.2 Ferromagnetic Material Approach

When a probe is approaching a ferromagnetic material, the reactance X_{cn} increases. This difference between the behaviour of ferromagnetic and non-ferromagnetic materials is shown in Figure 5.5. The impedance plane is divided in two semi-planes. In this way, the ferromagnetic materials can be separated from the non-ferromagnetic materials. For both type of materials, two different conductivity curves occur. The starting point of a material, without lift-off or discontinuities in the material, in the impedance plane is identified using these curves. The position depends on the magnetic properties and the conductivity of the material. From this point both the direction of the lift-off and the crack can be determined.

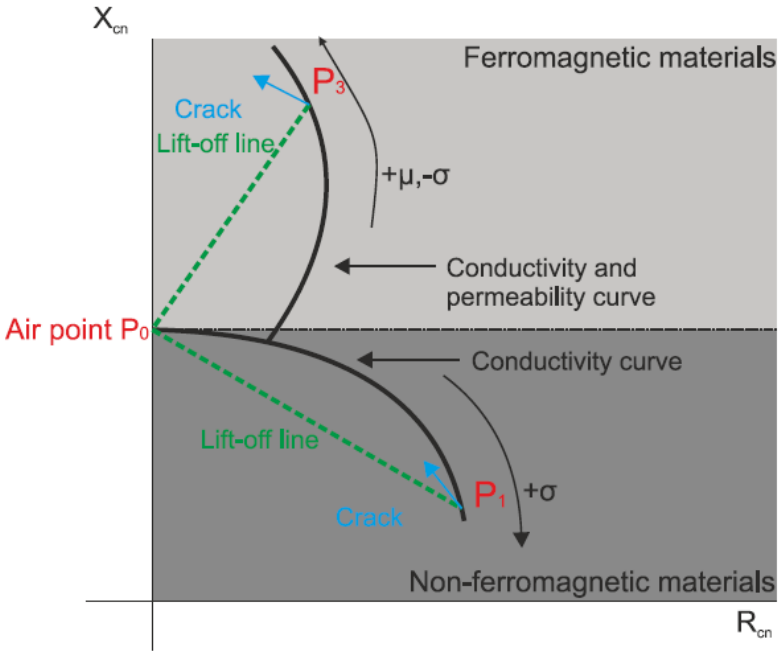

Figure 5.5: Impedance plane for ferromagnetic and non-ferromagnetic materials [1]

The primary magnetic field is increased, due to the higher relative magnetic permeability (μ_r>>1) of ferromagnetic materials. This causes an increase of the impedance, X_{cn}>1. Point P_3 is on the conductivity curve of ferromagnetic materials. The lift-off line is from P_0 to P_3. If a crack is present in the sample, the response on the signal is similar to that of non-ferromagnetic materials. There is a decrease in the power dissipation and hence in the real part of the impedance. The imaginary part of the impedance is increased. This is due to the longer pathway of the eddy currents, which increases the area encircled by the currents. Subsequently, the value for inductance increases.

5.1.6 Depth of Penetration

The thickness affected by the primary magnetic field depends on different factors, including the operational frequency of the probe. This phenomenon is quantified by the standard depth of penetration (δ) given in meters, which corresponds to the decrease of the eddy current density to the level of 37%. It can be calculated with the equation below.

$$\delta = \sqrt{\frac{2}{\mu\omega\sigma}} \tag{5.11}$$

where σ is the conductivity in $(\Omega m)^{-1}$, ω is the angular frequency in Hz and μ is the magnetic permeability Hm^{-1}. The true detectability of a subsurface crack depends on the eddy current density at that depth. A rule of thumb is that at least 5% of the surface density is necessary to detect a subsurface crack. This value is reached at 3δ, using equation (5.11). In practice, this value is often not reached due to the geometry of the sample or the skin effect. The skin effect arises when the eddy currents flowing in the specimen produces a magnetic field that opposes the primary field. This reduces the net magnetic field and causes a decrease in current flow as the penetration depth increases.

The penetration depth is increased by using the optimal exciting frequency and exciting field strength. Figure 5.6 shows that a lower exciting frequency increases the penetration depth. On the contrary, an increase of the exciting field strength increases the penetration depth, as shown in

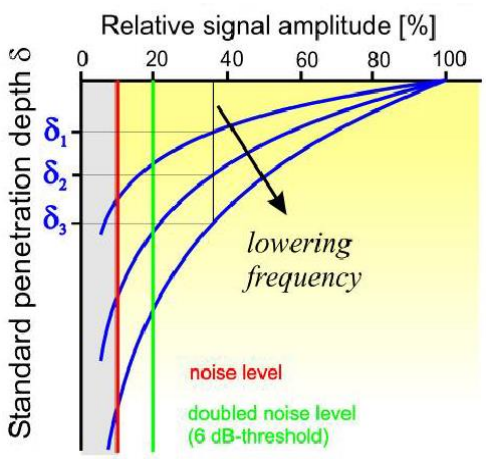

Figure 5.6: Influence of frequency on the penetration depth.

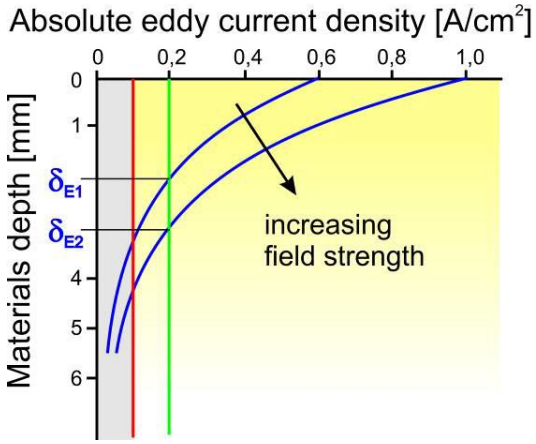

Figure 5.7: Influence of field strength on the penetration depth.

Figure 5.7. An increase in the exciting field strength can be reached using a stronger current in the coil. The maximum current is limited by the properties of the coil, related to the number of windings. In the Figure 5.6, there is a difference between the relative and the absolute eddy current density. The latter is more of importance for the detection of subsurface cracks than the relative density. The absolute eddy current density is a function of the field strength and the frequency. An increase in the field strength causes an increase in the absolute eddy current density. On the other hand, the lowering of the frequency decreases the absolute eddy current density. This is due to the lower rate of magnetic flux alteration. A trade-off needs to be made for the exciting frequency, considering both the absolute and relative current density.

5.1.7 Probe Design

The sensitivity to different types of defects and the penetration depth of the method are partly determined by the used parameters, as frequency and field strength. However, they are largely influenced by the type of probe used. The probe can thus be designed to get an optimal applicability of eddy current testing.

Different kind of sensors can be used to induce and receive magnetic fields. The most often used sensor is the coil probe, due to its simplicity. Also among the coil probes, there is a large diversity. The right choice for a certain type of coil probe depends on the application. The most common used probe is the surface probe and many other probe designs originate from this probe. Surface probes have their probe axis normal to the surface. These sensors are used in flat surface inspection for detecting penetrating cracks. The produced magnetic field has a size comparable to the diameter of the coil. Laminar cracks cannot be detected, because they are aligned with the eddy current flow. Surface probes can detect surface and subsurface cracks, but are very sensitive to lift-off and inclination. The sensor is often protected against wear by using a protective coating.

There are two different configurations for probes: absolute and differential. The absolute-mode probe consists of one coil, whose impedance is measured directly. It is both sensitive to sudden and gradual changes. A disadvantage is the probe's is sensitivity to drift from a difference in temperature and to probe wobble. The differential-mode probe consists of two coils, connected in parallel. When both coils experience the same conditions, the signals are cancelled out. The main advantages of this method, in comparison with the absolute method, is that it is not sensitive to gradual changes and it is thus less sensitive to probe wobble, to lift off and to drift from a difference in temperature. This method is very competent in finding small discontinuities. The disadvantage is that it can detect only the end of long cracks.

Interesting parameters for the design of the coil are the diameter and the number of windings. An increase in the diameter results in an increase in the area affected by the magnetic field and thus the eddy currents. Considering the same current amplitude, larger area means that small defects in the material do not have a significant effect on the measured signal. The probe becomes thus less sensitive to small defects. On the other hand, the penetration depth is increased, because the measured field strength is increased. The number of windings influences the field strength produced by the coil. The field strength increases with a higher number of windings. This increases the penetration depth.

Loading and shielding of the coil improves its sensitivity to all types of defects [2], [3]. Usually they consist out of a core and a ring of ferromagnetic material, such as ferrite. The properties of the ferromagnetic materials used are a high magnetic permeability and a low electrical conductivity. The low electrical conductivity is to prevent the presence of eddy currents in the material. The high magnetic permeability of ferromagnetic materials causes a concentration of flux in the core and shield, which improves the sensitivity and the penetration depth. The main disadvantage of both shielding and loading is the reduction of its tolerance to lift-off.

Another option to reach a higher penetration depth is by selecting certain deep penetrating field trajectories [4]. Non-axial probes are able to optimize the distance between two coils for the selection of field trajectories. These kind of probes are often called remote field eddy current probes and are the basis of the customized probe discussed in Section 5.4.2. The principle of this technique is shown in Figure 5.8. The selection of deeper penetrated flux lines is done by increasing the distance between the coils. The distance between the centres of the two coils can be considered as the effective diameter of the probe. The increase of the effective diameter does cause a decrease in the sensitivity of the probe to defects, due to the lower density of the flux lines. Thus, a compromise needs to be made between the effective diameter and the corresponding sensitivity to defects.

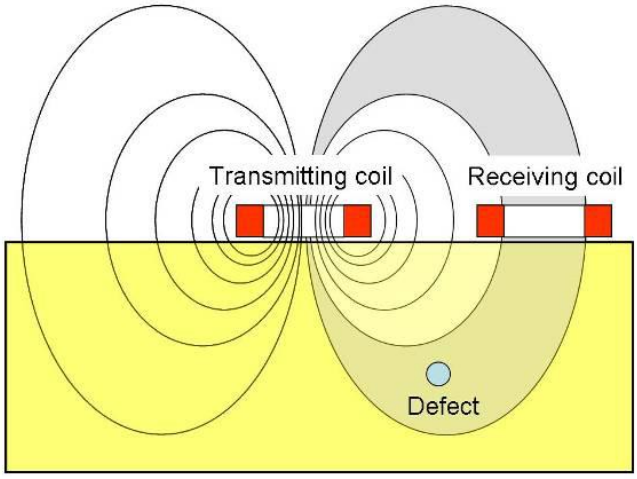

Figure 5.8: The principle behind remote field eddy current probes.

5.2 Requirements Case Study Duomo

The main purpose of the eddy current testing is the detection of dominant cracks along the tie rod. The exact position of the crack has to be measured and also obtaining more information about its geometry is favourable. The two main obstacles for using this method are the heterogeneity of the material and its rough surface. The sensitivity to sub surface cracks, the penetration depth and the execution time are the factors that need to be considered. These requirements imposed by the specific case should result in a clean signal for identifying subsurface cracks.

5.2.1 Characteristics of the Tie Rod

The geometry of the tie rod needs to be taken into account with the object to decide the measuring method. The tie rods have an average cross section of 55x83 mm^2. Section 3.1 describes the hypothesis of the presence of welds along the tie rod. These welds are the weakest part along the tie rod and are more prone to the presence of cracks. The welds are on average inclined at an angle of 27° with respect to the longitudinal direction. The average geometry of the tie rod including a crack is given in Figure 5.9.

The heterogeneity of the material causes an obstacle for the usage of ECT. The tie rod is made out of several bars; the response of ECT might differ in a single bar, but also among different bars. In a single bar, the heterogeneity might lead to false indications, due to the different local values of impedance. Among different bars, the measurements are affected by the difference in electrical conductivity. As explained in Section 5.1.3, the electrical conductivity might be altered due to chemical composition and the production process of the structural element. Both these factors were not strictly controlled by the bloomery method and the welding process in the time frame the tie rods were made. The electrical conductivity is slightly altered among the iron bars that are welded together, due to slight differences in the chemical composition between the different bars and the inability to strictly control the parameters used in the production process. Also the electrical conductivity varies slightly inside one single bar, due to the heterogeneous chemical composition.

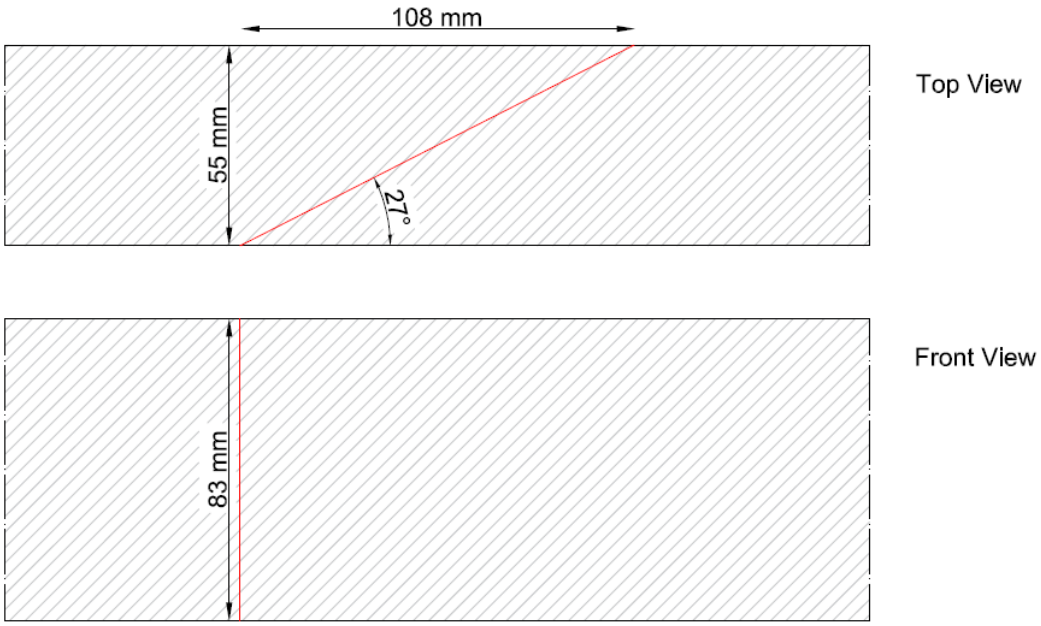

Figure 5.9: Average geometry of the geometry of a tie rod and crack, red line indicating the assumed crack geometry.

Another obstacle that needs to be taken into account is the rough surface of the tie rod, discussed in Section 2.4.1.The eddy current testing should not be sensitive to these surface properties, because the indications must solely come from the crack.

5.2.2 Requirements

The sensitivity needs to be adapted to the detection of dominant cracks. The signal-to-noise ratio can be increased by having a minimal influence of factors other than the dominant cracks. Thus, no signals should be present due to the roughness of the surface and the heterogeneity of the material.

High penetration depth is needed to be able to find flaws throughout the whole cross section of the tie rod. The probability of the nucleation of a crack in the bulk of the material is high for wrought iron. This is due to the amount and the size of the discontinuities present in the material, as discussed in Section 2.4. The best case scenario is that the probe has a high penetration depth, while it has a low sensitivity to surface variations and discontinuities inherent to the material.

The execution time of the ECT needs to be low, due to the high number of tie-rods present in the Duomo. A short execution time will reduce the costs of the inspection. To fulfil this requirement, the whole cross section should be inspected by as few scans as possible. This means that the magnetic field of the probe should cover a big part of the total cross section.

5.3 Low Frequency Probe

Low Frequency Eddy Current probes (LFEC) are suited to detect subsurface cracks. Due to the use of lower frequencies, they have a higher penetration depth and are thus able to detect cracks beneath the surface. The use of lower frequencies causes a decrease in the overall sensitivity to defects. This is counteracted by enlarging the coil diameter and increasing the number of turns of the coil. This probe is suitable for using it on the tie rods, because of its increased penetration depth.

5.3.1 Equipment

Eddy current equipment consists of an eddyscope detector and probes. The U8626005 Olympus probe is used, shown in Figure 5.10. This is an absolute probe, which works in the frequency range from 100 Hz to 2 kHz and has a diameter of 19.0 mm. The eddyscope detector used is the Nortec® 600D, shown in Figure 5.11. It supports a frequency range from 100 Hz to 12MHz and is compact for easy usage on-site. It allows the connection of customized probes.

5.3.2 Penetration Depth

A high penetration depth is one of the main requirements for the applicability of eddy current testing on the tie-rods. For this reason, an indication of the penetration depth of this probe is of importance. There are multiple difficulties for the calibration of the probe, due to the material characteristics of wrought iron. No standardized calibration block for this metal exists. Wrought iron is not only different from modern steel, but also wrought iron itself differs a lot from one piece to another. This is caused by the time span in which the elements were made, as well as the heterogeneity of the material. Therefore, the penetration depth might slightly differ among various elements.

The penetration depth is estimated experimentally by using a portion of the original tie rod 58-88. Figure 5.12 shows the block of wrought iron and the procedure for the approximation of the penetration depth. The external crust was removed from the surface to recover the bulk material. The visible crack is used as a benchmark. The probe was balanced where no defect was recognised. It was moved along the path indicated by the arrow, from the deeper part of the flaw to the emerging part. As the crack interrupts the eddy current, there will be a signal orthogonal to the lift-off signal. The start of this signal is found at point A. From this point on the amplitude of the signal increases gradually. The depth of the crack at point A is 15 mm. This value can be considered as an approximation of the effective penetration depth.

Figure 5.10: U8626005 Olympus probe.

Figure 5.11: Eddyscope detector Nortec® 600D.

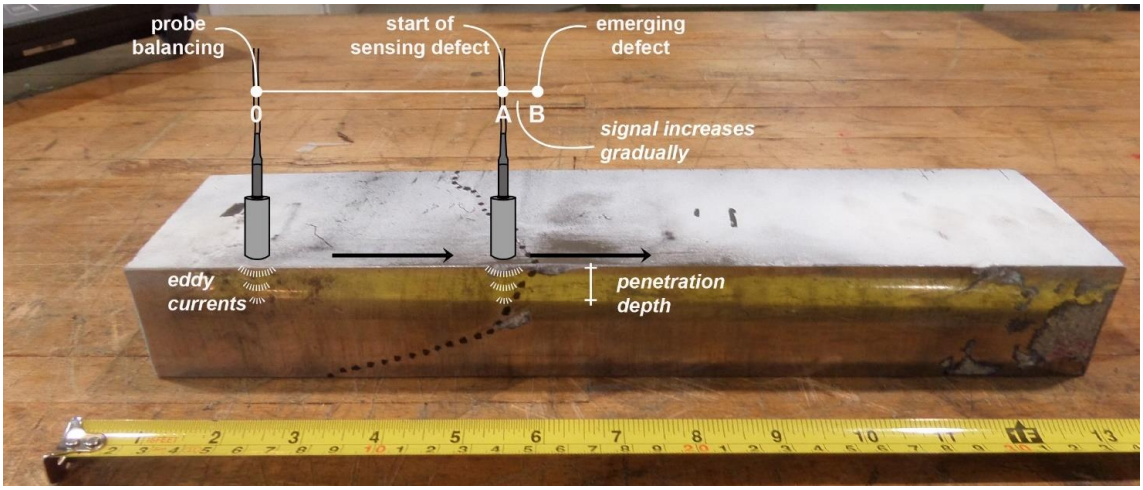

Figure 5.12: Procedure to determine the penetration depth.

Subsurface cracks can be detected if 5% of the surface eddy current density is present at that depth of the crack, as described in Section 5.1.6. This value is reached at 3δ, where δ is the standardised penetration depth. The estimation of the standardised penetration depth, for this probe with a frequency of 1 kHz, is 5 mm. This penetration depth is not sufficient for the inspection of the whole tie rod thickness, because it does not include the core of the tie rod. Moreover, the outer oxidised layer was removed from the element and the interaction between the surface layer and the magnetic field is unknown.

5.3.3 Analysis Compatibility of Probe

The requirements for the probe are described in Section 5.2. Based on these criteria, the compatibility of the LFEC probe will be discussed. The penetration depth was already discussed in the previous section. The sensitivity to surface features and the execution time of testing will be elaborated on in this section. In the end, the compatibility of this probe can be determined.

The sensitivity to small discontinuities and the uneven surface of this probe is still quite high. This is due to two main factors. The first one is the diameter of the probe. This value is equivalent to the diameter of the magnetic field produced. The diameter of the probe is 19 mm. This means that small discontinuities are able to interrupt a significant part of the total amount of eddy currents. This makes the probe more sensitive to small discontinuities. The second factor is the penetration depth, discussed in the previous section. A lower penetration depth means that a higher percentage of the total magnetic field is present at the surface and hence there is a higher sensitivity to surface features.

The execution time depends on the inspection procedure needed to obtain the necessary information. The scan of the tie rod should include the entire element. Since the diameter of the probe does not cover the entire cross section, also scans need to be carried out across the width and the height of the tie rod. However, it is still not possible to reach the central part of the cross section using this probe. The scheme of scanning the tie rod is represented in Figure 5.13. The high sensitivity to surface features discussed previously also has an influence on the inspection procedure, because not every indication signifies the presence of a crack. The probable geometry of the crack is described in Section 5.2.1. The presence of a crack can be confirmed if there are indications on multiple spots, due to the inclination of the crack. One single indication is often just a discontinuity. The execution time for this probe is high, due to the two factors described. The small diameter of the probe increases the execution time, since multiple scans over the same surface are necessary. The

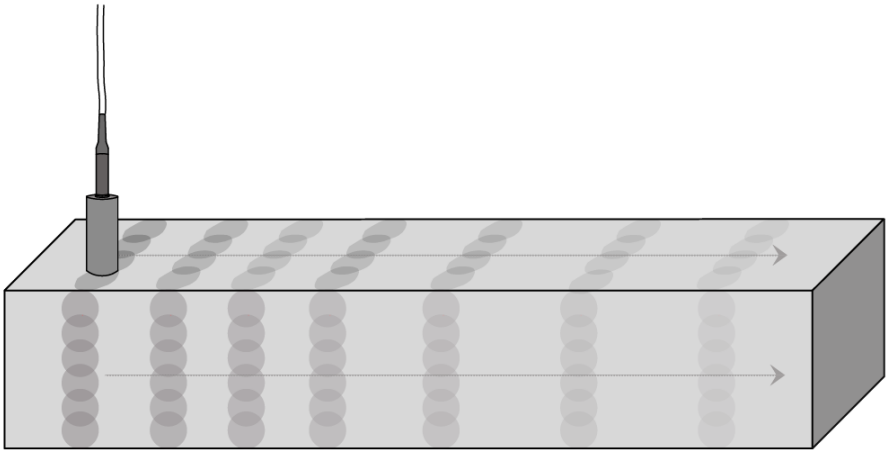

Figure 5.13: Scan procedure of the tie rod if the LFEC probe is employed.

need to have multiple indications for the determination of a crack also means an increase in the execution time. The consequence of receiving a signal is that the area around this signal should also be examined carefully, increasing the execution time.

Even though the LFEC probe is developed for detecting isolated subsurface cracks under ideal conditions, including a smooth surface and homogeneous composition. It still has some shortcomings for the application on the examined case study. The penetration needs to be increased in order to identify cracks that are deeper embedded in the bulk of the material. The scan procedure is not time efficient as well. An optimal scenario is that only a singular scan is necessary along the length of the element. The detected anomalous signals should only originate from major defects and cracks. According to this purpose, the sensitivity needs to be lowered, to ensure that discontinuities and the surface do not give any significant disruption of the eddy currents. These improvements can be made by developing customized probes, which will be described in the next section.

5.4 CUSTOMIZED PROBE

Eddy current probes consist out of one or more coils. Several features can be tuned to satisfy the test purposes. The flexibility of adjusting the probes makes eddy current testing interesting for many applications. The adjustment of the probe's features should result in an optimal sensitivity, while reaching a higher penetration depth and less noise. Therefore, two customized probes are designed to detect dominant flaws in structural elements made of a heterogeneous metal. The main focus is to increase the penetration depth without significant loss of sensitivity.

5.4.1 Pancake Probe

In order to optimize ECT for tie-rods inspection, a customized pancake probe was realized. Pancake-type probes are axial coils whose axis is perpendicular to the inspected surface. In this way, they are quite similar to the LFEC probe used in Section 5.3. The main difference is the flatter dimensions of the pancake probe. The general concept of this probe is given in Figure 5.14. The eddy currents flow parallel to the surface of the material. This means that a crack perpendicular to the surface is detected best, because this configuration will hinder the eddy currents the most.

This probe was especially designed to be able to intercept dominant cracks by testing the smaller side of the tie rod. In Figure 5.15 the trajectories of the eddy currents are shown for the dominant defect morphology. Two cases are considered, testing the smaller and testing the larger side. Scanning the smaller side, Figure 5.15a, gives a higher defect signal. The path of the eddy currents is perpendicular to the surface of the crack, which causes the eddy currents to be highly disrupted. This results in a high variation of impedance and thus a high signal amplitude. In the other configuration, Figure 5.15b, the eddy current path is under a low angle with the cracked surface. This leads to a small difference in impedance, because only a small part of the eddy currents is interrupted. This configuration will thus result in a much lower signal than for the former one.

The design of the pancake probe includes several considerations. The first consideration is a consequence of using a low frequency of 500 Hz, which increases the penetration depth. This low frequency results in a reduction of the strength of the magnetic field produced by the coil. The solution lies in the geometric features of the coil. The first step is to increase the probe diameter. The second step is to increase the amount of windings, which has a direct relationship with the strength of the field produced as explained in Section 5.1.7. These two steps will neutralize the loss of overall sensitivity, due to lowering the frequency. The second consideration is the execution time that is determined by the size of the probe diameter. As discussed before, the execution time is lowered by scanning the whole section in one single scan. The size of the diameter is thus chosen so that it will cover the width of the tie rod. Next to these considerations, a ferrite core is used to concentrate the magnetic flux and thus increase the sensitivity to defects of the probe.

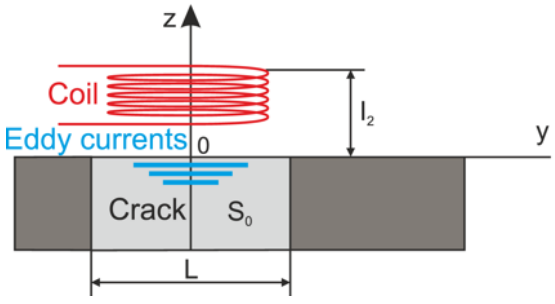

Figure 5.14: General concept of the pancake probe.

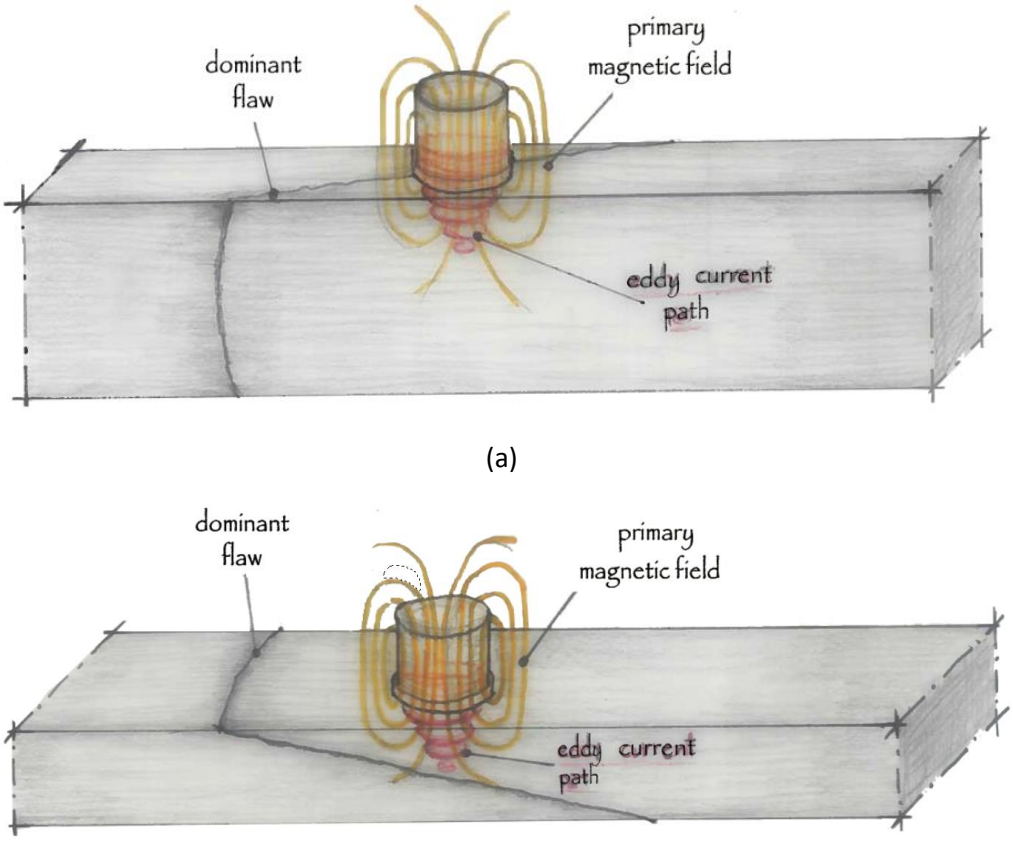

Figure 5.15: Eddy current trajectory with respect to the dominant crack, a) smaller side and b) larger side.

The considerations explained above resulted in the probe design shown in Figure 5.16. The coil is 12 mm high and has a total diameter of 40 mm. The total diameter is taken slightly smaller than the width of the tie rod to reduce the influence of the edge effect, explained in Section 5.1.3. Inside the coil a ferrite core is placed with a toroidal shape. Its inner and outer diameter are respectively 15 mm and 27 mm. The entire coil is inserted in a cylindrical case and the bottom is protected by a cap in order to reduce friction and avoid direct interaction between the wire and the metal. This protection causes a small lift off.

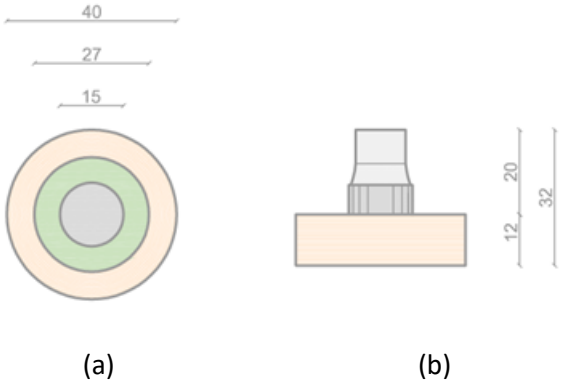

Figure 5.16: Design of the pancake probe in units mm, a) bottom view and b) front view.

In this version of the pancake probe, there is no shielding yet and hence it is influenced by edge effects. The width of the tie rod is only slightly bigger than the probe, to reduce the execution time. This results in that edge effects will always be present. Shielding needs to be added to ensure that the magnetic field is confined to the diameter of the probe and to eliminate edge effects. Once this modification is implemented, reliable results are expected to be obtained.

5.4.2 U-Probe

The second designed probe is related to a horseshoe probe, called the U-probe. An example of a horseshoe probe is shown in Figure 5.17. The main feature they have in common is the generation of a magnetic flux parallel to the test surface. This magnetic flux produces eddy currents perpendicular to the test surface, making it possible to identify cracks parallel to the test surface. The probe designed to inspect tie rods contains two coils connected in series. The two coils are positioned on the legs of a U-shaped support.

As discussed before, the optimal design of a probe depends on the shape of the dominant flaws. This probe is designed to inspect the larger side of the element. Figure 5.18 shows the configuration of the probe with respect to the tie rod and its dominant crack. As can be seen for the larger side, the eddy currents produced are perpendicular to the surface of the crack. The distance between the coils for this design is not adjustable. This causes the need to rotate the probe to inspect the smaller side. Figure 5.18a shows a 90° degrees rotation of the probe, giving a lower signal in this configuration. To receive a higher signal, a different rotation can be adopted. The probe needs to be parallel to the dominant flaw to reach a maximum signal. All though, the probe is especially designed for the larger side, also information can be obtained from the smaller side.

This design needs to take into consideration the low frequency of 500 Hz, as does the pancake probe. The resulting low sensitivity is increased by using two coils in series and thus doubling the number of turns. Further, ferrite cores are incorporated to concentrate the magnetic flux and a big diameter of the coil is used to increase the sensitivity. Another consideration is the distance between the centres of the two coils. The distance is chosen so that the probe can scan the larger side of the tie rod in a single scan. The final design is shown in Figure 5.19. The front view shows clearly how the coil is made. The total probe width is 95 mm. The ferrite cores, which guide the magnetic field, are separated by 45 mm with a total width of 85 mm. The two ferrite cores are protected from direct contact with the rough surface by applying a protective layer.

The U-probe does not have shielding and is thus affected by the edge effect. The resulting edge effect has less influence on the U-probe than on the pancake probe, devised in the previous section. This is due to the configuration with the two coils, which already guides the magnetic field inside the bulk of the material. In the pancake probe the guidance of the magnetic field lines can only be

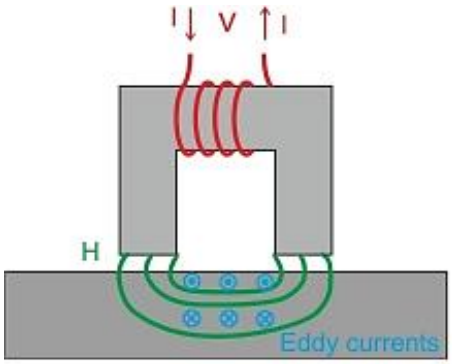

Figure 5.17: Example of a horseshoe probe.

achieved by using shielding. This makes the U-probe more reliable. The distance between the coils is still fixed with the current U-probe. An improvement can be made by making this distance adjustable. This will widen the applicability of this probe by being able to adjust on-site depending on the specific dimensions of the examined tie-rods. Next to the adjustment to the size of the tie rod, it can also be used to select certain penetrating magnetic field trajectories, as explained Section 5.1.7. This signifies that the penetration depth can be chosen, while paths that cause noise can be ignored.

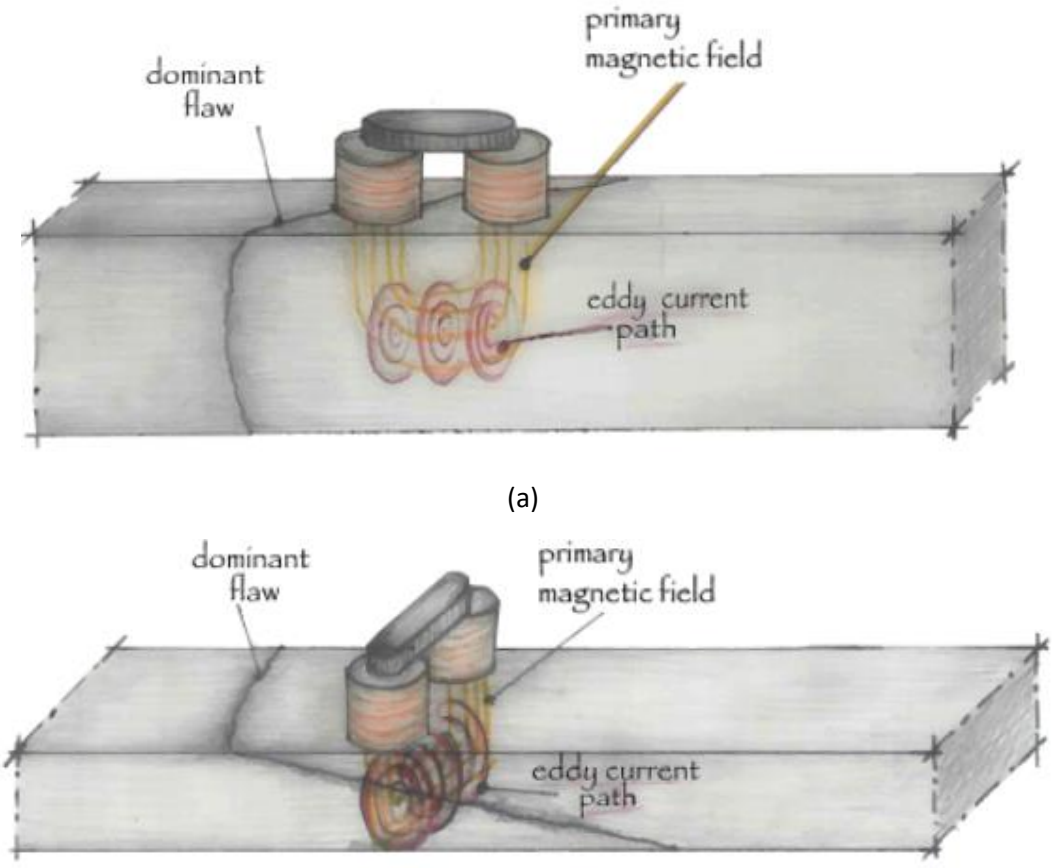

Figure 5.18: Eddy current trajectory with respect to the dominant crack, a) smaller side and b) larger side.

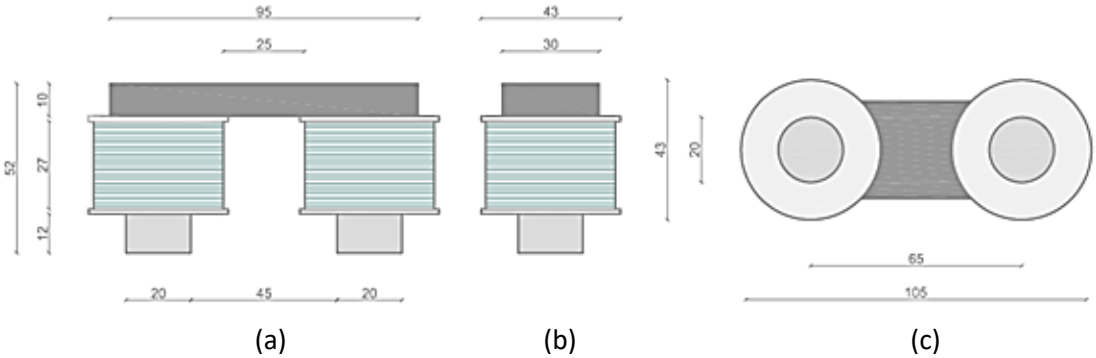

Figure 5.19: Design of the U-probe in units mm, a) front view, b) side view and c) bottom view.

5.5 In-Field Application

The in-field application of the above mentioned ECT probes proves their effective applicability for the discussed case study. The applicability on-site is tested for the low-frequency probe and the U-probe. The pancake probe is not tested on site yet, because it is still too much affected by edge effects. Improvements in the laboratory are still needed before the in-field application of this probe. The other two probes are developed enough to be used on site. The low-frequency probe is used on the two failed tie rods stored in the basement of the Duomo. The U-probe is used on several tie-rods still in service in the Duomo. One of these tie rods with interesting results is taken as an example.

5.5.1 Low-Frequency Probe

In 1470 the four tie rods connecting the piers of the *tiburio* broke, when hidden arches were built on top of the *tiburio* with an offset. Two of them fell to the ground and the other two were found broken near the anchorage during the restoration works in the 1980's. The broken tie rods were removed and stored in the basement of the Duomo. On these rods the testing of the low-frequency probe is done. The main reason to test this probe on these tie rods is the long execution time of the testing using the LFEC probe. Since they were easy accessible the drawback of the long execution time of testing is not relevant.

Two out of the four planes for both tie rods were accessible for measurements, due to the way the rods were stored. One short side of the tie rods was not reachable, because these sides were faced towards the ground, leaving too little space to use the probe. The tie rods were placed next to each other, with two long sides facing each other. These two sides were not available for testing due to a shortage of space. The scan procedure is similar to the one depicted in Figure 5.13. The probe is moved in the longitudinal direction. If a peak is measured, also the area around it is inspected in both the longitudinal and the transversal direction.

The determination of a possible weld depends on three factors: the indications surrounding the major signal, the strength of that signal and the repetitiveness of the signals along the tie rod. The most important factor of a possible weld is the presence of indications surrounding the signal. If these indications are under an angle on a possible plane as shown in Figure 5.9, then a possible weld may be found and may correspond to a crack. The strength of the signal gives information about the severity of the disruption present in the material. The signal strength is classified in three categories: low, medium and strong. An example of each category is given in Figure 5.20, by using the same settings and receiving different amplitudes. The last factor is the repetitiveness of the signal. As explained in Section 3.1, the length of the bars used to make the tie rods from are about 1 to 1.5

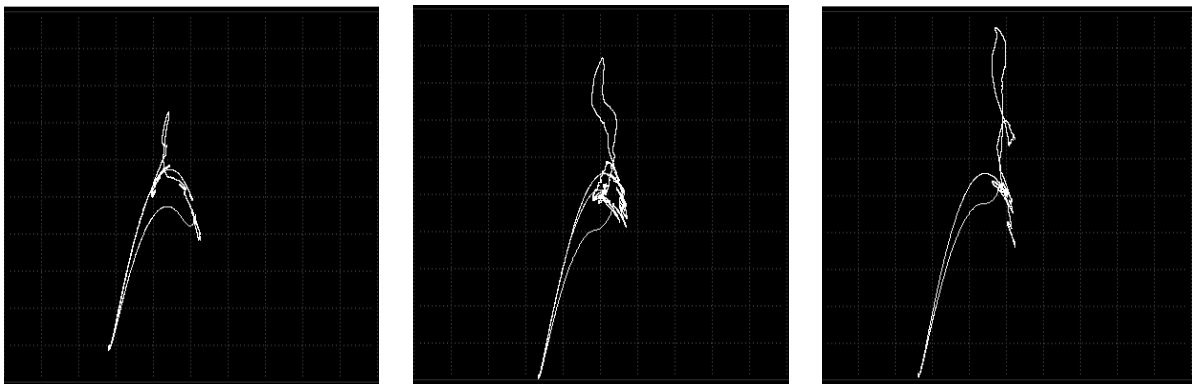

(a) (b) (c)

Figure 5.20: Categorisation of the signals, a) low, b) medium and c) strong.

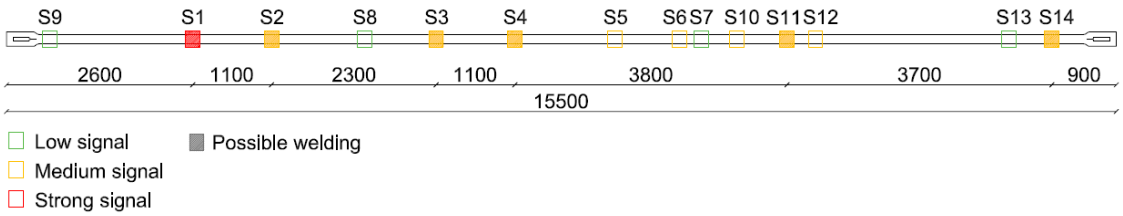

Figure 5.22: Results testing with low-frequency probe, lengths are in units [mm].

meter long. It is thus expected that the signals due to welds are periodic, often starting from a signal near the clevis.

The results of the testing done are shown in Figure 5.21. Six possible welds are found and they could contain cracks. All the signals of possible welds have at least medium amplitudes and locally more indications are found, which are under an angle on top of the bar. The repetitiveness of the signals is found for these signals as well. This is observed clearly between signals S1/S2 and S3/S4. There could be two bars present between S2 and S3, with an average length of 1150 mm. The same reasoning can be used for the signals S4/S11 and S11/S14, each having three bars between them with an average length of 1250 mm. The signal S14 has another reason for being a weld, because it is closely positioned to the clevis. The other signals are isolated and do not have the combination of signals that the possible welds have. These indications might be due to inclusions or irregularities on the surface or sub-surface.

5.5.2 U-Probe

The applicability of the U-probe is tested on the tie rods still in function in the Duomo. The tie rods are at a height of 16.5, 23.5, and 34.5 meter. The chosen tie rod is 41-11, located in the Duomo as shown in Figure 5.22a. Due to the operative conditions, the testing equipment must be compact.

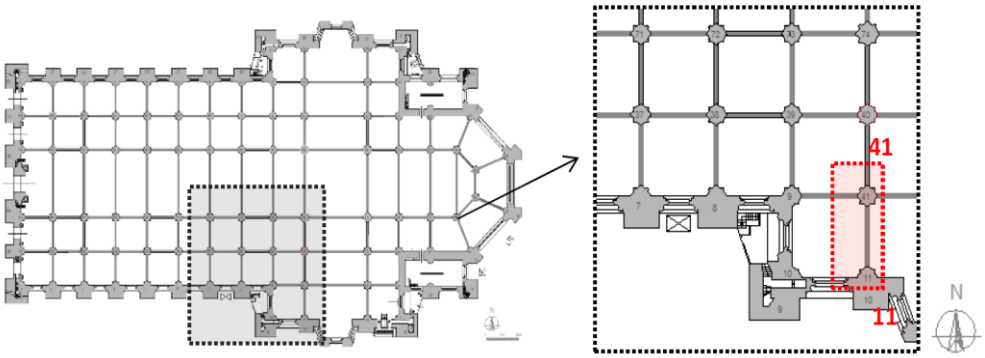

(a)

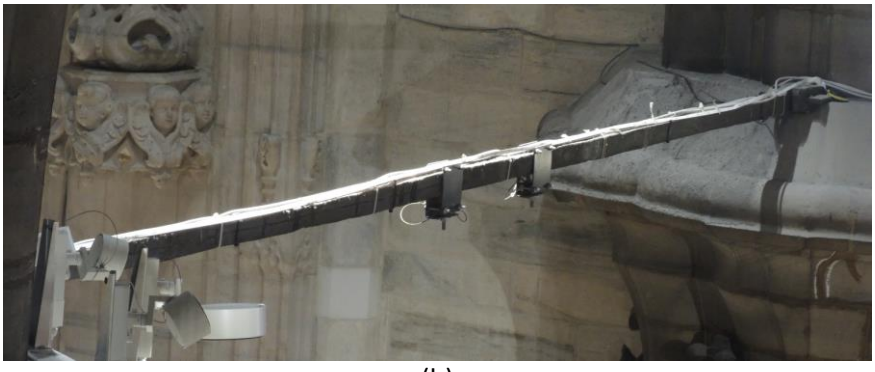

(b)

Figure 5.21: a) The position of tie rod 41-11 in the Duomo and b) the appearance of a tie rod in service.

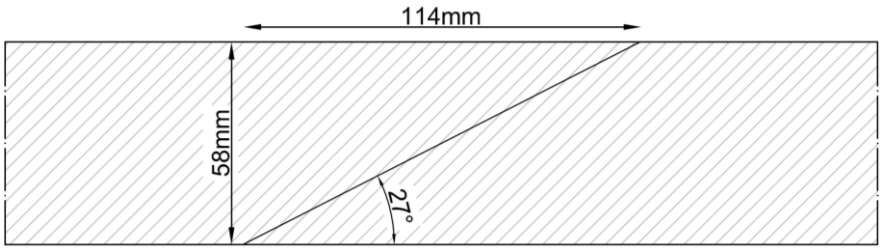

Figure 5.23: First criterion, distance between two signals on opposite sides (top view).

Moreover the equipment must be easy in use to guarantee a short execution time. Figure 5.22b displays the tie rod. The accessibility to the tie rod is limited on the top of the tie rod, because it is covered with cables. Only the larger lateral sides and the bottom are accessible for testing. There are two connections for lamps and the cables are held with tie wraps. These components cause interruption of the eddy current testing along the tie rod. The U-probe is used on the larger sides of the tie rod, as explained in Section 5.4.2. This is favourable for the accessibility to the tie rod. If the probe comes across an obstacle, the obstacle is tried to be moved along the tie rod. This is often possible. Only the connections for the lamps are not moveable and are thus blind spots in the measurements. Another aspect of this tie rod, is that it is completely covered with grey paint. It is unknown when this paint was applied and it might cover up emerging cracks.

There are three criteria for finding a possible crack. As explained in Section 3.1, the probability of finding a crack is highest on the weld. The weld has an average angle of 27° and the width of tie rod 41-11 is 58 mm. This leads to the first criterion, shown in Figure 5.23. The U-probe should measure signals on both sides of the tie rod to find a possible crack. With the given geometry and the average angle of a weld, the distance between signals on opposite sides should be around 114 mm. The second criterion is the strength of the signal, categorised as in Figure 5.20. As a rule of thumb, it is possible to say that at least one of the two signals needs to be strong. The possible crack is closer to the side of the stronger signal. The repetitiveness of the signals along the tie rod is determined by the length of the bars of wrought iron, welded together to obtain the tie rod. The length of the bars differs between 1.0 and 1.5 meter. The length of the tie rod, excluding the clevises, is about 6.40 meter. This leads to the assumption that there are 5 bars involved in the production of this tie rod.

The results are given in Figure 5.24. The possible cracks are S2/S3, S9/S10 and S11/S12. All three possible cracks satisfy the second criterion, of having at least one strong signal. The indications S2/S3 and S9/S10 both satisfy the first criterion. The distance between the signals is 120 mm and they are identified on opposite sides of the tie rod. The signals S11 and S12 are on opposite sides of the tie rod, but have a distance of 190 mm between them. This would mean an angle of 17°, which is low. On the other hand, it is the only possible crack with both a medium and a high signal. This could mean that the crack might have extended further and thus that the signals are picked up earlier. The direction of the inclination is reversed, however it is not predetermined that all inclinations are in the same direction. The repetitiveness between the possible cracks is another concern. The distance

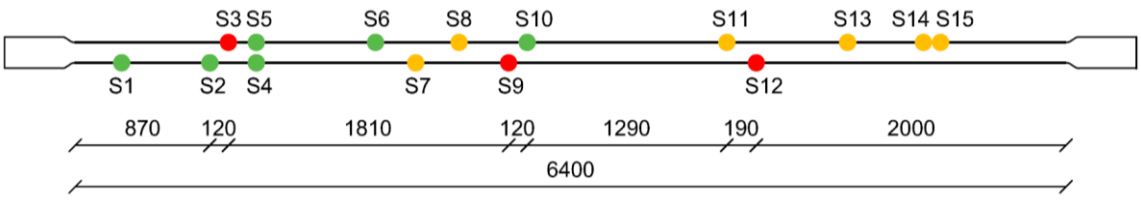

Figure 5.24: Results ECT on tie rod 41-11, including distance (mm) between possible cracks.

between S9/S10 and S11/S12 is fair. On the other hand, the distance between S2/S3 and S9/S10 is too big for 1 bar and too small for 2 bars of wrought iron.

There are another three regions of interest. The first region is the area containing the signals S4 and S5. They are both on opposite sides, but their amplitudes are low and there is no angle between them. This combination of signals does not lead to an identification of a possible crack along a weld. This might be a coincidence of two local discontinuities at the same location, or a discontinuity in the middle of the tie rod. The second region concerns signals S6, S7 and S8. These are all separated by a distance of around 180 mm. The distance between combined with the strength of the signals makes it not likely that these are possible cracks, originating from a forged weld. The last interesting region is around the signals S14 and S15. These are medium signals closely spaced to each other. It might be a surface defect or delamination of the surface.

5.6 Discussion

Eddy current testing is used to locate possible cracks in the tie rod. The low frequency eddy current probe and one of the two customized probes are employed for this task. The second customized probe, the pancake probe, is not developed far enough for on-site testing. The most important requirement is the depth of penetration, because the cracks might originate from inside the rod and indications from the surface layer should be minimized. However, it is not yet possible to determine the penetration depth for these probes on this material. This is mainly due to the absence of a proper calibration block. This calibration block cannot be made, because of a shortage of material for destructive testing. The depth of penetration can be determined by using modelling techniques, like FEM [5]–[7]. This way the behaviour of the eddy currents produced by the probe in the material can be understood and thus the penetration depth can be approximated in future research.

The low-frequency probe is useful for the detection of welds and their geometry. As determined in Section 5.3.2, the penetration depth is not high for this probe and this makes the interpretation of the results complicated. The main issue is whether the probe detects just the weld, or also a possible crack. For this, extra investigation needs to be done using different non-destructive testing to define the presence and the geometry of the crack.

The design of the customized probes can still be improved. The first step is to add proper ferrite shielding to guide the magnetic field. This is most important to the pancake probe, because this probe is severely affected by the edge effects. Another aspect to take into account is the availability of the sides of the tie rods on site. The top of the tie rod is not available for measurements, because it is in use for the wiring of the electronics used in the Duomo. The lateral sides are the most accessible and thus the development for probes on this face is the most valuable. The U-probe is used for these sides and can be adjusted further to improve its applicability to the tie rods. This improvement can be reached by making the distance between the two coils of the probe adjustable. In this way, the probe can be adjusted for the height of the tie rod. The design of this probe is derived from remote field eddy current testing [8], [9]. This means that by adjusting the distance between the two coils also the depth of the penetrating flux lines can be chosen, as depicted in Figure 5.8.

The U-probe is employed for on-site testing. Using this probe combined with the criteria mentioned in Section 5.5.2, a good analysis can be made of the presence of possible cracks in tie rod 41-11. Three possible cracks have been found. Further analysis needs to be done, in order to verify whether the detected indications are in fact cracks and possibly to determine their geometry. The strength of the signal may give more information about the crack. A crack could be closer to the side with the stronger signal. Also a higher signal amplitude can be picked up due to an increased crack opening.

An important issue is still the verification of the possible crack and its geometry. Using eddy current testing in a very heterogeneous material such as historical wrought iron, only the location of the crack can be determined. It is not possible yet to quantify the size of the crack. Another non-destructive testing method needs to be employed to tackle this issue. Concerning this issue the employment of infrared thermography is examined in the next chapter.

5.7 REFERENCES

[1] J. Garcia-Martin, J. Gomez-Gil, and E. Vazquez-Sanchez, “Non-destructive techniques based on eddy current testing,” *Sensors*, vol. 11, no. 3, pp. 2525–2565, 2011.

[2] T. G. Kincaid and R. O. McCary, “Eddy-Current Probe Design,” in *Review of Progress in Quantitative Nondestructive Evaluation: Volume 2A*, D. O. Thompson and D. E. Chimenti, Eds. Boston, MA: Springer US, 1983, pp. 171–188.

[3] S. Tumanski, “Induction coil sensors—a review,” *Meas. Sci. Technol.*, vol. 18, no. 3, p. R31, 2007.

[4] V. Mook, Gerhard and Hesse, Olaf and Uchanin, “Deep Penetrating Eddy Currents and Probes,” *Mater. Test.*, vol. 49, no. 5, pp. 258–264, 2007.

[5] F. Thollon, B. Lebrun, N. Burais, and Y. Jayet, “Numerical and experimental study of eddy current probes in NDT of structures with deep flaws,” *NDT E Int.*, vol. 28, no. 2, pp. 97–102, 1995.

[6] T.-O. Kim, G.-S. Lee, H.-Y. Kim, and J.-H. Ahn, “Modeling of eddy current sensor using geometric and electromagnetic data,” *J. Mech. Sci. Technol.*, vol. 21, no. 3, pp. 465–475, 2007.

[7] Z. Zeng, L. Udpa, and S. S. Udpa, “Finite-Element Model for Simulation of Ferrite-Core Eddy-Current Probe,” *IEEE Transactions on Magnetics*, vol. 46, no. 3. pp. 905–909, 2010.

[8] W. Lord, Y. S. Sun, S. S. Udpa, and S. Nath, “A finite element study of the remote field eddy current phenomenon,” *IEEE Transactions on Magnetics*, vol. 24, no. 1. pp. 435–438, 1988.

[9] X. Xu, M. Liu, Z. Zhang, and Y. Jia, “A Novel High Sensitivity Sensor for Remote Field Eddy Current Non-Destructive Testing Based on Orthogonal Magnetic Field,” *Sensors*, vol. 14, no. 12, pp. 24098–24115, 2014.

CHAPTER 6: ACTIVE INFRARED THERMOGRAPHY

Infrared thermography is a non-destructive technique that allows the mapping of thermal patterns on the surface of objects using an infrared imaging instrument, such as an infrared camera. In active thermography, an external stimulus is employed to induce relevant thermal contrasts. Active infrared techniques are widely used for the inspection of existent buildings, especially in the field of cultural heritage [1], [2]. Their main use is the identification of masonry texture, hidden structural elements, voids and detachments. The downside of this technique is the requirement of very long thermal stimulation often needed for historical structures, due to the low thermal diffusivity of masonry and great thickness of the structural elements. Although it is widely employed in metal components, no former works are available on the applicability of active infrared thermography on historical metallic elements, such as historical tie rods.

Eddy current testing allows the identification of the areas affected by damage, but it is unlikely to be able to detect the precise geometry of cracks in the tie rod. For this reason, active infrared thermography is employed to tackle this problem. The high thermal conductivity of metals lowers the time needed for the thermal stimulation. On the other hand, the thickness of the tie rod and the heterogeneity of the material increase the time needed for the thermal stimulation.

The theoretical background on active infrared thermography is covered in Section 6.1. Then two-dimensional numerical simulations are performed to evaluate the effects of crack geometry on the diffusion of heat in the tie rod. This is done in Section 6.2. Lastly, experimental testing is carried out on the crack of a tie rod, described in Section 6.3.

6.1 THEORY

In this section, first the general concepts needed for understanding infrared (IR) thermography will be introduced. Then the possible test methods are described. This will be taken into consideration for making the decision which method is usable for the tie rods. Lastly, the chosen method will be examined.

6.1.1 Emissivity

Infrared (IR) thermography is part of radiometry, which measures electromagnetic radiation. The emissivity of the surface of a material is the most important factor for the use of IR thermography. The emissivity defines the effectiveness of a surface to emit energy as infrared radiation, which can be picked up by an IR camera. This value depends on many parameters such as temperature, angle of emission, radiation wavelength and surface conditions. The first three parameters can be prescribed in the test method. The surface conditions depend on the specimen, which includes roughness, oxide layers and contaminations. A surface having a low emissivity tends to behave as a mirror. This results in the reflection of IR radiation from other sources, which causes the presence of extra noise in the measurements. The surface conditions can alter the emissivity of the material by 5-20%. Normally iron has a low emissivity, with a value around 0.1. However concerning the tie rods, the emissivity is increased due to the oxidation and the roughness of the surface, becoming around 0.61-0.85 [3]. Radiation measurements can be performed successfully if the material emissivity is higher than 0.2. Therefore this method can be used on historical tie rods

6.1.2 Heat Transport

Three mechanisms are involved for the heat transfer from one point to another. These are conduction, convection and radiation. Conduction is the transport of heat due to collision of particles on an atomic level and the movement of electrons in a body. Convection is based on bulk movement of liquids or gasses. The heat is transferred by the displacement of groups of molecules. The amount of convection is mainly determined by the temperature gradients in a fluid. Radiation is defined as the heat transport caused by the propagation of electromagnetic waves. This mechanism does not require a medium.

In practical situations, the total heat transfer is a combination of conduction, convection and radiation. The concept of heat transfer can be associated with an electric circuit, in which the heat transfer rate is the current and the temperature difference is the voltage. In this case, the electrical resistance is replaced by the thermal resistance. The heat transfer mechanisms act simultaneously and can be considered as thermal resistances in parallel. The difference in thermal conductivity of various parts in the specimen can be observed as thermal resistors in series.

6.1.3 Test Methods

Active infrared thermography uses an external stimulus to induce significant thermal contrast between the discontinuities and the bulk material of the test object. Different testing procedures can be used for this purpose. The first is pulsed thermography, which increases the surface temperature of the element by a short heat pulse. The change of temperature in time induced by the heat pulse is recorded. The diffusion of heat through the element is altered by the presence of subsurface cracks. This will lead to a difference of heat distribution on the surface. The second method is step heating thermography. This method is similar to the first, but in this case the heat is applied for a longer time step. Lock-in thermography is the third technique, in which the external heating induction is performed by a periodic input. This will result in oscillating infrared emission. Lastly, vibrothermography is considered, which uses external mechanical excitation as a source of energy.

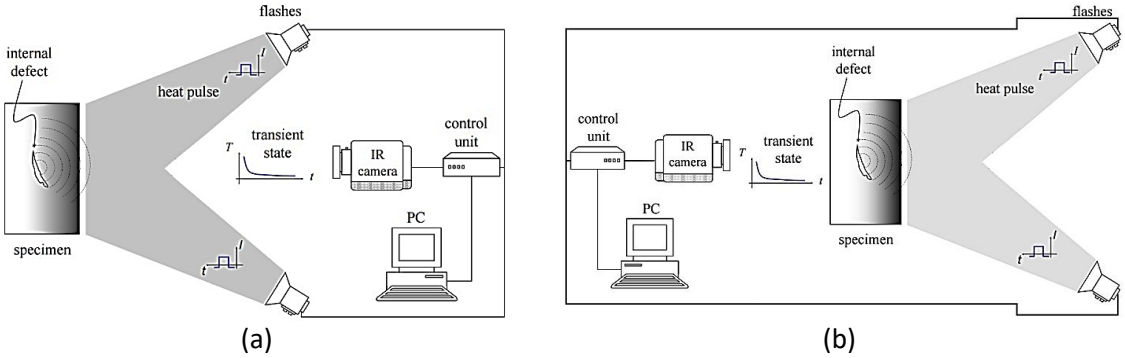

Figure 6.1: Observation methods a) reflection and b) transmission

The heat is released at the defects due to the induced friction. The generated heat diffuses towards the surface and is measured using an infrared camera.

Two observation methods are available for active infrared thermography. Figure 6.1 shows that the observation can be done by measuring the reflection or the transmission of the heat, depending on the position of the heating source. The reflection method has both the heating source and the IR camera on the same side of the specimen and thus measures the heat reflected from an internal defect. This method has the advantage that it does not require the accessibility to both sides of the sample, because all the equipment is placed on one side of the test specimen. Contrary to the reflection method, the transmission method measures the conduction of heat through the specimen. The IR camera is thus placed at the opposite side of the heat source. Its strong point is that the whole cross section of the test specimen can be examined.

The inspection will be done over the larger sides of the tie rods, because of the inclination of the crack. The chosen test set-up for the tie rods is pulsed thermography combined with the transmission observation method. The pulsed thermography technique is favoured, because of the high thermal conductivity of the material. The high thermal conductivity causes a fast diffusion of the heat through the material, which may lead to little contrast. By using heat pulses with a short time span, the redistribution of the heat perpendicular to the cross section is limited. The transmission method is employed to ensure that whole cross section is covered. The main obstacles for using thermography is the thickness of the tie rod, the size of the cracks and the surface conditions. Despite the high thermal conductivity of wrought iron, the thickness of the elements might be a drawback. The thickness mainly influences the time span of the thermal pulse. As mentioned before, a shorter pulse is preferred to avoid the redistribution of heat in the longitudinal direction of the tie rod. However, the time span should be long enough to induce enough heat to measure a contrast in temperature along the inspected surface. A trade off should be made between these two factors to find the optimal time span. The crack size relative to the dimensions of the tie rod also needs to be considered. There will be a minimum crack size that can be measured with infrared thermography, but this value will rise as the thickness of the specimen increases. Another drawback is that the values of emissivity along the surface might differ slightly. This is caused by the surface conditions of the tie rod, as roughness, rust and other surface contaminations. It will result in some noise in the thermal image.

6.1.4 Pulsed Thermography

Pulsed thermography is based on the evaluation of the flaw's effect on the thermal transient travelling inside the specimen. In pulsed thermography, the heating stimulus consists out of a very short pulse inducing a sudden thermal transient in the work piece. This pulse can last from a few milliseconds to a few seconds, depending on the thermal diffusivity and the thickness of the sample.

The main requirement of the heating source is to ensure a uniform heat deposit. The increment in temperature is usually only a couple of degrees above the initial temperature. After the pulse, the heat wave front propagates through the material by means of conduction. In the absence of any defect, the thermal waves propagate without any disturbances and hence the temperature on the detection surface will increase with a uniform distribution of temperature. The presence of a defect modifies the diffusion of heat due to the thermal resistance of the defect. This will lead to a region with lower temperature corresponding to the area of the defect.

The excitation time is very short in pulsed thermography. This can be compared to an ideal temporal pulse of null duration, having a uniform frequency distribution from 0 to ∞. The temperature decay ΔT (K) after the absorption of such a pulse can be described as follows;

$$\Delta T = \frac{Q}{e\sqrt{\pi t}} \quad , \tag{6.1}$$

where Q (Jm^{-2}) is the amount of absorbed energy and e ($Jm^{-2}K^{-1}s^{-1/2}$) is the thermal effusivity of the material. The thermal effusivity depends on the thermal conductivity λ ($Wm^{-1}K^{-1}$), density ρ (kgm^{-3}) and specific heat C ($JK^{-1}kg^{-1}$) and is described as:

$$e = \sqrt{\lambda \rho C} \quad . \tag{6.2}$$

Equation (6.1) shows that the surface temperature decays as a function of $t^{-1/2}$. This equation can also be assumed to be true in test conditions, when using the pulsed thermography. Defects result in a variation of the temperature decay slope. This is shown in Figure 6.2, where T_d is the temperature evolution curve, for the transmission method, if a defect is presence. The deviation of the curve is due to the higher thermal resistivity of the defect.

Active thermography is most sensitive to flaws close to the surface, captured by the infrared camera. The flaw depth influences the measurements in two ways: the maximum contrast between defective and non-defective region and the time at which this contrast is observed. In transmission observation mode, defects further away from the heated surface result in a time lag in the thermal wave propagation. Both effects are examined more in depth in the next sections.

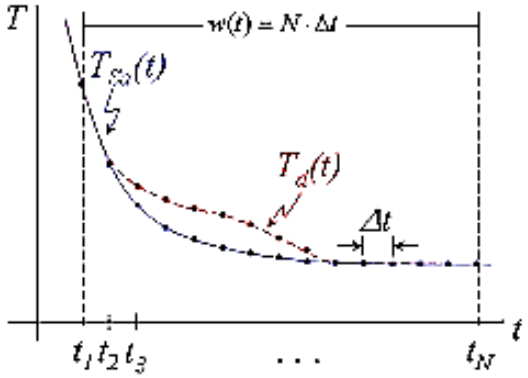

Figure 6.2: Temperature evolution curve in time after absorption of heat pulse.

6.2 2D Numerical Simulation

Two-dimensional numerical simulation is helpful to understand the thermal wave propagation in the structural element. This study is used to explain the test results presented in Section 6.3. Due to the complexity of the problem, finite element simulations are employed to solve it. These simulations will take into account several phenomena, like: presence of a crack, size of the crack and conduction to neighbouring parts of the tie rod.

The geometry of the model is given in Figure 6.3. The structural element has a length of 1500 mm and the thickness is 60 mm, representing a real tie rod. The discontinuity is placed in the middle of the model. The discontinuity is modelled with an angle of 27°, since the dominant flaws in the tie rods are the forged welds. The inclination causes the maximum width of the crack to be 120 mm. The tie rod is seen from top view and has a heated and a cold side. The "heated side" has a length of 500 mm, where the heating is assumed to be uniform. The "cold side" is the side on which the measurements are done and covers the whole section of interest. The initial temperature of the bar and its surroundings is 20 °C and an increment of 10 °C is applied. The heat pulse therefore has a temperature of 30 °C and lasts 20 seconds. When the pulse is finished, the surrounding temperature lowers to its initial value of 20°C for the rest of the simulation. The whole simulation lasts for 600 seconds. The initial temperature is assigned as boundary conditions to the opposite edges of the model. Convection and radiation have been assumed over the remaining surfaces of the tie rod. The aim of this simulation is the study of the thermal front propagation in time through the thickness of the element.

Four main cases are thoroughly evaluated. Their configuration is given in Figure 6.4. The first case is a tie rod without a crack (NoC). The second case has a crack through the whole thickness of the tie rod, ($C_{3/3}$). The third case has a crack of two-third of the cross section emerging from the heated side ($C_{h2/3}$). The last case also has a crack with length of two-third of its cross section, but it emerges from the cold side ($C_{c2/3}$). Using these cases, the propagation of the thermal wave front is investigated and then the influence of the crack size is examined. Lastly, the surface temperature on the cold side is evaluated in time. These results will be compared with the results of the experiments. The

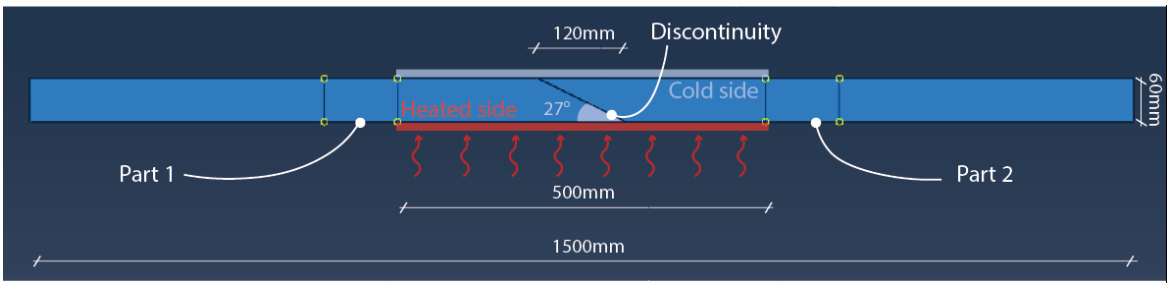

Figure 6.3: Geometry of the model for thermal wave propagation.

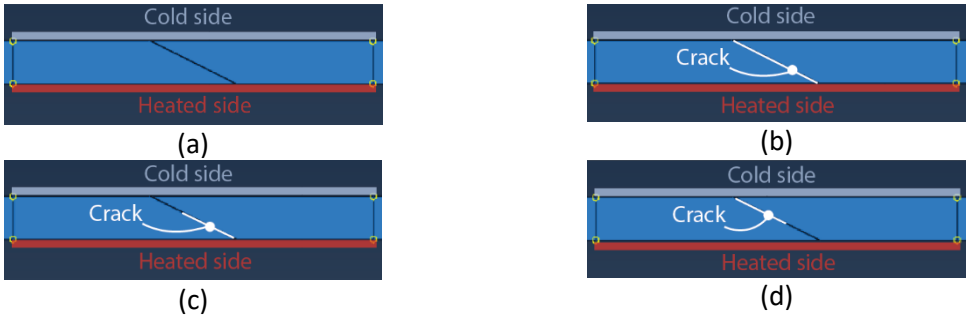

Figure 6.4: Configuration of the inspected cases, a) NoC, b) $C_{3/3}$, c) $C_{h2/3}$ and d) $C_{c2/3}$

interpretation of the test results will be easier, when the link between model and experimental results can be made.

6.2.1 Propagation Thermal Wave Front

The propagation of the thermal wave front is examined using nodal temperature contour pictures. These contour pictures are given at fixed times for every case, where the top is the cold side and the bottom is the heated side. They give a first indication of the influence of the crack on the thermal wave propagation.

In crack-free condition, the thermal wave propagates homogeneously from the heated side to the cold side, as observed in Figure 6.5. Once the heat pulse has travelled through the whole thickness, the thermal wave propagates only in the longitudinal direction.

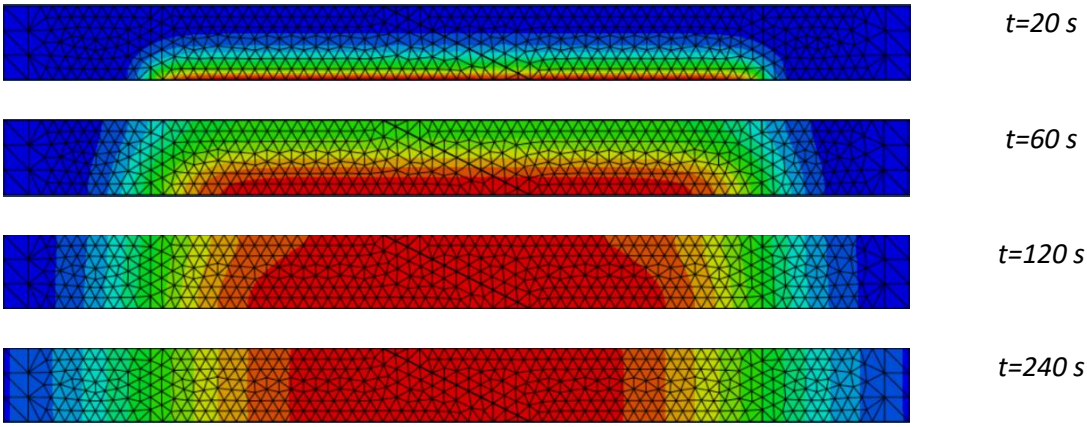

Figure 6.5: Nodal temperature contour pictures of the cross section for different values in time, illustrating the concept of heat propagation, from the environmental temperature of 20°C (dark blue) to maximum temperature (red), NoC.

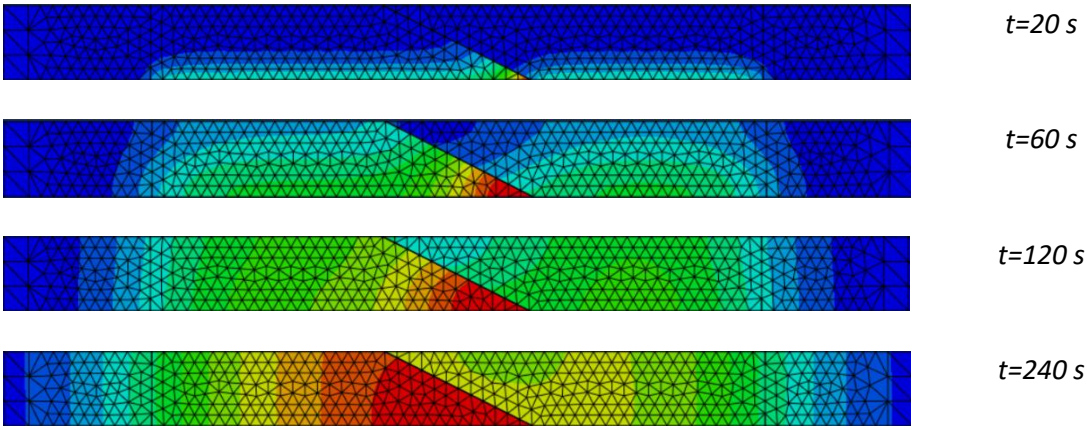

Figure 6.6: Nodal temperature contour pictures of the cross section for different values in time, illustrating the concept of heat propagation, from the environmental temperature of 20°C (dark blue) to maximum temperature (red), $C_{3/3}$.

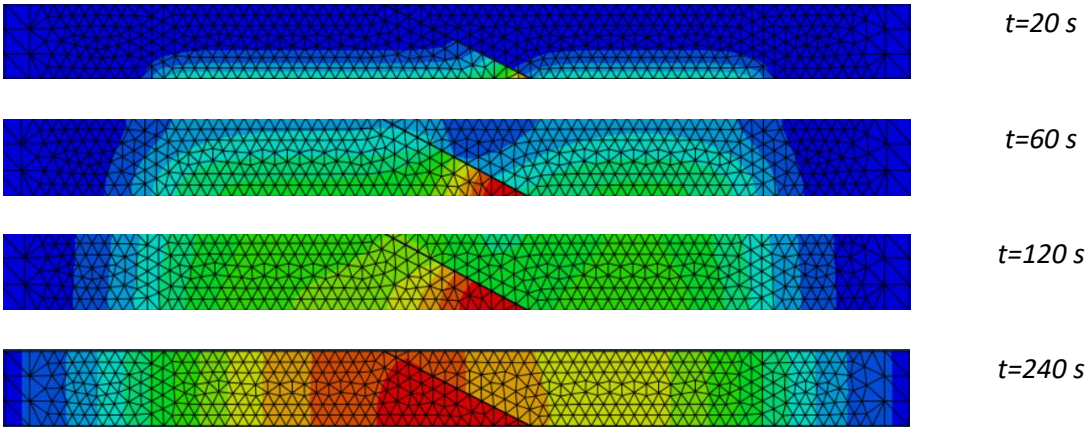

Figure 6.7: Nodal temperature contour pictures of the cross section for different values in time, illustrating the concept of heat propagation, from the environmental temperature of 20°C (dark blue) to maximum temperature (red), $C_{h2/3}$.

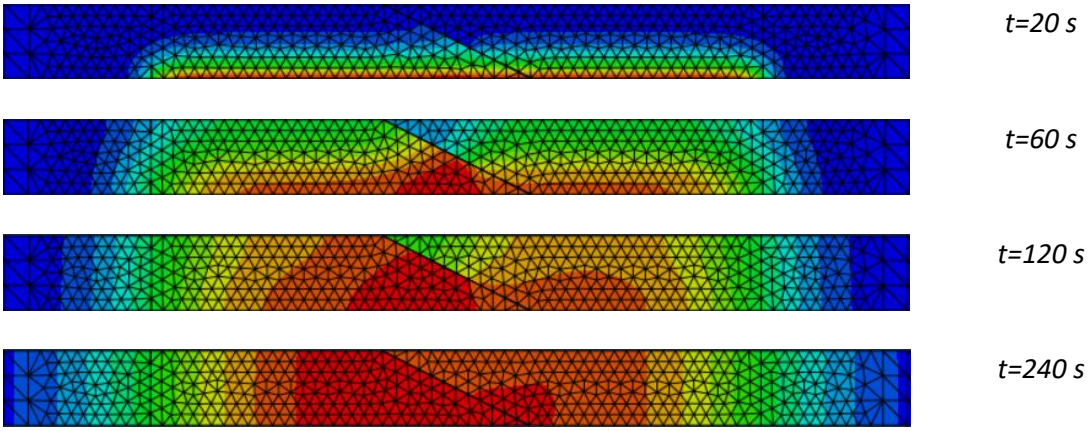

Figure 6.8: Nodal temperature contour pictures of the cross section for different values in time, illustrating the concept of heat propagation, from the environmental temperature of 20°C (dark blue) to maximum temperature (red), $C_{c2/3}$.

The presence of a crack alters the thermal wave propagation. The crack has a high thermal resistance and this minimizes the diffusion of heat over the crack. The heat accumulates behind the crack and spreads out to areas with lower heat resistance. This results in a lower temperature in the area corresponding to the defective region, as shown in Figure 6.6. At t=240 s, the crack opening at the cold side is clearly visible, because of the contrast between temperatures. The exact position of the crack opening at the heated side is not apparent, due to the spreading of the heat in the longitudinal direction. This effect can also be observed in Figure 6.7 and Figure 6.8, for a crack that emerges from respectively the heated side and the cold side. In Figure 6.7, the biggest contrast can be observed at t=60 s. At this time the first part of the thermal wave front arrives at the cold side and the coldest area can be identified as the position of the crack. In Figure 6.8, at the position of the crack opening there is a sharp contrast between the left and right side of the crack. On the other hand, the position of the crack tip cannot be determined using this set-up.

The defect delays the thermal wave propagation front. Therefore, the maximum temperature is reached later than in surrounding areas. The tilted crack creates additional factors affecting the conduction of heat. The angled corner of the crack concentrates the heat behind the crack, due to the high thermal resistance of the crack. This induces the diffusion rate of heat towards undamaged material. The crack tip splits the thermal wave propagation, which increases the heat flux along the crack surface. These factors increase the complexity of analysing the thermal wave front propagation.

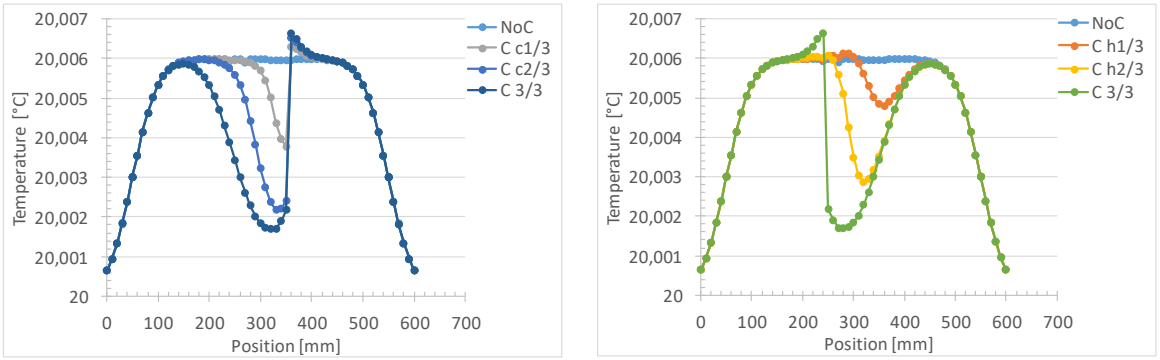

Figure 6.9: Comparison of heat profile after 60 seconds for different crack lengths, a) emerging from the cold side and b) emerging from the heated side

6.2.2 Influence of Crack Length

The crack length influences the thermal wave propagation in the specimen. For this section two extra cases are introduced, having a crack length of one-third of the cross section emerging from the cold side ($C_{c1/3}$) and from the heated side ($C_{h1/3}$). This allows the investigation of the trend of the heat propagation depending on the crack size. The outcome is given in Figure 6.9. These graphs show the temperature profile on the cold side after 60 seconds of the simulation. This time is chosen because it gives the biggest contrast in temperature over the cold side.

Figure 6.9a displays the heat profile for cracks of different length emerging from the cold side. An increase in crack length causes an increase in contrast in temperature. At a position of 360 mm, the crack emerges from the cold side. This results in a big contrast of temperature around this position. The temperature is lower at positions below 360 mm, due to the resistance of the crack to let heat travel across the crack. At the position between 360 mm and 410 mm, an accumulation of heat is observed. These two aspects of the graph emphasize the position of the crack. On the other hand, the crack tip cannot be pin-pointed, because there is a smooth trend where the crack tip should be. Figure 6.9b shows the heat profile, when the cracks are emerging from the heated side. Also for this graph the contrast in temperature is increased, with increasing crack length. However, the contrast is smaller than for the same crack size emerging from the cold side. The heat accumulation is visible as well, but only in small amounts. Also defining the exact location of the emerging crack is not evident.

6.2.3 Evolution of Temperature Variation

The time it takes for every position on the cold side to reach its maximum temperature, should be evaluated to comprehend the effect of the cracks on the heat wave front. These graphs are given in Figure 6.10. For every individual position, the temperature is normalized in time using a scale from 0 to 1. The highest temperature reached in time for every point is denoted as 1, while the coldest temperature is 0. In this way, the time in which the maximum temperature is reached can be found for every position. The white transparent area in the figure indicates the crack length projection on the examined surface, while the white lines represent the through-wall crack dimension. The red lines depict the length of the heated region.

Figure 6.10a displays the undamaged case. Complete symmetry around the centre position is observed. The diffusion of heat in the longitudinal direction of the rod in the adjacent non-heated parts is visible, as well. This effect of diffusion of heat to adjacent parts is also observed in the other graphs. Figure 6.10b shows the graph for a fully cracked rod. This graph is not symmetrical because the crack is under an angle. In the time scale from 0 to 150 seconds, a smooth temperature transition in space can be seen in the area of the left white line. At the right white line, however, the temperature response is sharp, resulting from the position where the crack emerges on the cold side.

Another feature of this graph is the delay in time of the maximum temperature in the area of the crack. The width of this delayed maximum temperature correlates closely to the width of the crack of 120 mm. The third case is the crack emerging from the heated side, shown in Figure 6.10c. In the beginning of the time scale, it shows the same behaviour as in Figure 6.10b. In this time scale, it is difficult to recognize the position of the crack. The maximum temperature is observed at the time scale between 300 and 350 seconds, the time lag of this crack. This position of this delay is similar to the exact position of the crack, but with a small shift to the right. Figure 6.10d shows the heat profile for the crack emerging from the cold side. In this graph the accumulation of heat, as discussed in the previous section, is clearly visible. The time delay in maximum temperature for the area of the crack has the same time span as in the previous case. Only this time, there is a small shift towards the left. There is still a good correlation between the position of this delay and the true crack size. The analysis on these thermographs leads to the conclusion that the position and the size of the crack can be estimated by looking at the temperature profile in time and space.

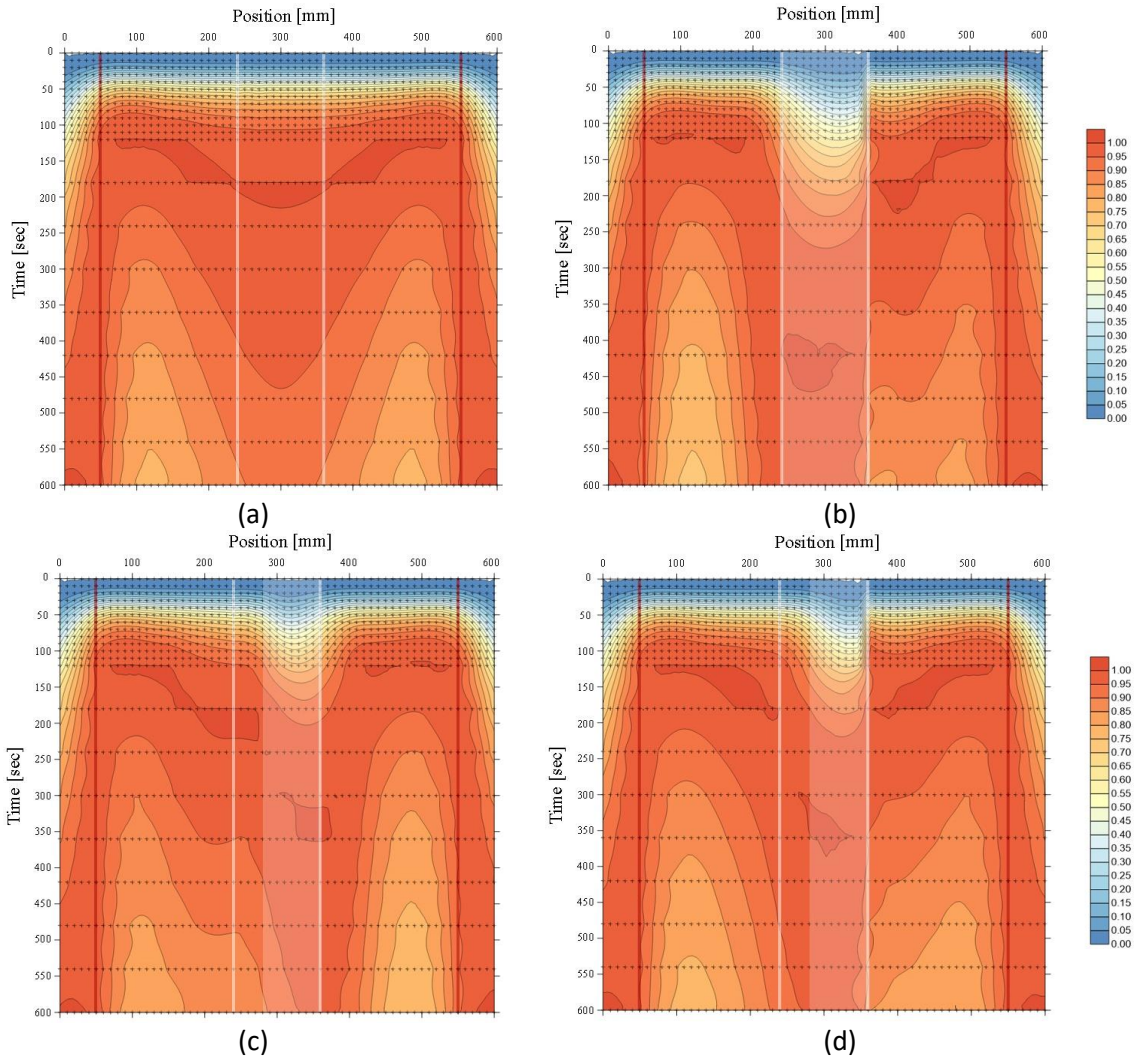

Figure 6.10: Evolution of heat along the cold surface in time, a) NoC, b) $C_{3/3}$, c) $C_{h2/3}$ and d) $C_{c2/3}$, where red signifies the highest temperature reach per position (normalized to 1) and blue the coldest temperature (normalized to 0).

6.3 EXPERIMENTAL TESTING

The effectiveness of pulsed thermography on the tie rods of the Duomo di Milano has been evaluated by performing tests on the crack present in tie rod 61-91, according to the transmission observation method. The experimental set-up is made such that it approximates a 2D problem. This is done to simplify the thermal analysis and to be able to compare the results with the numerical simulations. In the 2D approach, the thermal exchange between the upper and lower sides of the tie rod and the environment are neglected. Therefore, propagation through the tie rod thickness can be assumed as the only admissible thermal wave path.

6.3.1 Set-up and Signal Processing

The aim of the test is the evaluation of the temporal temperature response over the tie rod surface after a sudden heating pulse on the opposite side. This is done using the set-up shown in Figure 6.11. The infrared camera Testo 890 has been employed. This camera has a spectral range of 8-14 μm and a resolution of 1280x960 pixels. It has been placed at 50 cm distance from the inspected surface. A heat gun has been chosen as the thermal source, because of its high heating power for a high thermal contrast. In the same time, the uniformity of the heat distribution is reasonable. The upper and lower surfaces of the tie rods are insulated, as shown in Figure 6.12. This is done to avoid heat

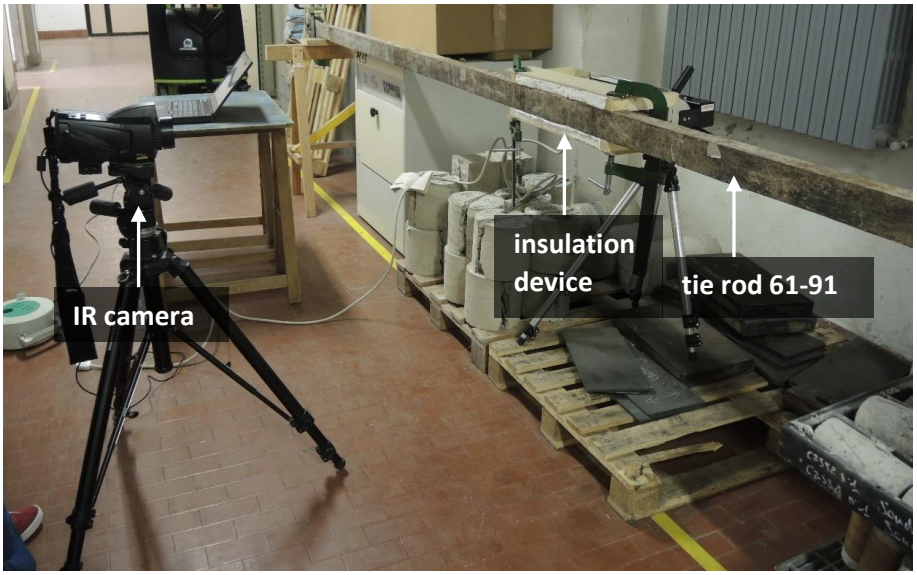

Figure 6.11: Test set-up for active infrared thermography.

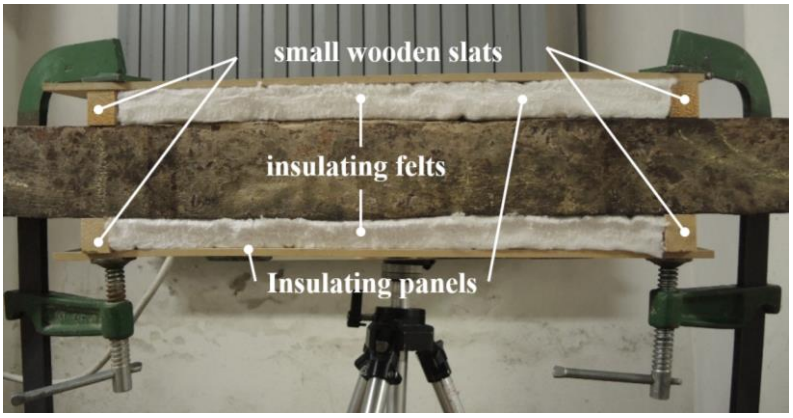

Figure 6.12: Insulation devices in test set-up for active infrared thermography.

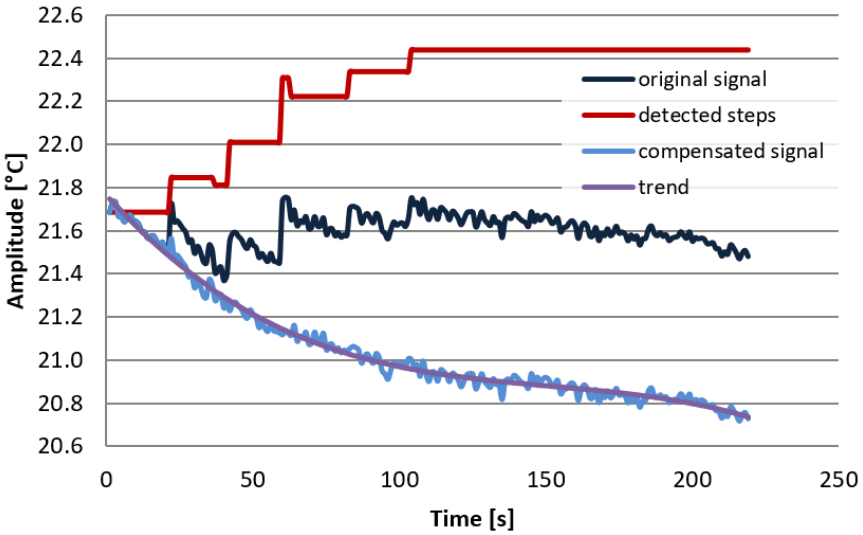

Figure 6.13: Compensation of the original signal for automatic resets of the measurement range.

leakage along these surfaces and to approximate the conditions used for FEM described in the previous section.

During the test, the infrared camera automatically resets its temperature measurement range over time, which would alter the recorded temperatures. In order to take into account this effect, it is necessary to quantify the offset in temperature due to the automatic resetting. For this purpose, a reference target with a stable temperature has been applied on the examined surface. It consists out of a small iron cube, having similar emissivity, enveloped by the insulating material Styrofoam over all sides, except for the side facing the IR camera. The target is hereby isolated from the thermal variation induced by the heating source on the tie rod and can be used during the inspection as a reference for the sudden temperature variations of the camera. From this reference, the temperature offset over time will be determined using the signal processing explained in the next paragraph.

During the signal processing phase, the amplitude of temperature changes caused by the reset can be estimated and used to correct the obtained data. The procedure of a signal compensation for sudden temperature changes is shown in Figure 6.13. The detected steps of resetting have been computed by defining a threshold for a sudden change in temperature and adding these values in time to form the red curve as given in the graph. This curve is deducted from the original signal to obtain the compensated signal. After the compensation, only the general noise is still present in the signal and thus a trend can be established. This trend is found by evaluating the best fit to this signal. After this correction and the calculation of this best fit, the rest of the signal processing can be done. The extracted information is the general evolution of temperature variation along a path, the maximum temperature for every position on the detected surface and the time corresponding to the maximum temperature for each position.

6.3.2 Results

The visible crack present in tie rod 61-91 is used for the following measurements. The crack is slightly opened, which makes conduction across the crack impossible. This results in a high thermal resistance for the transport of heat over this area. Both sides of the tie rod are investigated. The same abbreviations as employed in Section 6.2 are used. The crack is investigated emerging from the cold side (C_c) and from the heated side (C_h).

6.3.2.1 Maximum Temperature

The maximum temperature for every position on the detected surface is determined and is given in Figure 6.14, where the area within the red rectangle is the reference target. Figure 6.14a displays the case corresponding to the crack emerging from the cold side. The position of the emerging crack is visible in the dark area of this figure. However, the total geometry cannot be deduced, because the embedded crack tip cannot be distinguished. The upper part of the crack seems to be colder than the lower part. This might suggest that here the crack reaches deeper in the bulk of the material, causing more resistance to the heat propagation. Figure 6.14b shows the case if the crack emerges from the heated side. Also here a colder area can be distinguished, but with less sharp contrast. The colder area is due to the crack and can thus be approximated as the total area of the crack.

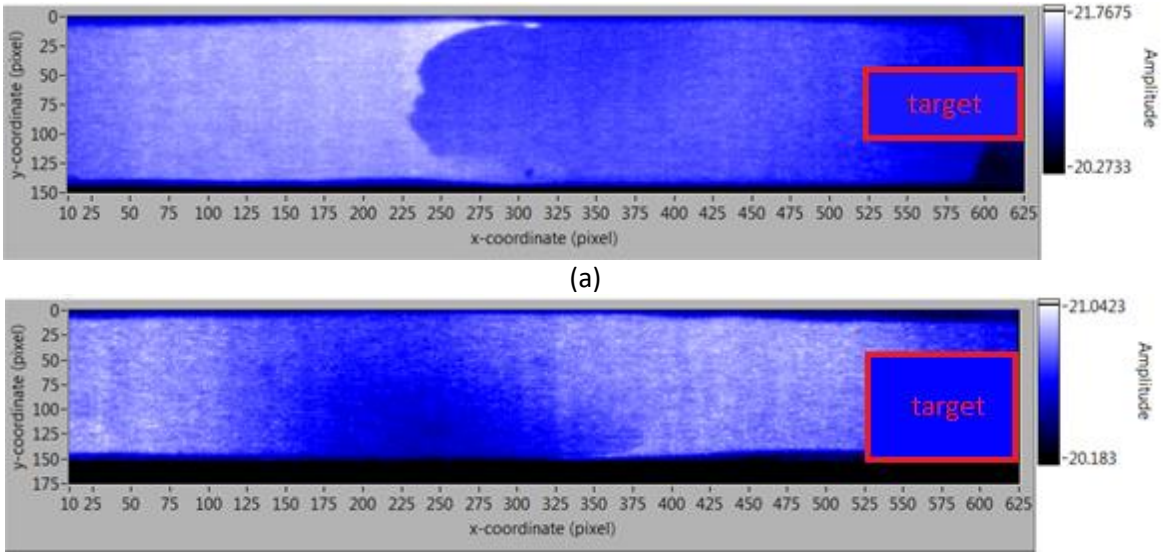

Figure 6.14: Maximum temperature reached for all positions on the surface for a) C_c and b) C_h.

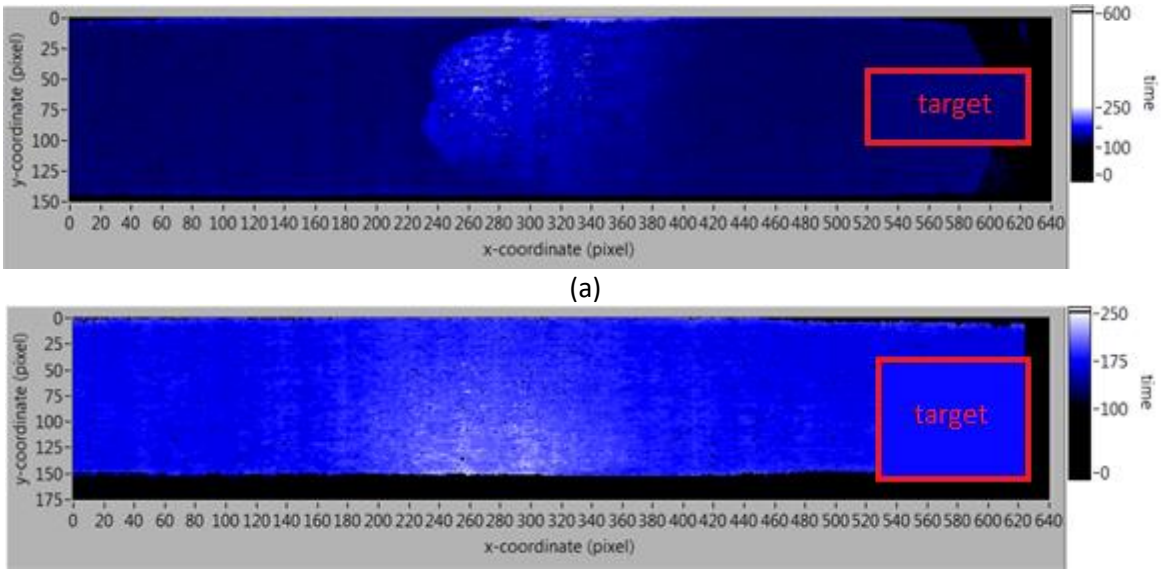

Figure 6.15: Time to reach maximum temperature for a) C_c and b) C_h.

6.3.2.2 Time Corresponding to the Maximum Temperature

After the extraction of the maximum temperature, the corresponding time is to be evaluated. This is given in Figure 6.15. Also for this analysis the crack can be distinguished for both configurations. A higher time lag can be due to a larger crack opening or a position closer to the inspected area. Figure 6.15a displays the emerging of the crack on the cold side of the tie rod. The time lag decreases, when the crack becomes deeper, as discussed in Section 6.1.4. Thus the gradient of the time lag supports the assumption of the tilted geometry of the crack. However, the embedded crack tip can still not be identified. Figure 6.15b shows the situation if the crack emerges from the heated side. This figure shows an area of delay in the maximum temperature, but does not show clear boundaries.

6.3.2.3 Evolution of Temperature Variation along a Path

The evolution of temperature variation along a longitudinal path over the cold surface is determined in the following section and the plots are compared with the plots from Section 6.2.3. The experimental results agree with those achieved from the 2D numerical simulation.

Figure 6.16a is compared to Figure 6.10d, the evolution of temperature variation modelled with FEM. A clear disruption of the thermal wave propagation, due to the crack opening at the cold side, is observed in both figures. Unfortunately, the complete influence of the crack on the thermal wave propagation cannot be seen, because the captured region is too small.

Figure 6.16b is compared to Figure 6.10c. The time delay of the observed maximum temperature is also clearly shown in this figure and agree with Figure 6.10c . The contrast is not as pronounced as with the previous case, but the region where the crack is present can be distinguished.

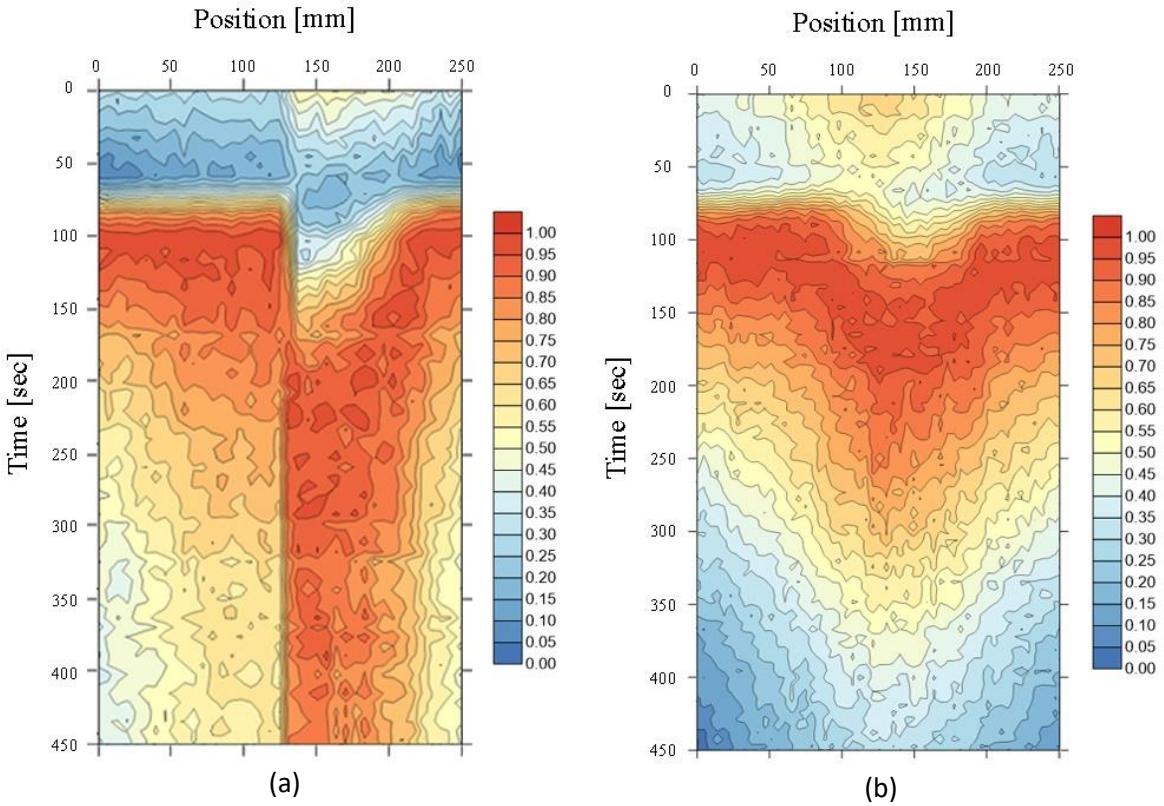

Figure 6.16: Temperature variation along a path, for a) C_c (crack at 140-190 mm) and b) C_h (crack at 130-180 mm), where red signifies the highest temperature reach per position (normalized to 1) and blue the coldest temperature (normalized to 0).

6.4 DISCUSSION

Pulsed thermography has been done on a visible crack in lab conditions. These results enabled the determination of the exact position of the crack. However, only a first estimate can be made with respect to the crack size and the crack geometry. The resulting graphs in Section 6.3.2 show the location of the crack, but do not yet give a sharp distinction between crack and bulk material.

The current experimental set-up should be enhanced for in-situ application on the tie rods at a height between 16 and 35 meters. This is due to the many components involved in the testing equipment, which is not convenient at these heights. Also the transmission method is problematic, due to the conditions at the tie rods in the Duomo. The main problems is the inability to work on both sides of the tie rods simultaneously. Therefore, a more efficient test procedure should be developed, which takes into account the working conditions in the Duomo. This can be done by taking a closer look at the reflection observation mode, but also by making the test set-up more compact. This can be done by using a heating source that can be coupled closely to the tie rod and by using a wide-angle lens on the IR camera.

6.5 REFERENCES

[1] C. A. Balaras and A. A. Argiriou, “Infrared thermography for building diagnostics,” *Energy Build.*, vol. 34, no. 2, pp. 171–183, 2002.

[2] L. Binda, C. Modena, F. Casarin, F. Lorenzoni, L. Cantini, and S. Munda, “Emergency actions and investigations on cultural heritage after the L’Aquila earthquake: the case of the Spanish Fortress,” *Bull. Earthq. Eng.*, vol. 9, no. 1, pp. 105–138, 2011.

[3] X. Maldague, *Theory and practice of infrared technology for nondestructive testing*. Wiley, 2001.

CHAPTER 7: FRACTURE MECHANICS

The research into fracture mechanics started with Griffith in 1920 [1]. He considered the propagation of a brittle crack in glass, using an energy approach. He was followed by Irwin, who defined the energy release rate (G), the total energy released during cracking per unit increase in crack size . Irwin also introduced the stress intensity approach in 1957 [2]. The concept being that fracture happens if a critical stress distribution ahead of the crack tip is reached. This is translated into the material property called the critical stress intensity factor (K_c). Equivalent to this material property is the critical value in terms of the energy release rate (G_c). These material properties are the basis of the linear elastic fracture mechanics (LEFM). The downside of this discipline is that it can only take into account plasticity until a certain extent. For this reason, elastic-plastic fracture mechanics is developed. The elastic-plastic fracture mechanics (EPFM) parameter the J-integral, was introduced by Rice in 1968 [3]. This parameter is based on the energy approach and is able to describe elastic-plastic material behaviour by assuming non-linear elastic behaviour.

There are three modes of crack surface displacement, as shown in Figure 7.1. Depending on these modes, the stress system around the crack tip can be explained. Failure in mode I is the most relevant mode in most practical cases and will thus be used for testing in this chapter.

The goal in this work is to gain understanding about the mechanical behaviour and the failure modes of wrought iron in the tie rods. The material's response to an applied (cyclic) stress is evaluated, by doing mechanical testing, with as the ultimate goal: the determination of the maximum stress that may be applied to the tie rod containing a crack without causing structural failure.

First the principles of linear elastic fracture mechanics are introduced in Section 7.1, which concludes with fracture toughness and fatigue testing. In Section 7.2, elastic-plastic fracture mechanics is used to be able to take into account more extensive plasticity. Lastly in Section 7.3, the effect of crack geometry, including the influence of its inclined nature, will be discussed. The fracture toughness values found in the previous sections are used to determine the maximum stress that can be applied to a tie rod containing a crack with a specific crack size.

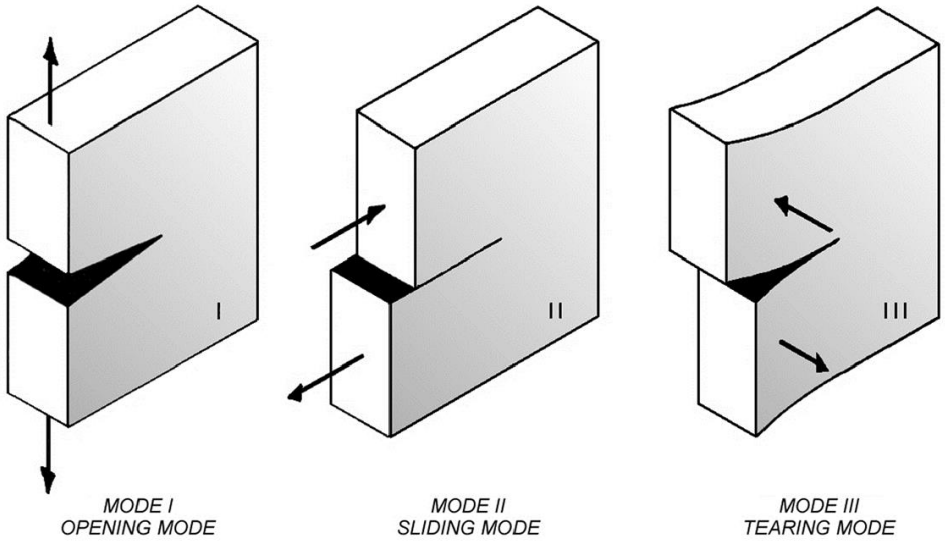

Figure 7.1: The three modes of crack surface displacement [24].

7.1 Linear Elastic Fracture Mechanics

Linear elastic fracture mechanics is based on the material exhibiting perfect linear elastic behaviour. Only small scale yielding is allowed. This means that the plastic zone around the crack tip should remain small compared to the crack length and other relevant dimensions (e.g. the uncracked ligament size).

7.1.1 Theory

7.1.1.1 Fracture Toughness

The mode I stress intensity factor (K_I) describes the stress intensity at the crack tip for a mode I crack. The stress distribution around the crack tip can be described using this parameter, as follows:

$$\sigma_{ij} = \frac{K_I}{\sqrt{2\pi r}} f_{ij}(\theta) \ , \tag{7.1}$$

where σ_{ij} (i,j=1,2) refer to the in-plane stress components, r and θ are the polar coordinates with the origin at the crack tip, as shown in Figure 7.2, and $f_{ij}(\theta)$ are angular functions. The mode I stress intensity factor is calculated as follows:

$$K_I = Y\sigma\sqrt{\pi a} \ , \tag{7.2}$$

where Y is the geometry factor, σ is the applied nominal stress and a is half the length of a central crack, or in the case of a crack emanating from an edge, the whole crack length..

Equation (7.1) indicates that the stresses become infinite as r goes to zero. However, infinite stresses do not exist. They are kept finite by the generation of plastic zone at the crack tip. A first-order estimate of the plastic zone size (r_y) ahead of the crack is obtained by the following equation:

$$r_y = \frac{1}{2\pi}\left(\frac{K_I}{\sigma_{ys}}\right)^2 \ , \tag{7.3}$$

where σ_{ys} is the yield strength. This equation is only applicable for perfectly elastic materials. If stress redistribution as a result of plastic yielding at the crack tip is taken into account, the plastic zone would be larger. This leads to the following equation for the plastic zone size:

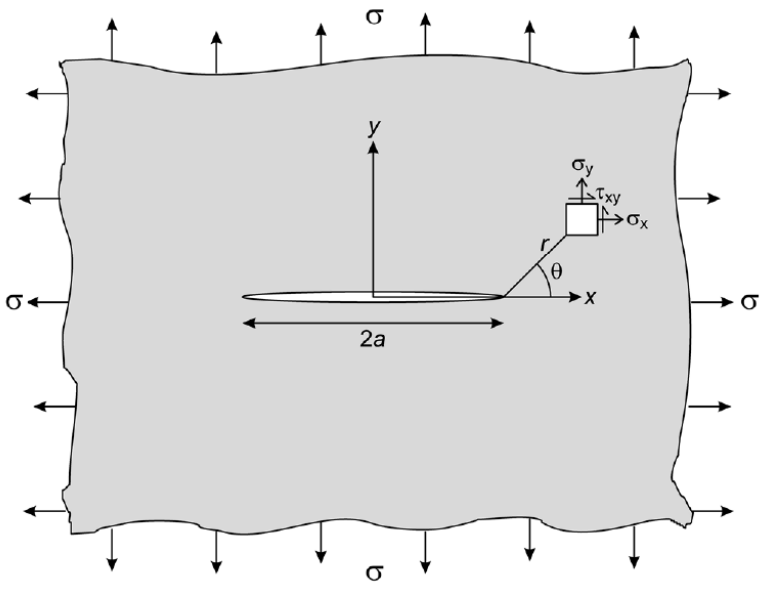

Figure 7.2: Coordinate system for representing the stress intensity factor for a mode I crack [24].

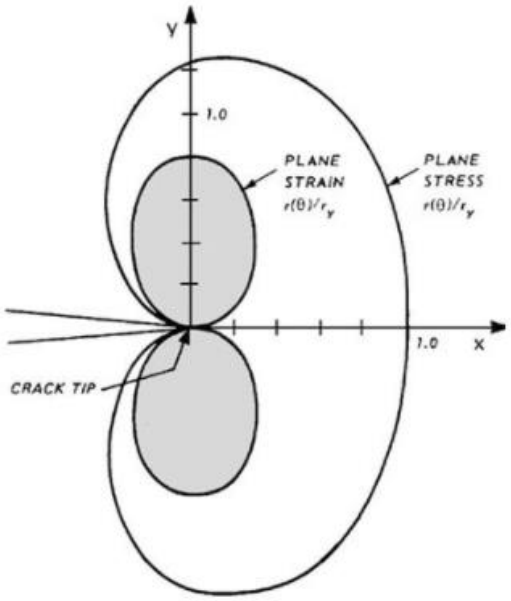

Figure 7.3: Plastic zone shape for a Mode I crack in plane stress and plane strain conditions, following the Von Mises criterion [24].

$$2r_y = \frac{1}{\pi}\left(\frac{K_I}{\sigma_{ys}}\right)^2 . \tag{7.4}$$

After the stress redistribution, the plastic zone size is twice the first order approximation.

Equations (7.1) and (7.4) shows that the stress intensity factor describes both the stresses and plastic zone size at the crack tip in a unique manner. If these quantities reach a critical value, the crack will start to grow. This signifies that fracture can be expected if K_I reaches a critical value, called fracture toughness (K_{Ic}). Fracture toughness is a material property that describes the resistance of a linear elastic material against fracture.

Fracture mechanics mostly deals with 2D cases, in which nothing depends on the z coordinate. Two 2D special cases are plane stress and plane strain. For the plane stress condition, no stress is present in the z direction, while in the plane strain condition, no strain is present in the z direction. These conditions affect the distribution of stresses and strains around the crack tip, and thus influence the plastic zone around the crack tip. Figure 7.3 shows the difference between the plastic zones. Another consequence is the Young's modulus (E') used in calculations concerning elastic deformation,

$$E' = \begin{cases} E \text{ for plane stress} \\ \dfrac{E}{1-\nu^2} \text{ for plane strain,} \end{cases} \tag{7.5}$$

where ν is the Poisson's ratio.

Fracture toughness is a material property, but also depends on the crack tip constraint caused by thickness, size and configuration of the cracked object. The plastic zone size at the crack tip compared to the thickness of the specimen is determinative for the thickness constraint. High constraint results in higher crack tip stresses with less crack tip yielding, as is the case in the plane strain condition. This promotes a more brittle material behaviour and a lowering in fracture toughness. The thickness constraint is divided in two main conditions: plane stress and plane strain. The plane strain fracture toughness is regarded as the lower bound value, due to its high constraint. Therefore testing is usually done in plane strain conditions.

The energy release rate (G) is defined as the energy available per increment of crack extension and per unit thickness. It can be described as follows:

$$G = -\frac{dU_p}{da} = \frac{d(F - U_a)}{da} \ , \tag{7.6}$$

where U_p is the potential energy, F is the work performed by the loading system during the introduction of the crack and U_a is the change in the elastic energy of the plate caused by introducing a crack. In this 2D description, all these energies are defined per unit thickness.

The crack resistance (R) is the energy required per increment of crack extension if there is no plasticity and is defined as:

$$R = \frac{dU_\gamma}{da} \ , \tag{7.7}$$

where U_γ is the change in surface energy per unit thickness of a cracked plate due to the introduction of a crack. The crack will grow, if the energy release rate is higher than the crack resistance. This signifies that this crack resistance is a critical value for crack growth and the parameter is thus often referred to as G_c.

There is a direct relation between the stress intensity factor and the energy release rate. This relation is given as:

$$G = \frac{K_I^2}{E'} \ . \tag{7.8}$$

In the following of Section 7.1, the energy release rate will not be used directly. However, the concept of this parameter and the equation above become of importance in Section 7.2.

7.1.1.2 Fatigue

Fatigue is described as crack growth in a material due to a cyclic load, involving lower stress levels than needed for static failure (as described above). Fatigue loads can be described as is shown in Figure 7.4. The amount of crack growth per load cycle is defined by the crack growth rate $\frac{da}{dN}$.

The concept behind the stress intensity factor can also be applied in fatigue. The stress intensity range (ΔK) due to an alternating load ($\Delta\sigma$) is described as follows:

$$\Delta K = Y\Delta\sigma\sqrt{\pi a} \ , \tag{7.9}$$

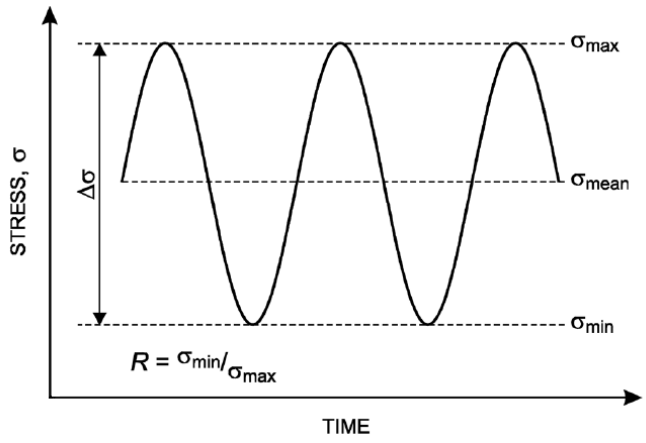

Figure 7.4: The paramaters describing cyclic loading leading to fatigue [24].

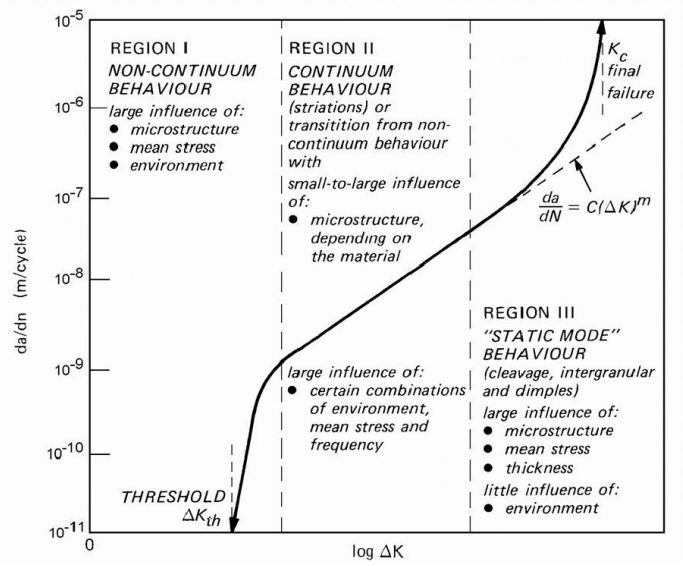

Figure 7.5: The fatigue crack-growth rate curve [24].

where Y is the geometry factor depending on the crack size (a) and the specimen width (W), as further explained in Section 7.3. Figure 7.5 displays the overall trend of the crack growth rate $\left(\frac{\mathrm{da}}{\mathrm{dN}}\right)$ as a function of ΔK. The curve is divided in three regions. The first region is the threshold region, containing the threshold stress intensity range (ΔK_{th}). Below ΔK_{th}, the crack propagation is very slow or not present. This value permits the calculation of the threshold crack length, above which crack growth due to fatigue occurs. Above ΔK_{th}, the crack growth rate increases rapidly. The second region is the Paris region, where Paris type crack growth occurs. The slope can be described using the following equation:

$$\frac{da}{dN} = C_1(\Delta K)^{C_2} \,, \tag{7.10}$$

where C and m are constants that can be obtained from experimentally obtained curves. Finally, in region III the crack growth rate curve rises rapidly, ending when K_{max} exceeds K_{Ic}.

Linear elastic fracture mechanics can be applied to fatigue in most cases, because the applied stress is much lower than the yield strength. This results in a limited amount of crack tip plasticity, since the applied stress stays in the elastic region of the material. The size of the cyclic plastic zone ($2r_y^c$) around the crack tip is given as:

$$2r_y^c = \frac{1}{\pi}\left(\frac{\Delta K}{2\sigma_{ys}}\right)^2 \,. \tag{7.11}$$

The equation above results in a plastic zone much smaller than that of the monotonic plastic zone, given in Equation (7.4). This fact results in residual plastic deformation along the crack flanks normal to the crack plane. At σ_{min}, the crack flanks showing such residual plastic deformation will be pressed onto each other. This may lead to a phenomenon called crack closure, which lowers the stress intensity range that the crack actually experiences to ΔK_{eff}. This leads to lower crack propagation velocities.

7.1.2 Experiments

Test procedures for measuring fracture toughness are for example described in ASTM codes, developed by the American Society for Testing and Materials in the United States. The procedures for K_{Ic} testing and fatigue testing both use the compact tension (CT) specimen shown in Figure 7.6.

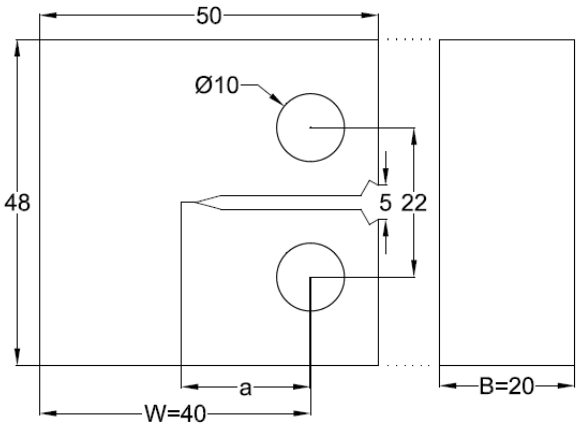

Figure 7.6: CT specimen used during testing, with its dimensions in mm.

Determining the thickness-independent plane strain toughness K_{Ic} is done in accordance to ASTM E399-12 [4]. This test is done on two samples. For testing the fatigue properties, ASTM E647-15 is used [5]. Three tests are done, using three load ratios (R), i.e. 0.3, 0.5 and 0.7.

7.1.2.1 ASTM E399-12

ASTM code E399-12 is used to determine the fracture toughness K_{Ic}. First fatigue precracking is required for producing a sharp crack, where the initial crack size a_0 is between 0.45W and 0.55W. The applied load and crack opening displacement (COD) are required to be recorded. Figure 7.7 shows three typical types of load-displacement curves. The critical load P_Q is defined for each type of curve. In the 5% secant method, P_5 is determined by constructing a slope equal to 95% of the initial elastic loading slope. It should be noted that the origin of the initial elastic loading slope may have an offset, due to some non-linearity in the beginning of the test. The 5% secant method is proposed to determine P_Q for type I, with the intention to determine K_{Ic} at a stable crack extension of about 2%. The nonlinearity of the curve can be caused by plasticity, subcritical crack growth or both. For the type II case, there is a pop-in present, a sudden small amount of instable crack growth. The value for P_Q is the value at the pop-in initiation. For the type II case, the specimen fails before achieving 5%

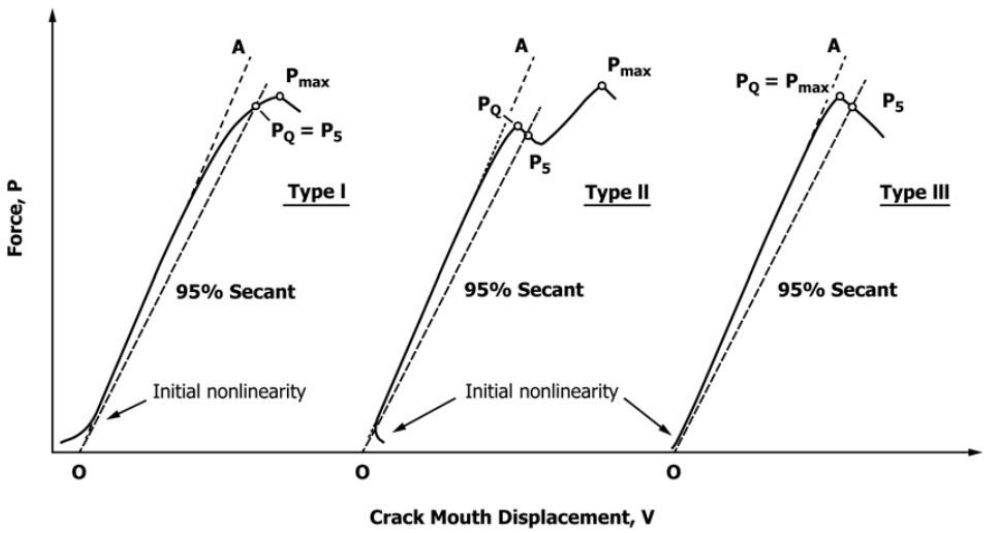

Figure 7.7: Three types of load-displacement curves with their respective critical load P_Q [4].

nonlinearity, meaning that P_Q=P_{max}. The conditional fracture toughness K_Q is calculated from the P_Q value and its corresponding measured crack length, using the following equation:

$$K_Q = \frac{P_Q}{B\sqrt{W}} f\left(\frac{a}{W}\right) , \tag{7.12}$$

where W is the width of the specimen, B is the thickness and $f\left(\frac{a}{W}\right)$ is a geometry function depending on the ratio between the crack size and the specimen width. For the CT specimen, the following equation is applied:

$$f\left(\frac{a}{W}\right) = \frac{\left(2+\frac{a}{W}\right)\left(0.886 + 4.64\frac{a}{W} - 13.32\left(\frac{a}{W}\right)^2 + 14.72\left(\frac{a}{W}\right)^3 - 5.6\left(\frac{a}{W}\right)^4\right)}{\left(1-\frac{a}{W}\right)^{1.5}} . \tag{7.13}$$

The crack length at which the specimen fails can be calculated as follows:

$$\frac{a}{W} = 1.000 - 4.500U + 13.157U^2 - 172.551U^3 + 879.944U^4 - 1514.671U^5 , \tag{7.14}$$

where U is dependent on the compliance, described in the equation below:

$$U = \frac{1}{1+\sqrt{\frac{E'BV_m}{P}}} , \tag{7.15}$$

where V_m is the crack opening displacement at load P. The calculation of the crack length using compliance deviates from the method used in ASTM E399-12, which measures the crack length from the fracture surface.

There is a requirement imposed, to ensure that a K_{Ic} measurement resembles the lower bound value of the plane strain condition. The following conditions must be met:

$$\frac{P_{max}}{P_Q} \leq 1.10 \tag{7.16}$$

$$W - a \geq 2.5\left(\frac{K_Q}{\sigma_{ys}}\right)^2 \tag{7.17}$$

The requirement in Equation (7.16) is to assure that the nonlinearity observed is related to crack initiation and not to the growth of a large plastic zone. The second requirement, Equation (7.17), combines the two following aspects: a globally elastic behaviour of the specimen, dependent on W, and the guarantee of a plane strain condition, dependent on B. The width W and the thickness B of the specimen are related, therefore only one equation is necessary to ensure these two aspects. If these requirements are met, K_Q=K_{Ic}.

7.1.2.2 ASTM E647-15

ASTM code E647-15 is applied to obtain the fatigue crack growth rate as a function of ΔK and to determine ΔK_{th}. This test method applies cyclic loading to a precracked specimen, e.g. a CT specimen with the proportions given in Figure 7.6. First fatigue precracking is required for producing a sharp crack, where the length of the fatigue precrack shall not be less than 0.1B. After precracking the specimen, the cycling loading can be applied. The applied load and crack opening displacement are to be recorded. The range load (ΔP) and its corresponding COD's (V_m) have to be extracted from the data. The compliance is obtained from these values and used to measure the crack length. Using the compliance, the data manipulation can be completed with the equations given below.

The stress intensity range can be calculated, using the following equation:

$$\Delta K = \frac{\Delta P}{B\sqrt{W}} \frac{\left(2+\frac{a}{W}\right)}{\left(1-\frac{a}{W}\right)^{1.5}} \times \left(0.886 + 4.64\frac{a}{W} - 13.32\left(\frac{a}{W}\right)^2 + 14.72\left(\frac{a}{W}\right)^3 - 5.6\left(\frac{a}{W}\right)^4\right) . \quad (7.18)$$

The ratio $\frac{a}{W}$ is defined for a CT specimen, can be obtained as follows:

$$\frac{a}{W} = 1.0033 - 2.35U + 1.3694U^2 - 15.294U^3 + 63.182^4 - 74.42U^5 , \quad (7.19)$$

where U is defined as:

$$U = \frac{1}{1+\sqrt{\frac{E'BV_m}{P}}} . \quad (7.20)$$

Having established the crack size, the fatigue crack growth rate and the stress intensity range can be calculated.

The crack growth rate is determined, using the equation below:

$$\left(\frac{da}{dN}\right) = \frac{(a_{i+1} - a_i)}{(N_{i+1} - N_i)} . \quad (7.21)$$

Since the computed $\frac{da}{dN}$ is an average rate over the interval (a_{i+1}-a_i), the average crack size over this interval is applied to Equation (7.18) for the calculation of ΔK in the fatigue crack growth rate curve. The average crack size (ã) is given as:

$$\tilde{a} = 0.5\ (a_{i+1} + a_i) . \quad (7.22)$$

The threshold fracture toughness range ΔK_{th} is deduced from the obtained fatigue crack growth rate curve, as shown in Figure 7.5. This method to define ΔK_{th} deviates from the ASTM code. Therefore, small variations from the real value might be expected.

7.1.3 Results

7.1.3.1 Fracture Toughness K_{Ic}

The resulting load-displacement curves are given in Figure 7.8. The value for P_Q is determined by the intersection of the 5% secant line, as explained in Section 7.1.2.1. Also for both samples the origin shows an offset of the elastic loading line, due to nonlinearity at the beginning of the testing. This nonlinearity can be caused by some resettling of the clip gages in the specimen, when a small load is being applied.

The resulting values for K_Q are given in Table 7.1. This table includes whether or not the requirements given in Equations (7.16) and (7.17) are met. The values for K_Q are not valid, because these requirements are not met for both samples. This indicates that there is too much plasticity present to use LEFM testing. For this reason, elastic-plastic fracture mechanics will be introduced in Section 7.2.

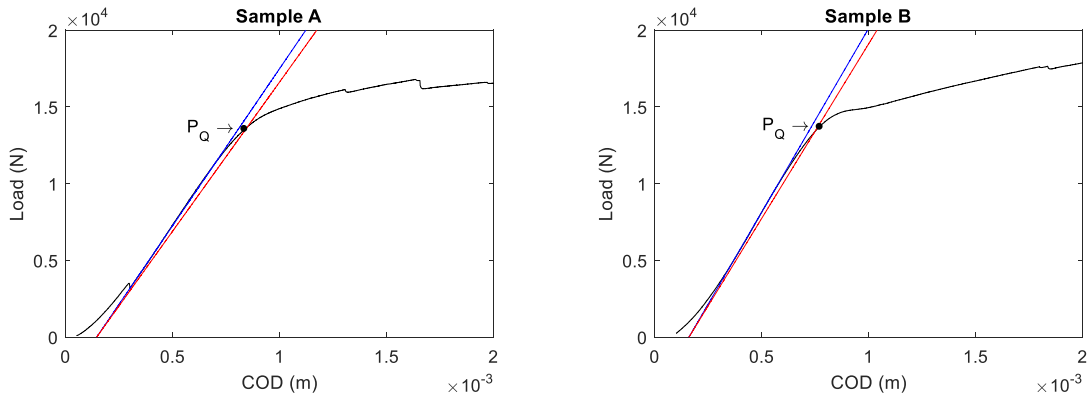

Figure 7.8: Load-displacement curves of a) sample A and b) sample B, including P_Q. The blue line indicates the initial elastic loading line and the red line the 5% secant slope.

Table 7.1: Results for K_Q and requirements for samples A and B.

Sample	**P_Q (kN)**	**a_q (mm)**	**K_Q $\left(\text{MPa}\sqrt{\text{m}}\right)$**	**$\frac{P_{max}}{P_Q}$ (-)**	**W-a (mm)**	**$2.5\left(\frac{K_Q}{\sigma_{ys}}\right)^2$ (mm)**	**K_Q=K_{Ic}**
A	13.7	21.8	19.7	1.22	18.2	29.8	No
B	13.4	21.3	18.9	1.64	18.7	27.2	No

7.1.3.2 Fatigue

The results of fatigue testing are shown in Figure 7.9, using the data processing as described in Section 7.1.2.2. The regions I and II are visible. However, region III is not present. From region I, the threshold stress intensity range (ΔK_{th}) can be deduced. This value corresponds to:

$$\Delta K_{th} = 5.6\ \text{MPa}\sqrt{\text{m}}$$

Paris' equation is given in Equation (7.11). The constants C and m are found using least-squares fits of the linear part of the curves in Figure 7.9b. The results are given in Table 7.2. These constants will be used in Section 7.3.5.1 for a fatigue life prediction.

7.1.3.3 SEM Images

Scanning electron microscopy (SEM) is used to make images of the fracture surface after fatigue testing. Figure 7.10a displays the fracture surface containing inclusions. Both around the inclusions and in the bulk, the material exhibits transgranular brittle fracture behaviour. Fine faceted cleavage is observed around the inclusions. Transgranular brittle fracture is also shown in Figure 7.10b. Figure 7.10c and Figure 7.10d both contain an inclusion and microcracking is observed around these inclusions. These SEM images reveal that the fracture happens with transgranular brittle behaviour and that microcracking occurs around inclusions. Fatigue testing makes use of lower applied loads than for testing to determine the fracture toughness. Therefore, it can be assumed that microcracking also occurs during fracture toughness testing.

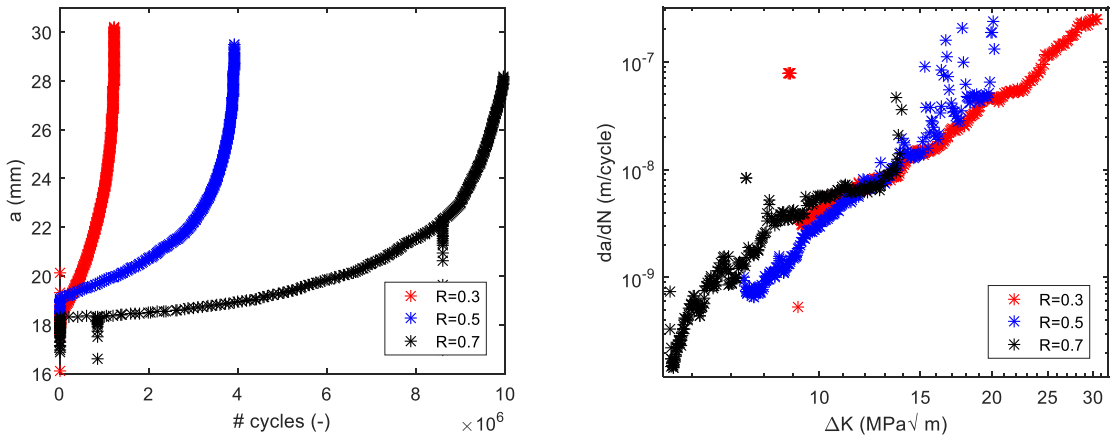

Figure 7.9: Results of fatigue testing: a) crack length versus the number of cycles and b) fatigue crack growth rate curve, da/dN versus ΔK

Table 7.2: Results fatigue testing, the constants C_1 and C_2.

R	**0.3**	**0.5**	**0.7**	**average**
C_1 ((m/cycle)(MPa√m)^-C_2)*	$4.32*10^{-13}$	$4.93*10^{-14}$	$9.74*10^{-11}$	$3.26*10^{-11}$
C_2 (-)	3.85	4.77	1.73	3.44

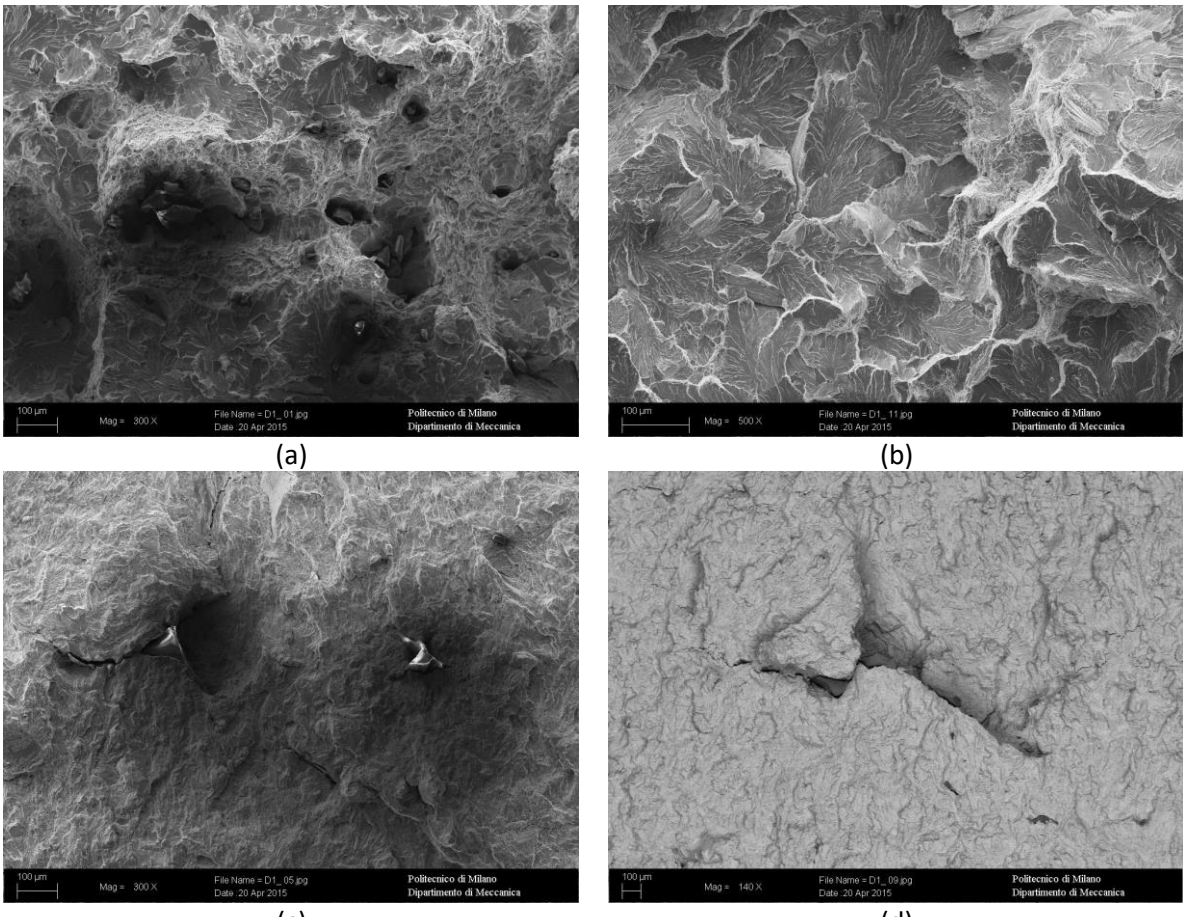

Figure 7.10: SEM images of fracture surface after fatigue testing: a) fracture surface including inclusions, b) displays typical brittle behaviour, c) and d) show inclusions with microcracking.

7.2 Elastic Plastic Fracture Mechanics

Linear elastic fracture mechanics (LEFM) describes the fracture behaviour under elastic conditions and plasticity may only be present in a very small region around the crack tip. These conditions are only met for intrinsically brittle materials and high strength metallic materials in plain strain. A different method needs to be used if the material exhibits more plastic behaviour. In this case elastic-plastic fracture mechanics (EPFM) should be used. The ranges of applicability of LEFM and EPFM are shown in Figure 7.11. the disadvantage of EPFM is that these methods require more effort.

7.2.1 J-integral

7.2.1.1 Concept

The J-integral is a path-independent integral that equals the decrease in potential energy per increment of crack extension in a linear or nonlinear elastic material. It can be seen as both an energy parameter and as a stress intensity parameter. The material is assumed to exhibit a non-linear elastic behaviour, because it enables the usage of the elastic energy (U_a). The energy balance can thus be applied to define the J-integral. The energy definition of J can be written as:

$$J = -\frac{dU_p}{da} = \frac{d}{da}(F - U_a) \ . \tag{7.23}$$

For a linear elastic material J is equal to the energy release rate G, as described in Section 7.1.1.1.

7.2.1.2 Mathematical Description

A two-dimensional cracked body of a nonlinear elastic material is shown in Figure 7.12. The contour over which J is integrated, Γ, surrounds the crack tip as in Figure 7.12. The area A is defined as the area enclosed by Γ. The potential energy is given by the following equation.

$$U_p = U_a - F = \int_A W dA - \int_\Gamma T_i u_i ds \ , \tag{7.24}$$

where W is the strain energy density, T_i is the traction acting on perimeter Γ on and u_i is its corresponding displacement. Equation (7.24) can be evaluated by considering an arbitrary but finite

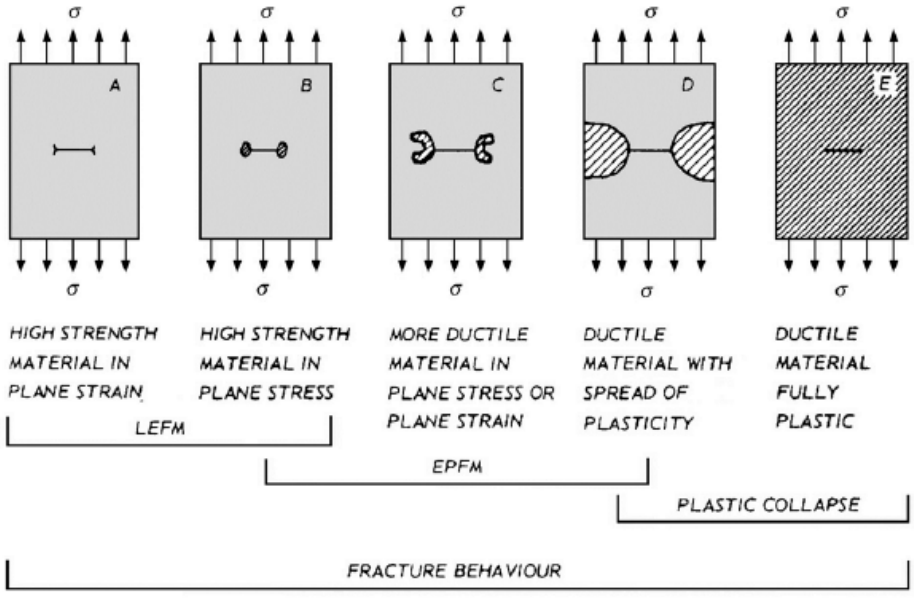

Figure 7.11: Ranges of applicability for LEFM and EPFM [24].

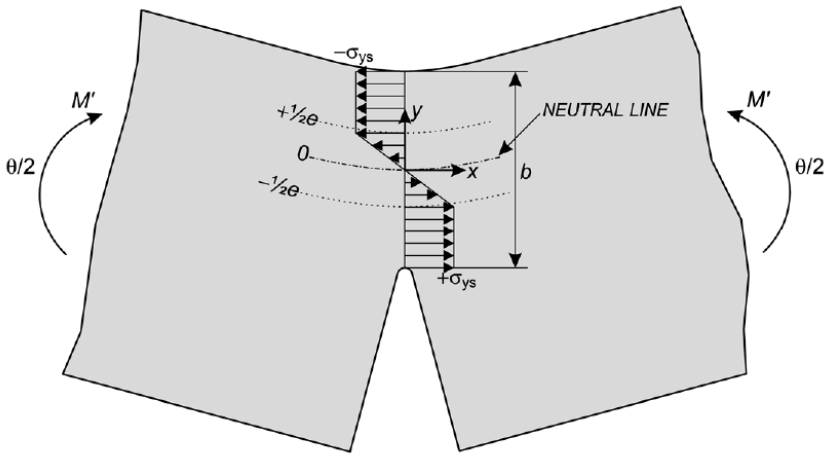

Figure 7.12: Stress distribution in critical ligament [24].

part of the body in which the crack tip is embedded. A difference in potential energy will be considered. This difference is caused by a change in the crack length (Δa). This will ultimately lead to the following expression of the J-integral:

$$J = \int_{\Gamma} \left(W dx_2 - T_i \frac{\partial u_i}{\partial x_1} \right) . \tag{7.25}$$

This integral is path-independent and gives information about stresses and strains at the crack tip. This concept can only be used under the condition that there is no unloading anywhere in the cracked body. This means that strictly speaking crack growth is not allowed.

7.2.2 Experiments

The method to experimentally determine the J-integral is based on crack extension either under constant displacement or under constant load. The J-integral can be expressed under these conditions in the following way:

$$J = -\int_0^v \left(\frac{\partial P}{\partial a} \right)_v dv = \int_0^P \left(\frac{\partial v}{\partial a} \right)_p dP \ , \tag{7.26}$$

where P is the load and v is the load-line displacement. The load-line displacement is the displacement along the line of the applied load. This equation can be used to determine the instantaneous J value for a deeply cracked bar loaded in bending:

$$J = \frac{2}{Bb} \int_0^{\Theta} M \, d\Theta \ , \tag{7.27}$$

where B is the thickness of the bar, b is the size of the uncracked ligament ahead of the crack, M is the bending moment and Θ is the total bending angle. In this specific geometry, shown in Figure 7.12, plasticity is confined to the critical ligament, since the specimen's halves remain elastic during loading. Under these conditions there is a relation between M and P and between Θ and v and Equation (7.27) can be rewritten as:

$$J = \frac{2}{Bb} \int_0^v P \, dv \ , \tag{7.28}$$

The initiation of crack growth and thus also the critical J value are difficult to determine. Therefore, during a J_{Ic} test, a load is applied to a test specimen to introduce a distinct but small amount of crack

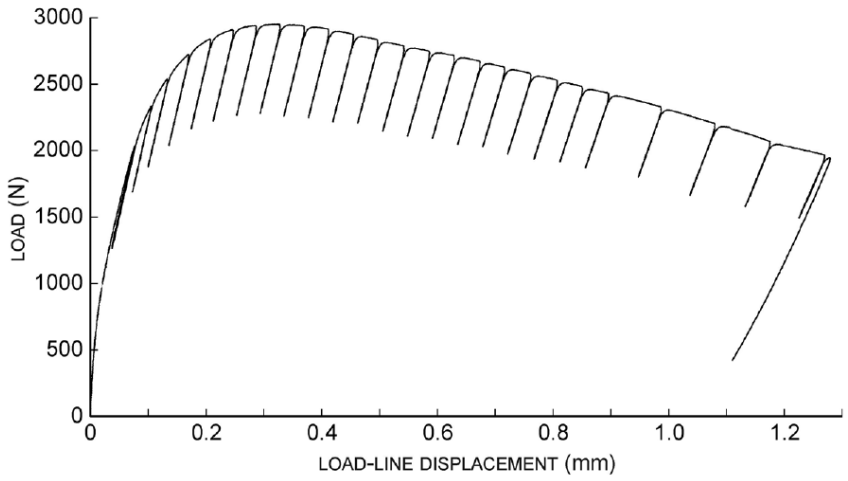

Figure 7.13: Graph showing an example of the unloading compliance technique [24].

extension. From this small amount of crack extension, the value of Δa should be extrapolated to zero. The unloading compliance technique is a procedure that can be used to monitor this crack extension, Δa. For this, the load is partially removed and then reapplied, as shown in Figure 7.13. The description of this test method is given in ASTM E1820-11 [6] and is discussed in detail in the next part.

7.2.2.1 ASTM E1820-11

The type of data collected in Figure 7.13 can be translated into the type of graph given in Figure 7.14. The critical J value can be deduced from such a graph. This section will give the mathematical tools for the data manipulation to obtain J_{Ic}.

The calculation of the J-integral is subdivided in an elastic component (J_{el}) and a plastic component (J_{pl}), as follows:

$$J = J_{el} + J_{pl} \ , \tag{7.29}$$

Incremental equations are applied for each unloading cycle, where the J-integral is evaluated always from the previous step. This is done using the overall equation:

$$J_{(i)} = \frac{\left(K_{(i)}\right)^2 (1-\nu^2)}{E} + J_{pl(i)} \ , \tag{7.30}$$

where the first part is J_{el}, which is not dependent on the previous step. The value of $J_{pl(i)}$ does depend on the previous step and will be described below.

The following equation is applied to calculate K_I:

$$K_{(i)} = \left(\frac{P_i S}{B W^{1.5}}\right) f\left(\frac{a_i}{W}\right) \ , \tag{7.31}$$

where S, B and W depend on the geometry of the specimen as given in Figure 7.15 and $f\left(\frac{a_i}{W}\right)$ is calculated as:

$$f\left(\frac{a_i}{W}\right) = \frac{3\left(\frac{a_i}{W}\right)^{0.5}\left(1.99 - \left(\frac{a_i}{W}\right)\left(1-\frac{a_i}{W}\right)\left(2.15 - 3.93\left(\frac{a_i}{W}\right) + 2.7\left(\frac{a_i}{W}\right)^2\right)\right)}{2\left(1+2\frac{a_i}{W}\right)\left(1-\frac{a_i}{W}\right)^{1.5}} \ . \tag{7.32}$$

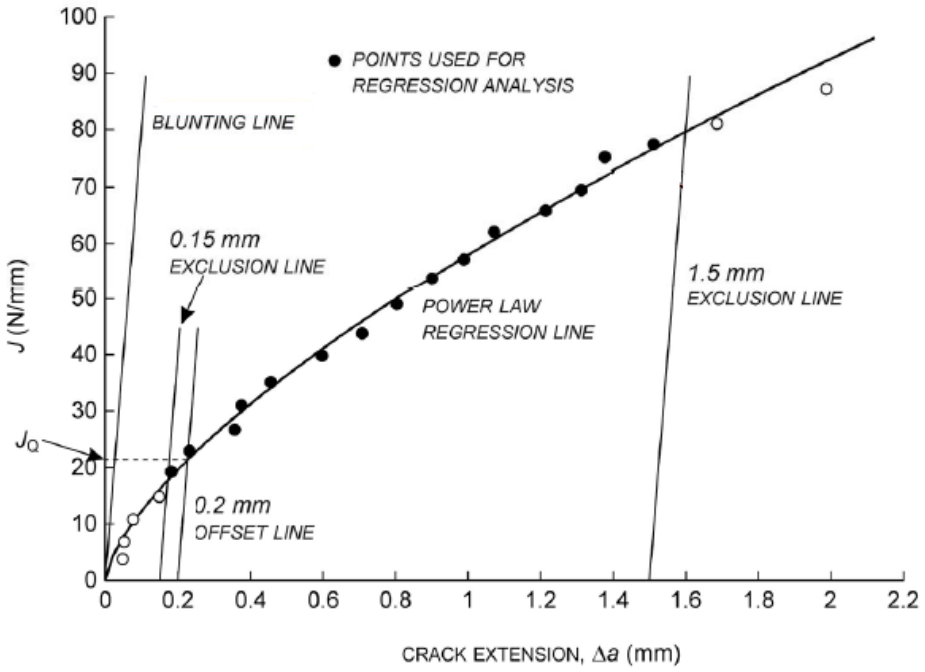

Figure 7.14: Graph J versus Δa [6].

The plastic component of J is determined by incremental equations, starting with the following equation:

$$J_{pl(i)} = \left(J_{pl(i-1)} + \left(\frac{\eta_{pl(i-1)}}{b_{(i-1)}}\right)\left(\frac{A_{pl(i)} - A_{pl(i-1)}}{B}\right)\right) \times \left(1 - \gamma_{pl(i-1)}\left(\frac{a_{(i)} - a_{(i-1)}}{b_{(i-1)}}\right)\right), \tag{7.33}$$

where η and γ are plastic geometry factors, described by the following equations:

$$\eta_{pl(i-1)} = 3.667 - 2.199\left(\frac{a_{(i-1)}}{W}\right) + 0.437\left(\frac{a_{(i-1)}}{W}\right)^2 \tag{7.34}$$

$$\gamma_{pl(i-1)} = 0.131 + 2.131\left(\frac{a_{(i-1)}}{W}\right) - 1.465\gamma_{pl(i-1)}\left(\frac{a_{(i-1)}}{W}\right)^2 \tag{7.35}$$

while $A_{pl(i)}$ will be calculated in Equation (7.36). The values of $A_{pl(i)}$, used in Equation (7.33), refer to the plastic area under the graph given in Figure 7.13. This value can be calculated using the next equation:

$$A_{pl(i)} = A_{pl(i-1)} + \frac{\left(P_{(i)} + P_{(i)}\right)\left(v_{pl(i)} - v_{pl(i-1)}\right)}{2}, \tag{7.36}$$

where $v_{pl(i)}$ is the plastic part of the crack mouth opening displacement, $v_{pl(i)} = v_{(i)} - \left(P_{(i)}C_{(i)}\right)$. The elastic compliance (C) is defined by $\left(\Delta v_{(i)}/\Delta P_{(i)}\right)$.

The calculation of the crack size (a_i) is done as follows:

$$\frac{a_i}{W} = 0.999748 - 3.9504U + 2.9821U^2 - 3.21408U^3 + 51.51564U^4 - 113.031U^5, \tag{7.37}$$

where U is derived from the following equation:

$$U = \frac{1}{1 + \sqrt{\frac{EBC}{S/4}}} \ . \tag{7.38}$$

The equations above are needed to derive the J-Δa graph, given in Figure 7.14. The crack extension Δa is the initial crack size a_0 subtracted from the calculated crack length a_i. A blunting line is used to account for apparent crack growth due to crack tip blunting and is given as:

$$J = 2\sigma_y \Delta a \ , \tag{7.39}$$

where σ_y is the flow stress, given as $\frac{1}{2}(\sigma_{ys} + \sigma_{uts})$. Work hardening is taken into account by suing this flow stress. Parallel to the blunting line, two exclusion lines and an offset line are defined. The two exclusion lines have offset values of 0.15 mm and 1.5 mm respectively. Only the data points between these two lines are valid data points and are applied for the calculation of the provisional J_{Ic} value, J_Q. The offset line is drawn for 0.2 mm of real crack growth, i.e. discarding the apparent crack growth caused by blunting. Using the method of least square fit, a power-law regression line is determined only using the valid data points. The regression line has the following form:

$$J = C_1 + \left(\frac{\Delta a}{k}\right)^{C_2} \ , \tag{7.40}$$

where k = 1.0 mm. The provisional J_{IC} value, J_Q, is found as the intersection of the power-law regression line and the 0.2 mm offset line, as shown in Figure 7.14. The provisional J_Q can be confirmed as J_{Ic}, if the two following requirements are met:

$$B > \frac{10J_Q}{\sigma_y} \text{ and } W - a_0 > \frac{10J_Q}{\sigma_y} \ . \tag{7.41}$$

Both requirements have the goal to ensure that a size-independent value of the fracture toughness is measured.

The last step is to calculate the fracture toughness in terms of a critical stress intensity factor (K_{JIc}) from J_{Ic}, a value which will be used in Section 7.3.3. This value is determined using the equation below:

$$K_{JIc} = \sqrt{\frac{EJ_{Ic}}{1 - \nu^2}} \ . \tag{7.42}$$

7.2.2.2 Samples

For J_{Ic} integral testing Single Edge Notched Bend (SENB) specimen are used. The dimensions of the specimen are given in Figure 7.15. These specimen are made from a part of tie rod 61-91. After removing the rough surface, a weld was observed in the middle of the wrought iron sample. From this sample, two types of specimen have been made: with the notch on the weld (W) and with the notch in the bulk material (B). The specimens are named after the position of their respective notch.

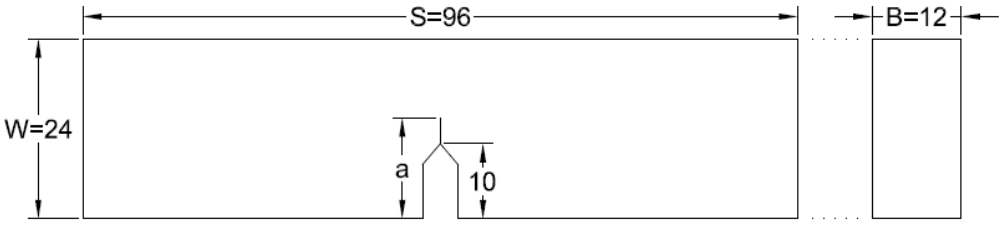

Figure 7.15: SENB specimen, with its dimensions in mm.

7.2.3 Results J_{Ic}

J-integral testing has been done on multiple specimen. There are two types of results after the data manipulation descried in the previous section. The first type is the expected shape of the graph, as in Figure 7.14. Five samples fit in this first category and will be discussed first. The second type of graph exhibits an unexpected behaviour and will be discussed later on in this section.

The results of the specimen in the first category are given in Table 7.3. The values taken for the flow stress is 230 MPa, for the Young's modulus is 200 GPa and the Poisson ratio is 0.3, as given in Section 2.4.3. All specimen have valid J_{Ic} values, because they all satisfy the imposed requirement of Equation (7.41). The average J_{Ic} value is 11.1 kN/m and the average J_{max} value is 98.2 kN/m. The average value of K_{JIc} is 48.0 MPa√m with a standard deviation of 12.5 MPa√m. This value will be used in Section 7.3.4.

Figure 7.16 shows the results for specimen W1, part of the first category. The measured load-COD curve is given in Figure 7.16a and the resulting J-Δa_p curve in Figure 7.16b. The load-COD curve shows two discontinuities at a COD of 0.26 mm and 0.60 mm respectively. Suddenly, less load is needed for an increase in COD. This implies that at those two points, a weakness in the material is present. The J-Δa_p curve displays linear behaviour. The measurements and the resulting J-Δa_p curve of the other specimen of the first category are given in Appendix C.

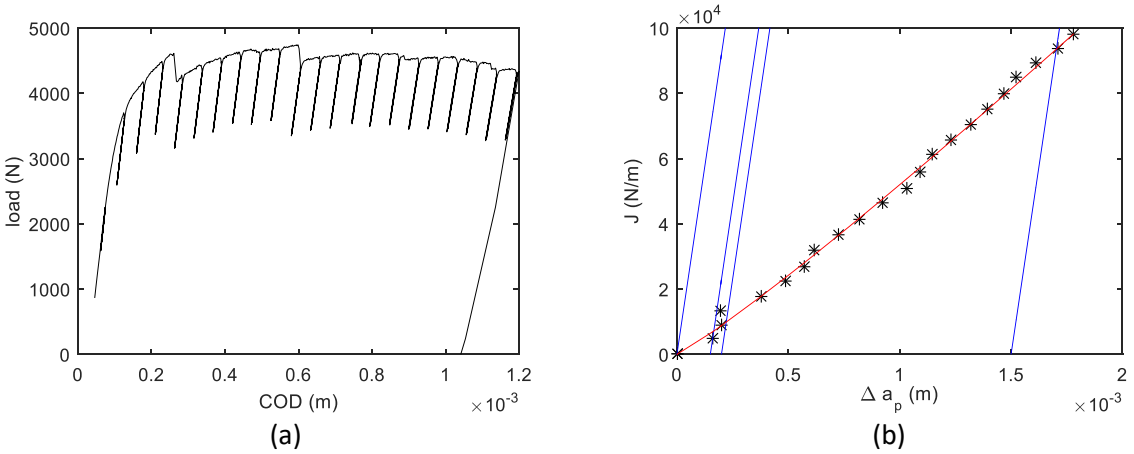

Figure 7.16: Results for specimen W1: a) Load versus COD graph and b) J versus Δa_p.

Table 7.3: Results J integral testing of the first category.

Specimen	J_Q (kN/m)	J_{max} (kN/m)	$\frac{10J_Q}{\sigma_y}$ (mm)	B (mm)	W-a_0 (mm)	J_Q=J_{Ic}	K_{JIc} (MPa√m
W1	9.86	98	0.43	11.50	11.0	Yes	46.6
W2	4.96	91	0.22	11.70	8.5	Yes	33.0
W3	8.76	113	0.38	11.70	10.9	Yes	43.9
W4	20.7	73	0.90	11.75	9.7	Yes	67.5
B1	11.0	116	0.48	11.70	11.8	Yes	49.2

The second category of test results only shows an increase in Δa_p for the first few unloading steps. After these first unloading steps, Δa_p fluctuates around the same value. An example is given in Figure 7.17, for specimen B2. The compliance for this sample first increases for two unloading cycles, and then fluctuates around one value. The stagnation of the compliance means that there is no crack growth. The first two unloading steps result in crack growth, but after these steps the crack growth stops. However the COD still increases, which might be caused by plastic deformation in the sample.

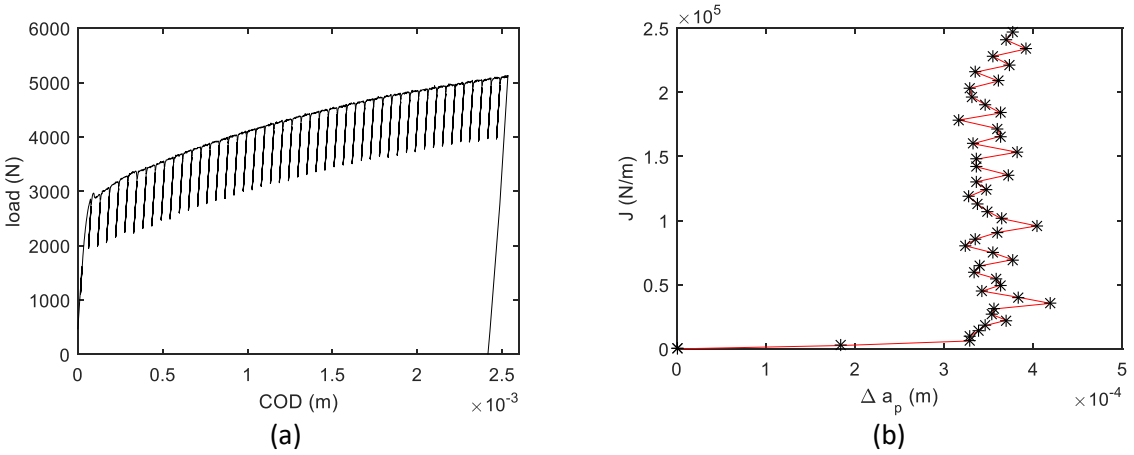

Figure 7.17: Results specimen B2: a) Load versus COD graph and b) J versus Δa_p.

7.3 Load Capacity Tie Rods

The goal of fracture mechanics testing is to be able to predict the critical stress at which cracks found using NDT starts growing. The equation used for this prediction is:

$$K_{Ic} = Y\sigma_c\sqrt{\pi a}\ , \tag{7.43}$$

where Y the geometry factor is, σ_c is the critical applied stress and a is the crack length. The fracture toughness, K_{Ic}, can also be deduced from J-integral testing, leading to K_{JIc}. This parameter takes into account the elastic-plastic behaviour of the material.

Mode I testing is done, as described in the previous section, but an inclined crack will also have a mode II component. Figure 7.18 displays an inclined crack as typically present in the tie rod, as discussed in Section 3.1. A projection of this crack is made, such that only Mode I is applied to the crack. This is the starting point of the crack geometry analysis, followed by the geometry factors of an inclined crack. The geometry factors of these two cases will be compared. This will lead to a rough estimate for the critical applied stress of a tie rod.

7.3.1 Geometry Factors, "Uninclined" Crack

The geometries discussed in this section are given in Figure 7.19. These three geometries all are pure mode I. Knowing the geometry factor, the critical applied stress can be calculated using Equation (7.43) and implementing the value for K_{JIc} obtained in Section 7.2.2.2.

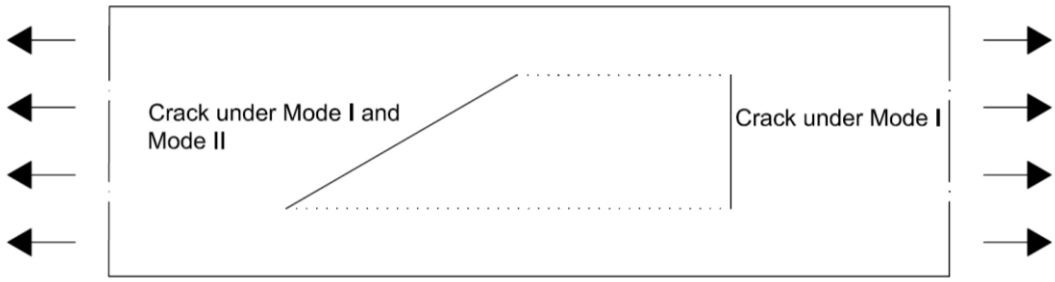

Figure 7.18: Projection of an inclined crack, that only consists of Mode I

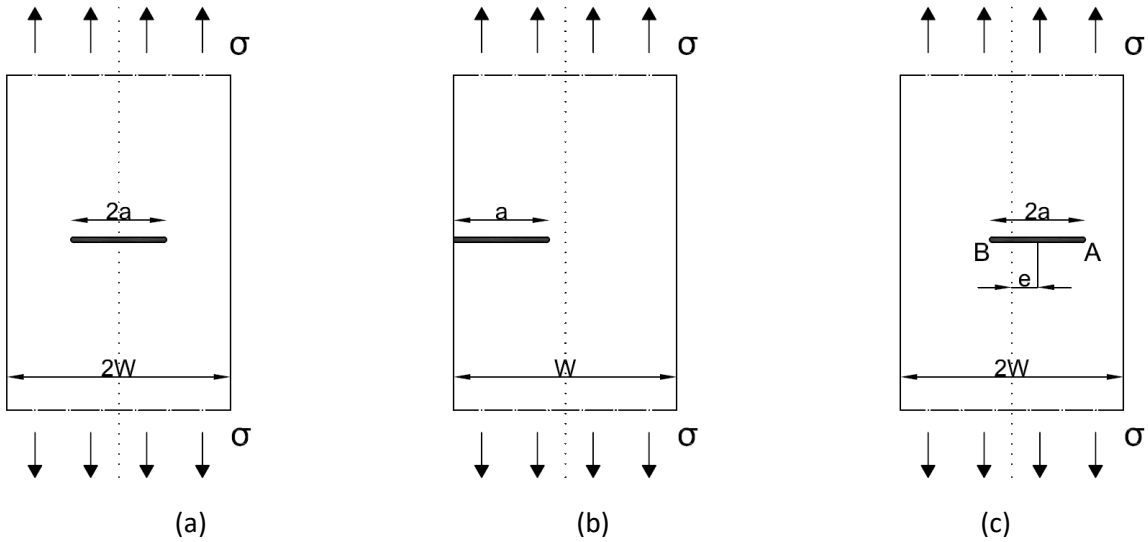

Figure 7.19: Geometries of Mode I crack of a) a centre-cracked plate, b) an edge-cracked plate and c) an eccentric internally cracked plate.

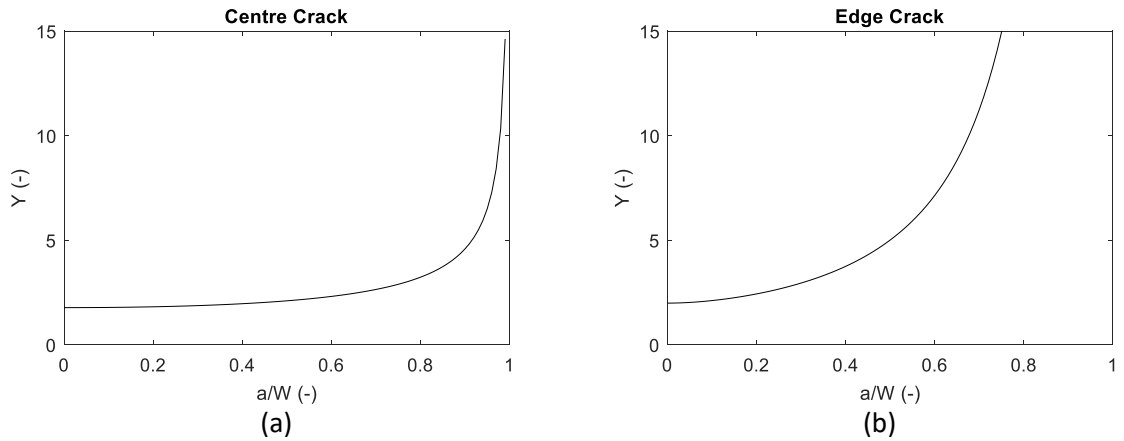

Figure 7.20: Geometry factor versus crack length over width, for a) central cracks and b) edge cracks.

The first geometries discussed are the centre-cracked plate, Figure 7.19a, and the edge-cracked plate, Figure 7.19b. These are the two simplest geometries. The geometry factor of the centre crack plate is described as follows [7]:

$$Y = \sqrt{\pi}\left(\frac{1 - 0.5\frac{a}{W} + 0.37\frac{a}{W}^2 - 0.044\frac{a}{W}^3}{\sqrt{1-\frac{a}{W}}}\right) \tag{7.44}$$

and the geometry factor of the edge cracked plate is described in the following equation [8]:

$$Y = 1.988\left(\frac{0.026778\left(0.427103 + \frac{a}{W}\right)^{-2.73895} + 0.26514\frac{a}{W} + 0.72475}{\left(1-\frac{a}{W}\right)^{1.5}}\right). \tag{7.45}$$

Figure 7.20 shows the trend of the geometry factors with increasing crack length for the central and the edge crack. Comparing the trends of the geometry factors, the geometry factor of the edge-cracked plate increases faster with increasing crack length than that for the centre-cracked plate. This leads to the conclusion that an edge crack reaches its critical crack size earlier than a central crack.

The third geometry is the eccentric internal crack, given in Figure 7.19c. For this configuration, the two crack tips have different values for the geometry factor. The critical crack size is therefore different for crack tips A and B. The geometry factors for both crack tips can be calculated with the following equations [9]:

$$Y_A(\varepsilon,\lambda) = \sqrt{\pi}\left(1 + \sum_{n=2}^{19} C_n\lambda^n\right) \tag{7.46}$$

$$Y_B(\varepsilon,\lambda) = \sqrt{\pi}\left(1 + \sum_{n=2}^{19} (-1)^n C_n\lambda^n\right), \tag{7.47}$$

where $\varepsilon = e/W$, $\lambda = \frac{a}{W-e}$ and the constants C_n are given in Appendix D.

Figure 7.21 shows the geometry factor for the eccentric crack tips for different values of ε. Crack tip A has higher values for the geometry factor than crack tip B, because this crack tip is closer to the edge. The crack growth can thus expected to start at crack tip A, which will reach the edge first. This will lead to the configuration of the edge crack, where crack tip B becomes the general crack tip.

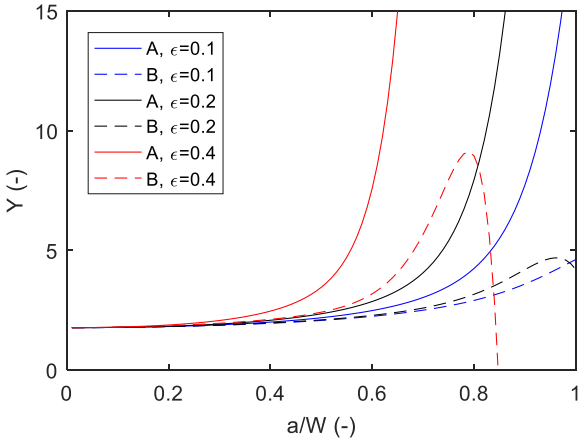

Figure 7.21: The geometry factor for an eccentric internal crack for different values of ε.

The edge crack is the most critical situation and the central crack is the safest. Taking this into account, the safety limits of the stress applied to a tie rod can be calculated. This will be done in Section 7.3.4.

7.3.2 Geometry Factors, Inclined Crack

The presence of cracks in the tie rods and their geometry is discussed in Section 3.1 The angle between the surface and the weld is on average around 27°. This signifies that crack growth will occur under mixed mode I and mode II conditions. The simplest case of a geometry with an inclined crack is given in Figure 7.22. Figure 7.22b shows the corresponding geometry factor as a function of the angle β. The geometry factor for mode I decreases rapidly with decreasing angle. For mode II, the geometry factor has a maximum at 45°.

Figure 7.23 shows crack geometries for inclined cracks in a semi-infinite plate. Note that the angle θ is taken from the normal of the edge. The angle θ of interest is 63°. For convenience, an angle of 60° is taken. Figure 7.24 gives the geometry factors for an oblique edge crack. These graphs follow a similar trend to Figure 7.22b. For mode I, the geometry factor increases with decreasing angle θ. The value of the geometry factor is between 0.5 and 1.1 for an angle of 60°. For mode II, the geometry

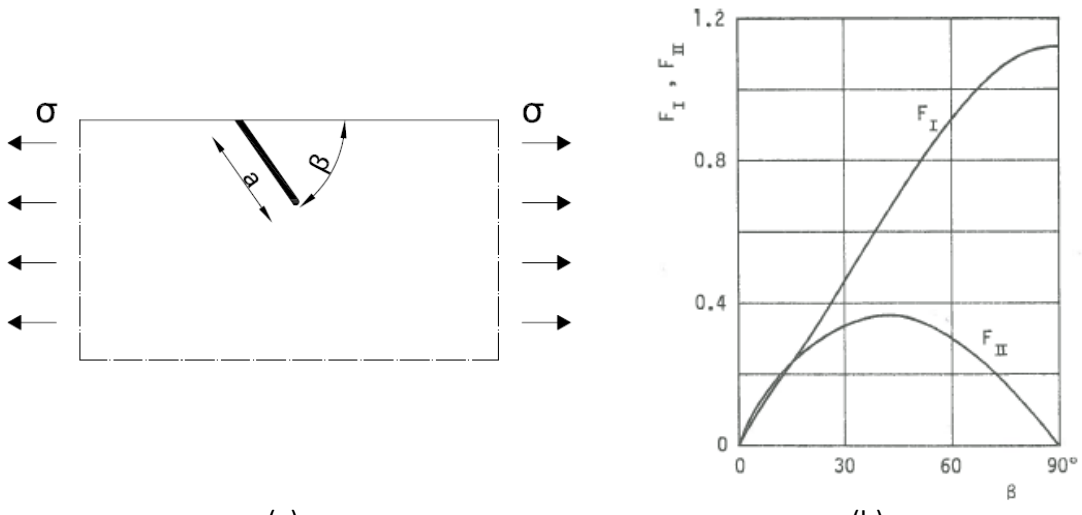

(a) (b)

Figure 7.22: Oblique edge crack in a semi-infinite plane, a) the geometry with b) the resulting geometry factor for mode I and mode II [25].

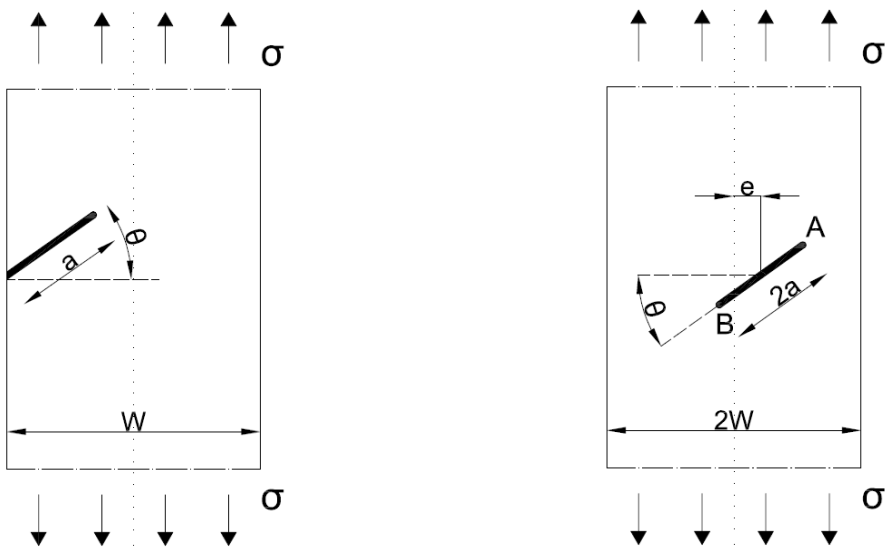

(a) (b)

Figure 7.23: Crack geometries of a) oblique edge crack in a rectangular plate and b) oblique eccentric crack in a rectangular plate.

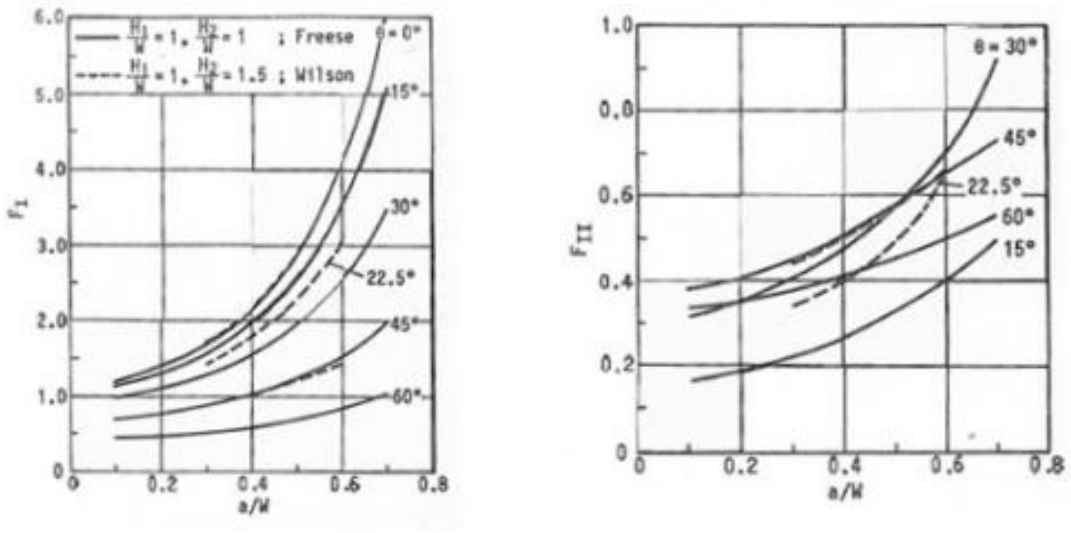

(a) (b)

Figure 7.24: Geometry factors for oblique edge crack for a) mode I and b) mode II [25].

factor first increases with increasing angle and then decreases after reaching an angle of 30° or 45° depending on the ratio a/W. For an angle of 60°, the value is between 0.3 and 0.6.

The geometry factor for the eccentric oblique crack is given in Figure 7.25. In this configuration, the same trends can be distinguished for the geometry factor as for the inclined edge and the inclined central crack. However, these values are lower than for the edge crack. The geometry factor increases as the relative crack size increases, but the dependence on relative crack size is larger for crack tip B.

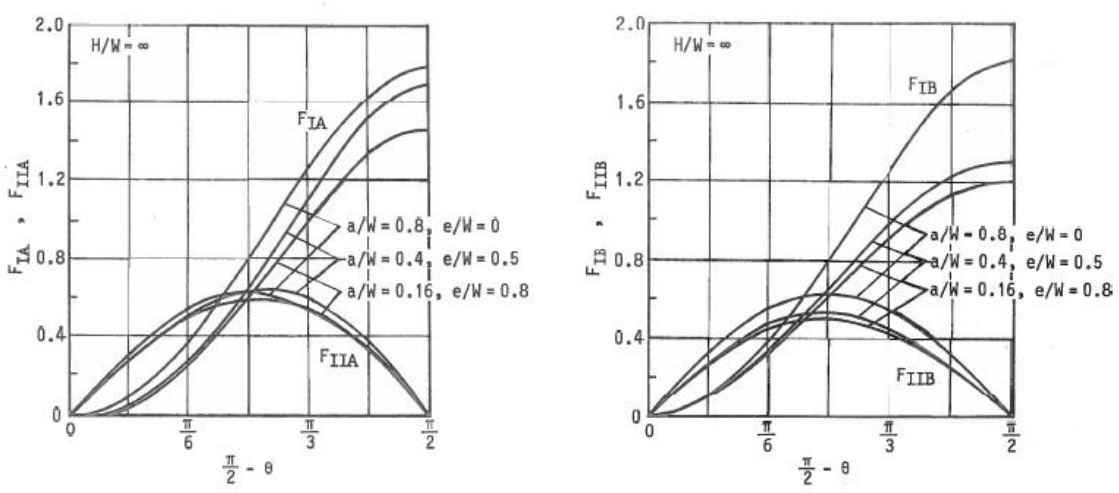

(a) (b)

Figure 7.25: Geometry factor for oblique eccentric cracks for a) crack tip A and b) crack tip B [25].

7.3.3 Influence Inclination

In previous sections, the different geometry factors are given for cracks with and without an inclined nature. The influence of an inclined crack on the critical applied stress (σ_c) is examined in this section. For this purpose, Equation (7.43) is rewritten into the following form:

$$\frac{\sigma_c}{K_{Ic}} = \frac{1}{Y\sqrt{\pi a}} \,. \tag{7.48}$$

The equation is split up into two parts. The quantities after the equal sign are dependent on crack geometry, while those before are not. The values obtained on the right hand side will be used for the analysis of the influence of the inclination, using the three examples of oblique eccentric crack in Figure 7.26. A critical condition is reached first for the lowest value of $\frac{\sigma_c}{K_{Ic}}$, referred to as a lower bound value.

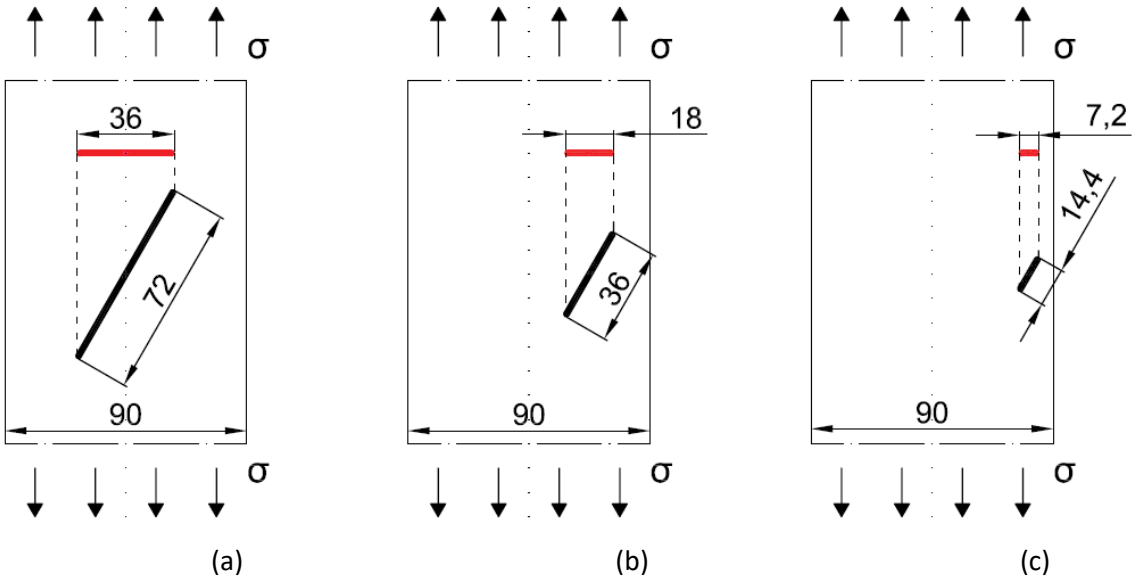

(a) (b) (c)

Figure 7.26: Three examples for the determination of the influence of the inclination of a crack in a tie rod with a width of 90 mm: a) a/W=0.8 and e/W=0, b) a/W=0.4 and e/W=0.5 and c) a/W=0.16 and e/W=0.8. The lengths given are in mm.

Table 7.4: Comparison between the three cases for Mode I, represented in Figure 7.26, for the uninclined crack (0°) and the inclined crack (60°).

case	θ (°)	a (mm)	tip	Y (-)	$\frac{\sigma_c}{K_{Ic}}\left(\frac{1}{\sqrt{m}}\right)$
1	**0**	**36**	**A**	**3.2**	**0.92**
			B	**3.2**	**0.92**
	60	72	A	0.40	5.3
			B	0.40	5.3
2	**0**	**18**	**A**	**3.1**	**1.4**
			B	**2.3**	**0.80**
	60	36	A	0.25	11.9
			B	0.30	9.9
3	**0**	**7.2**	**A**	**2.7**	**25**
			B	**2.1**	**3.2**
	60	14.4	A	0.25	18.8
			B	0.30	15.7

An angle θ of 60° is chosen for the inclined crack, since this is the expected crack angle in the tie rod. The width is chosen to be 90 mm. This length represents the height of the tie rod. The resulting values for Y and σ_c/K_{Ic} are given in Table 7.4, with the lower bound values shown in bold. In all three cases, the critical stress would be reached first by an uninclined crack. This signifies that the values for the uninclined crack give the lower bound value for a critical condition, based on mode I failure.

The comparison above does not take into account failure due to mode II. In practice, failure under mode II occurs less often. However, it is useful to examine the influence of its geometry factor Y. The ratios between mode I and mode II for the inclined crack of 60° are:

$$Y_{II} = 2Y_I \; for \; crack \; tip \; A$$

$$Y_{II} = 1.5Y_I \; for \; crack \; tip \; B$$

The values of Y of an inclined crack (θ=60°) for mode II are thus higher than for mode I, both for crack tip A and B. This means that K_{IIc} must be much lower than K_{Ic} to get failure in predominantly mode II. Therefore, it can be assumed that doing the failure assessment only involving the mode I component is conservative.

An inclined crack may undergo failure under mode I, mode II or mixed mode circumstances. Failure in predominantly mode II is mostly affected by the friction between the two fracture surfaces and the inclination of the crack. A small amount of mode I loading can result in the opening of the fracture surfaces, decreasing the amount of friction and therefore increasing the probability of mode II failure. Under mixed mode conditions, both modes I and II have influence on the fracture behaviour of the crack. The effective fracture toughness of mixed mode loading depends on many factors, like: angle of inclination and type of material. The exact values for the critical stresses cannot be calculated for mixed mode and for mode II, because the critical stress intensity factors for these modes are unknown. Mode II and mixed mode failure is thus out of the scope of this thesis and further research is needed to be able to take these modes into account. The configuration of an uninclined crack can be assumed to achieve conservative results, because it has the lowest values for σ_c/K_{Ic}, as given in Table 7.4.

7.3.4 Critical Applied Stress: Monotonic Loading

The ultimate goal of this chapter is to determine the critical applied stress for a certain crack length or *vice versa*. The critical stress is calculated using the following equation:

$$\sigma_c = \frac{K_{Ic}}{Y\sqrt{\pi a}} \ . \tag{7.49}$$

As discussed in 7.3.3, the inclined crack has a lower value for the geometry factor for mode I than the uninclined crack. This makes the uninclined crack the lower bound value and is thus used for the calculation of the critical stress. Section 7.3.1 discusses the influence of the eccentricity of the uninclined crack. The results were that the central crack is the safest configuration and the edge crack the most critical. These two aspects will thus be used as the basis for determining the structural safety of cracked tie rods.

Figure 7.27 displays the safety of a tie rod with a height of 90 mm containing a crack, as used in previous examples. The green area is the low risk zone, meaning that no crack growth is expected. The transition line depends on the geometry factor of an uninclined edge-cracked configuration. This is the lower limit, because it is the most unsafe configuration for a crack. The medium risk is present above the transition line. In this area, there might be some crack growth depending on the eccentricity of an internal crack. The upper limit of the medium risk zone is the critical curve. The critical curve is for the situation of a central crack. The zone above the critical curve is a high risk zone for crack propagation, because for all configurations of the crack the critical stress level is exceeded.

The tensile stress in the tie rods in the Duomo is between 0-140 MPa [10]. The height of the tie rods are used as the width W in the calculations. The minimum, average and maximum heights are 67 mm, 83 mm and 100 mm respectively. For these values, the transition and critical curves are given in Figure 7.28. The main observation is that at high values of stress, the critical crack length is about the same. At lower values of stress, there is more spread in critical crack size for the different heights. Also the maximum stress state, 140 MPa, of the tie rods in the Duomo is given in Figure 7.28. The area under this value gives the possible range of stresses in the tie rods and thus of the area of interest. The critical crack size of the transition curve at a stress state of 140 MPa is 8.4±0.3 mm and the critical crack size of the critical curve is 11.7±0.1 mm. At these crack sizes, the transition curve and the critical curve enter the area of interest.

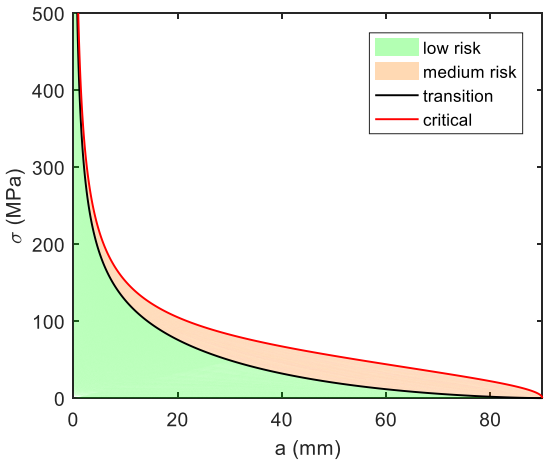

Figure 7.27: σ versus a for a tie rod, indicating the low and medium risk zone.

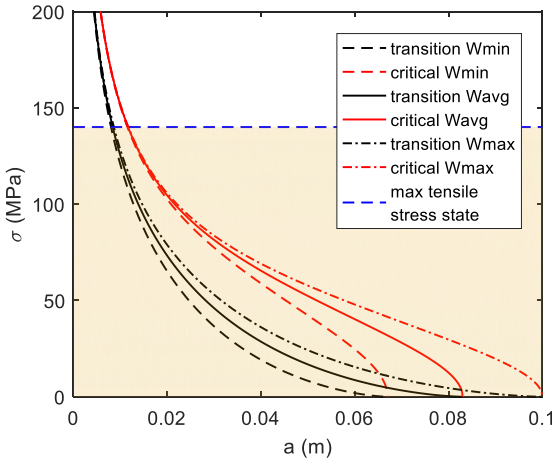

Figure 7.28: Transition and critical curves for different heights (W) of the tie rods in the Duomo, including the maximum tensile stress in the tie rods.

7.3.5 Threshold Crack Size: Cyclic Loading

The tie rods in the Duomo also endure fatigue. The main reason for fatigue is the seasonal temperature variation. The stress variation in the tie rod induced by the temperature variations over a year is shown in Figure 7.29 [11] and was measured by dynamic testing. The stress range ($\Delta\sigma$) is 24 MPa and the load ratio R ($\sigma_{min}/\sigma_{max}$) is 0.69.

The threshold crack size (a_{th}) is the minimal crack size at which crack growth due to fatigue is expected for a certain stress range. Equation (7.43) needs to be altered to determine the threshold crack size, as follows:

$$\Delta K_{th} = Y\Delta\sigma\sqrt{\pi a_{th}} \ . \tag{7.50}$$

The equation is solved for a_{th}, keeping in mind that Y is also a function of a_{th}. The result for an edge crack is given in Figure 7.30 for the height range of the tie rods present in the Duomo. It can be seen, that the spread of values is little and the difference is only 0.13 mm between the two extreme cases. This small difference cannot be observed with that precision yet using NDT. Therefore, the critical crack sizes are assumed to be 4.2±0.1 mm for an edge crack and 5.5±0.1 mm for a central crack. For eccentric internal cracks, the threshold crack length is between these two values.

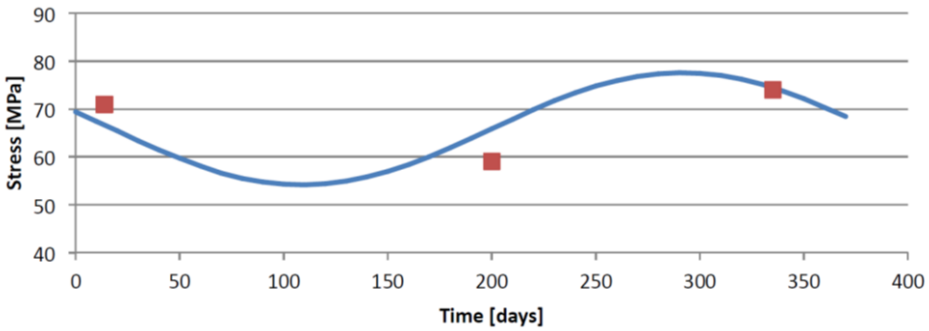

Figure 7.29: The expected stress variation over a year in a tie rod, due to seasonal temperature changes, experimental results (red squares) and theoretical fitting (blue line) [11].

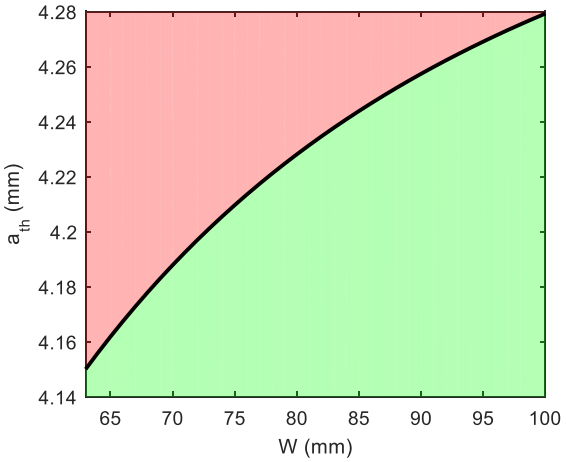

Figure 7.30: Treshold length for edge cracks versus the range of heights (W) of the tie rods in the Duomo, indicating a low risk zone (green) and a high risk zone (red) for crack propagation due to fatigue.

7.3.5.1 Fatigue Life Prediction

The fatigue life prediction can be done combining Equation (7.50) with Paris' law, in Equation (7.10). The number of cycles needed to grow a crack from the threshold crack length until the critical crack length (N_f) is calculated as follows:

$$N_f = \frac{1}{C_1\left(\Delta\sigma\sqrt{\pi}\right)^{C_2}} \int_{a_{th}}^{a_c} \frac{1}{\left(Y\sqrt{a_{th}}\right)^{C_2}} da \quad , \tag{7.51}$$

where for the constants C_1 and C_2 the average value are taken from Table 7.2.

This calculation is done for an edge crack and central crack. The threshold crack length is taken from the previous section, which is based on fatigue due to the yearly temperature cycle. The resulting number of cycles until fracture are given in Table 7.5. The resulting number is too high to cause a significant amount of crack propagation in practice.

Table 7.5: Fatigue life prediction for the edge crack and the central crack.

	Edge	**Central**
a_{th} *(mm)*	4.2	5.5
a_c *(mm)*	8.4	11.7
N_f *(# cycles)*	$1.8*10^5$	$2.6*10^5$

7.4 DISCUSSION

This chapter dealt with the fracture mechanics of wrought iron. Testing has been done for monotonic loading and fatigue. Using EPFM, the average value for the stress intensity factor, K_{JIc}, is 48.0 MPa√m. The maximum tensile stress on a tie rod is 140 MPa. At this stress level, the critical crack size is between 8.4 and 11.7 mm, depending on the eccentricity of the crack. The fatigue treshold stress intensity range, ΔK_{th}, is 5.6 MPa√m. This resulted in a threshold crack length of 4.2-5.5 mm, also depending on the eccentricity of the crack. These results are obtained using a simplified model for the crack geometry. It implies that for a crack length of 4.2 mm fatigue can cause crack growth. From a crack length of 8.4 mm, also monotonic loading may result in crack growth.

Currently, the concept of fatigue is only applied to variations in stress due to seasonal temperature changes. This resulted in a fatigue life prediction of around $2*10^5$ cycles to reach the critical crack length for failure due to monotonic loading by 140 MPa. Other reasons for fatigue should be investigated, like vibrations due to traffic. A simple evaluation of the variation of stresses with time can be done using strain gauges and applying them on the tie rods in the Duomo at strategic points.

The noteworthy outcome from the J-integral testing is the steep and linear slope of the J-Δa_p curve. In research done by A. Miserez *et al.* on aluminium composites [12], the J-Δa_p curve can be divided into three domains. These zones are visualized in Figure 7.31. Zone I is the steep part, attributed to crack-tip blunting and internal damage build-up. Following by zone II, which corresponds to macroscopic crack propagation. Full stable crack propagation occurs in zone III. The steep slope of the J-Δa_p curve and the big difference between J_{Ic} and J_{max} might thus be due to failure of the specimen before it reaches zone II, caused by a constant damage build up during testing. The damage build up could lead to a misconception that there is a crack extension of 1-2 mm, because the increase of the compliance is due to the formation of microcracks and not due to crack growth.

The transition from zone I to zone II can be observed from the load versus COD graph. The observation is that this transition happens when the load starts decreasing. In Figure 7.16, no significant decrease is present. The only reason for a decrease in load are pop-ins. This phenomenon is observed in the results for specimen W4, given in Figure C.3 in Appendix C. The last eight data points show a less steep behaviour as the data points before. This corresponds to the final eight unloading steps in the load-COD curve.

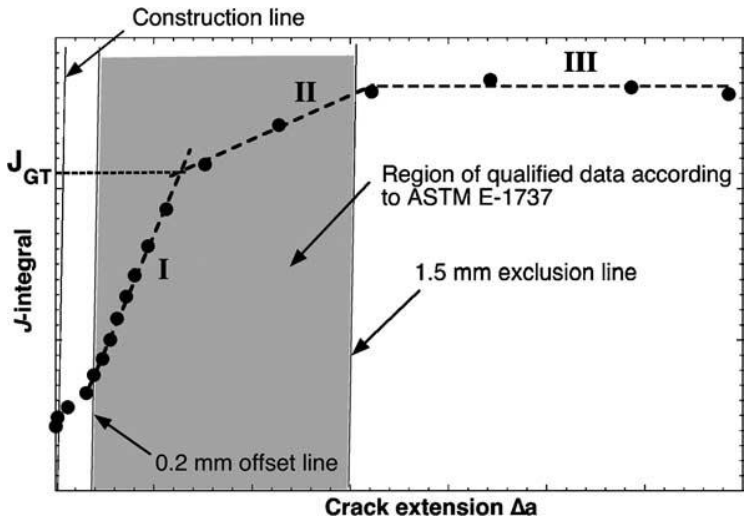

Figure 7.31: The J-Δa_p curve divided into three zones [12].

The internal damage build-up, corresponding with zone I, may be attributed to microcracking ahead of the crack tip. During fatigue testing, microcracking has been observed around inclusions, as can be seen in the SEM images of Figure 7.10. Fatigue testing imposes lower stress levels than for tests using monotonic loading. Therefore, it can be assumed that during J-integral testing microcracking also occurs. If the interfacial strength between an inclusion and the metal matrix is low, microcracking on the interface of inclusions can occur ahead and around the crack tip. This damage build-up will continue as the crack grows, because more inclusions ahead of the crack tip will experience elevated stress levels. Therefore, more microcracking can be observed as the crack grows, leading to a constant damage build up. This can result in that the J-Δa_p curve remains in zone I, during the J-integral testing.

The fracture toughness K_{Jlc} is higher than K_Q, determined in Section 7.1.3.1. This is a reasonable outcome, considering that in this section also the plastic part contributes to the fracture toughness. This can be further explained using the following equation:

$$J = J_{el} + J_{pl} = \frac{K^2(1-\nu^2)}{E} + J_{pl} \ ,$$

where, if J = J_{Ic}, K can considered to be the fracture toughness that is related to linear elastic conditions, as is K_Q. The fracture toughness K_{Jlc} is calculated from the total J value, including both J_{el} and J_{pl}.

In this chapter, no testing for mixed mode failure is performed. There are currently no standardised tests for mixed mode testing. However, different test specimen have been developed for mixed mode testing [13]–[15]. Two interesting examples are given in Figure 7.32. For both specimen, the angle between the crack and the applied load can be altered. The resulting fracture toughness is that for a combination of mode I and mode II. The literature mostly refers to mixed mode crack growth that leads to branching of the crack in mode I. This means that they do not take into account the presence of a weak plane, as is the case in the tie rods in the Duomo. Crack growth is guided by this weak plane, keeping the same ratio between K_I and K_{II}.

In Section 7.3.4, a simplified crack geometry is assumed. To further increase the understanding of the influence of the crack geometry, more intricate modelling tools need to be employed. Finite element method (FEM) is the first possibility [16], [17]. With this modelling tool, a diverse set of variables can be handled, like mixed mode loading, friction between crack surfaces and cracks in 3D bodies. FEM includes the use of a mesh for dividing a complex problem into small elements. However, this mesh

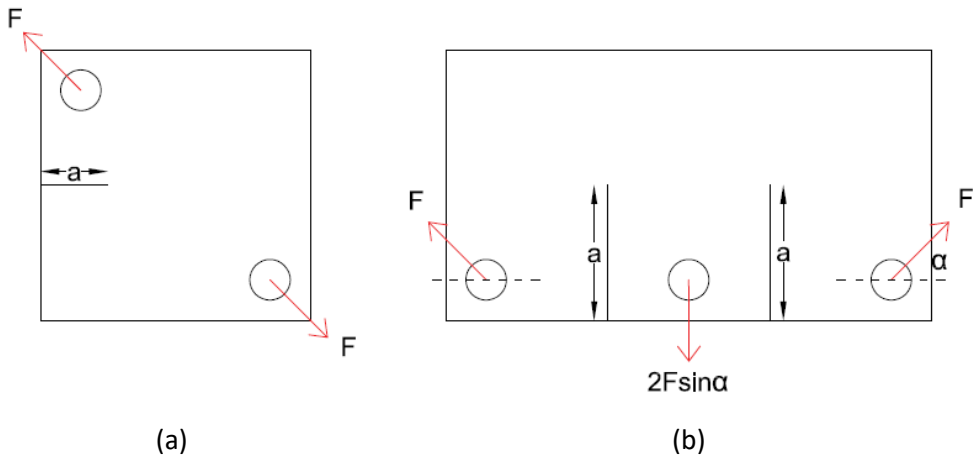

Figure 7.32: Specimen for mixed mode testing, a) CT specimen and b) double CT specimen.

could become distorted by large deformations or rotations. Another disadvantage of this method is difficulty with modelling the crack propagation. Therefore, other meshless models have been introduced to overcome these disadvantages [18]–[20]. One of these methods is the material point method (MPM) [21]. This method uses a collection of discretized material points, which are analysed by updating at each time step for all required properties such as position, velocity, acceleration and stress state. The advantage of this method is that it is able to cope with large deformations and rotations.

There are several characteristics of wrought iron, which might be involved during crack propagation. Crack closure during fatigue is a phenomenon that can affect the threshold fracture toughness range (ΔK_{th}) and the crack growth rate. Crack closure can arise from, among others, microcrack toughening or crack wake plasticity [22]. Microcrack toughening also influences the fracture toughness, by reducing the stresses around crack tip. In wrought iron, microcracks might originate from the slag inclusions. The shape of the plastic zone for mixed mode crack tips may differ and may result in a modification in crack closure [23]. The heterogeneity of the material may increases the roughness of the crack surface, which increases the effect of crack closure.

7.5 REFERENCES

[1] A. A. Griffith, “The phenomena of flow and rupture in soldis,” *Trans. Roy. Soc. Lond. Ser. A*, vol. 221, pp. 163–198, 1920.

[2] G. R. Irwin, “Analysis of stresses and strains near the end of a crack traversing a plate,” *J. Appl. Mech.*, vol. 24, pp. 361–364, 1957.

[3] J. R. Rice, “A path independent integral and the approximate analysis of strain concentration by notches and cracks,” *J. Appl. Mech.*, vol. 35, pp. 379–386, 1968.

[4] ASTM E399-12, “Standard test method for linear-elastic plane strain fracture toughness K_Ic of metallic materials,” *Am. Soc. Test. Mater.*, 2011.

[5] ASTM E647-15, “Standard test method for measurement of fatigue crack growth rates,” *Am. Soc. Test. Mater.*, 2015.

[6] ASTM E1820-11, “Standard test method for measurement of fracture toughness,” *Am. Soc. Test. Mater.*, 2011.

[7] H. Tada, P. C. Paris, and G. R. Irwin, *The Stress Analysis of Cracks Handbook*. Del Research Corporation, 1986.

[8] T. Fett, “Stress Intensity Factors and Weight Functions for the Edge Cracked Plate Calculated by the Boundary Collocation Method, KfK-Report 4791,” 1990.

[9] M. Isida, “Stress intensity factors for the tension of an eccentrically cracked strip,” *trans. ASME, J. Appl. Phys.*, vol. 33, p. 674, 1965.

[10] M. Vasic, “A Multidisciplinary Approach for the Structural Assessment of Historical Constructions with Tie-rods,” Politecnico di Milano, 2015.

[11] I. G. Stefanova, “Fatigue behaviour of the historical wrought iron tie-rods in the Duomo di Milano,” Politecnico di Milano, 2014.

[12] A. Miserez, A. Rossoll, and A. Mortensen, “Investigation of crack-tip plasticity in high volume fraction particulate metal matrix composites,” *Eng. Fract. Mech.*, vol. 71, no. 16, pp. 2385–2406, 2004.

[13] D. K. Mahanty and S. K. Maiti, “Experimental and finite element studies on mode I and mixed mode (I and II) stable crack growth—I. Experimental,” *Eng. Fract. Mech.*, vol. 37, no. 6, pp. 1237–1250, 1990.

[14] J. Qian and A. Fatemi, “Mixed mode fatigue crack growth: A literature survey,” *Eng. Fract. Mech.*, vol. 55, no. 6, pp. 969–990, 1996.

[15] R. J. Buzzard, B. Gross, and J. E. Srawley, “Mode II fatigue crack growth specimen development,” *Fract. Mech. ASTM STP 905*, vol. 17, pp. 329–346, 1986.

[16] J. Dolbow, N. Moës, and T. Belytschko, “An extended finite element method for modeling crack growth with frictional contact,” *Comput. Methods Appl. Mech. Eng.*, vol. 190, no. 51–52, pp. 6825–6846, 2001.

[17] C. A. Duarte, O. N. Hamzeh, T. J. Liszka, and W. W. Tworzydlo, “A generalized finite element method for the simulation of three-dimensional dynamic crack propagation,” *Comput. Methods Appl. Mech. Eng.*, vol. 190, no. 15–17, pp. 2227–2262, 2001.

[18] R. C. Batra and H. K. Ching, “Analysis of elastodynamic deformations near a crack/notch tip by the meshless local Petrov-Galerkin (MLPG) method,” *Comput. Model. Eng. Sci.*, vol. 3, no. 6,

pp. 717–730, 2002.

[19] E. Ferretti, “Crack propagation modeling by remeshing using the Cell Method (CM),” *Comput. Model. Eng. Sci.*, vol. 4, no. 1, pp. 51–72, 2003.

[20] Z. D. Han and S. M. Atluri, “SGBEM (for cracked local subdomain)-FEM (for uncracked global structure) alternating method for analyzing 3D surface cracks and their fatigue-growth,” *Comput. Model. Eng. Sci.*, vol. 3, no. 6, pp. 699–716, 2002.

[21] Y. Guo and J. A. Nairn, “Calculation of J-integral and stress intensity factors using the material point method,” *Comput. Model. Eng. Sci.*, vol. 6, pp. 298–308, 2004.

[22] R. O. Ritchie, “Mechanisms of fatigue crack propagation in metals, ceramics and composites: role of crack tip shielding.,” *Mater. Sci. Eng.*, vol. A103, pp. 15–28, 1988.

[23] L. P. Pook, *Crack Paths*. Southampton, Boston: WIT Press, 2002.

[24] M. Janssen, J. Zuidema, and R. Wanhill, *Fracture Mechanics*. Delft: VSSD, 2006.

[25] Y. Murakami, *Stress intensity factors handbook: Volume 1*. Elsevier Science Limited, 1987.

CHAPTER 8: DISCUSSION, CONCLUSION AND FUTURE RESEARCH

8.1 DISCUSSION

Lamb waves is the non-destructive technique used to determine the presence of cracks in a tie rod. The behaviour of Lamb waves in tie rods was successfully modelled. The cut-off frequency for a tie rod was determined to be 20.1 kHz on average. Usually, this would be the frequency above which higher wave modes are being introduced. However, the array transducer used can only sense mode 1, 2 and 7 and higher. The effective cut-off frequency is thus moved from that of the fourth mode to that of the seventh mode, increasing the cut-off frequency to 31.5 kHz.

The measurements done using Lamb waves can already be improved by using optimal settings of the ultrasonic tomograph MIRA. The best results were found for a combination of 25 kHz and 4 cycles. The determination of the position of the possible crack in the obtained signal is best done using the Akaike Information Criterion (AIC). Further improvement can be obtained by applying signal processing techniques to increase the quality of the signals. Basic techniques are the overlapping of measured signals and applying the envelope of the signal using the Hilbert transform. The next step is to develop advanced processing techniques to improve the quality of the signal further. The main investigated technique is the dispersion compensation. The application of this technique still needs extra attention, due to flaws in the numerical implementation.

Lamb waves is found to be an optimal non-destructive technique to use on-site. This is due to the compactness of this technique and to the possibility to analyse the data afterwards, making the time spend on-site using this technique little. The ultimate goal would not just be to find cracks, but also to be able to find their accurate position and to get a first approximation of their sizes. However, at this stage eddy current testing must be used for the localization of the cracks and active infrared thermography for the determination of the crack size.

A second non-destructive technique that is considered is eddy current testing (ECT), which can localize the crack in the tie rod. The main obstacle for using eddy current testing is the compatibility of the probes for the tie rods, because of the heterogeneous character of wrought iron and the rod's rough surface. A commercial low frequency eddy current probe has been used, but this probe is still sensitive to the rough surface and its penetration depth is quite low. Therefore, two customized probes are developed. The U-probe is the customized probe with the most potential and is based on the remote field testing technique. The possibility to adjust the distance between the two coils leads to a better probe handling, because the size of the probe can be adapted to the size of the tie rod. The change in distance between the two coils also gives the opportunity to choose specific penetration depths. This probe has been used for on-site testing on the lateral face of the tie rod. Using this probe, multiple possible cracks were identified. If it is possible to verify these findings by coinciding signals found using Lamb waves or active infrared thermography, the existence of these cracks can be proven.

Using eddy current testing, the position of the cracks along the tie rod can be determined. However, the severity and geometry of the crack cannot be concluded from these measurements. No proper calibration of the U-probe is possible yet. If the probe is able to be calibrated for the tie rods, also the severity of the crack size can be estimated. This could be favourable, because eddy current testing is compact and easy to use on-site. However, currently active infrared thermography is needed to determine the severity and the geometry of the crack.

Active infrared thermography is utilized to reveal the crack geometry. First numerical modelling is done to establish the best approach for the experimental tests and their data analysis. The time at which the maximum temperature is reached for each position gives the most precise information about the crack size. However, the embedded crack tip itself is still difficult to distinguish, due to the redistribution of heat along the longitudinal direction. This phenomenon is already reduced by thermally isolating the top and bottom of the tie rod. The redistribution needs to be further decreased, to be able to distinguish the crack tip with more precision.

Fracture mechanical testing has been done, based on linear elastic fracture mechanics (LEFM) and elastic-plastic fracture mechanics (EPFM). The fracture toughness values determined by LEFM were not valid, because too much plasticity was involved. Therefore, J-integral testing has been done, which is based on EPFM. The average value of K_{Ic} is 48.0 MPa√m, determined using ASTM code E1820-11. The second fracture mechanical aspect of is fatigue. The threshold stress intensity range (ΔK_{th}) is 5.6 MPa√m. The average constants of the Paris' equation, C_1 and C_2, are respectively $3.26*10^{-11}$ (MPa√m)^C_2 and 3.44. These values may deviate slightly from the real values, because the ASTM code E647-15 was not followed strictly. SEM images were made of the fracture surfaces of the test specimen. These images show that, at relatively low stress levels, microcracking occurs around inclusions in the sample. These microcracks can be caused by a low interface strength between the inclusions and the wrought iron matrix.

The noteworthy result is the linear relationship between the J-integral and the crack extension and the big difference between J_{Ic} and J_{max}. This phenomenon is probably caused by a constant damage build up in the test specimen, due to the microcracking found around the inclusions. Other recurring observations are pop-ins, also probably due to the inclusions present in the material. If the crack tip reaches the inclusion, the load needed for crack extension suddenly drops and this causes the pop-ins. The influence of the inclusions on the overall mechanical behaviour of the material is unknown.

The fracture mechanical testing done until now was focused on mode I failure. The inclined nature of the crack contains also a mode II component. Only mode I is included in the failure assessment. This is done not only because of lack of mixed mode testing, but also to simplify the problem while keeping the results conservative. Also a 2D-body has been assumed. These simplifications are used to approximate the threshold crack size for cyclic loading and the critical crack size for monotonic loading. The value for the fracture toughness is used to determine the load capacity of the tie rods. An edge crack is the least safe configuration of the crack. The tensile stress acting on the tie rods in the Duomo is between 0-140 MPa. At the maximum applied tensile stress of 140 MPa, the critical crack size for an edge crack is 8.4 mm. From this size, monotonic loading could lead to crack growth and failure of the structural element. The seasonal temperature variation during a year causes variation in tensile stress acting on the tie rods, leading to fatigue. The threshold crack length for an edge crack in a tie rod, the most dangerous configuration, is 4.2 mm.

Using the threshold and critical crack size, a fatigue life prediction can be made. The fatigue life prediction of an edge crack is $1.8*10^5$ cycles. This prediction assumes that the crack grows due to fatigue from the threshold crack size to the critical crack size. These crack sizes are thus of importance for the search for cracks using non-destructive testing. It should be possible to find cracks with the dimensions of the threshold crack size. At this size it is not yet necessary to find the exact crack geometry, because this situation will not lead to immediate failure of the tie rod. However, monitoring of cracks, having sizes between the threshold crack size and the critical crack size, should be done. The exact crack geometry becomes important when approaching the critical crack size. At this crack size, the exact crack geometry should be known to make a good estimation of the structural safety of the tie rod. Therefore, a fast technique, like Lamb waves or eddy current testing,

should be employed to find cracks with the dimensions of the threshold crack. While, infrared thermography should be used for cracks reaching the critical crack size to be able to precisely determine the crack geometry and to establish the structural safety of the element.

8.2 CONCLUSION

Different non-destructive techniques have been analysed to find and to investigate cracks in the historical tie rods of the Duomo di Milano. The fracture mechanical behaviour of wrought iron was examined and the resulting crack sizes of interest have been found. The combination of these two parts gives a basis for the structural assessment of the tie rods.

Lamb waves (Chapter 4):

1. The cut-off frequency was determined to be 20.1 kHz for an average tie rod.
2. The array transducer used can only sense mode 1, 2 and 7 and higher, making the effective cut-off frequency 31.5 kHz.
3. Optimal settings of a diagnostic pulsed emitted by the ultrasonic tomograph MIRA are 25 kHz and 4 cycles.
4. The Akaike Information Criterion (AIC), applied before post-processing, is best suited for the determination of the position of a crack.

Eddy current testing (Chapter 5):

5. The low-frequency probe can be used for the detection of welds and their geometry, but is not time effective.
6. Two customized probes have been developed: the U-probe (vertical face) and the pancake probe (horizontal face).
7. Employing the U-probe on-site, a good analysis can be made of the location of possible cracks. Three possible cracks have been found in tie rod 41-11.

Active infrared thermography (Chapter 6):

8. The exact position of the crack can be determined using pulsed thermography. However, only a first estimate can be made with respect to the crack geometry.
9. The current experimental set-up cannot yet be applied on-site.

Fracture mechanics (Chapter 7):

10. The average value of K_{Ic} is 48.0 MPa√m, determined using ASTM code E1820-11.
11. Stress intensity factor range (ΔK_{th}) is 5.6 MPa√m. The average constants of the Paris' equation, C_1 and C_2, are respectively $3.26*10^{-11}$ (MPa√m)^C_2 and 3.44. ASTM code E647-15 was employed, but not followed strictly. Therefore, some deviation from the obtained values is possible.
12. Microcracking was observed around inclusions in SEM images of the fracture surfaces after fatigue testing.
13. The critical crack size for an edge crack is 8.4 mm, at the maximum applied tensile stress of 140 MPa.
14. The threshold crack length for an edge crack is 4.2 mm, due to fatigue caused by seasonal temperature changes.
15. The fatigue life prediction of an edge crack configuration is $1.8*10^5$ cycles.

8.3 Future Research

Lamb waves (Chapter 4):

1. Studying the interaction between Lamb waves and inclined cracks.
2. Examine signal processing techniques that include mode conversion introduced by the inclined nature of the crack.
3. Optimize the sequence of applying processing techniques, to reduce loss of information present in the signal.
4. Use new promising techniques like mode extraction using 2D-FFT [1].

Eddy current testing (Chapter 5):

5. A proper calibration block is needed to be able to calibrate all probes, including the effects from the rough surface.
6. The design of the customized probes need to be improved, i.e. by adding magnetic shielding.

Active infrared thermography (Chapter 6):

7. Find solutions to reduce redistribution of heat in the longitudinal direction.
8. Compact the experimental set-up to facilitate testing on-site.

Fracture mechanics (Chapter 7):

9. Perform fracture toughness testing in mixed mode conditions, for a crack under an angle of 27^{o}.
10. Imaging of the fracture surface to gain more understanding about how the material fails and what the influence is of the inclusions on the crack propagation.
11. Increasing the complexity of the crack geometry used for the failure assessment, by taking into account the inclined nature of the crack and the presence of the crack in a 3D body.
12. Analysing other sources of fatigue, like: vibrations due to traffic. The stress variations can be measured by using, i.e., strain gauges.

Additional:

13. Further on-site research to examine the current state of the tie rods, including an overview of cracks in the tie rods in combination with their applied tensile stress.
14. Materials research on the difference between the bulk material and the weld material, with the focus on the mechanical properties to confirm that the welds are the weak link.

Ultimately the points above lead to the main focus of achieving a precise failure assessment of cracks present in the tie rods in the Duomo.

8.4 REFERENCES

[1] T. HAYASHI and K. KAWASHIMA, “Single Mode Extraction from Multiple Modes of Lamb Wave and Its Application to Defect Detection,” *JSME Int. J. Ser. A Solid Mech. Mater. Eng.*, vol. 46, no. 4, pp. 620–626, 2003.

APPENDIX A: ELEMENTS OF THE MATRICES, EQUATION (4.26)

$$\boldsymbol{A_{11}^{j,p,m,n}} = \left[C_{55}\frac{\partial^2 U}{\partial z^2} - k^2 C_{11} U\right] I(y,z) + C_{55}\frac{\partial U}{\partial z}\frac{\partial I(y,z)}{\partial z} + C_{66}\frac{\partial U}{\partial y}\frac{\partial I(y,z)}{\partial y}$$

$$\boldsymbol{A_{12}^{j,p,m,n}} = ik(C_{12} + C_{66})\frac{\partial V}{\partial y} I(y,z) + C_{66} ikV \frac{\partial I(y,z)}{\partial y}$$

$$\boldsymbol{A_{13}^{j,p,m,n}} = ik(C_{13} + C_{55})\frac{\partial W}{\partial z} I(y,z) I(y,z) + C_{55} ikW \frac{\partial I(y,z)}{\partial z}$$

$$\boldsymbol{A_{21}^{j,p,m,n}} = ik(C_{12} + C_{66})\frac{\partial U}{\partial y} I(y,z) + ikC_{12} U \frac{\partial I(y,z)}{\partial y}$$

$$\boldsymbol{A_{22}^{j,p,m,n}} = \left[C_{44}\frac{\partial^2 V}{\partial z^2} - k^2 C_{66} V + C_{22}\frac{\partial^2 V}{\partial y^2}\right] I(y,z) + C_{44}\frac{\partial V}{\partial z}\frac{\partial I(y,z)}{\partial z} + C_{22}\frac{\partial V}{\partial y}\frac{\partial I(y,z)}{\partial y}$$

$$\boldsymbol{A_{23}^{j,p,m,n}} = (C_{23} + C_{44})\frac{\partial^2 W}{\partial y \partial z} I(y,z) + C_{44}\frac{\partial W}{\partial y}\frac{\partial I(y,z)}{\partial z} + C_{23}\frac{\partial W}{\partial z}\frac{\partial I(y,z)}{\partial y}$$

$$\boldsymbol{A_{31}^{j,p,m,n}} = ik(C_{13} + C_{55})\frac{\partial U}{\partial z} I(y,z) + ikC_{13} U \frac{\partial I(y,z)}{\partial z}$$

$$\boldsymbol{A_{32}^{j,p,m,n}} = (C_{23} + C_{44})\frac{\partial^2 V}{\partial y \partial z} I(y,z) + C_{23}\frac{\partial V}{\partial y}\frac{\partial I(y,z)}{\partial z} + C_{44}\frac{\partial V}{\partial z}\frac{\partial I(y,z)}{\partial y}$$

$$\boldsymbol{A_{33}^{j,p,m,n}} = \left[C_{33}\frac{\partial^2 W}{\partial z^2} - k^2 C_{55} W + C_{44}\frac{\partial^2 W}{\partial y^2}\right] I(y,z) + C_{33}\frac{\partial W}{\partial z}\frac{\partial I(y,z)}{\partial z}\frac{\partial I(y,z)}{\partial z} + C_{44}\frac{\partial W}{\partial y}\frac{\partial I(y,z)}{\partial y}$$

$$\boldsymbol{M_{j,p,m,n}} = -\rho\omega^2 I(y,z)\begin{bmatrix} U \\ V \\ W \end{bmatrix}$$

APPENDIX B: MATLAB CODE, DETERMINATION DISPERSION CURVES

Elastic constant

```
poisson=0.30;

C=(1/((1+poisson)*(1-2*poisson)))*[1-poisson poisson poisson 0 0 0;poisson 1-poisson poisson 0
0 0;poisson poisson 1-poisson 0 0 0;0 0 0 1/2-poisson 0 0;0 0 0 0 1/2-poisson 0; 0 0 0 0 0
1/2-poisson];
```

Legendre polynomials

```
syms y z

% Legendre polynomial and their derivatives as a function of y or z
Py=[ 1, y, (3*y^2)/2 - 1/2, (5*y^3)/2 - (3*y)/2, (35*y^4)/8 - (15*y^2)/4 + 3/8, (63*y^5)/8 -
(35*y^3)/4 + (15*y)/8, (231*y^6)/16 - (315*y^4)/16 + (105*y^2)/16 - 5/16, (429*y^7)/16 -
(693*y^5)/16 + (315*y^3)/16 - (35*y)/16, (6435*y^8)/128 - (3003*y^6)/32 + (3465*y^4)/64 -
(315*y^2)/32 + 35/128, (12155*y^9)/128 - (6435*y^7)/32 + (9009*y^5)/64 - (1155*y^3)/32 +
(315*y)/128, (46189*y^10)/256 - (109395*y^8)/256 + (45045*y^6)/128 - (15015*y^4)/128 +
(3465*y^2)/256 - 63/256];
Pz=[ 1, z, (3*z^2)/2 - 1/2, (5*z^3)/2 - (3*z)/2, (35*z^4)/8 - (15*z^2)/4 + 3/8, (63*z^5)/8 -
(35*z^3)/4 + (15*z)/8, (231*z^6)/16 - (315*z^4)/16 + (105*z^2)/16 - 5/16, (429*z^7)/16 -
(693*z^5)/16 + (315*z^3)/16 - (35*z)/16, (6435*z^8)/128 - (3003*z^6)/32 + (3465*z^4)/64 -
(315*z^2)/32 + 35/128, (12155*z^9)/128 - (6435*z^7)/32 + (9009*z^5)/64 - (1155*z^3)/32 +
(315*z)/128, (46189*z^10)/256 - (109395*z^8)/256 + (45045*z^6)/128 - (15015*z^4)/128 +
(3465*z^2)/256 - 63/256];

P1y=[ 0, 1, 3*y, (15*y^2)/2 - 3/2, (35*y^3)/2 - (15*y)/2, (315*y^4)/8 - (105*y^2)/4 + 15/8,
(693*y^5)/8 - (315*y^3)/4 + (105*y)/8, (3003*y^6)/16 - (3465*y^4)/16 + (945*y^2)/16 - 35/16,
(6435*y^7)/16 - (9009*y^5)/16 + (3465*y^3)/16 - (315*y)/16, (109395*y^8)/128 - (45045*y^6)/32
+ (45045*y^4)/64 - (3465*y^2)/32 + 315/128, (230945*y^9)/128 - (109395*y^7)/32 +
(135135*y^5)/64 - (15015*y^3)/32 + (3465*y)/128];
P1z=[ 0, 1, 3*z, (15*z^2)/2 - 3/2, (35*z^3)/2 - (15*z)/2, (315*z^4)/8 - (105*z^2)/4 + 15/8,
(693*z^5)/8 - (315*z^3)/4 + (105*z)/8, (3003*z^6)/16 - (3465*z^4)/16 + (945*z^2)/16 - 35/16,
(6435*z^7)/16 - (9009*z^5)/16 + (3465*z^3)/16 - (315*z)/16, (109395*z^8)/128 - (45045*z^6)/32
+ (45045*z^4)/64 - (3465*z^2)/32 + 315/128, (230945*z^9)/128 - (109395*z^7)/32 +
(135135*z^5)/64 - (15015*z^3)/32 + (3465*z)/128];

P2y=[ 0, 0, 3, 15*y, (105*y^2)/2 - 15/2, (315*y^3)/2 - (105*y)/2,(3465*y^4)/8 - (945*y^2)/4 +
105/8, (9009*y^5)/8 - (3465*y^3)/4 + (945*y)/8, (45045*y^6)/16 - (45045*y^4)/16 +
(10395*y^2)/16 - 315/16, (109395*y^7)/16 - (135135*y^5)/16 + (45045*y^3)/16 - (3465*y)/16,
(2078505*y^8)/128 - (765765*y^6)/32 + (675675*y^4)/64 - (45045*y^2)/32 + 3465/128];
P2z=[ 0, 0, 3, 15*z, (105*z^2)/2 - 15/2, (315*z^3)/2 - (105*z)/2, (3465*z^4)/8 - (945*z^2)/4 +
105/8, (9009*z^5)/8 - (3465*z^3)/4 + (945*z)/8, (45045*z^6)/16 - (45045*z^4)/16 +
(10395*z^2)/16 - 315/16, (109395*z^7)/16 - (135135*z^5)/16 + (45045*z^3)/16 - (3465*z)/16,
(2078505*z^8)/128 - (765765*z^6)/32 + (675675*z^4)/64 - (45045*z^2)/32 + 3465/128];

% Legendre polynomials and their derivatives at -1 and at 1, this is both for y and z the same
Pm1 = [1, -1, 1, -1, 1, -1, 1, -1, 1, -1, 1];
Pp1 = [1, 1, 1, 1, 1, 1, 1, 1, 1, 1, 1];
P0 = [1.0000, 0, -0.5000, 0, 0.3750, 0, -0.3125, 0, 0.2734, 0, -0.2461];
P1m1 = [0, 1, -3, 6, -10, 15, -21, 28, -36, 45, -55];
P1p1 = [0, 1, 3, 6, 10, 15, 21, 28, 36, 45, 55];
```

Others

```
% dimensions
r=0.06/0.09;

% material
E=2*10^11;
rho=7850;
omega0=sqrt(E/rho);

% nth polynomial
N=7;
M=7;
s=0:1:N*M-1;
t=0:1:N*M-1;
```

A11

```
A11k=zeros(N^2-1);
A11a=zeros(N^2-1);
A11b=zeros(N^2-1);
A11c=zeros(N^2-1);
A11d=zeros(N^2-1);

% A11k
for T=t(2):t(end)+1;
for S=s(2):s(end)+1;
    mm=floor((T+N-1)/N);
    nn=mod(T+N-1,N)+1;
    jj=floor((S+N-1)/N);
    pp=mod(S+N-1,N)+1;
    m=mm-1;
    n=nn-1;
    J=jj-1;
    p=pp-1;
if nn==pp && mm==jj;
    A11k(S,T)=-1*C(1,1);
end
end
end

% A11a
for T=t(2):t(end)+1;
for S=s(2):s(end)+1;
    mm=floor((T+N-1)/N);
    nn=mod(T+N-1,N)+1;
    jj=floor((S+N-1)/N);
    pp=mod(S+N-1,N)+1;
    m=mm-1;
    n=nn-1;
    J=jj-1;
    p=pp-1;
if nn==pp && mod(jj-mm,2)==0;
    A11a(S,T)=(2*r^2*C(5,5)*sqrt((2*J+1)*(2*m+1)))*int(Pz(jj)*P2z(mm),z,-1,1);
end
end
end
```

```
% A11b
for T=t(2):t(end)+1;
for S=s(2):s(end)+1;
    mm=floor((T+N-1)/N);
    nn=mod(T+N-1,N)+1;
    jj=floor((S+N-1)/N);
    pp=mod(S+N-1,N)+1;
    m=mm-1;
    n=nn-1;
    J=jj-1;
    p=pp-1;
if jj==mm && mod(pp-nn,2)==0;
    A11b(S,T)=(2*C(6,6)*sqrt((2*p+1)*(2*n+1)))*int(Py(pp)*P2y(nn),y,-1,1);
end
end
end

% A11c
for T=t(2):t(end)+1;
for S=s(2):s(end)+1;
    mm=floor((T+N-1)/N);
    nn=mod(T+N-1,N)+1;
    jj=floor((S+N-1)/N);
    pp=mod(S+N-1,N)+1;
    m=mm-1;
    n=nn-1;
    J=jj-1;
    p=pp-1;
if nn==pp && mod(jj-mm,2)==0;
    A11c(S,T)=(2*r^2*C(5,5)*sqrt((2*J+1)*(2*m+1)))*(Pm1(jj)*P1m1(mm)-Pp1(jj)*P1p1(mm));
end
end
end

% A11d
for T=t(2):t(end)+1;
for S=s(2):s(end)+1;
    mm=floor((T+N-1)/N);
    nn=mod(T+N-1,N)+1;
    jj=floor((S+N-1)/N);
    pp=mod(S+N-1,N)+1;
    m=mm-1;
    n=nn-1;
    J=jj-1;
    p=pp-1;
if jj==mm && mod(pp-nn,2)==0;
    A11d(S,T)=(2*C(6,6)*sqrt((2*p+1)*(2*n+1)))*(Pm1(pp)*P1m1(nn)-Pp1(pp)*P1p1(nn));
end
end
end
```

A12

```
A12a=zeros(N^2-1);
A12b=zeros(N^2-1);
```

```
% A12a
for T=t(2):t(end)+1;
for S=s(2):s(end)+1;
    mm=floor((T+N-1)/N);
    nn=mod(T+N-1,N)+1;
    jj=floor((S+N-1)/N);
    pp=mod(S+N-1,N)+1;
    m=mm-1;
    n=nn-1;
    J=jj-1;
    p=pp-1;
if mod(pp-nn,2)~=0 && mm==jj;
    A12a(S,T)=(C(1,2)+C(6,6))*sqrt((2*p+1)*(2*n+1))*int(Py(pp)*P1y(nn),y,-1,1);
end
end
end

%A12b
for T=t(2):t(end)+1;
for S=s(2):s(end)+1;
    mm=floor((T+N-1)/N);
    nn=mod(T+N-1,N)+1;
    jj=floor((S+N-1)/N);
    pp=mod(S+N-1,N)+1;
    m=mm-1;
    n=nn-1;
    J=jj-1;
    p=pp-1;
if jj==mm && mod(pp-nn,2)~=0;
    A12b(S,T)=(C(6,6)*sqrt((2*p+1)*(2*n+1)))*(Pm1(pp)*Pm1(nn)-Pp1(pp)*Pp1(nn));
end
end
end
```

A13

```
A13a=zeros(N^2-1);
A13b=zeros(N^2-1);

% A13a
for T=t(2):t(end)+1;
for S=s(2):s(end)+1;
    mm=floor((T+N-1)/N);
    nn=mod(T+N-1,N)+1;
    jj=floor((S+N-1)/N);
    pp=mod(S+N-1,N)+1;
    m=mm-1;
    n=nn-1;
    J=jj-1;
    p=pp-1;
if mod(jj-mm,2)~=0 && nn==pp;
    A13a(S,T)=r*(C(1,3)+C(5,5))*sqrt((2*J+1)*(2*m+1))*int(Pz(jj)*P1z(mm),z,-1,1);
end
end
end

% A13b
```

```
for T=t(2):t(end)+1;
for S=s(2):s(end)+1;
    mm=floor((T+N-1)/N);
    nn=mod(T+N-1,N)+1;
    jj=floor((S+N-1)/N);
    pp=mod(S+N-1,N)+1;
    m=mm-1;
    n=nn-1;
    J=jj-1;
    p=pp-1;
if mod(jj-mm,2)~=0 && nn==pp;
    A13b(S,T)=r*(C(5,5)*sqrt((2*J+1)*(2*m+1)))*(Pm1(jj)*Pm1(mm)-Pp1(jj)*Pp1(mm));
end
end
end
```

A21

```
A21a=zeros(N^2-1);
A21b=zeros(N^2-1);

% A21a
for T=t(2):t(end)+1;
for S=s(2):s(end)+1;
    mm=floor((T+N-1)/N);
    nn=mod(T+N-1,N)+1;
    jj=floor((S+N-1)/N);
    pp=mod(S+N-1,N)+1;
    m=mm-1;
    n=nn-1;
    J=jj-1;
    p=pp-1;
if mod(pp-nn,2)~=0 && mm==jj;
    A21a(S,T)=(C(1,2)+C(6,6))*sqrt((2*p+1)*(2*n+1))*int(Py(pp)*P1y(nn),y,-1,1);
end
end
end

% A21b
for T=t(2):t(end)+1;
for S=s(2):s(end)+1;
    mm=floor((T+N-1)/N);
    nn=mod(T+N-1,N)+1;
    jj=floor((S+N-1)/N);
    pp=mod(S+N-1,N)+1;
    m=mm-1;
    n=nn-1;
    J=jj-1;
    p=pp-1;
if jj==mm && mod(pp-nn,2)~=0;
    A21b(S,T)=(C(1,2)*sqrt((2*p+1)*(2*n+1)))*(Pm1(pp)*Pm1(nn)-Pp1(pp)*Pp1(nn));
end
end
end
```

A22

```
A22k=zeros(N^2-1);
A22a=zeros(N^2-1);
A22b=zeros(N^2-1);
A22c=zeros(N^2-1);
A22d=zeros(N^2-1);

% A22k
for T=t(2):t(end)+1;
for S=s(2):s(end)+1;
    mm=floor((T+N-1)/N);
    nn=mod(T+N-1,N)+1;
    jj=floor((S+N-1)/N);
    pp=mod(S+N-1,N)+1;
    m=mm-1;
    n=nn-1;
    J=jj-1;
    p=pp-1;
if nn==pp && mm==jj;
    A22k(S,T)=-1*C(6,6);
end
end
end

% A22a
for T=t(2):t(end)+1;
for S=s(2):s(end)+1;
    mm=floor((T+N-1)/N);
    nn=mod(T+N-1,N)+1;
    jj=floor((S+N-1)/N);
    pp=mod(S+N-1,N)+1;
    m=mm-1;
    n=nn-1;
    J=jj-1;
    p=pp-1;
if nn==pp && mod(jj-mm,2)==0;
    A22a(S,T)=(2*r^2*C(4,4)*sqrt((2*J+1)*(2*m+1)))*int(Pz(jj)*P2z(mm),z,-1,1);
end
end
end

% A22b
for T=t(2):t(end)+1;
for S=s(2):s(end)+1;
    mm=floor((T+N-1)/N);
    nn=mod(T+N-1,N)+1;
    jj=floor((S+N-1)/N);
    pp=mod(S+N-1,N)+1;
    m=mm-1;
    n=nn-1;
    J=jj-1;
    p=pp-1;
if jj==mm && mod(pp-nn,2)==0;
    A22b(S,T)=(2*C(2,2)*sqrt((2*p+1)*(2*n+1)))*int(Py(pp)*P2y(nn),y,-1,1);
end
end
```

```
end

% A22c
for T=t(2):t(end)+1;
for S=s(2):s(end)+1;
    mm=floor((T+N-1)/N);
    nn=mod(T+N-1,N)+1;
    jj=floor((S+N-1)/N);
    pp=mod(S+N-1,N)+1;
    m=mm-1;
    n=nn-1;
    J=jj-1;
    p=pp-1;
if nn==pp && mod(jj-mm,2)==0;
    A22c(S,T)=(2*r^2*C(4,4)*sqrt((2*J+1)*(2*m+1)))*(Pm1(jj)*P1m1(mm)-Pp1(jj)*P1p1(mm));
end
end
end

% A22d
for T=t(2):t(end)+1;
for S=s(2):s(end)+1;
    mm=floor((T+N-1)/N);
    nn=mod(T+N-1,N)+1;
    jj=floor((S+N-1)/N);
    pp=mod(S+N-1,N)+1;
    m=mm-1;
    n=nn-1;
    J=jj-1;
    p=pp-1;
if jj==mm && mod(pp-nn,2)==0;
    A22d(S,T)=(2*C(2,2)*sqrt((2*p+1)*(2*n+1)))*(Pm1(pp)*P1m1(nn)-Pp1(pp)*P1p1(nn));
end
end
end
```

A23

```
A23a=zeros(N^2-1);
A23b=zeros(N^2-1);
A23c=zeros(N^2-1);

% A23a
for T=t(2):t(end)+1;
for S=s(2):s(end)+1;
    mm=floor((T+N-1)/N);
    nn=mod(T+N-1,N)+1;
    jj=floor((S+N-1)/N);
    pp=mod(S+N-1,N)+1;
    m=mm-1;
    n=nn-1;
    J=jj-1;
    p=pp-1;
if mod(pp-nn,2)~=0 && mod(jj-mm,2)~=0;

A23a(S,T)=r*(C(2,3)+C(4,4))*sqrt((2*J+1)*(2*m+1)*(2*n+1)*(2*p+1))*int(int(Pz(jj)*P1z(mm)*Py(pp
)*P1y(nn),z,-1,1),y,-1,1);
```

```
end
end
end

% A23b
for T=t(2):t(end)+1;
for S=s(2):s(end)+1;
    mm=floor((T+N-1)/N);
    nn=mod(T+N-1,N)+1;
    jj=floor((S+N-1)/N);
    pp=mod(S+N-1,N)+1;
    m=mm-1;
    n=nn-1;
    J=jj-1;
    p=pp-1;
if mod(pp-nn,2)~=0 && mod(jj-mm,2)~=0;
    A23b(S,T)=r*C(4,4)*sqrt((2*J+1)*(2*m+1)*(2*n+1)*(2*p+1))*(Pm1(mm)*Pm1(jj)-
Pp1(mm)*Pp1(jj))*int(Py(pp)*P1y(nn),y,-1,1);
end
end
end

% A23c
for T=t(2):t(end)+1;
for S=s(2):s(end)+1;
    mm=floor((T+N-1)/N);
    nn=mod(T+N-1,N)+1;
    jj=floor((S+N-1)/N);
    pp=mod(S+N-1,N)+1;
    m=mm-1;
    n=nn-1;
    J=jj-1;
    p=pp-1;
if mod(pp-nn,2)~=0 && mod(jj-mm,2)~=0;
    A23c(S,T)=r*C(2,3)*sqrt((2*J+1)*(2*m+1)*(2*n+1)*(2*p+1))*(Pm1(nn)*Pm1(pp)-
Pp1(nn)*Pp1(pp))*int(Pz(jj)*P1z(mm),z,-1,1);
end
end
end
```

A31

```
A31a=zeros(N^2-1);
A31b=zeros(N^2-1);

% A31a
for T=t(2):t(end)+1;
for S=s(2):s(end)+1;
    mm=floor((T+N-1)/N);
    nn=mod(T+N-1,N)+1;
    jj=floor((S+N-1)/N);
    pp=mod(S+N-1,N)+1;
    m=mm-1;
    n=nn-1;
    J=jj-1;
    p=pp-1;
if mod(jj-mm,2)~=0 && pp==nn;
```

```
    A31a(S,T)=r*(C(1,3)+C(5,5))*sqrt((2*J+1)*(2*m+1))*int(Pz(jj)*P1z(mm),z,-1,1);
end
end
end

% A31b
for T=t(2):t(end)+1;
for S=s(2):s(end)+1;
    mm=floor((T+N-1)/N);
    nn=mod(T+N-1,N)+1;
    jj=floor((S+N-1)/N);
    pp=mod(S+N-1,N)+1;
    m=mm-1;
    n=nn-1;
    J=jj-1;
    p=pp-1;
if pp==nn && mod(jj-mm,2)~=0;
    A31b(S,T)=r*(C(1,3)*sqrt((2*J+1)*(2*m+1)))*(Pm1(jj)*Pm1(mm)-Pp1(jj)*Pp1(mm));
end
end
end
```

A32

```
A32a=zeros(N^2-1);
A32b=zeros(N^2-1);
A32c=zeros(N^2-1);

% A32a
for T=t(2):t(end)+1;
for S=s(2):s(end)+1;
    mm=floor((T+N-1)/N);
    nn=mod(T+N-1,N)+1;
    jj=floor((S+N-1)/N);
    pp=mod(S+N-1,N)+1;
    m=mm-1;
    n=nn-1;
    J=jj-1;
    p=pp-1;
if mod(pp-nn,2)~=0 && mod(jj-mm,2)~=0;

A32a(S,T)=r*(C(2,3)+C(4,4))*sqrt((2*J+1)*(2*m+1)*(2*n+1)*(2*p+1))*int(int(Pz(jj)*P1z(mm)*Py(pp
)*P1y(nn),z,-1,1),y,-1,1);
end
end
end

% A32b
for T=t(2):t(end)+1;
for S=s(2):s(end)+1;
    mm=floor((T+N-1)/N);
    nn=mod(T+N-1,N)+1;
    jj=floor((S+N-1)/N);
    pp=mod(S+N-1,N)+1;
    m=mm-1;
    n=nn-1;
    J=jj-1;
```

```
    p=pp-1;
if mod(pp-nn,2)~=0 && mod(jj-mm,2)~=0;
    A32b(S,T)=r*C(2,3)*sqrt((2*J+1)*(2*m+1)*(2*n+1)*(2*p+1))*(Pm1(mm)*Pm1(jj)-
Pp1(mm)*Pp1(jj))*int(Py(pp)*P1y(nn),y,-1,1);
end
end
end

% A32c
for T=t(2):t(end)+1;
for S=s(2):s(end)+1;
    mm=floor((T+N-1)/N);
    nn=mod(T+N-1,N)+1;
    jj=floor((S+N-1)/N);
    pp=mod(S+N-1,N)+1;
    m=mm-1;
    n=nn-1;
    J=jj-1;
    p=pp-1;
if mod(pp-nn,2)~=0 && mod(jj-mm,2)~=0;
    A32c(S,T)=r*C(4,4)*sqrt((2*J+1)*(2*m+1)*(2*n+1)*(2*p+1))*(Pm1(nn)*Pm1(pp)-
Pp1(nn)*Pp1(pp))*int(Pz(jj)*P1z(mm),z,-1,1);
end
end
end
```

A33

```
A33k=zeros(N^2-1);
A33a=zeros(N^2-1);
A33b=zeros(N^2-1);
A33c=zeros(N^2-1);
A33d=zeros(N^2-1);

% A33k
for T=t(2):t(end)+1;
for S=s(2):s(end)+1;
    mm=floor((T+N-1)/N);
    nn=mod(T+N-1,N)+1;
    jj=floor((S+N-1)/N);
    pp=mod(S+N-1,N)+1;
    m=mm-1;
    n=nn-1;
    J=jj-1;
    p=pp-1;
if nn==pp && mm==jj;
    A33k(S,T)=-1*C(5,5);
end
end
end

% A33a
for T=t(2):t(end)+1;
for S=s(2):s(end)+1;
    mm=floor((T+N-1)/N);
    nn=mod(T+N-1,N)+1;
    jj=floor((S+N-1)/N);
```

```
    pp=mod(S+N-1,N)+1;
    m=mm-1;
    n=nn-1;
    J=jj-1;
    p=pp-1;
if nn==pp && mod(jj-mm,2)==0;
    A33a(S,T)=(2*r^2*C(3,3)*sqrt((2*J+1)*(2*m+1)))*int(Pz(jj)*P2z(mm),z,-1,1);
end
end
end

% A33b
for T=t(2):t(end)+1;
for S=s(2):s(end)+1;
    mm=floor((T+N-1)/N);
    nn=mod(T+N-1,N)+1;
    jj=floor((S+N-1)/N);
    pp=mod(S+N-1,N)+1;
    m=mm-1;
    n=nn-1;
    J=jj-1;
    p=pp-1;
if jj==mm && mod(pp-nn,2)==0;
    A33b(S,T)=(2*C(4,4)*sqrt((2*p+1)*(2*n+1)))*int(Py(pp)*P2y(nn),y,-1,1);
end
end
end

% A33c
for T=t(2):t(end)+1;
for S=s(2):s(end)+1;
    mm=floor((T+N-1)/N);
    nn=mod(T+N-1,N)+1;
    jj=floor((S+N-1)/N);
    pp=mod(S+N-1,N)+1;
    m=mm-1;
    n=nn-1;
    J=jj-1;
    p=pp-1;
if nn==pp && mod(jj-mm,2)==0;
    A33c(S,T)=(2*r^2*C(3,3)*sqrt((2*J+1)*(2*m+1)))*(Pm1(jj)*P1m1(mm)-Pp1(jj)*P1p1(mm));
end
end
end

% A33d
for T=t(2):t(end)+1;
for S=s(2):s(end)+1;
    mm=floor((T+N-1)/N);
    nn=mod(T+N-1,N)+1;
    jj=floor((S+N-1)/N);
    pp=mod(S+N-1,N)+1;
    m=mm-1;
    n=nn-1;
    J=jj-1;
    p=pp-1;
if jj==mm && mod(pp-nn,2)==0;
    A33d(S,T)=(2*C(4,4)*sqrt((2*p+1)*(2*n+1)))*(Pm1(pp)*P1m1(nn)-Pp1(pp)*P1p1(nn));
```

```
end
end
end
```

Ma

```
Ma=zeros(N^2-1);

for T=t(2):t(end)+1;
for S=s(2):s(end)+1;
    mm=floor((T+N-1)/N);
    nn=mod(T+N-1,N)+1;
    jj=floor((S+N-1)/N);
    pp=mod(S+N-1,N)+1;
    m=mm-1;
    n=nn-1;
    J=jj-1;
    p=pp-1;
if nn==pp && mm==jj;
    Ma(S,T)=-1;
end
end
end

kref=0.2;
K=2:70;
kappa=K/5;
```

Final elements

```
% A11
A11ref=A11a+A11b+A11c+A11d+kref^2*A11k;

% A12
A12ref=1i*kref*(A12a+A12b);

% A13
A13ref=1i*kref*(A13a+A13b);

% A21
A21ref=1i*kref*(A21a+A21b);

% A22
A22ref=A22a+A22b+A22c+A22d+kref^2*A22k;

% A23
A23ref=A23a+A23b+A23c;

% A31
A31ref=1i*kref*(A31a+A31b);

% A32
A32ref=A32a+A32b+A32c;

% A33
A33ref=A33a+A33b+A33c+A33d+kref^2*A33k;
```

Concatenation of the matrices

```
Aref=[A11ref A12ref A13ref; A21ref A22ref A23ref; A31ref A32ref A33ref];
```

M

```
M0=zeros(N^2);
Mmref=[Ma M0 M0; M0 Ma M0; M0 M0 Ma];
```

Reference for sorting

```
Bref=(Aref*(Mmref^-1));

[vectorsref,Dref]=eig(Bref);
valuesref=eig(Bref);
valuesTref=transpose(valuesref);
refV1=transpose(sortrows(transpose([valuesTref; vectorsref])));
vref=transpose(refV1([1],[1:1:3*N*M]));
v=transpose(refV1([1],[1:1:3*N*M]));
refV=refV1([2:1:3*N*M+1],[1:1:3*N*M]);
```

Eigenvalue problem

```
for i=1:length(kappa);

% final elements
% A11
A11=A11a+A11b+A11c+A11d+kappa(i)^2*A11k;

% A12
A12=1i*kappa(i)*(A12a+A12b);

% A13
A13=1i*kappa(i)*(A13a+A13b);

% A21
A21=1i*kappa(i)*(A21a+A21b);

% A22
A22=A22a+A22b+A22c+A22d+kappa(i)^2*A22k;

% A23
A23=A23a+A23b+A23c;

% A31
A31=1i*kappa(i)*(A31a+A31b);

% A32
A32=A32a+A32b+A32c;

% A33
A33=A33a+A33b+A33c+A33d+kappa(i)^2*A33k;

% concatenation of the matrices

A=[A11 A12 A13; A21 A22 A23; A31 A32 A33];
```

```
% M
M0=zeros(N^2);
Mm=[Ma M0 M0; M0 Ma M0; M0 M0 Ma];

% Eigen
B=(A*(Mm^-1));

[vectors,D]=eig(B);
v=eig(B);
vectorsT=transpose(vectors);

msort=transpose(refV)*conj(vectors);
[rowvalue,columnnumber]=max(msort);
columnnumberT=transpose(columnnumber);

sorted=transpose(sortrows([columnnumberT v vectorsT]));

sortedv=sorted([2],[1:1:3*N*M]);
sortedV=sorted([3:1:3*N*M+2],[1:1:3*N*M]);

refV=sortedV;

vvalues(:,i)=real(sortedv);
end

vtotal=[vref vvalues];
```

Determination velocities (phase/group)

```
OMEGA=omega0*transpose(sqrt(vtotal));
kappac=repmat(transpose(kappa),1,3*N*M);
kappa1=repmat(transpose((1:70)/5),1,3*N*M);

hy=0.060; %hy=1 for normalized

C44=6.73*10^9;
E2=2*10^11;
C44=E2/(2*(1+poisson));
rho2=2*7850;
vt=sqrt((C44)/rho2); %vt=1 for normalized

%frequency
freq=(OMEGA/(2*pi*1000));
freq2=freq/hy;

% phase velocity
vp=(((freq./kappa1)*1000*2*pi)/sqrt((E*C(4,4))/rho)*vt)/1000;

% group velocity
vgm1=(diff(OMEGA)./diff(kappa1))/sqrt((E*C(4,4))/rho);
vg=[vgm1; vgm1(69,:)];
```

APPENDIX C: RESULTS J TESTING, FIRST CATEGORY

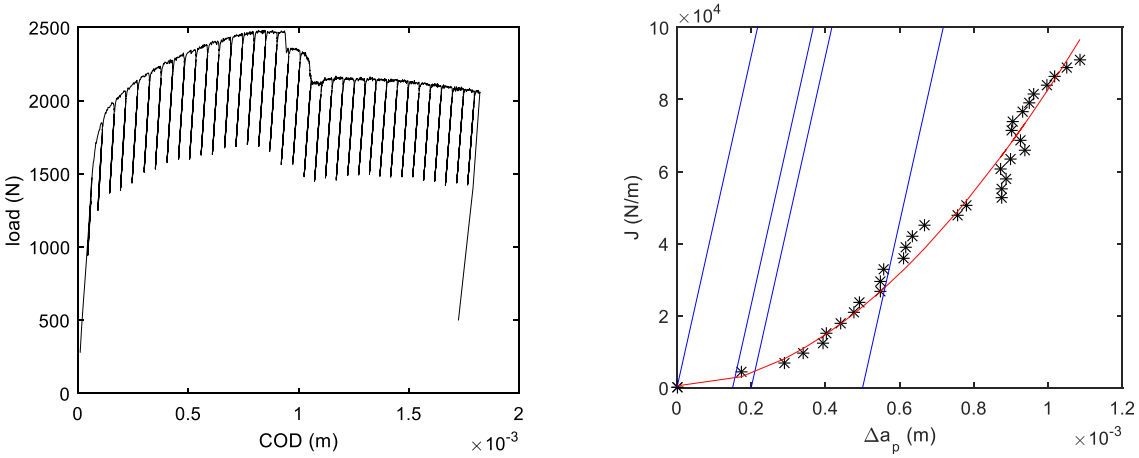

Figure C.1: Results for specimen W2: a) Load versus COD graph and b) J versus Δa_p.

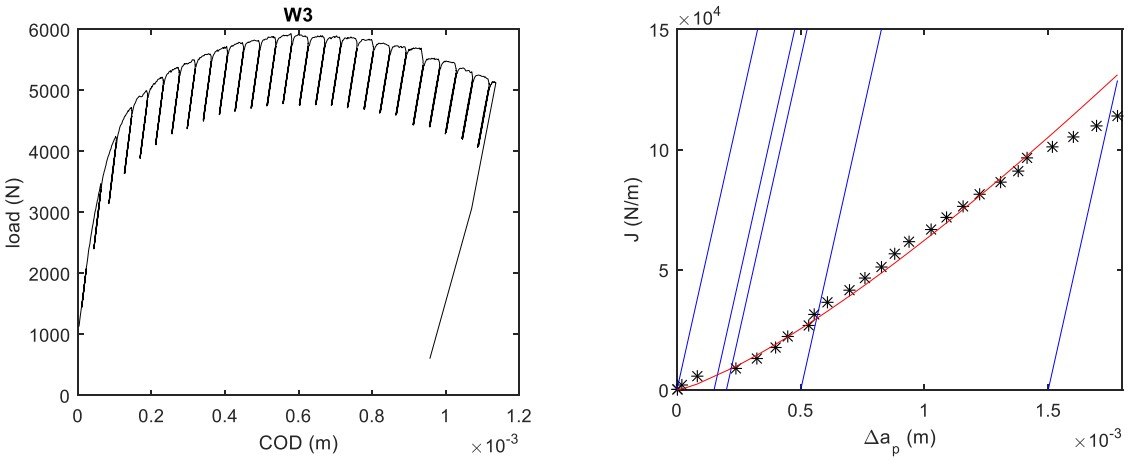

Figure C.2: Results for specimen W3: a) Load versus COD graph and b) J versus Δa_p.

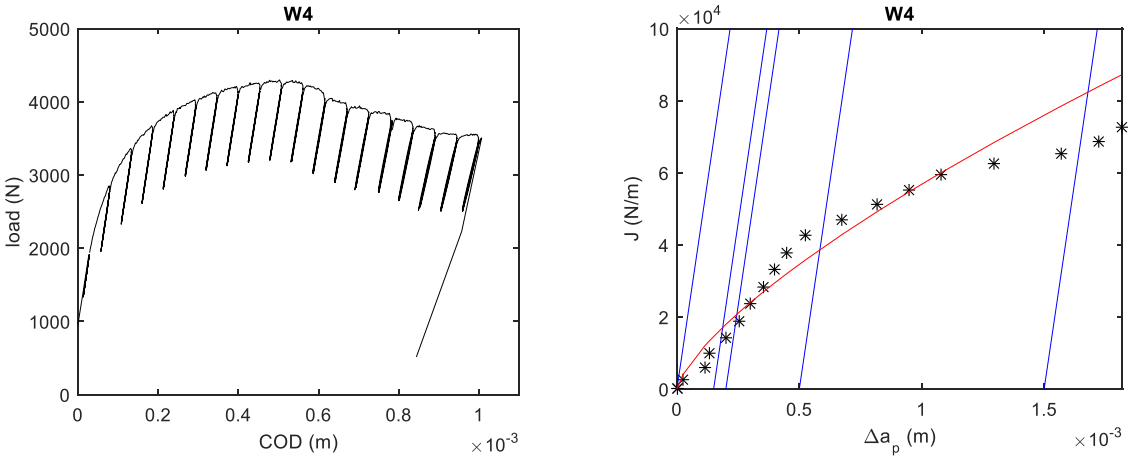

Figure C.3: Results for specimen W4: a) Load versus COD graph and b) J versus Δa_p.

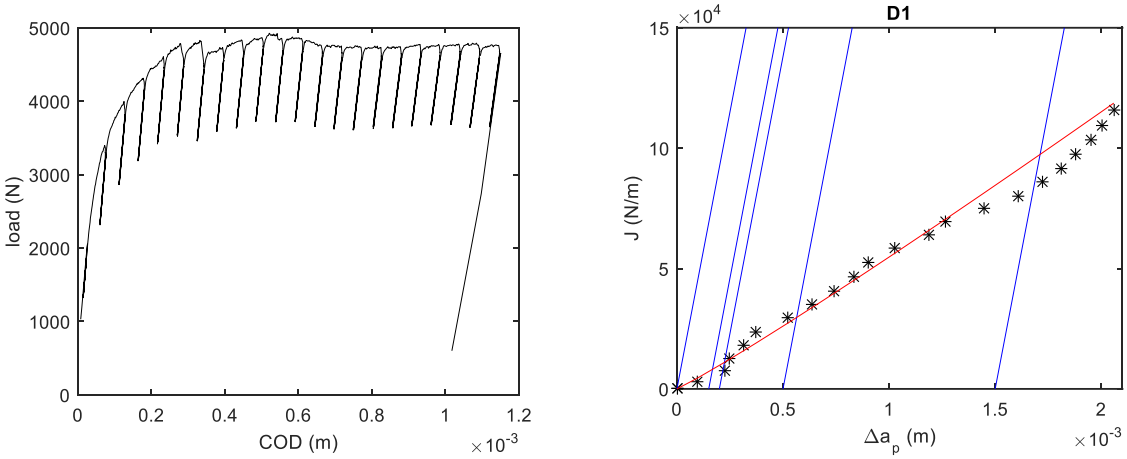

Figure C.4: Results for specimen B1: a) Load versus COD graph and b) J versus Δa_p.

APPENDIX D: CONSTANTS C_N FOR THE ECCENTRIC INTERNAL CRACK

	Constants								
ε	2	3	4	5	6	7	8	9	10
0	0,5948	0	0,4812	0	0,3963	0	0,3367	0	0,2972
0,02	0,5726	0,0339	0,4462	0,0315	0,3548	0,0433	0,2917	0,0464	0,2498
0,04	0,5535	0,0639	0,4173	0,0574	0,3234	0,0759	0,2608	0,0788	0,2208
0,06	0,5371	0,0903	0,3936	0,0785	0,2998	0,1003	0,24	0,1014	0,2035
0,08	0,5231	0,1134	0,3743	0,0958	0,2823	0,1185	0,2263	0,1172	0,1939
0,1	0,5112	0,1335	0,3585	0,1099	0,2694	0,1319	0,2175	0,1281	0,189
0,2	0,4761	0,1975	0,3155	0,1485	0,2428	0,1576	0,2073	0,1467	0,1904
0,3	0,4635	0,2179	0,3016	0,1571	0,2374	0,1538	0,2083	0,1428	0,1936
0,4	0,4555	0,2126	0,2922	0,1507	0,2292	0,1405	0,2012	0,131	0,186
0,5	0,4404	0,1939	0,2754	0,1364	0,2113	0,1236	0,1832	0,1154	0,1677
0,6	0,4123	0,1707	0,2473	0,1192	0,1841	0,1061	0,1574	0,0989	0,1429
0,7	0,3704	0,1495	0,2108	0,1029	0,1529	0,0905	0,1298	0,0841	0,1175
0,8	0,3197	0,1341	0,1735	0,0899	0,1246	0,0783	0,1063	0,0727	0,0969
0,9	0,2729	0,1264	0,1449	0,0814	0,1051	0,0706	0,091	0,0656	0,0837
1	0,25	0,125	0,1328	0,0781	0,0967	0,0671	0,0836	0,0618	0,0766

	Constants								
ε	11	12	13	14	15	16	17	18	19
0	0	0,2713	0	0,2535	0	0,2404	0	0,23	0
0,02	0,0533	0,2219	0,0576	0,2021	0,0627	0,1873	0,0669	0,1756	0,0711
0,04	0,0878	0,1948	0,092	0,1774	0,0974	0,165	0,1011	0,1558	0,1048
0,06	0,1099	0,181	0,1127	0,1668	0,1167	0,1575	0,1189	0,1512	0,1212
0,08	0,1241	0,1749	0,1251	0,1638	0,1275	0,157	0,1284	0,1528	0,1294
0,1	0,1331	0,1731	0,1325	0,1644	0,1336	0,1594	0,1334	0,1567	0,1337
0,2	0,1447	0,1817	0,1413	0,1772	0,1396	0,1748	0,1383	0,1735	0,1376
0,3	0,1387	0,1854	0,1355	0,1806	0,1336	0,1776	0,1324	0,1757	0,1318
0,4	0,1266	0,1771	0,1236	0,1715	0,1218	0,1679	0,1205	0,1654	0,1197
0,5	0,1111	0,1585	0,1082	0,1526	0,1063	0,1487	0,1049	0,1459	0,104
0,6	0,0949	0,1343	0,0921	0,1289	0,0902	0,1252	0,0888	0,1225	0,0877
0,7	0,0804	0,1104	0,0779	0,106	0,0761	0,103	0,0747	0,1007	0,0736
0,8	0,0694	0,0915	0,672	0,0881	0,0655	0,0858	0,0643	0,084	0,0632
0,9	0,0626	0,0796	0,0606	0,077	0,0591	0,752	0,0579	0,0737	0,057
1	0,0585	0,0724	0,0562	0,0697	0,0544	0,0678	0,0529	0,0662	0,0517

Source: T. Fett and D. Munz, Stress Intensity Factors and Weight Functions, Southampton, UK, Computational Mechanics Publications,1997